UNIVERSITÀ DEGLI STUDI DI ROMA "TOR VERGATA"

FACOLTA' DI SCIENZE
MATEMATICHE FISICHE NATURALI

DOTTORATO DI RICERCA IN ASTRONOMIA

XXI CICLO (A.A. 2008/2009)

Analysis of the Rotational Behaviour and Evolutionary Scenarios of Accreting Millisecond Pulsars

Alessandro Papitto

Relatori: Prof. Roberto Buonanno,
Prof. Luciano Burderi

Coordinatore: prof. Pasquale Mazzotta

Contents

Abstract

I present in this study an analysis of the spin and orbital evolution of Accreting Millisecond Pulsars (AMSP). These sources are neutron stars (NS) emitting X-rays because of the accretion of the mass transferred by a nearby companion star, through an accretion disc. As AMSP own a magnetosphere that truncates the disc before the NS, thus channelling accreted matter in the vicinity of the magnetic poles, their X-ray emission is pulsed at the NS spin period, which is of few milliseconds for these NS.

My scientific project relies on the use of this invaluable property to evaluate the rotational reaction of the NS to the accretion of mass. As a matter of fact, mass orbiting in an accretion disc has a large specific angular momentum, especially close to the NS; when this matter is accreted it releases its angular momentum to the NS, that is therefore expected to accelerate. It is indeed through this mechanism that AMSP have been spun up to their present extreme rotational velocities (up to ~ 0.1 times the speed of light in vacuum). I therefore used the X-ray pulsations coming from the NS surface as a clock, to precisely measure the tiny variations of the accretor spin frequency during accretion. This is ultimately a measure of the accretion torques acting on the NS and allows a model dependent estimate of the physical quantities regulating these torques, that are mainly the rate at which mass is accreted on the NS and the magnetic field strength.

Such measurements can be very tricky, especially for an AMSP. In fact, they accrete mass for at most few months, and because of the large inertia of the NS, the expected frequency variations are of only few parts on 10^{10}. Therefore, Standard timing techniques were first tailored to the particular case of these sources, allowing for the first time reliable estimates of their spin state. Six among the ten AMSP discovered so far are considered in this work. In particular, the two sources I focused on the most show how the simple picture of the NS spin-up outlined above does not hold in every case. In fact, the outcome of accretion can also be the deceleration of the NS. The theories of accretion interpret this behaviour in terms of the interaction between the magnetic field and the accretion disc. This interaction may then brake the compact object, especially if the accretor is very fast. I show in this work how these spin-downs are effectively observed, and how this allows an estimate of the NS magnetic field.

The basics of the accretion picture onto a fast object are tested not only on the basis of a temporal analysis. I show in fact how the spectral information also supports the theoretical expectations. In particular a high spectral resolution observation of an AMSP shows the presence of a broadened iron line in its X-ray spectrum. The only viable location for the formation of a so-broadened line is the inner part of the accretion disc, thus allowing for the first time the measure of the size of the inner disc rim of a pulsar. This measure turns out to be perfectly consistent with the small range allowed by theories, thus representing a fundamental test of their consistency.

Temporal analysis also allows to enlighten the evolution of the binary system the NS belongs to. In the only case of a system which recurred more than once, we could find evidence of an evolution faster than expected. We interpret such behaviour as an indication of relevant mass lost by the system, as this mass can carry away with it the angular momentum needed to match the observations.

This supports the hypothesis that a rotation powered pulsar switches on during the quiescent phases of the binary. Moreover, this observation can be considered as one of the few astrophysical cases in which a highly non conservative evolution is directly observed.

The results presented in this thesis cover many aspects of the physics of these fast accretors, and show how X-ray temporal and spectral analysis can jointly supply a wealth of information on the physical state of these extreme and puzzling systems. These results confirm the basic theoretical expectations, also opening several very promising issues to shed some light on the environment surrounding these fast rotating NS and on their actual evolutionary progeny.

Estratto

In questo studio viene presentata un'analisi dell'evoluzione rotazionale ed orbitale delle Pulsar X al millisecondo (AMSP). Queste sorgenti sono delle stelle di neutroni (NS) che emettono energia in raggi X, accrescendo tramite un disco di accrescimento la materia trasferita da una stella compagna. Poichè le AMSP posseggono una magnetosfera che interrompe il flusso di materia nel disco prima della superficie, concentrando l'accrescimento nelle vicinanze dei poli magnetici, l'emissione X è pulsata al periodo di rotazione della stella, che è di qualche millisecondo per queste NS.

Il mio progetto di ricerca si basa sull'utilizzo di questa proprietà fondamentale per valutare la reazione della NS all'accrescimento di materia. Infatti le particelle di un disco di accrescimento posseggono un elevato momento angolare specifico, specialmente nelle vicinanze della NS; quando la materia viene accresciuta il suo momento angolare viene rilasciato alla stella, che tende quindi ad accelerare. È proprio questo meccanismo che ha condotto le AMSP alla estrema velocità di rotazione attuale (un decimo della velocità della luce). Avendo a disposizione un tale orologio solidale alla stella, ho utilizzato le pulsazioni X provenienti dalla superficie per misurare le piccole variazioni della frequenza di rotazione della NS mentre accresce massa. Se ne trae quindi una misura delle coppie che agiscono su di essa e la stima delle grandezze che le regolano, principalmente il tasso di accrescimento di massa e l'intensità del campo magnetico della NS.

Tali misure sono estremamente delicate, specialmente nel caso delle AMSP. Infatti queste sorgenti accrescono massa al più per qualche mese e, a causa dell'elevata inerzia di una NS, la variazione di frequenza attesa è solamente di poche parti su dieci miliardi. Innanzi tutto le tecniche standard di timing sono state quindi adattate al caso particolare di questi oggetti, permettendo per la prima volta una misura affidabile del loro stato rotazionale. Sono state prese in considerazione sei delle dieci AMSP scoperte sin ora. In particolare, le due alle quali mi sono dedicato maggiormente mostrano adeguatamente come il semplice schema di accelerazione della NS delineato sopra non valga in ogni caso, e come una AMSP possa anche decelerare durante l'accrescimento. La causa di tale decelerazione è individuata dalla teoria dell'accrescimento nell'interazione tra il campo magnetico e il disco di accrescimento, interazione che può quindi rallentare la stella specialmente se questa ruota molto rapidamente. In questo lavoro mostro come questi rallentamenti vengono effettivamente osservati e come consentano di ottenere stime del campo magnetico della NS.

Gli elementi basilari delle teorie dell'accrescimento su un rotatore veloce sono stati testati non solo sulla base dei risultati dell'analisi temporale. Si mostra infatti come le attese teoriche siano supportate anche alla luce dell'informazione spettrale. In particolare l'osservazione di una AMSP mostra la presenza di una riga del ferro molto larga nel suo spettro in raggi X. Essendo la regione interna del disco di accrescimento l'unica possibile regione di formazione di una riga così larga, è stato possibile misurare, per la prima volta nel caso di una pulsar, l'estensione del bordo interno del disco. Il valore misurato è perfettamente in accordo con il ristretto intervallo permesso dalla teoria, rappresentando così una verifica fondamentale della sua consistenza.

L'analisi temporale consente inoltre di valutare l'evoluzione orbitale del sistema binario al quale appartiene la NS. Nell'unico caso di un sistema che abbia mostrato più di un episodio di attività, si è trovata evidenza di una evoluzione molto più rapida di quella attesa. Questo comportamento può essere spiegato solo in termini di rilevanti perdite di massa, massa che porta con sé la quantità di momento angolare necessaria per rendere conto dell'evoluzione misurata. Ciò supporta inoltre l'ipotesi che tali perdite di massa siano dovute all'accensione di una pulsar alimentata dalla rotazione durante le fasi di quiete del sistema. Questo può in definitiva essere considerato uno dei pochi casi astrofisici in cui viene osservata in tempo reale un'evoluzione altamente non conservativa.

I risultati presentati in questa tesi coprono quindi molti aspetti della fisica di questi sistemi, mostrando come l'unione dell'analisi temporale e spettrale possa fornire una gran quantità di informazioni su questi sistemi estremi e per certi versi sconcertanti. In definitiva sono state confermate le attese teoriche di base sull'accrescimento su NS veloci, ma si aprono anche diverse questioni che promettono di gettare maggiore luce sulla fisica dell'ambiente immediatamente circostante la stella e sull'effettiva linea evolutiva delle AMSP.

1

Neutron Stars and their emission.

The case of Accreting Millisecond Pulsars (AMSP) concerns many physical and astrophysiscal issues, as these objects have a quite complex evolutionary history. This peculiarity can also be viewed as an indication of how much we know about these systems. Such a knowledge is yielded by the many observational probes we have about them. As a matter of fact, apart from the usual observables of an X-ray binary, such as its luminosity and its X-ray spectrum, here we also know the neutron star spin frequency, therefore allowing a deep understanding of its rotational state and of the dynamics of the binary system it belongs to. A broad introduction of the various topics involved in the study of these systems appears therefore mandatory. Despite this chapter is not intended (and could not be) as a complete review, we first introduce the physics of a neutron star (Sec. 1.1), and then the emission mechanisms that make a neutron star shine (Sec. 1.2). Despite AMSP are accretion powered neutron stars (Sec. 1.4), they represent the evolutionary link to produce rotation powered millisecond pulsars, according to the 'recycling' scenario of old neutron stars (Sec. 1.6). The emission mechanism of rotation powered pulsars is therefore also discussed (Sec. 1.3). The analysis presented in this thesis mainly deals with the rotational reaction of the neutron star to the torques exerted by the disc accretion of matter, so that the current theoretical understanding of this issue, as well as of the pulsar phenomenon, is broadly reviewed in Sec. 1.5. Finally, as this work presents also the observation of the orbital evolution of one of the AMSP discovered so far, the basics of the orbital dynamics in a transferring-mass binary system are given in Sec. 1.4.4.

1.1 Neutron Stars: basics and historical remarks.

A Neutron Star (NS hereafter) is an auto-gravitating object kept in equilibrium by the degeneracy pressure of the neutrons that mainly constitute it. This pressure ensues from the repulsive force between identical fermions (like neutrons are) when brought at nuclear distances ($\simeq 10^{-13}$ cm = 1 fm). The measured masses of NS are generally between $M_\odot$ and $\sim 2\ M_\odot$ (see e.g. Lattimer and Prakash, 2007 for a review). NS radii in the range $8 - 15$ km are therefore required to reach the densities ($\sim 10^{14} - 10^{15}$ g/cm^3) that make effective the degeneracy pressure among neutrons in cancelling out the gravitational tendency to collapse.

The idea of a possible gravitationally bound state for an object composed by neutrons long preceded the first observational evidences for their existence. The

concept of degeneracy pressure quickly followed the statement of the exclusion principle by W.Pauli in 1924. According to this principle, two (or more) particles cannot belong to the very same quantum state if the particles composing the system are of semi-integer spin (see e.g. Landau and Lifsits, 1976). First proposed to explain the regularities observed in the distribution of electrons around a nucleus, the exclusion principle can be viewed as the quantum rewriting of the common-sense principle of impermeability of bodies. Two identical particles are perfectly indistinguishable in the context of quantum mechanics, and the wave function describing their states has therefore to have a well definite symmetry under the exchange of particles. The relativistic theory of quantum mechanics subsequently pointed out how half integer spin particles (denoted fermions) have to be found in an antisymmetric state, while integer spin particles are described by symmetric wave functions. Therefore fermions cannot occupy the very same state and a repulsive force sets if they are forced to lie next to each other .

The first astrophysical application of the exclusion principle was proposed by Fowler (1926) to explain the large densities and effective temperatures observed in white dwarfs. Fowler guessed that the pressure equilibrium in these objects was set by the degeneracy pressure of plasma electrons, and it is somehow curious that the basic ingredient for the stability of a compact object was realized 3 yr before thermonuclear reactions in the core were identified as a viable source to sustain the equilibrium of a non degenerate star (Atkinson and Houtermans, 1929). It is for this reason that, at that time, the indefinite contraction of a degenerate core was one of the ideas proposed to solve the problem of the energy generation in a star (see below). It is worth noting that in a degenerate object the pressure is almost fully decoupled from the temperature, and depends only on the density, and therefore on the mass, of the object. It follows that the more massive the object, the smaller it is in size, as to develop the pressure required to sustain a larger mass the object must attain larger densities. This leads to a so-called inverse mass-radius relation, i.e. $M \propto R^n$, with $n < 0$. However, degenerate electrons cannot sustain an arbitrarily large mass, as at densities $\rho \gtrsim 10^7$ g/cm^3 they become relativistic and the degeneracy pressure scales less steeply with the density. As a consequence, equilibrium configurations set by degenerate electrons can be found only for masses below the so-called Chandrasekhar limit, $M_{Ch} \simeq 1.4(\mu_e/2)^2 M_\odot$, where μ_e is the average number of nucleons per free electron (Chandrasekhar, 1931).

Soon after the discovery of the neutron (Chadwick, 1932), it was realized that a stable configuration can be obtained also for masses beyond the Chandrasekhar limit, thanks to the pressure ensued by degenerate neutrons. In the ideal scenario of an ensemble of completely degenerate electrons, the beta decay ($\mathrm{n} \rightarrow \mathrm{p} + \mathrm{e}^- + \bar{\nu_e}$) is inhibited by the total occupation of the electrons phase space. The reciprocal reaction ($\mathrm{p} + \mathrm{e}^- \rightarrow \mathrm{n} + \nu_e$) takes therefore the lead. Ideally adding matter to a star with a mass larger than M_{Ch} leads to its contraction and to the neutronization of matter, until the densities become large enough ($\rho \gtrsim 10^{13}$ g/cm^3) that neutrons start becoming degenerate. At this point, the degeneracy pressure of neutrons is such to keep the object in a stable configuration (that is, a NS). The existence of NS was first invoked by Baade and Zwicky (1934) to explain the anomalously large luminosities emitted by supernovae (SN hereinafter). To account for the energy radiated and conveyed in the expelled mass motion they in fact guessed that a massive compact object should form, yielding the needed decrease of gravitational energy. As already stated, it was

only in those years that thermonuclear reactions as the p-p chain, and subsequently the CNO chain, were identified as the energy source for main sequence stars (Bethe and Critchfield, 1938; Bethe, 1939). Nevertheless these channels were not as ready as required to explain the energy output of giants, and it was therefore suggested that a degenerate neutron core could better match the observations (Gamow, 1938).

These considerations yielded a renewed interest in NS, and various authors, among whom L.Landau, tried to establish the minimum mass for a stable configuration ensued by degenerate neutrons. Oppenheimer and Serber (1938) derived a value close to 0.1 $M_{\odot}$, which was too large to account for the sizes and masses of Giants. Subsequently, Oppenheimer and Volkoff (1939) worked out an Equation of State for a NS, including the general relativity prescription about space-bending and accordingly considering the pressure as a source of field. The maximum equilibrium mass was derived as large as $\simeq 0.7\ M_{\odot}$, which is lower then the limiting mass for a white dwarf. The authors therefore stated that it seemed "unlikely that static neutron cores can play any great part in stellar evolution". What the authors did not take into account is the repulsive strong nuclear interaction among nucleons that takes place when the particles are brought at 'nuclear' distances ($\lesssim 1.4$ fm). This further raises above the Chandrasekhar limit the maximum mass that can be attained by an equilibrium configuration, thus 're-admitting' NS in the ensemble of viable astrophysical objects.

Interest in NS renewed in the late sixties, this time on an observational basis. J.Bell, a doctoral student at the University of Cambridge, observed a 1.337 s coherent modulation in the radio emission arising from the source CP1919 (Hewish et al., 1968, but see also Bell Burnell, 1977). This discovery was particularly stunning as the signal was highly coherently modulated, with variations of the period of 1 part on 10^{10}. One of the proposed scenario to explain a similar behaviour relied on the radiation emitted by relativistic electrons accelerated by the magnetic field of a rapidly rotating NS (Gold, 1968). The discovery of $P_C = 0.33$ ms pulsations from the Crab Nebula (Staelin and Reifenstein, 1968) proved this interpretation to be the right one. Assuming that the coherent signal reflects some property that regards the emitting object as a whole, its size $R_\star$ is in fact limited by a simple causality principle: any action or signal connecting the whole object cannot travel faster than light does in vacuum. We have therefore $R_\star < cP_C \simeq 1 \times 10^9$ cm $\simeq 10^{-2}\ R_{\odot}$, an indication that a degenerate object is probably involved in the emission. Furthermore, if it is assumed that the regular periodicity reflects the spin period of the star, one can equate the gravitational attraction at the surface of the object and the centrifugal action due to rotation, obtaining an upper limit on the radius of the object given its mass. It can be easily obtained that $R_{break} = [GMP_C^2/(4\pi^2)]^{1/3} = 1.6 \times 10^7 m^{1/3}$ cm, where m is the mass in solar units. This result, combined with the fact that the object has a solid surface from which the periodic signal is thought to arise, and therefore cannot be a black hole candidate (BH in the following), leaves almost no room for candidates other than a NS.

While radio astronomy thenceforth kept discovering radio pulsars with periods spanning to few 10^{-2} s to $\simeq 10$ s, the newly-born X-ray astronomy started to achieve its first results during the sixties. The first extrasolar X-ray source (Sco X-1) was discovered by Giacconi et al. (1962), and it's not surprising it is the brightest extrasolar X-ray object observable from the Earth. Sco X-1 emits up to 1.4×10^{-19} erg cm^{-1} s^{-1} Hz^{-1} in the 2–10 keV energy range (for an overall

X-ray luminosity of $\sim 2 \times 10^{38}$ erg s^{-1}; see e.g. Liu et al., 2007a). Its faint blue optical counterpart (Sco V1818) was identified only few years later. The system is in fact outclassed by more than 100 nearby stars in the optical, but outshines the others in X-rays. The huge amount of energy emitted quite continuously at high frequencies led Shklovskii (1967) (but see also Zel'Dovich and Shakura, 1969) to identify the accretion of mass as the most probable mechanism to power the source. While the first discoveries were achieved by hooking-up proportional counters on short-lived rockets, the first X-ray satellite was launched in 1970, Uhuru, performing the first survey of the X-ray sky. The longer time baseline granted by a satellite allowed Giacconi et al. (1971) to discover 4.8 s pulsations in the X-ray emission of Sco X-3, a source already observed in the 'rocket era'. The identification of a NS in the system was then immediate. Moreover, the period of the signal is sinusoidally modulated on a 2 d time-scale. Schreier et al. (1972) interpreted this modulation in terms of Doppler effect, a clear evidence that the source belonged to a binary system. The measured orbital parameters also allowed an estimate of the masses of the two stars, showing how a 20.5 $M_\odot$ star is orbiting the $\sim$1 $M_\odot$ X-ray source. This discovery put almost beyond any doubt the existence of NS, emitting X-rays as they accrete mass from a companion star.

In those years the structure of a NS was further investigated. Only by imposing the causality principle (the velocity of sound has to be lower than c), the Le Chatelier principle (the pressure has to be a monotonically non-decreasing function of density, i.e. no collapse is undergoing), and taking into account general relativity effects such as the field generated by the pressure, Rhoades and Ruffini (1974) found a very general and stringent upper limit for the NS mass, $M_{lim} = 3.2 M_\odot$. NS are the densest object without an event horizon and so represent ideal laboratories to study the Equation of State (EoS) of matter at high densities. The range in allowed masses and radii is depicted in Fig. 1.1 from Lattimer and Prakash (2007), where the various EoS for neutronic matter are also plotted. The reader is referred to their work for a recent and complete review on this subject. We recall that a stiffer EoS implies a larger radius given its mass, as the repulsive force among neutrons is supposed to be more intense. In Fig. 1.1, blue and green regions can be excluded on the basis of different reasons. Dark blue region is excluded by assuming that the NS is in a stable configuration according to General Relativity (GR hereafter), that is, its radius is not smaller than its Schwarzschild radius ($R_S = 2GM_*/c^2$); no known force could otherwise impede the gravitational collapse. Light blue excluded region follows from the requirement that the pressure in the interiors of the NS is finite, light green region follows instead from the assumption that the causality principle is not violated (Lindblom, 1984). Ultimately the lower dark green region is excluded as the fastest known pulsar (J1748–2446ad, $\nu = 716$ Hz, Hessels et al., 2006) must not be faster than the rotation speed that would imply a centrifugal break up of the NS.

From the beginning, the origin of a NS was thought in terms of one of the possible remnants of a SN explosion. This is not only because the formation of a compact object helps accounting for the energy output of a SN (see above), but also because many (even if not all) young rotation powered NS are discovered in association with SN remnants. The Crab Pulsar is a clear example of this association. SN are classified in two broad classes (type I and II) on the basis of the presence of hydrogen lines in the emitted spectrum. A Type I SN lacks

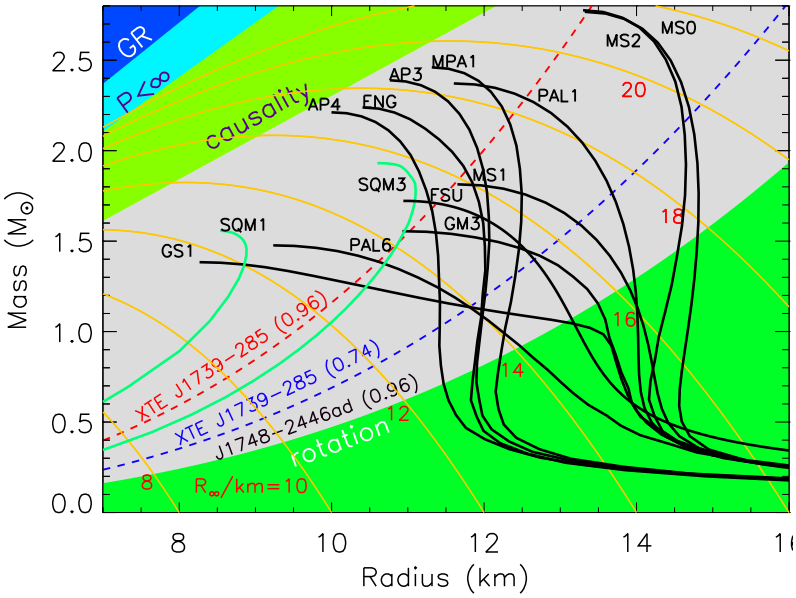

Figure 1.1: Typical relations assumed for NS masses and radii (see Lattimer and Prakash, 2001 for notation) are shown as black curves. Green lines refer to self bound quark stars. Orange tracks show different values of the so called radiation radius $R_*/\sqrt{1-2GM/R_*c^2}$. The dark blue region is excluded by the GR constraint that the radius must be larger than its Schwarzschild radius, $R_* > R_S = 2GM/c^2$; the light blue region is excluded after the request that the pressure is finite at the NS centre, $R_* > 9/8R_S$; the green region is excluded by causality $R_* > 1.45R_S$ and the lower dark green region is excluded by the requirement that the fastest confirmed pulsar, J1748–2446ad ($\nu = 716$ Hz, Hessels et al., 2006), is below the centrifugal break up limit (see Eq. 12 of Lattimer and Prakash, 2007). The red and blue dashed curves represent analogous lower limits if the spin frequency of 1122 Hz claimed by Kaaret et al. (2007) for XTE J1739-285 is confirmed. This figure is from Lattimer and Prakash (2007).

hydrogen and reaches an optical magnitude of ∼-20 ($L_{opt} \sim 4 \times 10^{40}$ erg/s), while type II show an hydrogen content and are typically fainter by a factor 10^3. Type I SN are further divided in three kinds: (i) type Ia lack He also, while showing Si absorption lines. They are thought to be white dwarfs reaching the Chandrasekhar limit, possibly because of accretion, therefore collapsing; as this limit is the same for all white dwarfs composed by the same elements, the energy output is grossly constant, so that type Ia SN are used as standard candles when building a distance ladder; (ii) type Ib and Ic do not have Si lines, and are thought to be produced by a massive star (possibly a Wolf-Rayet star) which has completely lost its hydrogen envelope. Type II SN are instead the natural endpoints of massive stars ($M \gtrsim 8$ M$_\odot$), and represent the most viable option to produce a NS or a BH as a remnant (see Ghosh, 2007, and references therein, for a complete review of this issue).

After having burnt H and He in its nucleus, a star of initial mass above 8 M$_\odot$ is also able to ignite the yield of C, Ne, O and Si at successive stages. While for masses $\simeq$ 8–9 M$_\odot$, the carbon ignition happens in a degenerate environment

and a positive feedback determines the complete disintegration of the nucleus[1], the burning stages proceed 'quietly' if the star has a mass above 11 $M_\odot$, and an iron core ultimately forms in the centre. However, thermonuclear fusion of iron atoms, as well as that of heavier atomic species, is an endothermic process and needs energy to proceed rather than producing it. The thermonuclear energy source which granted the dynamical and thermal equilibrium of the star from the Zero Age Main Sequence on is therefore on its way to be shut off completely. Neon burning carries on in the surrounding shells, determining a rapid growth of the iron core, until it reaches its Chandrasekhar limit (which in the environment of a hot core sustaining a 15 $M_\odot$ is 1.34 $M_\odot$). The core starts therefore to collapse, even if the process is slowed down to some extent by the copious emission of thermal neutrinos that helps removing a large part of the gravitational binding energy. The collapse ends when nuclei and atoms approach one next to the other and repulsive forces set up. The nucleus then bounces back and the interaction with the infalling mass determines a supersonic shock; this shock therefore starts travelling through the stellar structure, there releasing its energy. The energy deposition is nevertheless too fast to let the shock to reach the stellar surface, and to explain the observed SN explosions. It is nowadays believed that the shock is revived by the action of neutrinos emitted by the nucleus (it has to be noted that the great majority of the energy liberated by the gravitational collapse is indeed lost by the star in the form of neutrinos); due to the large densities, neutrinos can in fact actively interact with the stellar matter and are able to release enough energy just behind the location of the shock stalling to boost it towards the stellar surface.

When the envelope mass is lost, the proto-NS in the centre stops accreting mass, and achieves a global collapse. If at this time the nucleus core is heavier than the Oppenheimer-Volkoff limiting mass (that is, the complete analogue of the Chandrasekhar mass for a NS, $\simeq 5.7$ $M_\odot$), the collapse terminates in a BH, which can be defined as an object whose radius is smaller than its Schwarzschild radius, and which should therefore possess an event horizon[2]. If the core mass is lower than this threshold, the collapse is stopped when the density is so large that matter neutronizes (see above), and the NS is born. The successive stages are governed by the cooling of this, still hot, object. The NS cooling mainly happens through the emissions of neutrinos. Before the NS becomes transparent to these neutrinos, large convective motions involve the core structure, possibly leading to an amplification of the trapped magnetic field, as argued by the magnetar model to explain evidences of field in excess of 10^{15} G. However, it has to be noted that a NS is naturally a strongly magnetized object, as the magnetic flux ($\sim BR^2$) is conserved during the collapse. An initial value of the magnetic field of few hundreds of Gauss is enough to produce a NS field of $\sim 10^{12}$ G, due to the dramatic reduction of the radius by a factor ~ 70000 that concerns a Sun-like star when it contracts to a NS. On the other hand, we also expect the newly-born NS to be rapidly spinning, as the star angular momentum ($\sim vR$) is also conserved. The emitted neutrinos carry away most of the gravitational binding energy of the object, and dictate the cooling time of

[1] In a completely degenerate environment, the pressure is decoupled from the temperature, and the star becomes aware of the temperature rise due to the carbon burning only when it involves the whole nucleus and the degeneracy is removed. The dynamical reaction is therefore sudden and the star explodes, leaving no remnant at all.

[2] The formation of a BH is thought to descend from stars of $\gtrsim 30$ $M_\odot$

the star, which ultimately reaches temperatures of $\sim 10^6$ K in 10–100 yr. The cooling proceeds through various mechanism governed by neutrinos and, later, by photon cooling, until the NS becomes an undetectable cool object, unless other emission channels (e.g. rotation and accretion, see the next chapter) make these object shine in the electromagnetic spectrum.

1.2 The NS emission channels.

NS can be split in few categories, depending on the mechanism powering their emission. Namely, it is possible to recognize:

- **Rotation-powered NS**. NS possess the larger magnetic fields observed in the universe ($B_S \lesssim 10^{14}$–10^{15} G). The emission of energy from rotation-powered NS is due to the rotation of the electro-magnetic dipole, and leads to a simultaneous deceleration of the object. Rotation-powered NS can be observed as pulsars, if the voltage drop between the magnetic poles is large enough to accelerate charges and the line of sight is favourable (see 1.3), or by means of the nebular radiation arising from the interaction of the relativistic wind of particles emitted by the NS with a surrounding nebula. Rotation powered NS can be both isolated and part of a binary system.

- **Accretion-powered NS**. Their emission is due to the release of gravitational binding energy as mass transferred from a companion star hits the NS surface. Therefore they all belong to binary systems. A pulsar is observed in an accretion-powered system only if the magnetic field is large enough to form a magnetosphere around the NS, therefore channelling the accreted matter near its magnetic poles.

- **Magnetic-powered NS**. They show X-ray luminosities too large for the rotation power to account for, and no sign of an ongoing accretion process is observed. According to the magnetar model their emission is thought to be due to the decay of a huge ($\gtrsim 10^{14}$ G) magnetic field. They can also exhibit Giant Flares ($E \sim 10^{44}$–10^{47} erg), interpreted as global magnetic-field reconnection events.

- **Nuclear-powered NS**. As a subset of accretion-powered NS, these objects emit thermonuclear flashes as mass accumulated because of accretion goes beyond a certain critical density. The emission can be pulsed because of the containment of the energy by the magnetic field.

- **Thermal-powered NS**. These NS simply emit their heat content. The heat can be either the residual since the NS formation, or can be renewed by external or internal source, such as accretion.

Rotation and accretion power were the first means by which NS were observed, and nowadays still remain the two main engines that make observable these, otherwise cold, objects. Even if they are accretion-powered, the class of objects subject of this thesis, the AMSP, represent a link among the sources powered by these two emission mechanisms. Both are therefore reviewed in the following.

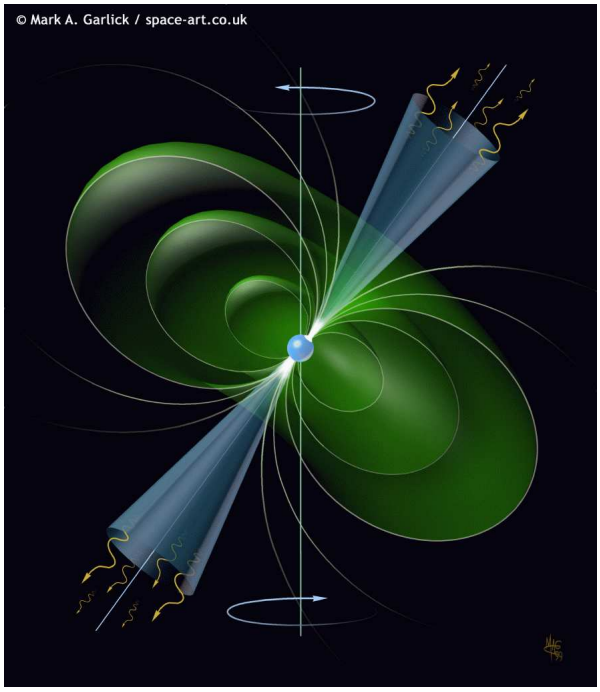

Figure 1.2: Artistic view of a rotation powered pulsar from http://www.space-art.co.uk. The emission is concentrated in the blue cone near the magnetic poles, and produces a lighthouse effect as the magnetic axis is offset from the rotation axis.

1.3 Rotation powered NS (Pulsars)

Historically, rotation powered pulsars were referred to as "Radio Pulsars" just because this was the first band of the electromagnetic spectrum the were discovered into. Soon after it was realized that their emission is mainly in the high energy part of the spectrum (X and γ ray; emission in radio band is just 10^{-6} of the overall energy budget), and when pulsars not emitting in the radio band were also discovered, the more physically motivated term "rotation-powered" started to be adopted. For reasons which will be clarified in the following, the emission of these objects is along the magnetic field lines, and is therefore concentrated near the magnetic poles of the NS. If the magnetic and rotation axes are misaligned, the NS rotation determines a modulation of the energy flux observed from the source, determining the so-called lighthouse effect. The period of these pulses is the rotation period of the NS that for this reason is called pulsar (pulsating star). An artistic view of a rotation powered pulsar, together with the NS magnetosphere (green) and the emission cone (blue), is plotted in Fig. 1.2.

Isolated Radio Pulsars in the Galactic field are all observed to decelerate, and after the discovery of the Crab Pulsar (PSR B0531+21) it was soon noted that the rotational energy released in the braking was enough to power the emission of the surrounding nebula (Ostriker and Gunn, 1969; Finzi and Wolf, 1969). As a matter of fact a decelerating rotating object releases energy at a

rate $\dot{E} = I\omega\dot{\omega} = -4\pi^2 I\dot{P}/P^3$, where I is the NS moment of inertia, $\omega = 2\pi/P$ the angular frequency, P the spin period, and $\dot{P}$ its time derivative. Assuming a value of I close to 10^{45} g cm^2, a measurement of P and $\dot{P}$ allows to find the energy budget available to power the emission,

$$\dot{E} = -4\pi^2 I\frac{\dot{P}}{P^3} \simeq 4\times 10^{33}\dot{P}_{13}P^{-3}erg/s, \qquad (1.1)$$

where $\dot{P}_{13}$ is the spin period derivative in units of 10^{-13}, and P is expressed in seconds.

For example, the Crab pulsar has a period $P_C = 0.033$ s and slows down at a rate $\dot{P}_C = 4.2\times 10^{-13}$; the rotational energy losses are therefore of the order of 10^{38} erg/s, well above what is needed to power the radiative emission of the pulsar and of its nebula ($\simeq 10^{35}$ erg/s). The rotational energy losses are therefore not only enough, but often much larger than what is actually observed as radiation in the accessible energy bands; for this reason rotation powered pulsars are also referred to as "dogs that don't bark in the night"(Arons, 2007), and the rest of the available energy is expected to power the emission of relativistic particles, which can also be collimated in jets steaming out along the magnetic axis.

The driver for the negative torque that brakes the NS was immediately searched in the rotation of a large magnetic field joint to the NS. Assuming that the magnetic field has a dipole configuration ($B(r) = \mu/r^3$, where $\mu = B_S R_\star^3$ is the magnetic dipole moment, B_S is the magnetic field strength at the surface, and $R_\star$ is the NS radius), and is offset by an angle α from the rotation axis, it is possible to derive the energy release rate from the Larmor formula, $\dot{E} = -2|\ddot{\mu}(t)|^2/3c^3$. The magnetic dipole moment varies with time because of rotation, leading to $\dot{E} = -\mu^2\omega^4\sin^2\alpha/6c^3$. Equating this relation to Eq. [1.1], one gets an estimate of the magnetic field strength needed to produce the observed braking:

$$B_S\sin\alpha = \left(\frac{3c^3 I}{8\pi^2 R_{NS}^6}\right)\sqrt{P\dot{P}} \simeq 3.2\times 10^{19}\sqrt{P\dot{P}}\,G \qquad (1.2)$$

This simple relation is often used to derive an order of magnitude estimate of the surface magnetic field of the pulsar. The first rotational powered pulsars discovered had spin periods in the range 0.1 – 10 s, and deceleration rates between 10^{-17} and 10^{-12}, indicating magnetic fields in the range 10^{10}–10^{13} G.

Even if it gets to a result not too far from those of more detailed calculations, this derivation of the rotational energy budget is nevertheless too simple. It can be shown in fact that a tilt between the magnetic and rotation axes is not required to power the emission (see e.g. Arons, 2007, and references therein). Indeed, as a NS is a good conductor, its charges must arrange themselves to cancel out the electro-magnetic force within the NS surface, i.e. $\mathbf{E}+(\mathbf{v}\times\mathbf{B})/c = 0$, where $\mathbf{v}$ is the rotational velocity of the star and $\mathbf{E}$ is the electric field. The rotation of the magnetic field therefore induces an electric field of the order $E \sim (\omega r/c)B_p$ at the NS surface, where B_p is the poloidal component of the magnetic field; it can be shown that the induced electric field has to have only a poloidal component (e.g. Vietri, 2006). To match the condition on the electromotive force stated above, currents develop and determine in turn a winding of the magnetic field, and therefore a toroidal component, $B_\phi \sim (\omega r/c)B_p$. The flux

of the Poynting vector, $\mathbf{S} = c\mathbf{E} \times \mathbf{B}/4\pi$, is therefore non zero and represents a significant channel of energy emission from the NS, indeed the dominant if the electromagnetic energy density overwhelms all the material energy densities (as it is the case for the space surrounding a non accreting NS). The field is expected to depart significantly from its dipolar structure at a radius R_d, which is of the order of the light cylinder radius $R_{LC} = c/\omega$, the radius beyond which the magnetic field lines cannot be connected to the NS anymore because of the causality principle. The rate of energy loss can therefore be calculated as:

$$\dot{E} = 4\pi R_d^2 \frac{E(R_d)B_\phi(R_d)}{4\pi} \simeq \left(\frac{\omega^4\mu^2}{c^3}\right)\left(\frac{R_{LC}}{R_d}\right)^2, \qquad (1.3)$$

which indeed gives the same qualitative result as Eq. [1.2]. A pulsar can then be considered as the prime example of an object that loses energy through a large scale Poynting flux.

The first pulsar models dealt with a rotator in vacuum (see Eq. [1.2]), but despite their ability in explaining grossly the energetic of a pulsar, it was soon clear that the large electric field induced by rotation in the direction normal to surface is so large that it overwhelms the gravitational force (Goldreich and Julian, 1969). Charges are therefore extracted from the surface in the attempt of cancelling the total electromagnetic force acting on them. Therefore, a charge density $\rho_G \simeq -\omega \cdot \mathbf{B}/(2\pi c)$ forms in the magnetosphere, resulting in a global short-out of the global electric field, which ultimately lets the magnetosphere to corotate with the star in a stationary configuration. Gaps are nevertheless thought to form where no charges are present, there letting an intense electric field to survive. It results that in these gaps charges can be accelerated to relativistic speeds (Ruderman and Sutherland, 1975). A highly magnetized NS is indeed an accelerator of particles (mainly electrons) powered by the electromagnetic field induced by rotation. The charge outflow follows the magnetic field lines as the energy density of the electromagnetic field is much larger than the material energy density, despite the presence of the above mentioned charge density. Moving along the field lines, the accelerated charges emit curvature and inverse Compton radiation with energies up to the γ-ray band. Those rays with energies above ~ 2 GeV are the seed for a copious creation of relativistic electron-positron pairs, which in turn break down the gap that started the accelerator mechanism. The so-created charged pairs further interact with the magnetic field, emitting in turn synchrotron radiation, in what is indeed an electromagnetic cascade. This model accounts nicely for the non-thermal part of the emitted spectrum (from the IR up to the X and γ-rays), where the largest part of the energy is emitted (more than 0.1 times the energy supply available from the deceleration). Plasma instabilities developing among plasma flows of different densities are instead identified as the origin of those electromagnetic oscillation that may lead to a radio coherent emission (e.g. Usov, 2002). It is worth noting that pulsations can be observed both in the soft and hard part of the broadband spectral energy distribution, and that their low duty cycle is due to the beaming of the radiation emitted by relativistic particles.

The acceleration of charges is thus widely recognized as the primer for the pulsar emission, but where this acceleration takes place, that is where the gaps are located, is instead still matter of debate (see e.g. Kaspi et al., 2004 for a review). According to polar-cap models, acceleration happens near the magnetic

poles at the NS surface; outer-gap models affirm otherwise that the acceleration takes place in vacuum gaps that form near the last closed field lines, that is near R_{LC}.

A more detailed discussion of the emission of rotation-powered pulsars is beyond the scope of this introduction. What is more relevant to realize is that , according to Eq. [1.2], it is possible to extract information on the NS magnetic-field strength, once P and $\dot{P}$ are measured. Nearly 1800 rotation powered pulsars were discovered at the time of the writing (Manchester et al., 2005, see http://www.atnf.csiro.au/research/pulsar/psrcat/). In Fig. 1.3 the periods and the period derivatives of these pulsars are plotted, and three large groups are immediately visible. Apart from the objects marked with a red asterisk in the upper right corner (belonging to the classes of Anomalous X-ray Pulsars and Soft Gamma Repeaters), which show luminosities well in excess of their rotation budget and are therefore thought to be magnetic-powered, the rotation-powered pulsars are divided in two classes given their spin period, 'classical' and 'millisecond' pulsars.

1.3.1 'Classical' Pulsar

The class is named so because it contains the first pulsars discovered. It is composed of $\sim$ 1500 objects with periods from few tenths to few seconds, and $\dot{P}$ in the range 10^{-17}–10^{-12}. Putting $\sin\alpha = 1$, we can use Eq. [1.2] to estimate their superficial magnetic fields, obtaining values in the range 10^{10} – 10^{13} G.

A practical time-scale to study the pulsar population is the spin-down age, τ_{SD}, defined as the time needed for a NS to reach its spin period P at the actual braking rate. It can be easily shown that if significant braking is supposed to have already taken place (i.e. $P >> P_0$, where P_0 is the spin period of the NS at its birth), τ_{SD} no longer depends on P_0 and can be expressed as:

$$\tau_{SD} \simeq P/2\dot{P}. \tag{1.4}$$

Spin down ages from 10^3 yr for the youngest objects, as the pulsar in the Crab nebula, to few $\times 10^9$ yr for the oldest, are found.

A first issue to note is that there are no pulsars with spin periods longer than $\sim$ 10 s; this non occurrence cannot be related to a selection effect involving the time needed to brake a NS to those periods, as $\tau_{SD}^{max} << t_H$, where $t_H \simeq 10^{12}$ yr is the Hubble time. It is instead commonly related to the effect of an energetic inability to produce the e^+-e^- pairs after a certain critical threshold on the period is leaped over. This is indeed often viewed as an indication of the fundamental role played by the pair production in making the emission mechanism of a pulsar to operate. In order to efficiently produce pair cascades, the Lorentz factor of the accelerated charges γ_{acc} must in fact be larger than a critical factor; while the critical threshold mainly depends on the chosen kind of pairs production (curvature radiation or inverse Compton scattering), it can be shown that γ_{acc} is proportional to the voltage drop along a field line ΔV, which is $\simeq (4\pi^2 R^3/2c^2)BP^{-2}$ (Harding et al., 2002, and references therein). Therefore, as a pulsar is thought to rotate very quickly at the moment of its birth, and decelerates throughout its life because of the magneto-dipole emission, it is expected to move from the left to the right in a diagram like the one of Fig. 1.3, until it crosses a so-called death line. This critical boundary corresponds to a

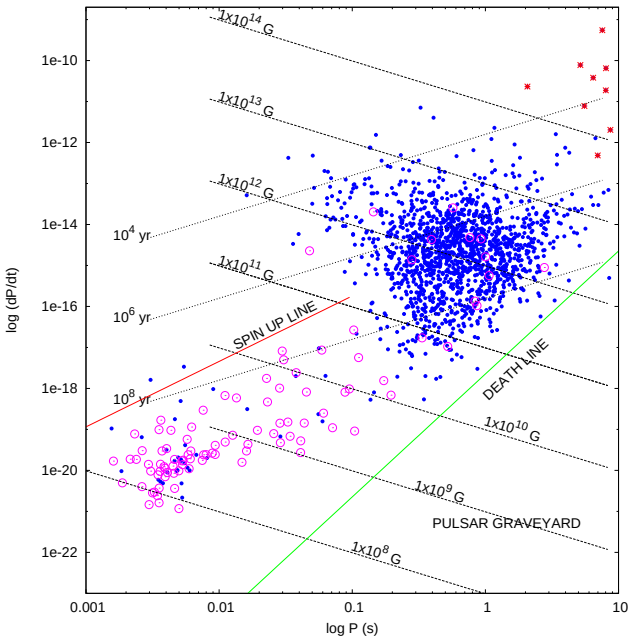

Figure 1.3: Plot of the spin periods and of the spin period derivatives of the $\sim$ 1800 pulsar discovered so far, as from the database at http://www.atnf.csiro.au/research/pulsar/psrcat/. Red asterisks are the magnetic powered pulsars (AXP and SGR), blue points are isolated rotation powered pulsars, while magenta circles refer to rotation powered pulsars belonging to binary systems. Dashed lines are the constant magnetic field lines derived using Eq. [1.2], where it was put $\sin\alpha = 1$. Dotted lines reflect the spin down ages evaluated using Eq. [1.4]. The green solid line is the locus of points with an expected voltage drop of 10^{11} V along the closed magnetic-field lines. Beyond this so-called 'death line', pulsars are not expected to accelerate efficiently charges any more and are therefore switched off. The spin-up line (red solid line) expresses the expected location for the recycled pulsar at the end of the accretion phase. It was evaluated using a relation like Eq. [1.29], but with different values of the indexes (a,b,c) for the relation $P_{eq} \propto \dot{M}^a B^b M^c$. This is because Eq. [1.29] is derived under the assumption of a disc dominated by gas pressure in its inner parts, while for fast rotating and weakly magnetized NS the assumption of a radiation dominated disc pressure has to be preferred (e.g. Ghosh, 2007 and references therein). The plotted relation refers to (a,b,c)=$(-0.38, 0.87, -0.82)$.

rotation induced voltage of $\simeq 10^{11}$ V, below which the accelerator, that is the pulsar, is not likely to work efficiently any more. From that moment on, if left alone, the NS is not able to accelerate the superficial charges and is therefore considered a 'dead-pulsar'.

It was also proposed during the first years of pulsar studies that the magnetic field should decay with time, accelerating the transition of pulsars towards the pulsar 'graveyard'. This was motivated by a certain disagreement between the spin down ages and the kinetic ages estimated for some pulsars, where the kinetic age of a pulsar is defined from its observed velocity and from its distance from the Galactic plane. However, this discrepancy became marginal when a larger pulsar statistics was achieved, and models with constant magnetic field are

nowadays preferred for isolated NS with fields $\lesssim 10^{14}$ G (e.g. Bhattacharya et al., 1992). As we'll see further, this is not the case for magnetars which are instead powered by the magnetic field decay, and for NS which can accrete mass from a compact star, as the accreted mass is thought to bury (or at least to reduce severely) the magnetic field under the NS surface.

1.3.2 Millisecond Pulsars

The first millisecond pulsar discovered was PSR 1937+21 (Backer et al., 1982). Its radio emission is in fact modulated at a period of 1.6 ms. This period is more than twenty times lower than the shortest known at that time, but this was not the only striking issue concerning this source. Most importantly, PSR 1937+21 was not found to possess any sign, such the presence of a SN remnant, of the extreme youth that this short period would have implied, according to the model for rotation powered pulsar. Arguing that the NS possesses a 'canonical' magnetic field of $\simeq 10^{12}$ G, the time needed to brake from the shortest rotation period allowed by the softest equation of state, $\simeq 0.5$ ms, to the period measured for PSR 1937+21, would be as short as ~ 750 yr. Even if a remnant was present, it would have been emitting 10^{-3}-10^{-4} times less than the Crab nebula, which was known to have exploded as a SN $\sim 10^3$ yr ago. From these considerations, Radhakrishnan and Srinivasan (1982) estimated a superficial magnetic field not larger than 4×10^8 G, and predicted a spin down rate of the order $\sim 10^{-19}$. Such a pulsar would then have been a completely different object with respect to the others already known.

At that time it was already proposed that the 59 ms pulsar PSR 1913+16, the first found with another NS companion, would have achieved that short period because of a long lasting phase ($\sim 10^7$ yr) of disc accretion of matter from a companion low mass star (Smarr and Blandford, 1976). Mass accreted from a disc possesses in fact a large specific angular momentum, and therefore spins up the NS. It will be shown in Sec. 1.6 that the minimum spin period that can be attained from the accretion of mass from a disc, before the NS attains spin equilibrium, grows as $B^{6/7}$.[3]. Periods as short as the ones attained by PSR 1937+21 were therefore identified by Alpar et al. (1982) as a clear evidence of a NS magnetic field in the range $10^8 - 10^9$ G. They also noted that this value would have put the source in the lower left corner of the plot of Fig. 1.3, in a region where the pulsar is expected to be outside the pulsar graveyard.

Therefore, the works of Radhakrishnan and Srinivasan (1982) and Alpar et al. (1982) independently stated that the first millisecond pulsar discovered had to have a magnetic field lower by 3-4 orders with respect to the pulsars previously found. Moreover, they proposed that the most probable evolutionary history for such an object was that of a 'recycling' of an old pulsar, which could shine again after having been beyond the death line, thanks to the acceleration imparted by the accretion of matter. The accretion of mass not only results in an acceleration of the star but also in a screening or burial of its magnetic field, how it was already envisaged in a seminal work by Bisnovatyi-Kogan and Komberg (1974). These hypotheses were brilliantly confirmed when the deceleration rate of PSR 1937+21 was measured to be $\simeq 1.2 \times 10^{-19}$, leading to variations of the

[3] A slightly different proportionality index is found if the disc is radiation-pressure dominated in its inner parts, as it extends very close to the NS surface (see also caption of Fig. 1.3) However, this does not change the qualitative picture presented here.

spin periods of 1 part on 10^{16} every second, a stability comparable with that of the most precise atomic clocks.

The problem with this interpretation was that, contrary to what is expected according to the recycling scenario, PSR 1937+21 has no companion star. Nevertheless the subsequent discovery of more millisecond pulsars, the majority of which belonged to a binary system, supported further the idea of recycled pulsars. The pathology with isolated millisecond pulsars was then tried to be recovered arguing that the companion star would have been lost in some way. This idea was then strikingly confirmed by the discovery a pulsar, PSR B1957+20, whose companion is actually being vaporized (Fruchter et al., 1988). The most appealing explanation was proposed by Ruderman et al. (1989) in terms of evaporation of the companion by the means of the high energy radiation emitted by the pulsar. Such objects are known as black-widow pulsars.

The class of millisecond pulsars is made of pulsars with spin periods $\lesssim 10$ ms and magnetic fields $\lesssim 10^9$ G, testifying their nature of old objects. At the moment ~ 150 sources satisfy these requirements, a great number of which resides in a globular cluster. This last occurrence is in itself an indication of how old these objects are, $t > 10^9$ yr. The fraction of millisecond pulsars members of binary systems is very high. The $\sim 90\%$ of millisecond pulsars in the Galactic disc has in fact a companion star, whereas this fraction among all known radio pulsars is at most $\sim 10\%$ (see Fig. 1.3, where pulsars belonging to a binary system are marked with a magenta circle). The population of MsP therefore strongly confirms the predictions of the recycling scenario, displaying an ensemble of old objects that could reach their short spin periods thanks to the accretion of matter from a companion. It will be shown in Sec. 1.4.4 that the companions should have been of low mass at the onset of the mass transfer ($M \lesssim M_\odot$) to fuel matter continuously to the NS, therefore enabling an effective spin-up to millisecond periods. It has to be finally noted that the MsP emission does not differ much with respect to 'Classical' PSR.

1.4 X-Ray Binaries

Accretion-powered NS belong to the broader class of X-ray binaries. These are systems in which a compact object (a NS or BH) accretes mass from a companion star, which overflowed or threw mass outside its sphere of gravitational influence. As a mass dm is accreted onto the compact object, denoted as M_1, either via a wind or an accretion disc, it releases its gravitational binding energy $dE = (GM_1/R_\star)dm$, where $R_\star$ is the radius of the accreting object. Taking the time derivative of the above relation yields an expression for the accretion luminosity:

$$L_X = dE/dt = GM_1\dot{M}/R_* \,. \tag{1.5}$$

The efficiency of this process is evaluated by comparison with the total rest energy available, $\eta_{accr} = L_X/\dot{M}c^2 = GM_*/R_*c^2 = R_S/2R_*$, where $R_S = GM_*/2c^2 = R_g/2$ is the Schwarzschild radius of the particular object, and R_g is called gravitational radius. The extraction of a significant amount of energy through this process requires the accreting object to be compact. Efficiencies as high as 0.2 are easily reached for a rotating NS . It has to be noted that the only possible emission in the case of a BH is the energy released before mass crosses the event horizon; nevertheless a rotating Kerr BH is able to convert up to 0.42

times the rest energy of the accreted mass. Accretion appears therefore as one of the most effective ways by which a star converts energy into radiation, as it is clear recalling that thermonuclear fusion of four hydrogen nuclei into one ^{4}He burns $\simeq 0.007$ times their rest energy.

The energy amount that can be released through accretion is indeed limited by the so called Eddington limit. This is the critical value of the luminosity for which the pressure of the emitted radiation (which Thomson scatters on the accreting electrons) overcomes the gravitational attraction towards the compact object. It is generally evaluated in the case of spherical accretion onto the compact object. The Eddington luminosity results to be a function only of the mass of the accreting object as:

$$L_{Edd} = \frac{4\pi G m_p c}{\sigma_T} M_1 \simeq 1.3 \times 10^{38} m \; erg/s, \tag{1.6}$$

where m is the mass of the accreting object in solar units, m_P the proton mass and σ_T the Thomson cross section. Using Eq. [1.5], this limit can be translated into a threshold of the accretion rate, which in turn depends only on the accretion radius:

$$\dot{M}_{Edd} = \frac{4\pi m_p c}{\sigma_T} R_* \simeq 1.5 \times 10^{-8} R_6 \; M_\odot/yr, \tag{1.7}$$

where R_6 is expressed here in units of 10^6 cm to fit the case of a NS.

To have an idea of which band of the electromagnetic spectrum the energy will be released into, we define a radiation temperature $T_{rad} = h\bar{\nu}/k$, where $\bar{\nu}$ is the frequency of a typically emitted photon, and k the Boltzmann constant. This temperature has to be in between the temperatures of the most and less thermally efficient ways of converting heat into radiation. T_{rad} must therefore be larger than the temperature of a black body emitting the accretion energy, $T_b = (L_X/4\pi R_*^2 \sigma)^{1/4}$, and lower than the temperature reached if the accretion energy is entirely converted in thermal energy, $T_{th} = GMm_p/3kR_*$. It turns out that for a solar mass NS, the emitted photons have energies between 1 keV and 50 MeV, clearly pointing to the X-ray/γ-ray band of the spectrum.

It will be shown in the following how the main properties of an X-ray binary, like the way, the stability and the duration of mass transfer, and even the NS magnetic field and minimum attainable spin period, do all descend more or less strictly from the ratio between the masses of the two objects, $q = M_2/M_1$ (the subscript 1 refers to the accretor and 2 to the donor). This is the reason why X-ray binaries are commonly split up in two classes: Low Mass X-Ray Binaries (LMXB) with $M_2 \lesssim 1 \; M_\odot$, and High Mass X-ray Binaries (HMXB) which have $M_2 > 1 \; M_\odot$. This classification is observationally based on the ratios between the optical and X-ray emission; whereas the optical emission due to the donor star of a HMXB dominates the X-ray content, the opposite happens for a LMXB (Bradt and McClintock, 1983).

1.4.1 The mass transfer: wind and disc fed binaries

The mass transfer takes place in a binary essentially in two ways: mass can be lost by the donor through a wind, or because the donor becomes larger than its gravitational influence sphere, so that mass overflows towards the accretor.

The first channel leads to a significant transfer of mass only if the wind emitted by the companion star is very strong; this requirement limits wind fed binaries to systems with evolved donors of spectral type O and B, and masses exceeding $\sim 10\ M_\odot$. A particular case of wind fed binaries is represented by the so called Be transients, which commonly have very eccentric orbits; the companion star here loses mass through an equatorial disc because of its rapid rotation and mass is transferred once per orbital period when the accreting object is at the periastron of the orbit.

Disc fed binaries can be described instead in the framework of Roche geometry. Two auto-gravitating bodies orbiting around a common centre of mass define three topological domains in the space, if the dynamical influence on a gravitationally bound test mass is considered: two closed volumes where the influence of one of the two stars dominates, the so called Roche lobes, and the rest of the space where the binary system would be seen as a point mass (see Fig. 1.4.1). The surface that defines these domains is the eight-shaped critical Roche surface, an equipotential surface that splits up the two lobes by just a point, the inner Lagrangian point L_1. As the donor star approaches the critical surface, its shape departs from being spherical and approaches the peer-like shape of the Roche Lobe; matter is therefore transferred through L_1 and starts to experience the gravitational pull of the compact object.

The shapes of the Roche Lobes are determined only by the mass ratio, q, whereas the overall scale is fixed by the binary separation a, which can be expressed from the third Kepler's law as, $a = [G(M_1 + M_2)P_{orb}^2/4\pi^2]^{1/3}$. An useful relation for the size of the Roche Lobes has been given by Paczyński (1971) from a fit of numerical calculations, and is strictly valid for $0.1 \lesssim q \lesssim 0.8$:

$$R_{L2} = a\frac{2}{3^{4/3}}\left(\frac{q}{1+q}\right)^{1/3} = 0.462a\left(\frac{M_2}{M_1+M_2}\right)^{1/3} \qquad (1.8)$$

An analogous relation for R_{L1} can be obtained from the previous relation simply by replacing q with $1/q$.

As low mass stars cannot produce the winds needed to yield a detectable X-ray emission, it is clear that while wind fed binaries are necessarily HMXB, disc accretion pertains both kind of binaries; as AMSP are all LMXB (see Sec. 1.6), we focus in the following exclusively on disc fed binaries, even if some of the discussed issues are valid also for the wind case.

1.4.2 Disc accretion

A detailed treatment of accretion discs can be found in Frank et al. (2002) and here only the basics results are recalled. An artistic view of a disc accreting X-ray binary is shown in Fig. 1.4.2.

The fate of Roche Lobe overflowing matter depends on how it gets rid of the excess angular momentum it owns. It is in fact easy to show that when mass overflows through L_1, it possesses the specific angular moment of the binary, $j_{L_1} = \omega_{orb}(R_{L1} - a_1)^2$, where a_i is the semimajor axis of the i-th star orbit ($i = 1, 2$, recall that $a_1/a_2 = M_2/M_1$ and $a = a_1 + a_2$, where a is the binary separation). The transferred mass dissipates energy faster than it looses angular momentum (see below), and it puts itself in the lowest energy orbit for a given angular momentum, a Kepler circular orbit. It is worth noting that

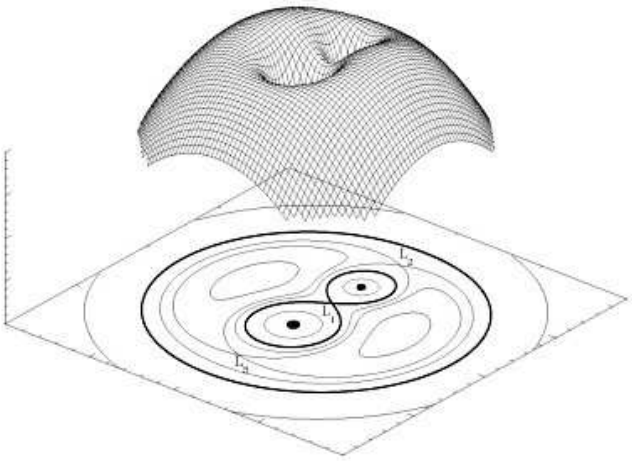

Figure 1.4: Three dimensional view of the gravitational potential wells determined by the components of a binary system. The equipotential lines are drawn in the 2-D projection below; the inner eight shaped solid line is the critical Roche equipotential which defines the areas of respective gravitational influence. From http://hemel.waarnemen.com/Informatie/Sterren/hoofdstuk6.html#mtr

the Keplerian assumption for the motion of particles in the disc, assumption which we make large use of in the following, relies indeed on the assumption that the cooling time-scale is shorter than the time-scale for angular momentum redistribution. Such an assumption will be shown to be valid if the disc is thin in its vertical displacement. The size of the initial orbit, called circularization radius R_{circ}, is dictated by j_{L_1}. As the velocity of a particle in a Keplerian orbit around an object of mass M_1 is $v_K(r) = (GM_1/r)^{1/2}$, the circularization radius can be expressed as $R_{circ} = j_{L_1}^2/\sqrt{GM_1}$. To accrete on the compact object, mass has therefore to lose a fraction $(R_{circ}/R_*)^2$ of its specific angular moment. As an example, we derive $R_{circ} \simeq 1 \times 10^{10} P_{hr}^{2/3}$ cm for a $q = 0.3$ binary, where P_{hr} is the orbital period in hours, so that the fraction of specific angular momentum the matter has to get rid of to accrete onto a NS is $\sim 10^8$.

This is the essential reason for an accretion disc forms, as it is indeed a machinery to transport angular momentum away from the accretor, and mass in the opposite direction. The agency for energy dissipation and for angular momentum redistribution is the viscosity, at least far from the compact object. As a matter of fact the dynamical influence of the magnetosphere may also become important, if not dominant, close to the accretor (see Sec. 1.5.1). Viscosity transports angular momentum from the inner to the outer rings of the disc, as adjacent annuli shear one past each other because of the dependency $v_k \propto r^{-1/2}$. Particles are therefore allowed to sink slowly to orbits at smaller radii. The particular mechanism to ensure this redistribution was unknown for long, as molecular viscosity results far too weak; however, recent developments showed that magneto-rotational instabilities (MRI) represent an ideal candidate, as they make small scale magnetic fields threading the disc to couple more or less adjacent rings (Balbus and Hawley, 1991).

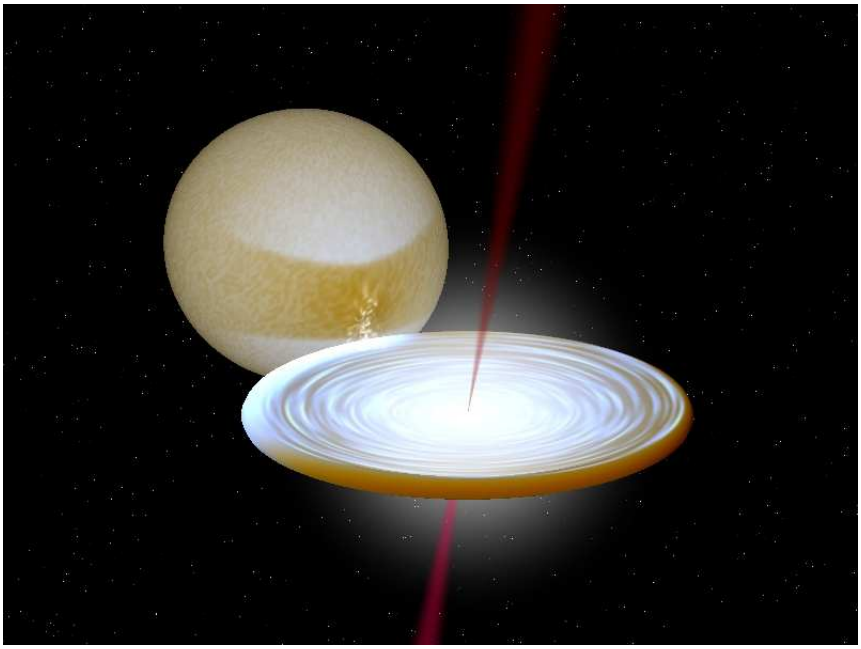

Figure 1.5: Artistic view from www.astro.soton.ac.uk/t̃jm/binary.jpg of an accreting X-ray binary. A jet launched in the direction of the normal to the orbital plane is also shown. Such jets are ubiquitous among Active Galactic Nuclei and Galactic BH X-ray binaries, even if they were also observed from NS LMXB.

The nature of the accretion disc is instead dictated by the efficiency with which it can cool. If it is assumed that the disc is optically thick in the vertical direction and that the opacity is dominated by free-free transitions (assumption that breaks down in the inner parts of the disc), it will cool as a black body, the most efficient way to release energy indeed. Under these hypotheses, the disc will be effectively 'cold' [$T_{rad} \simeq T_{bb}(r)$], thin [$H \simeq (c_S/v_K)R << R$, where H is the height of the disc], and particles will follow Keplerian orbits [$v_\phi = v_K(r) = (GM/r)^{1/2}$]. If these assumptions hold it can be shown that the dissipation rate needed to keep the thin disc in a steady state at the generic radius r will not depend on the viscosity, but only on the mass accretion rate it has to drive onto the compact object, once the latter has been specified. As a consequence the black body temperature of an annulus can be expressed as $T_{bb}(r) = T_*(r/R_*)^{-3/4}$, where

$$T_* = 3GM\dot{M}/8\pi R_*^3\sigma, \tag{1.9}$$

and σ is the Steffen-Boltzmann constant. Therefore, the overall disc spectrum is the superimposition of the black body spectra at different temperatures emerging from different annuli. The high energy cut-off of the disc emission, as well as the emitted luminosity, is a function of the inner rim of the disc and of the disc inclination, and can be used to infer the extent of the disc. For an accreting NS the cut-off is in the soft X-ray band ($\simeq$ 0.5 keV). An important and very general result is obtained if the luminosity emitted by the disc is integrated from its outer edge to the central object. It turns out that $L_{disc} = GM\dot{M}/2R_*$, that

is a disc extending all the way down to the compact object emits half of the gravitational energy available. This result also follows from the consideration that an optically thick (hence thin) accretion disc is in statistical equilibrium, and is therefore a virialized system. As matter collapses towards the central object, half of its gravitational energy is radiated, while the other half is retained as internal energy, and can therefore be released when it impacts onto the compact object. This is the reason why, in a BH binary, only half of the gravitational energy budget can be radiated away. If the disc does not extend all the way down to the compact object, the disc luminosity, as well as its inner temperature, is reduced as the inner rim of the disc is larger.

An useful approximation is obtained if all the ignorance on the particular viscosity mechanism is gathered in a parameter α; that is we express the viscosity coefficient ν, which relates the shear stress in the longitudinal direction to the change of the angular velocity of particles among adjacent rings, as $\alpha H c_S$, where $\alpha \lesssim 1$, and H, the height of the disc, and c_S, the sound speed, are the typical scales for the turbulent eddies that produce shear. Using the α prescription, Shakura and Syunyaev (1973) found a solution for a thin disc that expresses the main quantities of the disc, such as density, temperature and the velocity of the particles as functions of the radius, the accretion rate, the mass of the central object and α.

1.4.3 Time-scales and stability

Three time-scales can be defined to describe the behaviour of an accretion disc (see e.g. King, 2006):

- The dynamical time-scale is the time needed for the accretion disc to respond to a perturbation of its dynamical equilibrium, $\tau_{dyn} = R/v_K = (R^3/GM)^{1/2}$, where R is here the typical radial size of the disc
- The viscous time-scale is the time over which an annulus of matter changes significantly its surface density as it spreads because of viscosity; it can be shown that $\tau_{visc} = R^2/\nu$. Using the α parametrization this is equal to $\tau_{visc} = R^2/\alpha H c_S = 1/\alpha (H/R)^{-2} \tau_{dyn}$.
- The thermal time-scale is the time that characterizes the dissipation of the disc energy; given the dissipation rate needed to keep a disc in a steady state, we have $\tau_{th} = (H/R)^2 \tau_{visc}$

Therefore, in a thin disc we have $\tau_{dyn} \sim \alpha \tau_{th} \sim \alpha (H/R)^2 \tau_{visc}$. As α is ≤ 1 by definition, it is clear how the fundamental hypothesis that energy is dissipated much faster than angular momentum is redistributed holds in a thin disc ($H/R << 1$).

The parameter α can be further estimated, at least for orders of magnitude, from observations of X-ray transients. As a matter of fact, not all the X-ray binaries are observed to emit continuously X-rays. A large fraction of binaries shows X-ray luminosities in excess of $\sim 0.01 L_{Edd}$ only for limited periods of time (called outbursts, which are from weeks to years long), before switching to a quiescent state, where their emission is more than $2-3$ order of magnitude fainter and correspondingly harder.

The commonly accepted picture for the transiency is the Disk Instability Model (DIM, see e.g. Lasota, 2001), which implies two stable branches for an accretion disc: an hot, high viscosity, state (outburst, α_{hot}) and a cool, low viscosity, state (quiescence, $\alpha_{cool} << \alpha_{hot}$). The viscosity state of an accretion disc depends on its temperature; if the temperature is such to keep Hydrogen ionized ($T_H \gtrsim 6500$ K) the presence of charges leads to the high viscosity state, while the disc is in the low state if the disc is cooler. As the opacity depends very steeply on the H ionization fraction, all the intermediate states are unstable, and a disc switches from one state to the other in a thermal time-scale. The temperature of the disc is nevertheless fixed not only by the dissipation rate required by the mass transferred by the donor (Sec. 1.4.2), but is also influenced by the X-ray emission of the central object which indeed illuminates it with ionizing photons (van Paradijs, 1996). A persistent system is therefore one who can keep the outer edge of the accretion disc always in the hot, high viscosity, state, resulting in a condition on the accretion rate and the size of the system, $\dot{M}_{cr} \gtrsim 2 \times 10^{-10} m_1^{2/3} P_{hr}^{4/3}\ M_\odot/yr$ (King et al., 1996), where m_1 is the mass of the accretor in solar units, and P_{hr} is the orbital period in hours.

In a transient binary, the temperature of the outer-disc edge is normally lower than T_H, so that the disc will evolve over a long viscous time-scale ($\tau_{visc} \propto \alpha_{cool}^{-1}$). When enough mass has built to trigger the ionization instability at some radius $R_h \sim R_{disc}$, accretion starts and the resulting X-ray irradiation of the disc helps to remove ionization zones in the whole disc. King and Ritter (1998) showed how the light curve expected from a transient is exponentially decaying with a characteristic time scale, $R_h^2/3\nu \sim \tau_{visc}/3$. When X-ray luminosity has dropped below the level needed to maintain the disc in the hot state at R_h, the shape of the light curve changes to linear, witnessing the fact that accretion is proceeding only using the inner, still hot, parts of the disc. A cooling wave in fact travels from the colder to the hotter regions of the disc, therefore rapidly switching off accretion. The duration of outburst and quiescent states can then be used to infer the value of α, both in the hot and cool states. It turns out that $\alpha_{hot} \simeq 0.1 - 0.4$, while α_{cool} is at least two orders of magnitude lower (King et al., 2007).

As disc-fed HMXB have supergiant companions that transfer mass at near Eddington rates, it can now be understood how these systems are typically persistent; on the other hand LMXB have typically lower accretion rates, and the incidence of transients is much higher, especially for $P_{orb} \gtrsim 2$ hr. Nevertheless it has to be noted that compact ($P_{orb} < 2$ hr) LMXB can as well be transients if their average mass accretion rate is very low, as it is the case for all the AMSP. This model for transiency is further confirmed by the evidence that BH-LMXB are more easily found as transients, due to the dependence of $\dot{M}_{cr}$ on $M_1^{2/3}$ (King et al., 1996).

1.4.4 Evolutionary scenarios

Here we present an overview of the basic events yielding the formation of an X-ray Binary, and that determine its evolution while transferring mass. Detailed reviews this section is based on can be found in Verbunt (1993), Verbunt and van den Heuvel (1995) and Tauris and van den Heuvel (2006).

To produce an X-ray binary is a rather complicated task as it is witnessed

by the small number of systems of this kind discovered so far; the number of HMXB of the Galaxy is ~ 110, while LMXB are ~ 180, both at least an order of magnitude lower than, for example, the number of known radio pulsar. Despite that at least 1/3 of the Galaxy stars belong to binary or multiple systems, the primary reason for the low number of X-ray binaries has to be identified in how hard is to keep bound a binary system after the SN event that originates the compact object takes place.

As a matter of fact, if it is assumed that the orbit is circular before the SN, and that the time-scale over which the explosion takes place is much shorter than the orbital period (i.e. it can be considered instantaneous), the post-SN periastron distance is equal to the pre-SN orbital radius and, moreover, the post-SN periastron velocity is the same as pre-SN orbital velocity. Under these assumptions, the eccentricity of the post-SN orbit is equal to $e = \Delta M/(M_1 + M_2 - \Delta M)$, where ΔM is the mass lost in the explosion (Boersma, 1961). It is therefore clear that to keep the orbit bound after the explosion, i.e. $e < 1$, the mass lost must be less than half of the total mass of the system before the explosion. This requirement can be translated in asking that the star undergoing collapse is the less massive of the system, but this is rather awkward as the more massive star evolves faster. This problem can be circumvented by arguing that a phase of mass transfer from the more to the less evolved star precedes the SN event, so that at the moment of the explosion the more evolved star is also the less massive. What results from such a picture is nevertheless a compact object accreting from a high mass companion, so that this argument may account for the formation of a HMXB, but can't help explaining the existence of LMXB.

The formation of a LMXB is therefore even a more rare event and requires an exceptional evolutionary history, as the companion now has a mass $< 1.5\ M_\odot$.[4] The commonly proposed suggestions to overcome the SN problem are basically three: (i) a 'spiral-in' scenario in which the star that is going to explode as a SN enshroud with its envelope the MS companion ($\sim 1\ M_\odot$), while expanding because of nuclear evolution (on the RGB, or more preferably on the AGB); the friction may then lead to the ejection of the envelopes, helping the system in meeting the requirements on the mass distribution before the SN. As this dynamics is nevertheless not enough to guarantee the binary survival, a well imparted 'kick' is also argued. In other words, if the SN is not symmetric, a velocity in the direction of the line of the two centres of mass may act to keep the system bound. It is worth noting that a spiral in phase also removes angular momentum shrinking the binary system; (ii) a 'quiet' SN explosion, i.e. an explosion of a WD that reaches the Chandrasekhar limit because of slow mass accretion (type Ia SN); (iii) the problem of the formation of the compact object is completely circumvented by arguing that the binary system formed by tidal capture after the compact object formed. This mechanism obviously only works in a dense environment. This explanation has the advantage of accounting for the large number of LMXB in Galactic Clusters; it was further argued that the majority of the LMXB now in the Galactic field, if not all, formed in GC, and have been later dispersed in the Galaxy disc each time a cluster pass through it in its orbit (Grindlay, 1984; Podsiadlowski et al., 2002).

[4]Evolutionary scenarios show how a LMXB can also be the descendant of an intermediate mass X-ray binary (IMXB), where the companion has an initial mass of 2–4 $M_\odot$ (Podsiadlowski et al., 2002). In this case, the mass transfer proceeds on the thermal time-scale of the donor, at least in the first evolutionary stages (see Sec. 8.3)

As disc fed binaries are the only systems in which a NS may gain enough angular momentum to spin at millisecond spin periods, we focus on the evolution of these systems only. Once the compact object has formed, mass transfer will set up when the companion radius equals the Roche Lobe size [see Eq. (1.8)]. This can happen either because the secondary expands during its evolution, or because the orbit loses enough angular momentum that the Roche Lobes shrink enough. The size of the Roche Lobes depends solely on the mass ratio $q = M_2/M_1$, and on the orbital separation a, which in turn can be expressed in terms of M_1, M_2 and the orbital period, P_{orb}. Therefore, given the masses of the two stars, the range of possible orbital periods at the onset of the RL overflow depends essentially on the mass-radius relation followed by the donor, i.e. by its evolutionary state. It is clear that the case of RL overflow beginning when the donor is on the RGB and AGB have access to a much wider range of initial orbital periods than the case of a Main Sequence donor.

The subsequent evolution of the system when mass is transferred depends on the mass ratio q, and on the possible losses of angular momentum and mass from the binary. The total orbital angular momentum can be written as:

$$J_b = M_1 M_2 \sqrt{\frac{Ga}{M}}\,, \tag{1.10}$$

where we put $M = M_1 + M_2$ and further assumed that the angular momentum residing in the two objects because of their rotation can be neglected[5]. If we assume that the mass transfer may be non conservative, i.e. not all the mass transferred by M_2 is effectively accreted by M_1, the rate of changes of the masses of the system reads as $\dot{M}_1 = -\beta\dot{M}_2$ and $\dot{M} = (1-\beta)\dot{M}_2$. Taking the logarithmic time derivative of Eq. [1.10] therefore yields:

$$\frac{\dot{a}}{a} = 2\frac{\dot{J}_b}{J_b} - 2\left[1 - \beta q - \frac{1}{2}\frac{q(1-\beta)}{1+q}\right]\frac{\dot{M}_2}{M_2} \tag{1.11}$$

The conservative case is recovered simply by setting $\beta = 0$; in this case we can see that, if no angular momentum is exchanged by the binary, $\dot{a}/a = -2(1 - q)(\dot{M}_2/M_2)$, that is the net effect of a mass transfer from the donor to the accretor ($\dot{M}_2 < 0$) is to widen the orbit if $q < 1$, as it is the case for LMXB[6]. This is simply understood if it is noticed that, if $q < 1$, mass transfer redistributes more mass near the centre of mass, so that the binary has to widen if no angular momentum is lost from the system. The size of the donor Roche Lobe shrinks as the orbital separation a does, and because the RL overflow is assured if $R_{L2} = R_2$, this simple result shows how a mass transfer in a LMXB acts to end the contact phase, unless the binary loses angular momentum or the reaction of the donor star to mass lost is to expand more quickly than the RL does.

The stability of the Roche Lobe overflow depends on the relative changes of the sizes of the Roche Lobes and of the donor star. As a matter of fact, mass transfer not only modifies the Roche geometry, but it also determines a response from the donor star. To have a stable mass transfer, the donor's radius must be enclosed by its Roche Lobe critical surface, despite it keeps contact

[5]It is easily shown that even in the case of a millisecond spinning NS, its rotational angular momentum is at least two orders of magnitude lower than the one residing in the binary orbit

[6]More accurate calculations show that, allowing for a non conservative case also, the critical value of q is somewhere in between 1 and 1.28

with it if the mass transfer has not to be switched off ($R_{L2} \simeq R_2$). On the other hand, if the donor radius grows more rapidly than the RL, mass transfer becomes unstable and proceeds on shorter time-scales. These time-scales will be dynamical ($\tau_{dyn} = \sqrt{R^3/GM} \simeq 0.5(R/R_\odot)^{3/2}(M/M_\odot)^{-1/2}$ hr) or thermal ($\tau_{th} = GM^2/RL \simeq 3 \times 10^7 (M/M_\odot)^{-2}$ yr), depending on the driver for the rapid expansion of the star. Dynamical time-scales are so short that a system transferring mass in this way likely won't be observed.

If the donor has an almost radiative envelope, it will in general shrink or keep a roughly constant radius, upon mass lost. This can be understood by noting that there is very little mass in a radiative envelope, so that the star experiences a large shrinkage even if only little mass is removed from its outer layers. Given this property, a donor with a radiative envelope, residing in a binary with not too drastic mass ratio, will generally lead to a stable mass transfer proceeding on the shorter time-scale between the nuclear evolution time-scale ($\tau_{nuc} \simeq 1 \times 10^{10}(M/M_\odot)^{-2.5}$) and the one dictated by the angular momentum losses. Podsiadlowski et al. (2002) found an upper limit for stability of $M_2 = 2M_\odot$, thus encompassing nearly all the LMXB, except than those that may come from an IMXB, or those that are the relics of a system which experienced a common envelope phase (see 8.3 also). As this possibility will be discussed later (see Ch.8), it is useful to note here that a LMXB could evolve faster if the irradiation of the accreting object is such to modify the thermal equilibrium of the companion, and the mass transfer then proceeds on a thermal time-scale (Podsiadlowski, 1991).

On the other hand, if the donor has a deep convective envelope, not to mention if it is fully convective or degenerate, its adiabatic response to mass lost will be a growth in size. In other words, the star has an inverse mass-radius relation, $R \propto M^n$, with $n < 0$. If the envelope is convective, such M–R relation arises from the super-adiabatic temperature gradient in its outer layers, while if it is degenerate this is due to the decoupling between pressure and temperature (Sec. 1.1). This situation in general leads to an unstable mass transfer and to the formation of a common envelope, unless the mass transfer rates and the mass ratio are so low that a stable transfer is still possible. This may happen in those tight LMXB ($P_{orb} \lesssim$ few hr) near the end of their evolutionary history (like AMSP are), when very little mass is transferred ($\dot{M} \lesssim 10^{-10}$ M$_\odot$/yr).

These differences between the LMXB ($q \lesssim 1$) and HMXB ($q >> 1$) donors have a straightforward influence on the respective time-scales mass transfer can proceed over which; HMXB can exist for $\sim 10^5$ yr, while LMXB are much longer lived, with time-scales as long as 10^{10} yr. Although HMXB are more easily formed, their number is therefore of the same order of LMXB discovered so far. The longer time-scales of LMXB have also a consequence on which class may leave MsP as progeny. It will be shown in Sec. 1.6 that $\sim 0.1\ M_\odot$ are to be accreted by a NS to make it spin at millisecond periods. This takes 10^7 yr assuming an Eddington accretion rate, and MsP can therefore only be the recycled descendent of LMXB, among which AMSP have therefore to be searched.

1.4.5 Evolution of LMXB

It was already shown that a binary with $q \lesssim 1.3$ must lose angular momentum to keep the donor in contact with its Roche Lobe, unless the companion is evolved

and thus expands on its nuclear time-scale. The sinks for angular momentum in an X-ray binary to be inserted in Eq. [1.11], are of four kinds:

- **Non-conservative evolution** A fraction β of the mass transferred by the donor can be lost from the system, taking away its specific angular momentum. If we write the specific angular momentum of the mass lost as α times the specific angular momentum of the secondary, $j_2 = a_2^2\Omega_{orb}$, the relative change of J_b is:

$$\frac{\dot{J}_{ML}}{J_b} = \frac{\alpha j_2 \dot{M}}{J_b} = \frac{\alpha(1-\beta)}{1+q}\frac{\dot{M}_2}{M_2}\,, \tag{1.12}$$

  where we used the relation $a_2/a = M_1/(M_1+M_2)$, and wrote the binary angular momentum as $J_b = [M_1M_2/(M_1+M_2)]a^2\Omega_{orb}$. It is obvious to note that the angular momentum that can be lost by means of mass ejection crucially depends on where mass is expelled from. The parameter α depends in fact on the point of the orbit where matter is ejected, $\alpha = (\rho/a_2)^2$, where here ρ is the distance from the centre of mass of the ejection point. Mass lost from the vicinity of the accretor removes q^2 times the angular momentum that would have been lost if it was launched from the secondary. In a LMXB, $q << 1$, and, therefore, mass ejection significantly influences orbital evolution only if ejection takes place from the vicinity of the secondary. This result will be used to propose a scenario that explains the orbital evolution observed in SAX J1808.4–3658 (see Ch. 8).

- **Magnetic Braking**. A rotating star may lose a significant fraction of its rotational angular momentum because of magnetic stellar winds. The magnetic field present in the chromosphere of a $\lesssim 1.5\ M_\odot$ star is in fact able to anchor the wind particles, forcing them to corotate with the star up to large distances from the surface. The angular moment of the mass lost is therefore large even if the wind is weak, and this has an effect on the orbit as tight binaries are very fast to synchronize. As a matter of fact, the rotation of the secondary is locked to the orbital motion by tidal forces. Therefore, the sinchronization ultimately happens at the expense of the binary angular momentum. A relation for the orbital angular momentum lost through magnetic braking was derived by Verbunt and Zwaan (1981) as:

$$\frac{\dot{J}_{MB}}{J_b} = -3.8\times10^{-30}\frac{R_\odot^{4-\gamma}(M_1+M_2)R_2^\gamma\Omega_{orb}^2}{M_1a^2}\,, \tag{1.13}$$

  where $\gamma \simeq 4$ for a MS star. The magnetic braking is thought to stop when the donor becomes fully convective, as the magnetic field lines have no radiative envelope to anchor to any more. This deduction was made to explain the period gap between 2 and 3 hr, where Cataclysmic Variables (CV, i.e. white dwarfs accreting from a companion star) are no longer observed.

- **Gravitational waves emission**. Two stars revolving one another lose angular momentum via gravitational waves according to:

$$\frac{\dot{J}_{GW}}{J_b} = -\frac{32G^3}{5c^5}\frac{M_1M_2(M_1+M_2)}{a^4} \tag{1.14}$$

(Landau and Lifshitz, 1962). It is immediately noted that a copious amount of gravitational waves is emitted when the binary is extremely tight

- **Spin orbit coupling**. Exchanges of angular momentum between the orbit and the donor may take place because of the contraction/expansion of the latter. This effect is most prominent for periods > 2 d and is neglected in the following, as we are interested here only in short period binaries.

It was already stated how the evolution of the binary after the formation of the compact object is determined by q and by the evolutionary state of the donor when it transfers mass; if $q \lesssim 1$ and the companion is not evolved, the system will converge, the mass transfer is led by angular momentum losses (on a time-scale $\tau_{AML} = -[\dot{J}/J]^{-1}$) and the nuclear evolution of the companion is essentially frozen. If $q > 1$ instead, the mass transfer first passes through a short thermally-unstable phase ($\sim 10^6$ yr) as the convective layers of the companion become exposed; moreover, if the companion has already developed a significant He-core, the internal evolution is faster than τ_{AML} and controls the mass transfer also when the instability ceases, leading to an expanding binary system. Given an initial mass for the companion, this translates in a bifurcation period, which was indicated by Podsiadlowski et al. (2002) as $P_{bif} \simeq 18$ hr for a $1M_\odot$ companion. The evolution of systems that initiate mass transfer at periods lower than P_{bif} is driven to smaller periods by angular momentum losses, while systems with $P_{orb}^{(i)} > P_{bif}$ transfer mass because of the nuclear evolution of the donor and evolve towards larger periods.

The occurrence of a bifurcation period reflects the key role played by the evolutionary status of the companion (hence its nuclear evolution time-scale) at the onset of mass transfer. How this fact relates in a condition on the period at the onset of mass transfer is easily deduced, combining Eq. [1.8] and the third Kepler's law. Further imposing contact of the donor ($R_2 = R_{L2}$) yields a relation between the orbital period and the density of the companion at the onset of mass transfer:

$$P_{orb}^{(i)} \simeq 8.9 \left(\frac{R_2}{R_\odot}\right)^{3/2} \left(\frac{M_2}{M_\odot}\right)^{1/2} hr \,. \qquad (1.15)$$

Using a well defined mass-radius relation for the donor then allows to identify the initial orbital period as a function of the mass of the companion only. Evolved companions make therefore contact at larger periods than Zero Age MS stars do.

These two evolutionary channels roughly reflect the observational properties of two groups of MsP; those with $P_{orb} \gtrsim 1 - 2$ d are thought to descend from LMXB that initiated mass transfer with an evolved companion, while those at lower periods ($\lesssim 12$ hr) follow from systems where the angular momentum losses prevailed in determining the mass transfer (but see also Sec. 8.3).

As we are interested in close binaries, an useful example for the conservative evolution of converging LMXB can be made making use of Eq. [1.8], and imposing that the contact of the secondary exists ($R_2 = R_{L2}$) and continues ($\dot{R}_2 = \dot{R}_{L2}$):

$$\frac{\dot{R}_{L2}}{R_{L2}} = \frac{\dot{a}}{a} + \frac{1}{3}\frac{\dot{M}_2}{M_2} = \frac{\dot{R}_2}{R_2} = n\frac{\dot{M}_2}{M_2} \,, \qquad (1.16)$$

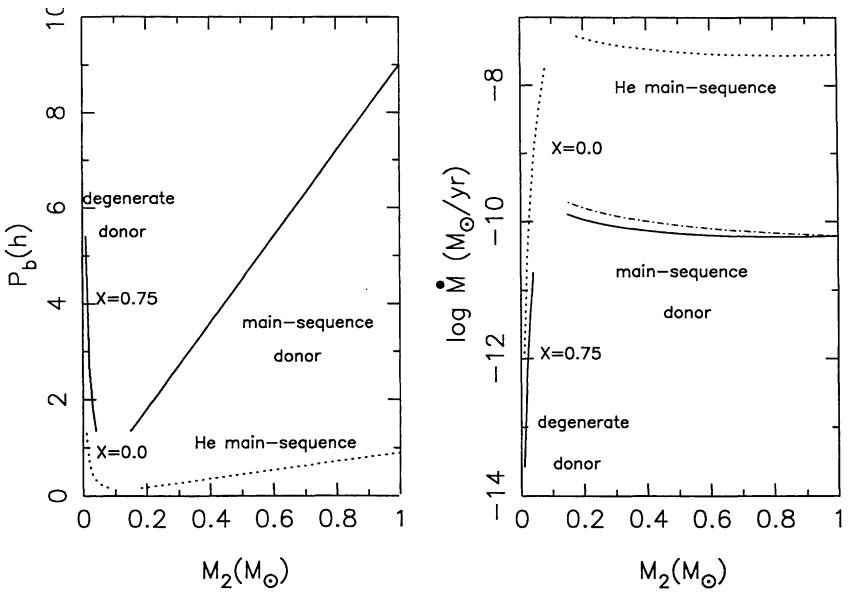

Figure 1.6: Orbital period (left) and mass-transfer rate (right) as a function of the mass of the donor, M_2, for systems evolving under the angular momentum lost because of the emission of gravitational waves (from Verbunt, 1993). For MS donors (solid and dashed line for stars on the hydrogen and helium main sequence, respectively), mass transfer leads to shrinkage of the binary, and the mass transfer rate is roughly constant. If the donor is degenerate, the orbital period evolution reverses, and mass is transferred at very low rates.

where in the left hand side we used a mass-radius relation, $R_2 \propto M_2^n$ for the donor. Using the above relation to eliminate $\dot{a}/a$ from Eq. [1.11], we obtain:

$$\frac{\dot{J}_b}{J_b} = \frac{\dot{M}_2}{M_2}\left(\frac{5}{6} + \frac{n}{2} - \frac{M_2}{M_1}\right) . \qquad (1.17)$$

Once the angular momentum losses are identified (GW emission in the later stages of a close LMXB), the orbital period and mass transfer rate runs are immediately obtained depending on the type of the donor (see Fig. 1.6 from Verbunt, 1993). A $1M_\odot$ Main-Sequence star makes contact with its Roche Lobe at ~ 9 hr, and transfers mass at a rate $\dot{M}_2 \simeq 10^{-10}\ M_\odot/yr \simeq 0.01\dot{M}_{Edd}$ while the binary shrinks to periods ~ 80 min[7]. At a certain point ($M_2 \simeq 0.1M_\odot$) the donor star no longer sustains H burning in its core, and becomes almost fully convective; the orbital period evolution is therefore reversed, with mass transfer rates 2 orders of magnitude lower than before. This reversal therefore introduces a minimum period for those LMXB which evolve under angular momentum losses.

The inclusion of magnetic braking in such a calculation has the effect to accelerate the evolution towards smaller orbital periods, and to explain mass transfer rates in excess of $10^{-9}\ M_\odot/yr$, observed in some LMXB.

[7]Shorter minimum orbital periods can be achieved if the donor is slightly off the main sequence at the onset of mass transfer, despite still under the bifurcation period (Podsiadlowski et al., 2002)

1.5 Accretion powered pulsars

A NS X-ray binary may show a coherently pulsed X-ray emission if its magnetic field is large enough for the actual accretion rate, to control the dynamics of the matter in the surroundings of the NS. If this happen at some radius larger than the NS radius, a magnetosphere forms around the NS. As it controls the motion of the accreting matter, a magnetosphere channels the accreted mass towards the NS magnetic poles, where two hotspots form (see Fig. 1.5 for an artistic view).

An order of magnitude of where and whether the magnetic field disrupts the disc flow, R_d, can be easily found in the case of spherical accretion. An estimate for R_d can be found equating the magnetic pressure, $[B(r)^2/8\pi]$, to the ram and thermal pressure of the infalling matter, $[p(r) + \rho(r)v(r)^2]$. As accretion is highly supersonic next to the compact object, the thermal pressure can be safely neglected with respect to the ram pressure. Further arguing that the magnetic field is dipolar, $B(r) = \mu/r^3$, and that the velocity of accreted matter is close to free fall, $v = (2GM/r)^{1/2}$, it is possible to put $|\rho v| = \dot{M}/4\pi r^2$, obtaining the radius for which the two pressures equate:

$$R_A = \mu^{4/7}\dot{M}^{-2/7}(2GM)^{-1/7} = 3.7 \times 10^6 B_8^{4/7} R_6^{12/7} \dot{m}_{-10}^{-2/7} m_1^{-1/7} cm \qquad (1.18)$$

(Lamb et al., 1973), where in the right hand side we defined $B_8 = (B_S/10^8 G)$, $R_6 = (R_*/10^6 cm)$, $\dot{m}_{-10} = [\dot{M}/(10^{-10} M_\odot/yr)]$ and m_1 is the mass of the NS in solar units. The radius so-defined is called Alfven radius and sets the scale-length of where the magnetic field begins to significantly influence the mass flow.

If $R_d \simeq R_A > R_*$, there exists therefore a certain region surrounding the NS, the magnetosphere, where the completely ionized accreting plasma no longer sits in the disc and rather follows the magnetic field lines because of its high conductivity, thereby corotating with the NS. Given the steep dependence of the magnetic pressure with radius ($\propto r^{-6}$), this transition happens in a thin layer, so that mass is forced to fall in a narrow region in the vicinity of the magnetic poles of the NS, the so-called hotspots. As soon as a tilt between the magnetic field and spin axes is introduced, the X-ray emitting regions rotate around the spin axis, and coherent X-ray pulsations at the period of rotation of the star will be observed if the line of sight is favourable.

1.5.1 Disc-Magnetic field interaction

This simple picture treats the magnetosphere and the accreting plasma as completely decoupled, that is, the accreting material is considered completely screened from the magnetic field (diamagnetic case). This approximation can barely hold for the case of spherical accretion, as the ionized plasma develops currents at its inner edge ($R \sim R_m$) screening the magnetic field, and matter ultimately enters the magnetosphere because of instabilities ensuing at the transition layer. However, it is rather immediate to realize how this hypothesis cannot hold for a thin accretion disc. In this case, in fact, the initially dipolar magnetic field would be significantly distorted in the radial direction next to the disc plane because of the screening currents flowing on both sides of the disc. This configuration is nevertheless non self-consistent, as a so-determined

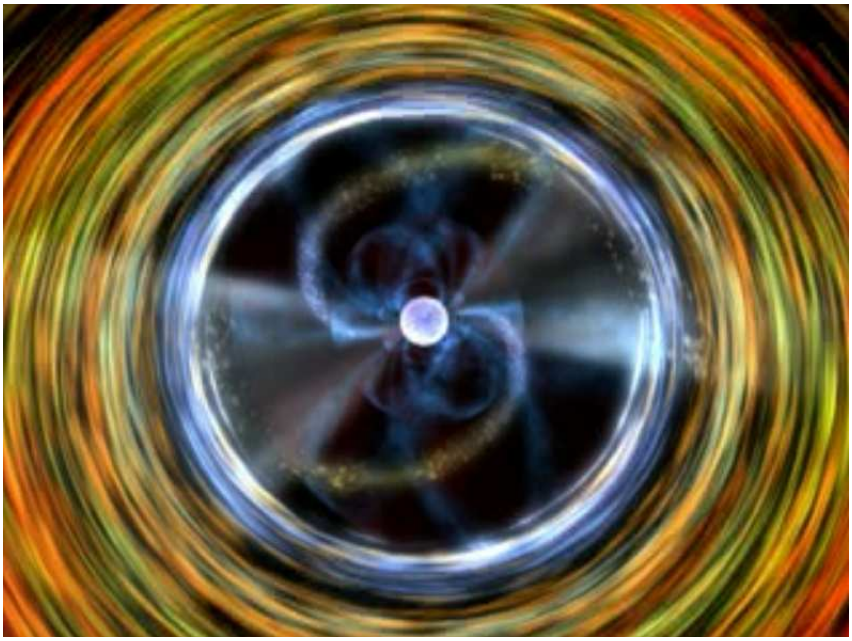

Figure 1.7: Artistic view of the accretion process onto a pulsar seen from the normal direction to the orbital plane (picture taken from an animation of Dana Barry of NASA/Goddard Space Flight Centre). The disc is truncated at some radius larger than the NS size, and mass is channelled towards the accreting poles by the magnetospheric field lines, falling onto small regions near to the magnetic poles. The resulting X-ray emission is therefore anisotropic and may result in the typical lighthouse effect of pulsars.

magnetic field would reconnect through the disc faster than matter sinks in the accretion disc. Ghosh and Lamb (1979a) (GL79a hereafter) showed that effective reconnection of the field lines through the disc may indeed happen because of, (i) Kelvin-Helmoltz instability growing as two fluids of drastically different densities, like the disc and the magnetosphere are, shear one past the other, ultimately mixing the disc plasma and the magnetic field; (ii) turbulent diffusion led by convective movements of the disc plasma, if this experiences large temperature gradients; (iii) reconnection of small-scale magnetic fields driven by the differential rotation up to a large scale reconnection. A thin accretion disc can therefore never confine a stellar magnetosphere, and this changes the nature of the problem, as for $r \gtrsim R_A$ the configuration of an initially dipolar magnetic field is significantly disturbed by the flow of disc plasma.

An important definition to treat the interaction of the magnetic field with the disc, as well as the viability at all of the disc accretion process for a magnetized NS, is the corotation radius, R_C. As matter in the disc follows Keplerian orbit with an angular frequency $[\Omega_K = (GM/r^3)^{1/2}]$, there will be a certain radius for which it will be equal to the one of the corotating system composed by the NS and the magnetosphere, $\Omega_K(R_C) = \Omega_*$. Solving for R_C yields:

$$R_C = \left(\frac{GM}{\Omega_\star^2}\right)^{1/3} \simeq 1.5 \times 10^6 m^{1/3} P_{ms}^{2/3}\ cm, \qquad (1.19)$$

where P_{ms} is the spin period of the NS in milliseconds. It is immediately seen that for an AMSP this radius is very close to the NS surface.

The role played by R_C is twofold; on one hand, if the inner disc radius R_d is larger than R_C, the mass flow encounters a centrifugal barrier impossible to step over if the magnetic field-disc interaction was not to significantly change the disc structure in the inner parts of the disc (see below). As such a situation was initially thought to effectively stop accretion, it is known as 'propeller' state (Illarionov and Sunyaev, 1975). On the other hand R_C represents the only radius for which, arguing that the disc is Keplerian despite the magnetic field influence, the magnetosphere and the accretion disc rotate at the same speed.

Away from R_C, in fact, the differential rotation between the field and the disc generates a toroidal component of the magnetic field, B_ϕ, from the poloidal field, B_p. This is because the foot-points of a disc line on the NS and on the disc are tightly anchored to very highly conducting materials. Differential rotation thus stretches the line. The so-called magnetic pitch, $\gamma_\phi = B_\phi/B_p$, is limited by the speed of reconnection of the disc threading field, so that it will have the form, $\gamma_\phi(r) \simeq \tau_\phi(r)[\Omega_\star - \Omega_K(r)]$, where $\tau_\phi(r)$ is the time-scale of magnetic field reconnection through the disc. Therefore, inside the corotation radius ($\Omega_K(r) > \Omega_\star$), the field will be dragged forward by the accretion disc, while the opposite happens if $r > R_{cor}$ (i.e. $\Omega_K(r) < \Omega_\star$). General considerations about the various possible reconnection mechanisms limit the pitch to values < 1.

It has to be noted that the influence of the matter flow on the magnetic field also introduces a radial component of the field, B_r, in the disc plane, from the dominant vertical component, B_z. This component is however expected to be small as v_r is, and the magnetic field is thus only slightly pinched because of the slow radial drift of the disc plasma.

The existence of a B-field toroidal component has a fundamental influence on the structure of the accretion disc in its inner parts (i.e. where the field is not yet reduced to the level where it can hardly influence the mass flow). The discontinuities of B_ϕ at the surfaces of the disc imply in fact a radial surface current flowing along the disc. The interaction of this current with the vertical magnetic field, B_z, leads to the loss of angular momentum at a rate $-2(rB_\phi B_z/4\pi)$ per unit surface area, where the factor 2 reflects the two sides of the disc upon which the magnetic torque applies. When imposing the conservation of angular momentum in a disc threaded by a magnetic field, not only the viscous stresses are therefore to be considered, as we did in Sec. 1.4.2, but also magnetic stresses. These considerations led Ghosh and Lamb (1979b) to divide the mass flow around a magnetized NS in three regions (see Fig. 1.8):

- An unperturbed region, $R_{br} < r$, where the magnetic field has little to no effect on the accretion disc, and angular momentum transport is assured by viscosity.

- A transition zone $R_d < r < R_{br}$ where magnetic stresses increasingly influence the plasma dynamics with respect to the viscous stresses. This transition region naturally divides itself in two parts: (a), an **outer transition zone** ($R_0 < r < R_{br}$) where the plasma motion is still Keplerian but nevertheless angular momentum starts being exchanged between the star and the disc by the means of magnetic stresses, and (b), an **inner transition zone** ($R_d < r < R_0$) where the angular moment is transported

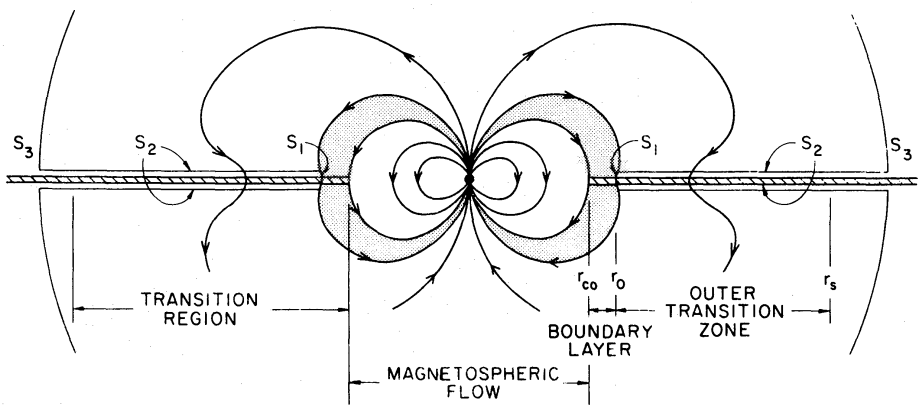

Figure 1.8: View of the accretion flow and of the different regions described in the text (from Ghosh and Lamb, 1979b). In the outer transition zone the magnetic stresses start to influence the matter motion, which is nevertheless still Keplerian. In this region a significant spin-down torque therefore starts ensuing. A boundary layer at R_0 marks the end of the Keplerian regime for accreting mass, which is in turn channelled by the magnetosphere from there to the magnetic poles, yielding to the rotating NS its specific angular momentum. The surfaces S_1, S_2 and S_3 used to derive the torque on the NS (see Eq. [1.24]) are also plotted.

nearly exclusively by the magnetic stresses, the dynamics of disc particles departs significantly from being Keplerian, and the plasma is therefore brought into corotation with the magnetosphere.

- The magnetosphere, $R_* < r < R_d$, where the magnetic pressure is so high with respect to matter pressure that it completely controls the flow, which therefore follows the field lines and impacts onto the NS surface near the magnetic poles.

GL79a showed how the inner transition zone is narrow with respect to the characteristic lengths over which the disc dynamical properties change elsewhere. It is essentially a boundary layer, in the sense that the flow must satisfy on a short length-scale the new boundary conditions imposed by the corotating magnetosphere, conditions which are entirely different from the ones encountered by the plasma in the outer zones. We have therefore $R_0 - R_d \simeq \delta << R_d$. By definition R_0 can be calculated as the point where the magnetic stresses become strong enough to brake the Keplerian motion over a large-scale δ. As this condition can be rephrased in terms of the angular momentum that can be captured by magnetic stresses, it is thus useful to write the relation for the angular momentum conservation in a thin disc.

Considering an annulus at distance r from the NS, and a stationary matter flow, i.e. $\dot{M}_d(r) = 4\pi r h |v_r| \rho$, the flux of angular momentum through the annulus is $\dot{M} r^2 \Omega$, where Ω is the angular frequency of matter in its azimuthal motion, and is taken here not necessarily as Keplerian. The rate of change of this flux is therefore :

$$\frac{d}{dr}(\dot{M}_d r^2 \Omega) = r^2 \Omega \frac{d\dot{M}_d}{dr} + B_\phi B_z r^2 + 4\pi r h \left(\eta r \frac{d\Omega}{dr} \right). \qquad (1.20)$$

The first term on the r.h.s. represents the angular momentum removed by matter that may leave the disc, while the other two account for the angular momentum exchanged by the magnetic and viscous torques. Here $\eta = \alpha\rho h$ is the coefficient of viscosity, already defined in Sec. 1.4.2.

The viscous stresses become negligible at the boundary layer, as their radial dependece ($\sim r^{-5/2}$) is much weaker with respect to that of magnetic stresses ($\sim r^{-6}$). To evaluate R_0 one has thus to equate the magnetic stress, $rB_\phi B_z/4\pi$, acting on an annulus at distance R_0 of width δ, with the angular momentum there conveyed by matter:

$$\frac{B_z B_\phi}{4\pi} 4\pi r^2 \delta \sim \dot{M} r^2 \Omega_K \, . \tag{1.21}$$

Here the matter azimuthal motion can be still considered Keplerian, as R_0 is by definition the radius where the mass flow starts to lose the Keplerian centrifugal support. Solving for the boundary layer structure yields:

$$R_0 \simeq 1.8 \times 10^6 B_8^{4/7} R_6^{12/7} \dot{m}_{-10}^{-2/7} m_1^{-1/7} cm \, . \tag{1.22}$$

An instructive rewriting of this equation is given by Wang (1996), where the contribution of the magnetic pitch at the inner disc radius, $\gamma_0 = B_\phi(R_0)/B_p(R_0)$, and of the magnetic field screening coefficient, η (defined from $B_p(r) = \eta\mu/r^3$), are explicated:

$$R_0 = \left[\frac{2\gamma_0 \eta^2 \mu^2}{\dot{M}(GM_1)^{1/2}} \right]^{2/7} \, . \tag{1.23}$$

The radii defined above have the same dependences on the relevant physical quantities as R_A (see Eq. [1.18]), but it has to be highlighted that the derivation is completely different (see e.g. Ghosh, 2007). While R_A is derived enforcing a static pressure balance in the radial-flow case, R_0 refers to a more realistic disc-fed magnetized NS, and follows indeed from consideration about where the magnetic stresses become able to remove enough angular momentum from the disc matter to make it lose its centrifugal support. These two quantities are similar and have the same scaling with the essential accretion variables simply because the radial dependences of magnetic and matter stresses are so different. It remains that the the only definition with a true physical meaning for the inner disc radius is Eq. [1.22]. We note that the particular values of the index of the relation between R_0 and $\dot{M}$ depends on the structure assumed for the inner parts of the disc. While the value $\alpha = 2/7$ of Eq. [1.22] holds for a disc whose pressure is dominated by the gas contribution, if the inner disc is dominated by radiation pressure (as it is expected to be the case for low-magnetized NS) a value $\alpha = 0.15$ should be considered (Ghosh, 1996).

The model proposed by GL found remarkable confirmations when 2D and 3D full magneto-hydrodynamic (MHD) simulations have become available in recent years. Romanova et al. (2002, RUKL) showed how the magnetic field starts to influence the motion of the disc-plasma at a radius, $R_{br} \sim 3$ times larger than the inner disc radius, $R_d \sim R_A$. It has to be noted that R_d follows from the very same considerations which led to R_A (i.e. the radius at which $B^2/8\pi = p + \rho v^2$). Here, however, no static assumption is made, as a dipolar field or free-fall velocities; the relevant quantities are rather evaluated at each point following the MHD equations. For $r < R_{br}$, angular momentum starts

then to be removed by magnetic stresses, which in turns become dominant and remove the centrifugal support for $r \gtrsim R_d$. At R_d matter is then conveyed into a funnel flow (FF hereafter) by the pressure gradient there existing, and further accelerated by the gravitational field. The fall on the NS happens at a velocity close to the free fall value. Nevertheless the flow remains strongly sub-Alfvenic everywhere, so that particles fall essentially along the field lines (recall that the Alfven speed, $v_A = B^2/\sqrt{4\pi\rho}$, is the maximum speed at which the magnetic field realizes the motion of the charged particles in which it is immersed).

A toroidal B_ϕ component is generated almost everywhere by the disc threading; the magnetic pitch γ is of the order of unity in the inner regions of the disc, while is much lower in the magnetosphere (~ 0.1), but large enough to slightly wind the field in the direction of the angular momentum flow, which is indeed carried essentially by the magnetic field through the entire FF.

RUKL also investigated the behaviour of an accreting PSR when $R_d \gtrsim R_C$, that is in the propeller regime. The most striking result is that matter can accrete even in this case thanks to the angular momentum that the threading field is able to release to the disc, therefore accelerating it beyond Keplerian speeds. The stability of the disc is ensued by the growth of the density in the inner rings, which, on one hand raises the effects of threading, and on the other redistributes outward the angular momentum received through the enhanced viscosity. The centrifugal barrier is leaped over at the expense of the rotating NS that indeed spins down (see below). The magnetic field inflates until it reaches a partially open configuration, forming anyway a closed magnetosphere capable of converging matter in a FF. If the propeller is particularly strong, $R_d >> R_{cr}$, strong supersonic outflows (jets) can be launched by the open field lines (see Romanova et al., 2004a; Ustyugova et al., 2006). Matter can nevertheless accrete in a cyclic way, but at a reduced rate, as enough matter has to build up at the inner disc radius to force some field lines to reconnect.

1.5.2 Torques on the NS

As this thesis mainly deals with the measure and the interpretation of the rotational behaviour of the AMSP when accreting matter, the theory for the torques acting on the NS plays a key-role. As a matter of fact, the relation $\dot{\nu} = N/2\pi I$, where I is the moment of inertia of the NS, relates the magnitude and the sign of the spin frequency derivative, $\dot{\nu}$, to the torques exerted on the star, N.

The theory developed by GL79b for the interaction between the magnetic field and the accretion disc readily leads to an evaluation of the torque, simply calculating the flow of angular momentum through a surface that encloses the star. In vector notation, the integral rephrasing of Eq. [1.20] is:

$$N = \int_S \left(-\rho \mathbf{v_p} r^2 \Omega_K + r \frac{\mathbf{B_p} B_\phi}{4\pi} + \eta r^2 \frac{d\Omega}{dr} \right) \cdot \hat{\mathbf{n}} dS. \qquad (1.24)$$

The three terms in the integral represent material, magnetic and viscous stresses, respectively, while $\mathbf{n}$ is the outward unit normal to S. GL79b showed how useful is to evaluate this integral on a surface composed by three parts (see Fig. 1.8): (a), a cylindrical surface, S_1, of height equal to the vertical displacement of the disc, located at the radius R_0, that is the radius where the matter flow departs from being Keplerian, (b), two sheets running parallel above and below the disc plane from S_1 to infinity, S_2, and (c), two hemispheres closing at infinity, S_3.

This choice is extremely opportune as it is easy to show that the only non-vanishing stresses are the material stresses through S_1, denoted as N_0, and the magnetic stresses through S_2, called N_{out}. This is because at S_1 the viscous stresses are negligible (see above) and the magnetic stresses has no component perpendicular to this surface. As the particles motion at R_0 is almost Keplerian, one thus have a positive torque on the NS of magnitude:

$$N_0 = \rho v_r R_0^2 \Omega_K(R_0) \cdot 4\pi R_0 h = \dot{M}\sqrt{GMR_0}\,. \tag{1.25}$$

On the other hand N_{out} is given by the magnetic stresses, as the viscous stresses have negligible component normal to the disc and no matter leaves the disc, so that:

$$N_{out} = \int_{S_2} r\frac{B_z B_\phi}{4\pi} dS = \int_{R_0}^{R_{br}} \gamma_\phi B_z^2 r^2 dr\,. \tag{1.26}$$

The integral on the surface closing at infinity is instead obviously null.

While the torque N_0 represents the angular momentum carried by mass crossing the inner disc radius, and is always positive, the torque N_{out} can have both signs depending on how far the inner disc radius is from R_C. As a matter of fact, inside the corotation radius the winding of the field is in the same sense of the rotation axis and the interaction brings angular momentum into the NS. The opposite happens instead outside R_C. It is then possible for a NS to spin-up or spin-down as a result of accretion, or even to show torque-less accretion, if positive and negative contributions cancel out. In fact, as the average accretion rate fades, the inner disc radius is expected to recede from the NS surface until it reaches the point where the total torque zeroes.

The actual value of N_{out}, and therefore the value of the spin equilibrium period (the period at which the total torque vanishes at a given accretion rate) depends obviously on how the B_ϕ component is treated. A simple prescription used when discussing some of the results of this thesis is to consider that the reconnection of the magnetic field occurs on the same time-scale of the shearing motion between the star and the disc (Wang, 1995), so that $\gamma_\phi(r) \simeq (1 - \Omega_K(r)/\Omega_*)$. Assuming that the pulsar is so fast that its inner disc radius is at the corotation radius, the integral of N_{out} yields:

$$N_{out}(R_{cor}) = \frac{\mu^2}{9R_{cor}^3}\,. \tag{1.27}$$

The issue of spin equilibrium can be further investigated by introducing the fastness parameter, defined as the ratio between the angular velocity of the star and the Keplerian velocity at the inner disc radius:

$$\omega_S = \frac{\Omega_*}{\Omega_K(R_0)} = \left(\frac{R_0}{R_C}\right)^{3/2} = 1.2 P_{ms}^{-1} \dot{M}_{-10}^{-3/7} B_8^{6/7} R_6^{18/7} m^{-5/7}\,, \tag{1.28}$$

where we inserted the relation for R_0 (Eq. [1.22]), and the scaled quantities in the r.h.s. are defined as in Eq. [1.18]. It is further possible to define a critical fastness, ω_C, for which the positive and negative torques on the NS, N_0 and N_{out}, exactly equal. The spin equilibrium period defined above is therefore $P_{eq} = (1/\omega_C) P_K(R_0)$, where, in obvious notation, $P_K(r)$ is the Keplerian rotation period at r. GL79b found $\omega_C \simeq 0.35$, and together with the relation [1.22] for the inner disc radius, it yields to:

$$P_{eq}^{GL} = 3.4 \dot{M}_{-10}^{-3/7} B_8^{6/7} R_6^{18/7} m^{-5/7} ms\,, \tag{1.29}$$

that reflects an inner disc radius put at $\sim 0.5 R_{cor}$. Despite the uncertainties on the actual value of P_{eq} (which depend critically on the particular value of ω_C; see e.g. Wang 1987, who finds $\omega_C \sim 1$), it is instructive to see that shorter periods can be attained through high accretion rates and, most importantly, if the NS has a relatively low magnetic field. As the accretion rate is limited by the Eddington rate, a high field pulsar with $B_S \sim 10^{12}$ G can in fact never attain equilibrium spin periods shorter than ~ 0.3 s. It is thus clear how a millisecond pulsar naturally descends from the population of 'low' field NS.

The simulation of RUKL confirmed the basic results depicted above, also for what concerns the accretion torques acting on a NS. The star may spin-up or spin-down depending on the ratio of its rotation rate to the rotation rate at the inner edge of the disc. In particular the value they find for torque-less accretion is $R_d/R_C \simeq 0.67 - 0.71$

Romanova et al. (2004b) and Ustyugova et al. (2006) further give valuable results for the torques acting on the star while the system is in the propeller state. They found that the star may spin down very rapidly while giving to the matter at the inner disc edge enough angular momentum to overcome the centrifugal barrier. This obviously happens at the expenses of the rotation of the NS, which thus spins down. Contrary to the usual spin-down theory, which predicts an increasing spin-down rate when the accretion rate falls, as the contribution of positive material torques becomes less important, their simulations show that the negative torque increases with the accretion rate. This is because, at larger accretion rates, a larger fraction of the field is forced to thread the disc in its inner parts, thus giving rise to an enhanced spin-down friction. The threading of the disc can be particularly extreme for the cases of 'strong' propeller (see above), as spin-down time-scales of 2.5×10^7 yr are reached, corresponding to $\dot{\nu} \sim -5 \times 10^{-13} Hz/s$ for a 2.5 ms pulsar.

1.6 The recycling scenario and AMSP

From the discussion of previous chapters it should be clear enough how an evolutionary link between MsP and LMXB must hold in order to produce quickly rotating and low-magnetized pulsar. Here we summarize the rationale of this scenario and how it was brilliantly confirmed by the discovery of AMSP.

Rotation powered Millisecond pulsars have the following noticeable properties, they are fast ($\lesssim 10$ ms) and their spin down rate indicates low magnetic fields ($\lesssim 10^9$ G). Their fastness could be explained in terms of a very young age, but the absence of any sign of this youth, as well as their low magnetic fields, rules out this possibility. The only viable option to explain these peculiarities is to argue that they were spun up to those periods by the accretion of matter, which on the other hand suppresses the initial magnetic field until it reaches the measured low values. This interpretation is strengthened by the fact that MsP are found in binary systems at a much larger occurrence rate than what happens for 'classical' pulsars.

Moreover, the values of P and B observed for MsP fit well within the predictions of the standard theory of accretion through a Keplerian disc onto a NS. The relation [1.29] defines in fact the predicted equilibrium period a NS achieves as a results of the balance between the spin up torque due to the accretion of the specific angular momentum of matter at the inner this radius R_0, and the

spin down torque arising as the field lines close beyond R_0, in regions where the magnetosphere is faster than disc matter. A spin equilibrium thus defined holds for a fixed mass accretion rate, NS magnetic field and mass. This is a hard to hold approximation, and is simple to show how simplistic it is. Nevertheless, it has the quality of giving an approximate value for the spin reached by a NS after an accretion phase long enough for the equilibrium to establish. A relation like Eq. [1.29] defines a straight line in the P–B diagram (see Fig. 1.3, but also the caption which describes under which modifications with respect to the quoted equation the plotted relation is derived), the 'spin-up' line, where the pulsars should appear at the end of the accretion phase, given the secular accretion rate and the details of the field–disc interaction. A major success of accretion theories is that all but two MsP lie below the spin-up line, where they are indeed expected to be found as they decelerate after the MsP switches on.

Despite the particular value of P_{eq} is still matter of debate, and mainly depends on the particular modelling of the disc–field interaction, it is clear that equilibrium periods smaller than 10 ms can be attained only if the NS is mildly magnetized ($\lesssim 10^9$ G). This is indeed the case for MsP.

A low magnetic field alone is nevertheless not enough to spin up a NS to millisecond periods; the binary must in fact transfer mass at a sustained rate (at least few tenths of the Eddington rate) for a long period. It can be shown that at least 0.05–0.1 $M_\odot$ are to be accreted by a NS to reach periods in the millisecond range (Burderi et al., 1999). This takes a time $t_{rec} \sim 2.5 \times 10^8 (\dot{M}/0.01\dot{M}_{Edd})^{-1}$ yr. It is not surprising this is of the same order of the spin relaxation time, that is the time needed for a NS to reach a certain frequency when it was slowly spinning at the beginning, $t_{spin} \sim 10^8 (\nu/300Hz)(\dot{M}/0.01\dot{M}_{Edd})^{-1+\alpha/3}$ yr (e.g. Lamb and Boutloukos, 2007), where α is the index of the relation $R_0 \propto \dot{M}^{-\alpha}$ (see Sec. 1.5.2). Such time-scales certainly rule out the possibility that short-lived HMXB produce MsP (Sec. 1.4.4). LMXB meet indeed these requirements and can account also for the orbital period distribution of MsP. 'Large' systems are thought to descend from LMXB in which the mass transfer is assured by the evolution of the donor, while angular momentum losses are the driver for mass transfer in closer systems (Sec. 1.4.5).

Such a scenario provides all the right answers to the questions posed by the discovery of MsP, and was thus generally accepted since it was proposed. The smoking gun was indeed missing, as the spin period of a LMXB was never been measured at that time, and the assumption that LMXB should have been rotating at short periods was just deducted from their low magnetic fields[8], from their oldness, and from the fact that disc accretion was known to spin up NS in HMXB. This embarrassing situation was due to the absence of known pulsar in LMXB at that time. However, quasi periodic oscillations (QPO) were discovered from the LMXB GX 5–1 in the eighties (van der Klis et al., 1985). These QPO had frequencies of few tenths of Hz, and if interpreted in terms of

[8]Many LMXB exhibit thermonuclear X-ray bursts, while HMXB do not. This is interpreted as a consequence of the larger magnetic fields in the latter. As in a HMXB mass is channelled far from the NS, the accreted material is steadily burned before it reaches the NS surface, thus preventing the onset of a thermonuclear flash at the surface (i.e. a burst). On the other hand, these bursts can be triggered in a low field LMXB when the accreted material on the NS surface crosses a certain threshold. In the case of a LMXB, in fact, mass accretes onto the magnetosphere close to the NS, and temperatures large enough to ignite the accreted material are reached only at the NS surface.

Table 1.1: Accreting Millisecond Pulsars discovered as far as 2008 December.

Source	ν (Hz)	$\mathbf{P_{orb}}$(hr)	Discovery of pulsations
SAX J1808.4–3658	401	2.01	Wijnands and van der Klis (1998)
XTE J1751–305	435	0.71	Markwardt et al. (2002)
XTE J0929–314	185	0.73	Galloway et al. (2002)
XTE J1807–294	191	0.67	Markwardt et al. (2003)
XTE J1814–338	314	4.27	Markwardt and Swank (2003)
IGR J00291+5934	599	2.46	Galloway et al. (2005a)
HETE J1900.1–2455	377	1.39	Kaaret et al. (2006)
SWIFT J1756.9–2508	182	0.91	Krimm et al. (2007)
4U 1908+005 (Aql X-1)	550	18.9	Casella et al. (2008)
SAX J1748.9–2021	442	8.77	Altamirano et al. (2008)

the beat frequency model (Alpar and Shaham, 1985)[9], indicate the presence of a NS spinning at few ms in the system. Such conclusions are however indirect and model dependent, so that the problem was still present and led to long searches for a ms pulsating LMXB (e.g. Vaughan et al., 1994).

These efforts remained fruitless until Wijnands and van der Klis (1998) discovered 401 Hz pulsations in a transient LMXB, SAX J1808.4–3658. This discovery was possible thanks to the *Rossi X-ray Timing Explorer* (*RXTE*, see Sec. 2.1.1) collecting capabilities and high temporal resolution, and definitely established how accretion onto a low magnetized NS can effectively spun it up to millisecond periods. Nine more AMSP were discovered in LMXB since then (see Table 1.1). They all belong to transient systems, even if in the case of HETE J1900.1–2455 activity is going on at an outburst-like luminosity level since its discovery, three years ago. This source also joins SAX J1748.9–2021 and Aql X-1 in the sub-class of AMSP that do not show pulsation every time they are observed in outburst, rather displaying very low duty cycles. The others instead always pulsate during outbursts, and are hence called 'persistent' AMSP. We stress that, here, the term persistence refers only to the presence of coherent pulsations.

Nearly all the sample of 'persistent' pulsators is considered in this work to draw informations about their rotational behaviour. Their orbital elements are typical of close binaries ($P_{orb} \sim$ few hours), and the average mass accretion rate is of few thousands of the Eddington rate, except for the afore mentioned case of HETE J1900.1–2455. The typical peak outburst luminosities are of 10^{36}–10^{37} erg/s, and spin frequency derivatives of 10^{-13}–10^{-12} Hz/s are expected for the NS in these systems, according to the accretion theory developed in Sec. 1.5.2 (Eq. [1.25]). One of the main results of the work presented here is to show how these derivatives are effectively observed.

The discovery of AMSP represents an important wedge for the recycling scenario, but nevertheless some issues remain open. The older, and maybe more noteworthy, is the statistics of MsP and LMXB populations. The supposed offspring outnumber in fact the number of progenitors by a factor 10–100, given the standard models for the duration of the LMXB phase. The main efforts to

[9]According to this model, the QPO frequency reflects a beat between the Keplerian frequency at the inner rim of the disc and the NS spin frequency, thus allowing at least an indirect estimate of the order of magnitude of the latter.

reduce this discrepancy rely on the possibility that the companion is bloated by the irradiation from the compact object, thus raising the mass transfer rate and shortening the time-scale of the accretion phase.

Despite the most important, this is not the only problem concerning the recycling scenario. First of all, despite the discovery of ten AMSP, they still are quite rare objects among LMXB (10 out of ~ 180). The reasons proposed for this scarcity are numerous. Many LMXB could have magnetic fields smaller than the ones needed to dynamically influence the accreting mass ($\lesssim 10^8$ G), given the particular accretion rate. An indication towards such an hypothesis could be represented by the smaller spin frequencies shown on the average by X-ray bursters, with respect to AMSP. During thermonuclear X-ray burst, in fact, LMXB often show pulsations which have an high internal coherency. Also three AMSP (SAX J1808.4–3658, XTE J1814–338 and HETE J1900.1–2455) are bursters, and the frequency of their burst oscillations was reported to the same value of the coherent pulsations, within 1% (Chakrabarty et al., 2003). This strengthens the interpretation of burst oscillation frequency in terms of the NS spin. Despite the low statistics forbids any definitive conclusion, it turns out that bursters show smaller frequencies on the average. According to the spin equilibrium theory, this would thus represent an indication of lower magnetic fields (or higher average mass accretion rates).

Furthermore, a fundamental issue is given by the spin frequency distribution of all the 22 NS for which the period is known (from coherent or burst oscillations). This distribution is sharply cut off beyond 730 Hz (95% confidence level), a value smaller than the generally assumed rotational break-up frequency (Chakrabarty, 2008). The break-up frequency is defined the spin rate at which a mass element on the surface of the NS star starts to experience the unbinding pull of the centrifugal force. Unless mechanisms other than the magnetic threading work to slow down the compact object (see below), NS in LMXB are expected to reach this limiting frequency after ~ 0.25 $M_\odot$ are accreted, which can easily happen in a LMXB history (Burderi et al., 1999). Considering the various EOS currently proposed for NS, Burderi et al. (1999) showed that the limiting frequency is of the order of Keplerian speed at the NS radius ($[GM/R_*^3]^{1/2}$), and varies in the range 670–1600 Hz. The lower end of this interval is populated by the stiffer EoS with larger radii, and the observed cut-off would therefore exclude the majority of the proposed EoS. To circumvent the problem posed by lack of sub millisecond pulsars, Bildsten (1998) proposed that gravitational waves emission could slow down a pulsar well before it reaches the break-up speed. This requires a non zero NS mass quadrupole, Q, as the GW emission reduces the NS angular momentum at a rate $N_{gw} \propto Q\nu^5$. It is immediate to note that such a mechanism increasingly works as the NS rotates at large frequencies. Hence, the ideal test bed among AMSP to check this hypothesis is the fastest spinning one, IGR J00291+5934. In this case a spin down at a rate $\dot{\nu}_{GW} \simeq -(10^{-13}$–$10^{-14})$ Hz/s is expected for $Q \gtrsim 1 \times 10^{36}$ g cm^2. The results we obtained from the temporal behaviour of this source, and their implications for this model, are discussed in the light of this scenario in Sec. 5.5.

Another mechanism which could efficiently limit the NS spin-up, at least for transient LMXB, is the spin-down asssociated to the rotation of the magneto-dipole, in perfect analogy to what happens for rotation-powered pulsars. This spin-dpon torque could in fact be important among transiently accreting systems, as it should be the only working during the quiescent phases. Moreover,

indications pointing to the energy release of a switched on magneto-dipole rotator also emerge on other grounds. The brightness of the optical counterparts in SAX J1808.4–3658 and IGR J00291+5934 (Burderi et al. 2003 and D'Avanzo et al. 2007, respectively) cannot in fact be explained in terms of the reprocessing of the X-ray flux emitted by these sources in quiescence. It is therefore argued that a magneto-dipole rotator of few $\times 10^8$ G switches on in quiescence, providing the right energy budget to explain the reprocessed optical luminosity. The spin-down yielded by this effect is of few $\times 10^{-14}$ Hz/s, the same order of the GW emission channel mentioned above, thus making the magneto-dipole rotator switch-on another viable option to explain why AMSP do not reach the break up speed (Di Salvo et al., 2005). It has to be finally noted that the absence of any measured radio pulsation from such a rotator could be simply due to the absorption of the circumventing matter.

2

Observations and Data Analysis

I review in this chapter the peculiarities of X-rays detection (Sec. 2.1), the observatories whose data were used in this thesis (Sec. 2.1.1 and 2.1.2) and the techniques used to perform a temporal analysis. Despite they were not used in the work presented here, Fourier technique naturally defines the fundamentals of whatever temporal analysis on a coherent signal, and are therefore briefly reviewed in Sec. 2.2.1. We then discuss the precision techniques used in the study of the fast signals emitted by AMSP. These techniques essentially rely on the folding of a X-ray light curve to let the pulse profile to emerge above the continuum emission (Sec. 2.2.2 and 2.2.3). These are usually named as 'timing techniques', and their importance already revealed when the study of the 'relativistic' pulsar earned R.A. Hulse and J.H. Taylor, jr the Nobel prize for physics in 1993. Nevertheless, these techniques were modified and tailored to the particular case of AMSP (Sec. 2.2.7), in order to produce the reliable results about their spin evolution, presented in the next chapters.

2.1 X-ray detection

The usual and arbitrary definition of the X-ray band encloses photons whose energy is between 0.1 keV and 100 keV. The energy of 10 keV is often referred to as the energy which divides 'soft' from 'hard' X-ray photons. X-rays are easily absorbed by few cm of Earth atmosphere so that none reaches the Earth surface. It turns out that X-ray astronomy must be space-borne[1]. Apart from photometry, the observational study of X-rays emitted by astronomical sources deals essentially with three kind of analysis: imaging, temporal and spectral analysis. Contrary to the optical astronomy, the relatively low photon fluxes emitted by X-ray sources excluded integrating detectors (like optical plates) from the history of X-ray astronomy. In this band, photons are rather counted 'one-by-one', as it is reflected by the nature of the statistics used to define the photons' detection. As a matter of fact, the probability of counting a certain number of events in a finite time interval, when the underlying process has a well definite average (the actual emitted flux in this case), and each count is independent on the others, is governed by Poisson statistics. This distribution has the property that the expected number of occurrences is not only by definition

[1]The pioneer age of X-ray astronomy was conducted using balloons and rockets which could reach the outer layers of the Earth atmosphere, where hard X-ray photons are still not completely damped down. Such observing strategy is anyway strongly restricted to short observing times.

the average, but also the variance. If the number of counts in a time interval is $\aleph$, the associated standard deviation is therefore $\sqrt{\aleph}$. It is thus immediately clear how the relative uncertainty in any intensity estimate is greatly reduced when the counts are large. This goal is achieved on one side, by using the largest photon collectors available, and on the other, with the use of techniques that fold the signal to improve its ratio to the noise (see Sec. 2.2.2).

Astronomical X-rays are detected basically in three ways. **Proportional counters** record the electrical discharge produced by the passage of an X-ray photon through a cell filled by noble gas (often Ar or Xe). In fact, the incoming radiation is able to ionize the atoms and to create electron-ion couples, therefore enhancing the gas conductivity. As the size of the yielded electrical pulse depends on the energy of the incident photon, such an instrument gives also spectral information. A proportional counter does not focus photons, and its imaging capabilities are therefore limited by the opening of a collimator that is generally put at the counter's window.

Scintillators use particular crystals which have the property of emitting optical light (between 300 and 500 nm) when hit by X-rays. The intensity and the energy of the incident spectrum is measured from the reprocessed radiation. This technique is particularly suited for the detection of hard X-rays.

Finally, X-ray imaging is achieved by **X-ray telescopes**. These are basically different from optical/UV telescopes, owing to the few degrees incidence angles that incoming photons have to make with respect to the mirrors to be reflected. Given the higher photons' energies, normally incident X-rays would in fact be absorbed rather than focused by the mirrors, so that grazing incidence is mandatory. Mirrors are therefore placed nearly parallel to the optical axis, but this is at the expenses of a greatly reduced projected area. Several mirrors are therefore nested in a co-axial and co-focal configuration to obtain the larger possible sensitive areas. Charge Coupled Devices (CCD) are placed at the focal surface to record the photons; given the photon high energies, enough charge is produced that the energy of each photon can be measured on the read-out. This is the basic reason because the very same X-ray photons can be used indifferently for spectral and photometric purposes. We present in the following the two observatories which were mostly used to perform the analysis presented in this work, *RXTE* and *XMM-Newton*.

2.1.1 *RXTE*

The Rossi X-ray Timing Explorer (*RXTE*) is an United States X-ray mission covering the 2.0–250.0 keV energy band, featuring an unprecedented temporal resolution, in combination with moderate spectral resolution, to explore the variability of X-ray sources. This mission indeed covers time scales from microseconds to months on a broad band spectral range. The spacecraft was launched on December 30, 1995 from NASA's Kennedy Space Center, and despite that it was designed for a five-years operation-time, it is in its twelfth year of lifetime and it is still performing well. The launcher put it in a low-earth circular orbit at an altitude of 580 km, corresponding to an orbital period of about 90 minutes.

The observatory is composed by three instruments:

- The **Proportional Counter Array** (PCA) is an array of five identical

aligned proportional counters filled with Xenon. They yield a total collecting area of 6500 cm^2. While all the units were fully operational at the beginning of the mission, some were totally or partially switched off during the lifetime of the observatory, and nowadays only unit 2 is always on. The counter in each unit contains three layers of anode grids for the detection of the signal produced by an X-ray passing through the gas filled volume, and one layer for signal rejection. A collimator stands above each unit, giving a Full Width Half Maximum of 1° for the field of view. Data can be recorded in two main modes, an 'event' mode that yields a time-series of unevenly spaced events (each described by an arrival time and an energy) and a 'binned' mode, giving data binned in a time series of regularly accumulated histograms. Event mode data are those used to perform timing analysis of fast signals, while binned mode are tailored for a spectral analysis. The maximum time resolution achieved in event modes is 1 μs (Good Xenon configuration), while a coarser 122 μs value is mostly used (Generic event configuration). The energy band covered by the PCA is 2–60 keV, for an energy resolution $< 18\%$ at 6 keV.

- The **High Energy X-ray Timing Experiment** (HEXTE) covers the high energy part of the X-ray spectrum (15–250 keV), and is made by two clusters of 4 NaI/CsI phoswich scintillation detectors. The crystals of HEXTE detectors are chosen for their marginal self-absorption of the emitted photons, and because they assure a reasonable energy resolution (<9 keV at 60 keV). Each detector has a net open area of 225 cm^2 (for a total area of $\sim 2 \times 800$ cm^2), and is passively collimated to a 1° field of view, co-aligned with that of the PCA. Each cluster has a rocking system, so that the background is always monitored while a particular source is observed. The time sampling is 8 μs, little enough to perform a temporal analysis for the faster signals emitted in the universe.

- The **All Sky Monitor** (ASM) is made of three shadow cameras each containing a proportional counter sensitive in the 1.5–12 keV band. The goal of the ASM is to perform a scan of the X-ray sky to monitor its high and often unpredictable variability. To this end the field of view of each camera is $9° \times 90°$, and the whole instrument is mounted on a motorized rotation drive, so that a randomly chosen source is observed 5 to 10 times each day.

2.1.2 *XMM-Newton*

The European Space Agency's X-ray Multi-Mirror Mission (*XMM-Newton*) is an X-ray telescope launched by an Ariane 5 launcher on December 10, 1999. It carries 3 high throughput X-ray telescopes with an unprecedented effective area, as well as an optical monitor, the first flown on a X-ray observatory. The spacecraft weights 4 tons and it is 10 m long, making it the largest scientific satellite ever launched by the European Space Agency. It was put in a very high 48 h orbit, with an apogee of 114000 km away from the Earth (i.e., one third of the distance to the Moon), to permanently work outside the radiation belt surrounding the Earth, and to allow long uninterrupted observations. *XMM-Newton* is made of three X-ray telescopes, each one having 58 Wolter I grazing-incidence mirrors, nested in a co-axial and co-focal configuration. Each

mirror shell consists of a paraboloid and an associated hyperboloid, which were replicated together in one piece to facilitate alignment and integration. The effective area ($\gtrsim$ 1500 cm^2 below 2 keV, 900 cm^2 at 7 keV, and 350 cm^2 at 10 keV) is the largest ever obtained in the energy band 0.1–12.0 keV by an X-ray telescope, and the field of view is reasonably large (30′). The point spread function describing its imaging capabilities is between 4 and 6 arcsec, depending on the considered instrument and on the energy. The spectral resolution of the X-ray instruments mounted on *XMM-Newton* is moderate ($\sim$ 70 eV) to large (few eV). The sensitivity to fluxes down to 10^{-14} erg s^{-1} cm^{-2} assured by the large mirrors is the largest among X-ray observatories flying at the moment.

XMM-Newton is made of three instruments:

- Three X-ray CCD cameras are mounted at the bottom of each X-ray telescope, and comprise the **European Photon Imaging Camera** (EPIC); two of the cameras are MOS (Metal Oxide Semi-conductor) CCD arrays, and are installed behind the two X-ray telescopes equipped with the gratings of the Reflection Grating Spectrometers (RGS, see below), so that only the 44 % of the original flux reaches the MOS cameras. The third X-ray telescope has an unobstructed beam; the EPIC instrument at the focus of this telescope uses pn CCDs and is referred to as the pn-camera. The sensitive energy band of the EPIC is between 0.1 and 12 keV. MOS and pn cameras differ not only for the amount of energy effectively collected, but also for the chip architecture which allows the pn to perform observations also in very fast timing and bursting modes (i.e. with a temporal resolution down to 30 μs), which are therefore suitable for the study of very quickly variable objects, like AMSP. The EPIC CCDs assure a spectral resolution of $\sim$ 70–80 eV

- Among the science instruments on board *XMM-Newton*, the RGS is best suited for high spectral resolution (down to few eV) X-ray spectroscopy in the range 0.33-2.5 keV. This range covers the energies of the K-shell transitions and He-like triplets of light elements (such as C, N, O, Ne, Mg and Si) and the L-shell transitions of heavier atoms (like Fe and Ni), thus representing a fundamental diagnostic tool to study the chemical and physical state of the emitting material, as well as the physics of the absorbing medium between the source and the observatory. The two RGS units mounted on the X-ray path to the two MOS cameras are composed by a Gold reflecting surface, forming a grating stack that deviates more than half of the incident photons to an assembly of 9 CCDs (similar to MOS CCDs) mounted at a secondary focus. The deviation angle is obviously given by the dispersion equation, therefore allowing fine spectral measurements. The chips are back illuminated to maximize the soft-energy response.

- Besides its X-ray instruments, *XMM-Newton* also has a co aligned 30-cm optical/UV telescope, to provide a simultaneous observation of the X-ray and optical/UV emission of a source. The sensitive band is between 180 and 600 nm. Despite its limited size, this telescope can observe fluxes down to the 20^{th} magnitude, thanks to the absence of the atmospheric extinction. The design of the telescope is that of a f/12.7 Ritchey-Chrétien optics.

2.2 Temporal analysis

2.2.1 Fourier techniques

Temporal analysis deals with the study of the temporal variations of the flux emitted by the source of interest. The basic tool to enlighten the time-scale over which a signal varies is the Fourier analysis. Even if the temporal analysis subject of this work is performed mainly through more accurate methods, a brief review of Fourier techniques seems mandatory for its basilar role in the statement of any temporal analysis (see van der Klis, 1988, for a detailed review).

The Fourier techniques essentially rely on the decomposition of a given signal (the source light curve in this context), $x(t)$, in a base of sine waves with different frequencies. The more the signal varies at a given frequency $\bar{\nu}$, the larger the coefficients relative to the sinusoidal function at that frequency are. It turns out that the Fourier analysis can be grossly outlined as the measure of the correlation between the given signal and the periodic functions used to decompose it.

The base used in the description of the function to decompose is formed by a set of waves of the form, $p_n = \sin(2\pi n\hat{\nu}t) - i\cos(2\pi n\hat{\nu}t) = e^{-2\pi i n\hat{\nu}t}$, where the Euler formula was used to introduce the more easier to handle complex notation, and $n \in \mathcal{Z}$. In general $\hat{\nu}$ describes the smallest frequency used in the decomposition of the signal; all the other waves have frequencies that are integer multiples of this fundamental frequency. The possibility to sensibly express a whatever function $x(t)$ in the base so defined relies on the completeness of this base. One thus has, $x(t) = \sum_n (x, p_n)p_n$, where (x, p_n) is the projection of the function $x(t)$ on the n-th wave p_n, or, in other words, the coefficient of the correlation between the signal and a periodic sinusoidal wave of frequency $\nu = n\hat{\nu}$. The form of these coefficients, called the Fourier transform of $x(t)$, is:

$$a(\nu) = \int_{-\infty}^{\infty} x(t)e^{2\pi i n\hat{\nu}t}dt, \tag{2.1}$$

where we argued the function $x(t)$ to be infinitely extended. Therefore, the signal we are interested in can be expressed in the so-called Fourier series:

$$x(t) = \sum_n \left[\int_{-\infty}^{\infty} x(t)e^{2\pi i n\hat{\nu}t}dt\right] e^{-2\pi i n\hat{\nu}t}. \tag{2.2}$$

This series converges on the average for every reasonably continuous function. An important case is represented by those functions that are strictly periodic, with frequency $\bar{\nu}$. In this case the Fourier theorem applies, stating how such a function can be expressed as the sum of an infinite number of sine waves, all of which have frequencies multiple of the fundamental frequency $\bar{\nu}$. The term relative to the frequency $\nu = n\bar{\nu}$ is called the n-th harmonic of the signal.

As it was mentioned above, the ability of Fourier techniques to identify periodicities relies on the measure of how large the coefficients of the decomposition are. It is therefore not surprising that, if $x(t)$ is a sinusoid of frequency $\bar{\nu}$, its Fourier transform is a delta function, $\delta(\nu - \bar{\nu})$ (see Eq. [2.1]).

Nevertheless, in the real world signals are not infinitely extended nor continuous, and rather come as binned temporal series; that is, the temporal baseline, T_{obs}, is divided in N temporal bins, t_k $(k = 0, ..., N-1)$, each $\delta t = T_{obs}/N$

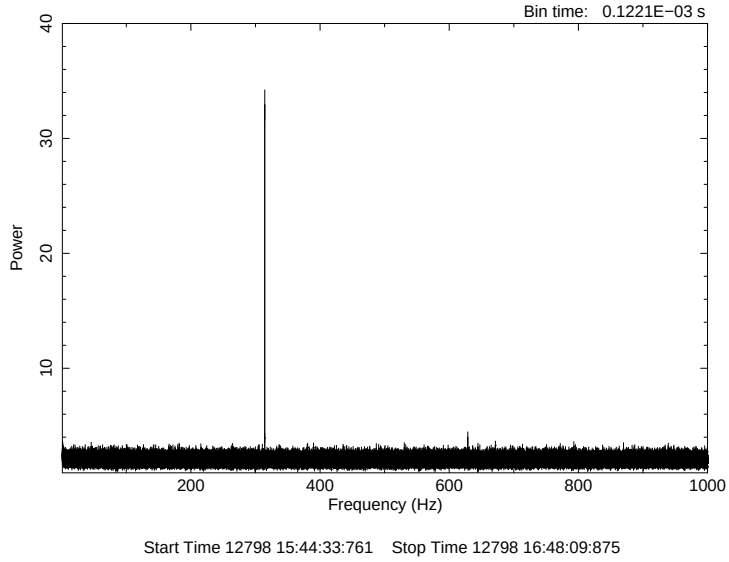

Figure 2.1: Power spectrum of a $\sim$ 3.8 ks RXTE/PCA observation of XTE J1814–338 (ObsId 80418-01-01-00, see Table 4.2). The time series is sampled at 122 μs. The spectrum is obtained averaging 60 power spectra of 524288 temporal bins ($\simeq$ 64 s) each, in order to maximise the signal-to-noise ratio. We note that the considered light curve was preliminarily corrected for the orbital motion of the source, using the orbital solution listed in Table 4.4. The spin frequency at 314.36 Hz is clearly visible, as well as an indication of a weak second harmonic component at the double of this frequency.

long, and the number of counts in each bin, $x_k = x(t_k)$, is recorded. It is still possible to define the Fourier transform of such a series, in an analogous way of what was done in Eq. [2.1]:

$$a_n = a(\nu = n\hat{\nu}) = \sum_{k=0}^{N-1} x_k e^{2\pi i n \hat{\nu} t_k}. \qquad (2.3)$$

The lowest frequency that can be sampled is $\hat{\nu} = 1/T_{obs}$, and the other considered in the decomposition are $\nu = n/T_{obs}$, with $n = -N/2, ..., N/2 - 1$[2]. The largest frequency needed for the complete description of the discrete signal is $\nu_{Ny} = \frac{1}{2}N/T$, the so-called Nyquist frequency. As a matter of fact, a wave at the Nyquist frequency completes its oscillation in two adjacent temporal bins. Larger frequencies are not accessible, as the information in the signal would be lost because of temporal binning. It is thus immediately understood how to detect periodicities at high frequencies, high temporal resolution is needed.

Fourier techniques are particularly useful in astronomy to detect previously unknown periodicities. This is realized by computing a power spectrum, that is the frequency distribution of the squares of the coefficients of the Fourier transform, $|a(\nu)|^2$. The Parseval theorem states in fact that $\sum x_k^2 = \frac{1}{N}\sum_n |a_n|^2$, that is, the squared modulus of a function is equal to the sum of the squares of its projection onto a complete basis. To detect periodicities it is then useful to use this theorem for the distribution of the x_k's around their temporal average

[2]Negative frequencies are also considered because the complex notation is used.

$< x_k >$, considering the base of Fourier waves defined above. It can be easily shown that:

$$\sum_k (x_k - < x_k >)^2 = \frac{1}{N} \sum_{j=-N/2, \neq 0}^{N/2-1} |a_n|^2, \quad (2.4)$$

The more a signal deviates from its average on a time-scale T_{obs}/n (hence having a larger variance), the larger $|a_n|^2 = |a(\nu = n/T_{obs})|^2$. The power spectrum is therefore defined as:

$$P(\nu) = \frac{2}{N_{ph}} |a(\nu)|^2, \quad (2.5)$$

where N_{ph} is total number of photons collected. This normalization is chosen on a statistical basis, because if the time series is composed by pure Poissonian noise, the distribution of the power spectrum will be the χ^2 distribution with 2 degrees of freedom. In this case therefore, the power spectrum fluctuates around 2, and the signals are to be detected above this well-established noise.

It was mentioned above that the Fourier transform of a sinusoidal signal is a Delta function; as we are here interested in coherent signals (i.e. strictly periodic), the Fourier theorem predicts the excess power to be found only at the fundamental frequency and at the other harmonics. The fact that the signal is not continuous, nor infinitely extended, modifies the profile of the Fourier transform of a sinusoid from being a Delta function. The expected power spectrum is indeed broadened by the binning of the data, but this effect can be minimized by a tighter binning. We have in fact, $|a(\nu)|^2 \sim 0.25 A^2 N^2 [\sin(\pi x)/(\pi x)]^2$, where A is the amplitude of the oscillation, and x is the offset of the 'true' frequency of the signal from the nearest frequency implied by the binning, $\nu_n = n/T_{obs}$. It results anyway that in the case of high temporal resolution data (e.g. $\delta t = T_{obs}/N = 125 \mu s$ for PCA data taken in event mode, see Sec. 2.1.1), all the power owing to the coherent periodicity of an AMSP is concentrated in a frequency bin, generating an evident spike in the power spectrum (see Fig. 2.2.1 for the case of XTE J1814–338). The accuracy in the determination of frequencies through the Fourier analysis is, in any case, limited by the finiteness of the temporal series. The frequency step, and therefore the maximum frequency resolution, is indeed $\delta\nu = 1/T_{obs} \simeq 3 \times 10^{-4} T_{hr}^{-1}$ Hz, where T_{hr} is the observation time in hours. A resolution of this order is too coarse to allow the measurements of the spin-frequency variations due to the accretion torques acting on an AMSP, which at most are of $few \sim 10^{-7}$ Hz during an entire outburst.

As it will be discussed in the following sections, the reconstruction of the pulse profile is needed to get more accurate estimates. Fourier techniques still hold anyway as the fundamental tool to detect previously unknown periodicities.

2.2.2 Light Curve Folding

A leap towards better temporal resolution is achieved by means of the reconstruction of the actual pulse profile shown by a pulsar. This cannot be immediately done, as the pulse profile of an X-ray pulsar is not generally visible from a glance to the light curve.

To understand this, a criterion to detect a pulse profile above the continuous emission has to be defined; it can be safely stated that a periodic profile is present, if its count rate deviates by, say, more than 5σ from the average, during an oscillation. If we define the fractional (peak to peak) amplitude of the pulse

profile as $A = (I_{max} - I_{min})/(I_{max} + I_{min})$, the resulting fluctuation in the light curve is $A \cdot F$, where F is the flux of the source in counts per second. The typically observed amplitudes are < 0.1.[3] For low amplitudes, and if we assume that the light curve is sampled in P/n long temporal bins, the above criterion can be written as, $AFP/2 \gtrsim 5\sqrt{FP/n}$. The flux needed to satisfy this requirement is $F \gtrsim 100/(nPA^2) = 2.5 \times 10^7\, n_4^{-1} P_{ms}^{-1} A_{0.1}$ c/s, where $n_4 = n/4$, P_{ms} is the spin period in milliseconds, and $A_{0.1} = A/0.1$. The intrinsic fluxes emitted by typical X-ray binaries are lower by at least four orders with respect to the actual collecting capabilities of X-ray observatories. The detection by-eye of the pulse profile emitted by a millisecond pulsar is therefore impossible.

It is clear from the above arguments how the pulse detection goes along with the improvement of counting statistics, i.e of the signal-to-noise ratio, where here the term noise comprises all the sources of non variable emission. Given the properties seen in Sec. 2.1, this can be achieved by raising the number of counts in each temporal bin. The periodicity properties of the underlying signal can be then exploited folding the light curve around the signal period. This procedure implies the branching of the light curve in T_{obs}/P segments, each of whom is sampled by P/n bins, with $n \gtrsim 10$ to reconstruct a profile accurate enough for the goals of timing techniques. The count rate of every bin $k = 1, ..., n$, in each of the T_{obs}/P segments, is then summed and averaged. The errors affecting the resulting points are lowered by a factor $\sqrt{T_{obs}/P}$, which can be easily $\sim 10^3$ in our case, thus allowing the pulse profile to emerge above the continuum emission.

Such a technique is very sensitive, but also requires a very accurate knowledge of the period of the signal, P. If a light curve is indeed folded around a period P_F, the position of a bin with respect to the real modulation moves of a quantity $\delta P = |P_F - P|$, every period. If δP is large compared to P, photons pertaining to the very same phases of the oscillation will be summed in different bins while folding the light curve. This effect, caused by the ignorance of the 'true' spin period, washes out the profile completely if

$$\Delta P > P^2/T_{obs} \simeq 3 \times 10^{-10} P_{ms}^2 T_{hr}^{-1}\ s. \tag{2.6}$$

In terms of frequencies, an accuracy better than 10^{-4} Hz is needed, and a comparison with the results of Sec. 2.2.1 shows how the one ensured by Fourier techniques is too small.

To ensure the desired better estimates of the spin period, a technique known as Epoch Folding Search is commonly used. The light curve is folded around many different periods, distributed around the best estimate available; the goodness of every single guess is tested by measuring how much the obtained folded profile deviates from being constant. The statistics used to this purpose is the χ^2 of the folded profile, defined as the squared sum of the deviations of the count rates, in every bin in which the profile is sampled, from the average count rate. This statistics is particularly suited for this case, as the squared sum of n numbers is maximum when maximum is the difference between these numbers.

The count rate in the k-th phase bin is defined as $R_k = \sum_j N_k^j (n/T_{obs})$, where N_k^j is the number of counts of the k-th bin of every segment, and the sum is extended to all the T_{obs}/P segments the light curve is divided in. The average

[3] This can be viewed as a general result of rapid rotation and General Relativity effects due to the compactness of the NS, see Sec. 6.2

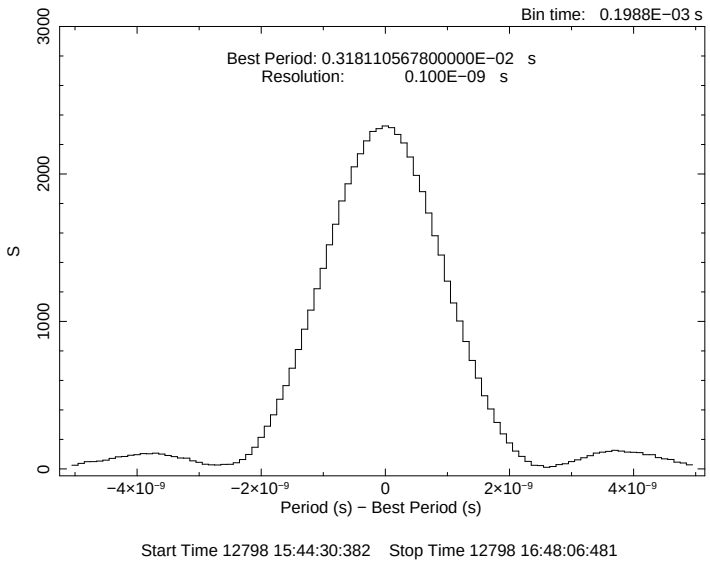

Figure 2.2: Epoch Folding Search performed on the same observation of XTE J1814–338 considered to produce the power spectrum of Fig. 2.1. The pulse profile is sampled in n=16 bins, the observation is considered in its entirety, and the periods are searched in steps of 10^{-10} s. The maximum of the chi-squared S is the best estimate achieved with Epoch Folding Search, with an uncertainty fixed by the chosen period step. Such an uncertainty can be further minimized by fitting the S vs. P profile with Eq. [2.9].

count rate is, similarly, $R = \sum_j R_j/n = N_{ph}/T_{obs}$, where the total number of counts is $N_{ph} = \sum_{j,k} = N_j^k$. The statistics used to measure the significance of a folded pulse profile is, therefore:

$$S = \sum_{k=1}^{n} \frac{(R_k - R)^2}{\sigma_k^2} \tag{2.7}$$

(Leahy et al., 1983). The variance of this statistics, $\sigma_k^2 = R/T_k = R \times n/T_{obs}$, simply reflects the counting noise.

In the absence of any signal, the statistics defined by Eq. [2.7] behaves by definition as a χ^2 distribution with $n-1$ degrees of freedom. This behaviour is ensured by the fact that the number of counts in each bin is usually so large that its Poisson distribution tends to be Gaussian. A signal can be detected at a given confidence level, c, if the χ^2 of the folded pulse profile, S, is beyond a certain threshold, S_0, implicitly defined by:

$$(1 - c/100) = N_p Q_{n-1}(\chi^2 = S_0), \tag{2.8}$$

where $Q_{n-1}(\chi^2 = S_0)$ is the probability that a $\chi^2 = S_0$ is obtained by chance (i.e. following a chi squared distribution with $n-1$ d.o.f.), and N_p is the number of period trials. This criterion will be used in the following also to state the significance of each detection at different times, even if the pulse period is already known ($N_p = 1$).

It was shown by Leahy (1987) that, when the light curve contains a sinusoidal signal, i.e. the count rate is described by $r(t) = R[1 + A \sin 2\pi t/P]$, the value

of the statistics S for a profile folded at P_F is:

$$S = S_{n-1} + \frac{1}{2}A^2 N_{ph} \frac{\sin^2 x}{x^2} f(n), \tag{2.9}$$

where the first term on the right hand side is the statistics of noise alone, $x = T_{obs}\pi\delta/P_F$, $\delta = P_F/P - 1$ and $f(n) = [1 - \pi^2/3n^2 + 2\pi^4/45n^4 + ...]$. An example of the trend followed by S, in the case of an AMSP (XTE J1814–338), is shown in Fig. 2.2.2. Modelling the centroid of such a distribution with Eq. [2.9] allows an accurate determination of the spin period. A first threshold on this accuracy can be derived arguing how far two periods have to be in order to produce two different profiles, within the statistical fluctuations. Arguments similar to those used above to derive Eq. [2.6] lead to:

$$\delta P_{min} = \frac{P^2}{nT_{obs}} = 1.74 \times 10^{-11} n_{16} P_{ms}^2 T_{hr}^{-1} s, \tag{2.10}$$

where $n_{16} = n/16$. Leahy (1987) performed Monte Carlo simulations to determine how accurate the estimates of period and amplitudes may be through the use of Epoch Folding Searches. They obtained:

$$\sigma_P = \frac{1}{2} n \delta P_{min} \left[\frac{\chi^2_{max}}{n-1} - 1 \right]^{-0.63}, \tag{2.11}$$

where χ^2_{max} is the peak of the observed S distribution. In the case of a source observed for 1 hr at a level of 200 c/s, and with a signal amplitude of 0.05, the use of Eq. [2.9] in [2.11] shows how accuracies of $few \times 10^{-2} \delta P_{min}$ s can be obtained with the EFS. It will be shown in the next section how these accuracies are still not large enough to detect the extremely small period variations produced by the physical phenomena we are interested in. It is for this reason that, once the period which maximizes S is found, and every available observation is folded around this estimate, we consider the temporal evolution of the profiles' phases to derive the desired physical information on the variations of the NS spin frequency.

2.2.3 Timing analysis

Timing analysis is the most accurate technique to follow the frequency evolution of a periodic signal. As it was previously anticipated, this technique relies on the measurement of the movements of the pulse profile as time runs. All the available observations of a source are therefore folded around a common period (which has too be very close to the true one, see Eq. [2.6]), thus defining a common 'sampling window'. Movements of the pulse profile with respect to this window are easily interpreted as variations of the period of the signal with respect to the folding one. This basilar result follows from the assumption that the shape of the pulse profile varies little with time, an hypothesis which unavoidably fails in some cases. This makes necessary a disentanglement of these 'geometrical' effects from 'true' changes of the spin period, in order to firmly establish the behaviour of the latter, which indeed reflects the rotational behaviour of the NS. In order to review the expected timing behaviour due to the evolution of the NS rotation, we assume from here on that the shape of the profile is constant.

A discussion of the cases in which this guess has to be necessarily withdrawn will be presented in Ch.6, where a possible model to explain phase movements due to pulse shape is also discussed.

The profiles of AMSP are very simple with respect to the ones showed by other accreting pulsar. While for slowly spinning accreting pulsars complex structures may appear in the folded profiles, the signal of an AMSP can be completely described with two harmonic components at most (see Fig. 3.2 and 4.2). The profiles are therefore here defined as:

$$r(t) = R \cdot \{1 + A_1 \sin[2\pi\nu(t - T_0)] + A_2 \sin[4\pi\nu(t - T_0)]\}. \quad (2.12)$$

Here, R is still the average count rate, A_1 and A_2 are the amplitudes of the two harmonics and T_0 is the start time of observation. The phases of the two harmonics are defined as the times (in units of the spin period) at which the arguments of the sinusoidal functions are equal to zero, that is:

$$\phi_n(t) = n \times \nu(t - T_0), \quad (2.13)$$

where n is the harmonic number. Without any loss of generality, we consider here on the case $n = 1$, calling $\phi(t) = \phi_1(t)$

Due to the periodicity of the signal, it is useful to divide the phase in its integer and decimal part. One thus has:

$$\phi(t) = [\phi(t)] + \{\phi(t)\} = [\nu(t - T_0)] + \{\nu(t - T_0)\}. \quad (2.14)$$

The first term on the right hand side is simply the integer number of cycles elapsed by the signal from the beginning of observation to the considered time. We have therefore $\sin 2\pi\phi(t) = \sin 2\pi\{\nu(t - T_0)\}$, so that what we measure and call phase in the following is literally only its decimal part.

To get the information about the temporal evolution of the signal, it is useful to follow the difference between the observed phases and the value that the phase should take according to a particular model. These differences, $R_\phi(t) = \phi_{pred}(t) - \phi_{obs}(t)$, are called phase residuals. This choice is well suited, as the various effects that cause the phases to vary are generally independent; therefore if only one of these effects is to be highlighted, it is enough to incorporate all the others in the predicted timing solution to make the residuals witness the desired effect. As an example, if a constant frequency solution is guessed, the phase is expected to be constant in time. Any mechanism that makes the frequency different from the one used in the folding will therefore make the residuals vary. Differentiating Eq. [2.13], one obtains:

$$R_\phi(t) = \phi_0 - \int_{T_0}^{t} \delta\nu(t')dt', \quad (2.15)$$

where $\delta\nu(t) = \nu(t) - \nu_F$ is the difference between the actual frequency at the time t, and the folding frequency, $\nu_F = 1/P_F$. In the case of an X-ray pulsar, the phase of the pulse profile can change because of the three effects discussed in the following:

- Genuine differences between the folding frequency and the spin frequency of the NS. They can be due to a inexact guess of the folding frequency, as well as to a frequency evolution due to the torques acting on the NS.

- Variations of the times of arrival of X-ray photons due to the motion of the source in a binary system. This translates in a Doppler effect that periodically modulates the observed spin frequency.
- The uncertainty on the position of the source. In fact, recorded times of arrival also depend on the position of the X-ray observatory at a particular time with respect to the direction of the line of sight.

We can therefore write:

$$R_\phi(t) = R_{\phi\, rot}(t) + R_{\phi\, orb}(t) + R_{\phi\, pos}(t) \tag{2.16}$$

2.2.4 Rotational evolution of the NS

The rotational evolution of the NS can be simply described in terms of its spin frequency as:

$$\nu(t) = \nu(T_0) + \int_{T_0}^{t'} \dot{\nu}(t')dt'. \tag{2.17}$$

Inserting this equation in [2.15] yields:

$$R_{\phi\, rot}(t) = -\int_{T_0}^{t'} [\nu(T_0) - \nu_F]dt' - \int_{T_0}^{t'}\int_{T_0}^{t''} \dot{\nu}(t'')dt''. \tag{2.18}$$

The first term owes to our ignorance of the 'true' spin frequency at the start time of the observation; calling $\Delta\nu = \nu(T_0) - \nu_F$, the trend induced in the residuals by this effect is linear in the temporal variable, $\propto \Delta\nu(t - T_0)$.

The second term in the right hand side expresses the rotational evolution of the NS, and obviously depends on the particular law guessed for the exchange of angular momentum between the star and the accreting matter. If the spin frequency derivative has a constant value, double integration of the relative term easily yields a quadratic term of the form, $\frac{1}{2}\dot{\nu}(t - T_0)^2$. However, the accretion theory reviewed in Sec. 1.5.2 shows that the expected temporal evolution of the spin frequency is more complex. Even if magnetic threading is not considered, $\dot{\nu}(t)$ depends on the instantaneous value of the accretion rate, $\dot{M}(t)$, and on the position of the inner disc radius, $R_0(t)$, with all the physics of the interaction between the magnetosphere and the accretion disc incorporated in the assumed relation between R_0 and $\dot{M}$.

Following Eq. [1.25], the material torque on the NS yields a spin frequency derivative:

$$\dot{\nu}(t) = \frac{1}{2\pi I}\dot{M}(t)\sqrt{GMR_0(t)}, \tag{2.19}$$

where the temporal dependences of the moment of inertia and of the NS mass are neglected over the time-scales of interest. The inner disc radius is a function of time via the mass accretion rate as $R_0(t) \propto \dot{M}^{-\alpha}$, where $\alpha \geq 0$. In fact, the disc is expected to recede when $\dot{M}$ drops because the disc pressure decreases. We have that in the Alfven case, $\alpha = 2/7$ (see Eq. [1.18]). Nevertheless, this proportionality index holds after a more accurate treating of the magnetic field-disc interaction also(see Eq. [1.22]).[4]. On the other hand, a measure of the

[4]The value $\alpha = 2/7$ is obtained under the assumption that the disc pressure is fixed by the gas pressure. In the case of a disc dominated by radiation pressure, $\alpha_{RPD} = 0.15$ (Ghosh, 1996).

instantaneous mass accretion rate is possible from the observed X-ray flux (see Eq. [1.5]):

$$\dot{M}(t) \propto F_X(t), \tag{2.20}$$

that is, the observed X-ray flux is assumed to be a good tracer of the mass accretion rate. As the light curve shape can be measured with high accuracy, it is therefore useful to factorize the evolution of $\dot{M}$ and R_0 in [2.19] in terms of the values assumed by these quantities at the start time of the outburst, T_0:

$$\dot{\nu}(t) = \frac{1}{2\pi I}\dot{M}(T_0)\sqrt{GMR_0(T_0)}f(t). \tag{2.21}$$

The function $f(t)$ expresses how the initial material torque, $\dot{M}(T_0)\sqrt{GMR_0(T_0)}$, changes in response to variations of the mass accretion rate (hence of the X-ray flux). It can be easily shown that:

$$f(t) = \frac{\dot{M}(t)}{\dot{M}(T_0)}\left[\frac{R_0(t)}{R_0(T_0)}\right]^{1/2} = \left[\frac{\dot{M}(t)}{\dot{M}(T_0)}\right]^{1-\alpha/2} = \left[\frac{F_X(t)}{F_X(T_0)}\right]^{1-\alpha/2}, \tag{2.22}$$

so that $f(t)$ is a function of the light curve shape only, given the assumption made. Inserting Eq. [2.21] in [2.18] finally yields:

$$R_{\phi\, rot}(t) = -\Delta\nu(t - T_0) - \dot{\nu}(T_0)\int_{T_0}^{t'}\int_{T_0}^{t''}\left[\frac{F_X(t'')}{F_X(T_0)}\right]^{1-\alpha/2} dt'', \tag{2.23}$$

where we have put $\dot{\nu}(T_0) = (1/2\pi I)\dot{M}(T_0)\sqrt{GMR_0(T_0)}$. The form of the integral in the rightmost term depends obviously on the particular shape of the light curve exhibited by the considered source. A successful modelling of the observed phase residuals thus allows a measurement of the spin frequency at T_0, as well as of the initial spin frequency derivative $\dot{\nu}(T_0)$, which in turn depends on the mass accretion rate and on the position of the inner disc radius, once a theory of angular momentum exchange is assumed.

2.2.5 The orbital motion

As an accretion powered pulsar belongs to a binary system, the time needed for the emitted X-ray photons to cover the distance to the observer varies cyclically as the NS performs its orbital motion around the centre of mass of the system. It is immediately clear that this Doppler effect concerns only the motion of the pulsar along the line of sight. We therefore define the line of nodes as the intersection between the orbit plane and the sky plane, where the latter is the plane perpendicular to the line of sight and containing the centre of mass of the system. The plane π, along which the orbital motion has to be projected, is therefore the one containing the line of sight and the line of nodes (see Fig. 2.2.5).

After Kepler laws, a binary orbit can be specified by seven parameters, five defining the shape and orientation of the orbit, and two times describing how the considered body performs the given orbit. We have therefore that:

- Two elements define the shape and size of the ellipsis: the semi-major axis, a_1, and the eccentricity, e, of the orbit. The semi-major axis is obviously defined with respect to the centre of mass of the system, so that $a_1 = [q/(1+q)]a$, where $q = M_2/M_1$, and a is the orbital separation (see Sec. 1.4.1).

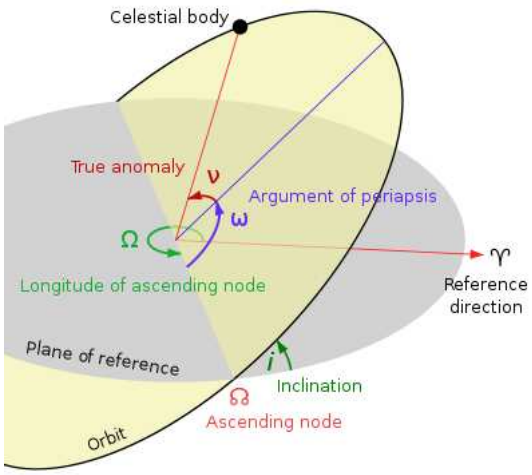

Figure 2.3: Orbital elements for a celestial body (the NS in this context) orbiting its centre of mass. The orbital plane is shadowed in yellow, while the plane of containing the line of sight, π, is grey. The line of nodes is the intersection of these two planes. In this context the reference direction points to the observer and $\Omega = \pi/2$. As the mean anomaly m does not represent a real angle, the true anomaly (the angle between the periapsis, the point of maximum approach to the centre of mass, and the position of the orbiting body) is instead plotted. Picture taken from http://en.wikipedia.org/wiki/Orbital_elements

- Two elements define the orientation of the orbital plane. The inclination, i, is the angle between the orbit plane and the plane π, while the longitude of the ascending node, Ω, orients the ascending node with respect to some reference direction. The ascending node is defined here as the point on the line of nodes where the object passes drifting away from the observer, while the chosen reference direction is the line of sight, so that $\Omega = \pi/2$ in our case.

- The periastron angle, ω, describes the orientation of the ellipse in the orbital plane. It is defined as the angle between the semi-minor axis of the orbit (where the body is closer to the centre of mass) and the line of nodes.

- T^* is the epoch at which the considered body passes through the ascending node of the orbit defined above ($\Omega = \pi/2$). The mean anomaly, $m = 2\pi(t - T^*)/P_{orb}$, defines instead the actual position of the body at time, t.

When such an orbit is projected onto the π plane, the distance of the body from the line of nodes, $Z(t)$, can be expressed with a first order approximation as:

$$Z(t) = a_1 \sin i \left[\sin(m + \omega) + \frac{e}{2}\sin(2m + \omega) - \frac{3}{2}e\sin\omega\right]. \qquad (2.24)$$

Here $Z(t)$ is measured from the line of nodes, and is positive when the pulsar is farther than the line of nodes with respect to the observer. The time lags

between emitted and observed photons can be therefore expressed by:

$$t_{arr} = t_{em} + \frac{Z(t_{em})}{c} + \frac{d}{c}, \tag{2.25}$$

where d is the distance to the system, and can be ignored in the following, itself being constant. The projected velocity of the pulsar is $\dot{Z}(t)$, and the resulting shift in frequency caused by the Doppler effect results:

$$\nu_{obs}(t) - \nu(t) = \nu(t)\frac{\dot{Z}(t)}{c} = x\frac{2\pi\nu(t)}{P_{orb}}[-\cos(m+\omega) - e\cos(2m+\omega)], \tag{2.26}$$

where we defined $x = a_1 \sin i/c$.

It is thus clear that, if not corrected, the orbital Doppler effect greatly limits the amount of time upon which we can integrate the light curves to obtain a folded pulse profile. Eq. [2.10] defines a threshold, such that, if the same light curve is folded over T_{obs} with periods differing by less than δP_{min}, the resulting profiles are identical among the statistic uncertainties. This criterion can be easily translated in terms of frequencies, $\delta\nu_{min} = 1/(nT_{obs})$. Moreover, it can be used to define the maximum observation time such that, even a variation $\delta\nu$ does not broadens the folded pulse profile. In a time interval Δt, the Doppler effect induces a frequency variation that can be evaluated as:

$$\delta\nu_{Dopp} \simeq \dot{\nu}_{Dopp}\Delta t \leq x\nu\left(\frac{2\pi}{P_{orb}}\right)^2. \tag{2.27}$$

In order to satisfy this criterion, one thus has to have, $\delta\nu_{Dopp} \leq \delta\nu_{min}$, that is:

$$\Delta t \leq \left(\frac{1}{nx\nu}\right)^{1/2}\frac{P_{orb}}{2\pi}. \tag{2.28}$$

Maximum time intervals of few hundreds of seconds are easily obtained for AMSP, thus yielding a consistent reduction of the integration time that can be used, with all the easily understood consequences on the statistics of the folded profiles.

To overcome this problem the strategy is to correct the observed photon arrival times with the relation [2.25]. The knowledge of the relevant orbital parameters is obviously required to produce a 'cleaned' light curve. To make the calculation easier, t_{em} is replaced by t_{obs} in the argument of the function $Z(t)$. The error made on Z due to this assumption is of the order of the space covered by the pulsar during the time needed for the light to travel through the entire width of the orbit. It is easy to show that this error is $\Delta Z/Z \simeq 2\pi a_1/(cP_{orb}) \simeq$ few $\times 10^{-5}$, for typical AMSP parameters. The arrival times can be thus corrected using:

$$t_{em} = t_{obs} - \frac{Z(t_{obs})}{c} \tag{2.29}$$

A first guess of the orbital parameters can be obtained by performing an epoch folding search on time intervals not longer than the threshold defined in Eq. [2.28]; the resulting plot of frequencies, ν vs. t, is then modelled by using the Doppler equation, Eq. [2.26], thus obtaining the a first estimate of

the set of parameters $(P_{orb}^{(0)}, x^{(0)}, T^{*\,(0)}, e^{(0)}, \omega^{(0)})$. Once corrected, the phases of the obtained profiles nevertheless may still show oscillation on the time-scale P_{orb}, due to the difference between the guessed and the *real* orbital parameters. To model these residuals, the frequency shift $\delta\nu_{Dopp}(t)$ has to be integrated in Eq. [2.15]. To make explicit the contribution of the uncertainty in any given parameter, we thus write:

$$\begin{aligned}\delta\nu_{Dopp}(t) = &\frac{2\pi}{P_{orb}}\nu\cos m\,\delta x + \\ &+ x\frac{2\pi}{P_{orb}^2}\nu(\cos m + m\sin m)\,\delta P_{orb} + \\ &- x\left(\frac{2\pi}{P_{orb}}\right)^2\nu\sin m\,\delta T^* + \\ &- x\nu\cos 2m\,\delta e\end{aligned} \tag{2.30}$$

Here we have put $\omega = 0$, as all the orbit of AMSP have negligible eccentricities (i.e. they are circular), so that it is impossible to define meaningfully such an angle. The quantities, δx, δP_{orb}, δT^* and δe are simply the differences between the guessed and *true* parameters. Performing the time integral and neglecting any constant term, we finally get the formula for orbital residuals:

$$R_{\phi\,orb}(t) = \nu x\left[sinm\frac{\delta x}{x} + \cos m\left(m\frac{\delta P_{orb}}{P_{orb}} + \frac{2\pi}{P_{orb}}\delta T^*\right) - \frac{\sin 2m}{2}\delta e\right] \tag{2.31}$$

Modelling the observed phase residuals with this relation allows the derivation of successive corrections to the orbital parameters, until the phases are no longer modulated on a time-scale P_{orb}.

2.2.6 The accuracy of the source position

As already stated in Sec. 2.2.3, phase residuals appear as a consequence of any effect that changes the signal spin frequency. As the orbital motion of the NS induces a Doppler effect, also the movements of the observing spacecraft in the Solar System have to be considered, as they change the times of arrival of the X-ray photons, with respect to the emission times, by a variable amount.

The observatory is put in orbit around the Earth, and both rotate around the centre of mass of the Solar System. Arrival times of X-ray photons have therefore to be related to some fixed reference, and this is naturally chosen as the Solar System centre of mass, itself considered inertial over the observing time with respect to the pulsar position. These corrections are performed by standard correction tools (e.g. faxbary included in the Heasoft 6.5.1 distribution, used for the analysis presented in this thesis), by using the most updated ephemerides available for the position of the satellite in the Solar System (J2000 in our case). The relation to link observed and barycentred photon arrival times, t_{obs} and t_{arr}, respectively, is:

$$t_{arr} = t_{obs} + \mathbf{r_E}\cdot\mathbf{n}/c, \tag{2.32}$$

(see e.g. Manchester and Peters, 1972), where $\mathbf{r_E}$ is the vector from the Solar System centre of mass to the observer, and $\mathbf{n}$ is the unit vector in the assumed

source direction. It is thus clear how, despite that $\mathbf{r_S}$ is known to an accuracy that can be considered indefinitely large for the purpose of timing analysis, the uncertainty on the source position introduces residuals in the phase evolution, $R_{\phi\, pos}$, even after a barycentric correction is performed. These residuals have a sinusoidal shape with a period equal to the Earth orbital period. In order to evaluate these effects, let us consider the expression of the phase delays induced by the Earth's motion for a small displacement, $\delta\lambda$ and $\delta\beta$, in the position of the source in ecliptic coordinates λ and β:

$$R_{\phi:pos} = \nu\frac{|r_E|}{c}[\sin(M_0+\epsilon)\cos\beta\delta\lambda - \cos(M_0+\epsilon)\sin\beta\delta\beta. \quad (2.33)$$

(see, e.g., Lyne and Graham-Smith 1990). Here $M_0 = 2\pi(T_0 - T_\gamma)/P_\oplus - \lambda$, T_γ is the time of passage of the Earth through the vernal point, and $\epsilon = 2\pi(t-T_0)/P_\oplus$.

In the case of pulsars active for periods $t \gtrsim P_\oplus$ (e.g. rotation-powered pulsars), the modelling of this effect with the above relation refines the position of the source with respect to the one determined from imaging observations. AMSP instead show pulsations for a couple of months at most, and one is left with the task of evaluating how largely the uncertainty in the position affects the precision of timing measurements. In fact, it is worth noting that, if considered on time-scales shorter than $P_\oplus$, the residuals expressed by Eq. [2.33] can be easily expanded in a series of linear and quadratic terms, and therefore directly manifest as a source of error on the estimates of frequency and of spin derivative, which indeed influence the observed phases with these trends.

After some algebraic manipulations, [2.33] can be written as

$$R_{\phi\, pos} = \nu|r_E|\sigma_\gamma \sin M_0 + \epsilon - \theta^* u/c, \quad (2.34)$$

where σ_γ is the positional error circle, $\theta^* = \arctan(\beta\delta\beta/\delta\lambda)$, and $u = [(\cos\beta\delta\lambda)^2 + (\sin\beta\delta\beta)^2)]^{1/2}/\sigma_\gamma$. Since the true position must lie within the error circle, the following inequalities hold: $(\cos\beta\delta\lambda/\sigma_\gamma)^2 \leq 1$, $(\delta\beta/\sigma_\gamma)^2 \leq 1$, and thus $u \leq (1+\sin^2\beta)^{1/2}$. This means that the uncertainty introduced by the source position is:

$$R_{\phi:pos} \leq \nu\frac{r_E}{c}\sigma_\gamma(1+\sin^2\beta)^{1/2}\sin(M_0+\epsilon-\theta^*). \quad (2.35)$$

(Burderi et al., 2007).

As $\epsilon << 1$ in AMSP orbits, we can expand this relation in series of the parameter ϵ, in order to find the systematic uncertainties induced on the linear and quadratic term. Note that, since the values of $\delta\lambda$ and $\delta\beta$ are the differences between the nominal and the *true* source position, their ratio is undetermined, and hence θ^* can have any value between 0 and 2π. The functions $\sin\theta^*$ and $\cos\theta^*$ can be therefore maximized with 1 when considered in the linear and quadratic terms of the series expansion. The resulting systematic error on the linear and the quadratic term of the phase residuals evolution , which correspond to the spin frequency and the average spin frequency derivative (see Eq. [2.18] and the following discussion), are therefore:

$$\sigma_{\nu,syst} \leq \nu\frac{r_E}{c}\sigma_\gamma(1+\sin^2\beta)^{1/2}\frac{2\pi}{P_\oplus}, \quad (2.36)$$

and

$$\sigma_{<\dot\nu>,syst} \leq \nu\frac{r_E}{c}\sigma_\gamma(1+\sin^2\beta)^{1/2}\left(\frac{2\pi}{P_\oplus}\right)^2. \quad (2.37)$$

It has to be noted that also the effects due to proper motion of the source with respect to the Solar System should be considered. AMSP generally belong to the Galactic plane, and the expected planar acceleration gives an apparent frequency derivative which is several order of magnitude lower than the one we observe in AMSP, $\dot{\nu}_{Gal}$ ∼few$\times 10^{-20}$ Hz/s (see, e.g., Damour and Taylor, 1991). This effect is therefore neglected in our analysis.

2.2.7 Timing of AMSP

According to standard timing techniques (see e.g. Blandford and Teukolsky, 1976), the predicted evolution of phase versus time is computed using a first guess of the parameters of the system, and the difference between the experimental and predicted phases, the residuals, are fitted with a multiple regression of the differential corrections to the parameters with the relations [2.16], [2.23], [2.31] and [2.33]. This technique has the obvious advantage of giving a self-consistent solution, where all the correlations in the covariance matrix of the system are fully taken into account. However, the convergence of the fit is not always guaranteed, and convergence to secondary minima might lead to inaccurate solutions. This is particularly true if the 'short' temporal lengths of AMSP outbursts are considered.

The approach we developed to perform an accurate timing analysis on AMSP is based on the remark that the time-scales over which the three effects discussed in the previous sections work are very different in these cases. All the sources considered in our work have in fact orbital periods of few hours at most, while the time-scale dictated by accretion torques to produce observable effects on the measured phases is at least a week. Orbital effects result therefore easily distinguishable from the spin evolution due to accretion, as well as from the effects induced by uncertainties on position, which introduce terms which have the same temporal fingerprint as a frequency derivative, as it was remarked in Sec. (2.2.6).

The procedure we apply goes therefore as follows (see e.g. Burderi et al., 2007; Papitto et al., 2007). The arrival times of all events, t_{arr}, are first reported to the Solar-System barycentre adopting the best estimate of the source position in the sky. If a previous estimate of the orbital parameters is available, we then use it to account for the effect produced by the orbital motion using Eq. [2.25]. If this is not the case, or the previously published orbital solution is too inaccurate to produce meaningful results, a preliminary estimate of the orbital parameters is found with the technique of epoch folding search on short time intervals, as described in Sec. 2.2.5. Once the photon arrival times are corrected for the binary motion, all the available light curves are folded around the best estimate of the spin frequency. The integration time of such foldings is still limited by the threshold defined by Eq. [2.28], as the preliminary orbital solution may be not accurate enough, so that broadening of the pulse profiles is still expected at this stage. The observed phase evolution of the folded profiles is then modelled through Eq. [2.16], where the rotational and orbital residuals are defined by Eq. [2.23] and [2.31], and the positional term is ignored. Differential corrections on the relevant parameters are therefore found, with particular attention to the spin frequency and the orbital elements.

The procedure based on the correction of arrival times for the binary motion and on the folding of the light curves is repeated with the new found

solution, until no orbital modulation is present in the phase evolution plot, and the phase residuals are rather normally distributed around the timing solution. The residual uncertainty on the orbital parameters defines an error on the phase determination, $\sigma_{\phi\, orb}$, that has to be summed in square to the statistical uncertainty affecting the phase residuals, $\sigma_{\phi\, stat}$, to give the overall error on the phase determination. The expression for $\sigma_{\phi\, orb}$ can be evaluated simply by differentiating Eq. [2.31], substituting the differentials of the orbital parameters with their errors, and summing in quadrature:

$$\begin{aligned}\sigma_{\phi_{orb}} &= \nu x \left\{ \sin^2 m \left(\frac{\sigma_x}{x}\right)^2 + \cos^2 m \left[m^2 \left(\frac{\sigma_{P_{orb}}}{P_{orb}}\right)^2 + \right.\right. \\ &+ \left.\left. \left(\frac{2\pi\sigma_{T^*}}{P_{orb}}\right)^2 \right] + \sin^2 m \cos^2 m \sigma_e^2 \right\}^{1/2} . \end{aligned} \tag{2.38}$$

As the effect of orbital motion is now considerably reduced, no broadening of the profiles reconstructed with the folding technique is expected. To improve the profile statistics, the entire observation length ($\sim$ 1 hr for RXTE data) is then used to fold the pulse profiles. The phase evolution plots obtained after the correction of orbital motion are therefore expected to contain only the effects of the NS rotational behaviour, and are then modelled with a relation like Eq. [2.23], to obtain the desired information on the spin frequency and on its derivative. It has to be borne in mind that these estimates are affected by systematic errors expressed by the relations [2.36], and [2.37], respectively, due to the uncertainty on the source position, which we recall, cannot be improved by a timing analysis on such short time intervals ($\lesssim$ 2 months).

3

The spin up of XTE J1751–305

I report in this chapter on a timing analysis of the accreting millisecond pulsar XTE J1751–305, observed during the 2002 April outburst by *RXTE*. After having corrected for Doppler effects on the pulse phases due to the orbital motion of the source, we performed a timing analysis on the phase delays, which gives, for the first time for this source, an estimate of the average spin frequency derivative, $\dot{\nu} = (3.7 \pm 1.0) \times 10^{-13}$ Hz s^{-1}. I thereby discuss the torque resulting from the spin-up of the neutron star deriving a dynamical estimate of the mass accretion rate, and comparing it with the one obtained from X-ray flux. Constraints on the distance to the source are discussed, leading to a lower limit of ~ 6.7 kpc. These results are published in Papitto et al. (2008)

3.1 Introduction

XTE J1751–305 was discovered on April 3, 2002 (Markwardt et al., 2002, M02 hereinafter) at a flux level of ~ 60 mCrab (2–10 keV), by the *RXTE* Proportional Counter Array (PCA) during a monitoring program of the Galactic bulge region (Swank and Markwardt, 2001). Subsequently, detections were made and the position was determined by the *BeppoSAX* Wide Field Camera and *XMM-Newton* (in 't Zand et al., 2002 and Ehle et al., 2002, respectively). All these measurements were consistent with a previously unknown source, situated 2°.1 away from the Galactic Centre.

Since the first *RXTE* pointings it became clear that the system harboured a pulsar spinning at 435 Hz. XTE J1751–305 thus became the second AMSP to be discovered, and *RXTE* kept monitoring this newly discovered transient from April 4.6 to 30.9 on a roughly daily basis. Using the data spanning the first week of *RXTE* observations, M02 could derive a connected timing solution that accounted for the orbital motion of the source (see Table 3.2).

In particular, the knowledge of the orbital period and of the projected semi-major axis, allows to constraint the companion mass, M_2, once a value for the NS mass is assumed. In fact, the mass function of a binary system is defined from the third Kepler law as:

$$f(M_1, M_2, i) = \frac{1}{G}(a_1 \sin i)^3 \left(\frac{2\pi}{P_{orb}}\right)^2 = \frac{(M_2 \sin i)^3}{(M_1 + M_2)^2} \qquad (3.1)$$

The sense of this definition relies on the fact that the mass function can be accurately measured once an orbital solution is found, and therefore it can be

used to get an estimate of the companion mass as a function of the mass of the compact object and of the unknown inclination angle. XTE J1751–305 is in a very tight orbital system ($P_{orb} \simeq 40$ min, $a_1 \sin i \simeq 10$ lt-ms $\simeq 0.005$ R$_\odot$), so that we obtain $f(M_1, M_2, i) \simeq 1.3 \times 10^{-6}$ M$_\odot$. The mass function provides the minimum possible companion mass, which would be the *real* one if the binary system were viewed edge on ($i = 90°$). For XTE J1751–305 we obtain $M_2^{min} = 0.0137 - 0.0174$ M$_\odot$ for a reasonable range of NS masses, $M_1 = 1.4 - 2.0$ M$_\odot$. A firm upper limit on M_2 cannot be derived using [3.1], as if the binary were viewed nearly edge on ($i \simeq 0°$) only a tiny fraction of the orbital motion would be projected onto the line of sight, resulting in almost no Doppler shifts. Nevertheless it can be noted that for an ensemble of binaries whose inclination is randomly distributed, the *a priori* probability of observing a system with inclination $\leq i_0$, is $(1 - \cos i_0)$ (see e.g. Chakrabarty and Morgan, 1998). If the source is drawn from such an ensemble, there is therefore a 95% probability that $i \geq 18°$, and the relative upper limit on M_2 at such confidence level is $M_2 \leq 0.04 - 0.06$ M$_\odot$, with M_1 in the same range as above. Such low values tend to exclude that the companion of XTE J1751–305 is an hydrogen burning star, rather indicating an H or He dwarf.

The X-ray light curve of 2002 outburst of XTE J1751–305, as observed by the PCA on board *RXTE*, is made of two exponential decays with different e-folding factors. The first one describes the first 8.5 d of observation and can be modelled with the function $L_X(t) = L_X(\bar{T}) exp[-(t-\bar{T})/\tau_d^{(1)}]$, where $L_X(\bar{T})$ is the luminosity at $\bar{T} = 52369.644$ MJD and $\tau_d^{(1)} = 7.2$ d (see Gierliński and Poutanen, 2005, GP hereinafter, for the $2 - 20$ keV light curve; see also M02). Subsequently the light curve experiences a sharp break and can be described with a similar decay function, this time with $\tau_d^{(2)} = 0.63$ d. The source then switches back to the quiescence emission levels, ~ 10 d after the first available observation.

The bolometric X-ray/γ-ray luminosity was estimated by GP to be $L_X(\bar{T}) = 2.7 \times 10^{37} d_{8.5}^2$ erg s^{-1}, where $d_{8.5}$ is the distance to the source in units of 8.5 kpc. This estimate is drawn from a physically plausible spectral model for the continuum formation, which is discussed in more details in Sec. 7.1.

After the 2002 event, this source was reported in an activity state during March 2005 and April 2007, but these outbursts have been very short ($\leq 2 - 3$ d), faint (fluencies of order of a tenth of that of 2002) and pulsation-less (Swank et al., 2005; Linares et al., 2007, and references therein). Despite having an effect on the long-term mass accretion rate estimate, these episodes of activity proved useless to refine the knowledge of the rotational and orbital behaviour of XTE J1751–305.

3.2 Observations and data analysis

The timing solution proposed by M02 gives an upper limit on the pulse frequency derivative of $|\dot{\nu}| < 3 \times 10^{-13}$ Hz/s. In the context of our scientific project we decided to reconsider the data observed by RXTE, applying our timing approach directly aimed to the timing studies of AMSP (see Sec. 2.2.7). The log of the considered observation is in Table 3.2. All of these data were collected by the PCA. Except for the observation of April 4, which was taken

in Good Xenon configuration with a 1 μs time resolution (2 s read out time and 256 energy channels), all the other PCA data we considered are Generic Event (E_125us_64M_0_1s) with a temporal resolution of $122\mu s$ and 64 energy channels. All the observations were public at the moment of this analysis, and were downloaded from the Heasarc Web Site (http://heasarc.gsfc.nasa.gov/).

Table 3.1: Log of the considered PCA observation of XTE J1751–305

OBSID	Obs.Date	Start Time	Exposure (s)
70134-03-01-00	2002-04-04	15:37:16.9	3521
70131-01-01-00	2002-04-05	15:23:59.4	13370
70134-03-02-00	2002-04-06	03:38:00.1	1493
70131-01-02-00	2002-04-06	12:46:12.6	13891
70131-01-03-01	2002-04-07	12:29:53.7	1508
70131-01-03-00	2002-04-07	14:08:21.7	10573
70131-01-04-00	2002-04-08	12:14:22.3	13875
70131-01-05-03	2002-04-09	01:12:16.4	1917
70131-01-05-02	2002-04-09	03:01:54.9	1627
70131-01-05-01	2002-04-09	04:39:18.1	1402
70131-01-05-04	2002-04-09	06:22:23.5	8169
70131-01-05-00	2002-04-09	12:00:54.4	24608
70131-01-06-00	2002-04-10	10:23:24.3	10027
70131-01-06-01	2002-04-10	14:56:54.2	10271
70131-01-07-00	2002-04-11	09:53:10.8	7054
70131-01-07-01	2002-04-11	13:06:54.1	13810
70131-01-08-00	2002-04-12	09:37:33.3	26454
70131-01-09-00	2002-04-13	07:47:33.2	27748
70131-01-10-00	2002-04-14	07:32:34.7	10270
70131-02-01-00	2002-04-14	12:26:07.3	20038
70131-02-02-00	2002-04-15	12:03:36.9	3582
70131-02-03-00	2002-04-15	13:44:44.7	16589
70131-02-04-00	2002-04-16	11:47:38.7	17802
70131-02-05-00	2002-04-17	13:13:24.7	14408
70131-02-06-00	2002-04-18	11:21:36.6	14925
70131-02-07-00	2002-04-19	14:14:42.7	10953
70131-02-08-00	2002-04-20	16:01:06.8	9879
70131-02-09-00	2002-04-21	15:31:07.1	10793

As it is extensively stated in Ch. 2, we first corrected X-ray photons arrival times to the Solar system barycentre considering the best position available for this source, which was obtained from a *Chandra* pointing (M02). In fact at the moment, *Chandra* provides the most accurate X-ray positions , with a 90% confidence error circle of $0''.6$; this accuracy is mandatory if an accurate determination of rotational parameters is desired (see Sec. 2.2.6 and below). We then focused on the orbital modulation of the phases to derive an accurate orbital solution. The evolution of the phases, measured by folding 90 s long intervals around the M02 estimate of the spin period, was modelled with Eq. [2.16], without considering the term owing to the position uncertainties. The chosen length of the intervals is such as not to broad the folded profiles because of a possible

Table 3.2: Orbital and timing parameters of XTE J1751–305

	M02	This work [a]
Orbital solution		
$a \sin i/c$ (lt-ms)	10.1134(83)	10.125(5)
P_{orb} (s)	2545.3414(38)	2545.342(2)
T^* (MJD)	52368.0128983(87) [b]	52368.0129023(4)
Eccentricity e	$< 1.7 \times 10^{-3}$	$< 1.3 \times 10^{-3}$
Timing Solution		
ν_0 (Hz)	435.317993681(12)	435.31799357(4)
$< \dot{\nu} >$ (Hz/s)	$< 3 \times 10^{-13}$ [c]	$(3.7 \pm 1.0) \times 10^{-13}$.
$\dot{\nu}(\bar{T})$ (Hz/s) $\alpha = 2/7$		$(5.6 \pm 1.2) \times 10^{-13}$

[a]Numbers in parentheses, referring to our values, are the 90% confidence level uncertainties in the last significant figure, while the ones referring to M02 are given at 3σ confidence level on the last significant digits. The same confidence levels are considered in giving upper limits on the eccentricity, e.

[b]The value reported here is revised with respect to the one originally quoted in M02 (Markwardt et al. 2007).

[c]This upper limit is to be considered on the absolute value of $< \dot{\nu} >$.

residual orbital modulation (see Eq. [2.28]). The orbital parameters we obtain, namely the projected semi-major axis measured in light ms, $a \sin i/c$, the orbital period, P_{orb}, the time of passage of the NS at the ascending node of the orbit , T^*, and the eccentricity, e, are listed in Table 3.2. Our orbital solution is in good agreement with the one derived by M02 within the quoted uncertainties.

The times of arrival of X-ray photons were then reported to the line of nodes of the binary system orbit, considering our orbital solution. As the time over which any uncertainty on the orbital parameters may possibly affect the phases of the X-ray pulsations (P_{orb}) is much smaller than the time required for the spin frequency derivative to produce a significant effect, the two effects on residuals can be decoupled. The effect in the pulse phases due to the remaining uncertainty on the orbital parameters, $\sigma_{\phi\, orb}$, is therefore treated as a normally distributed source of error (see Eq. [2.38] for an expression of $\sigma_{\phi\, orb}$). The final uncertainty σ_ϕ on the phase residuals we consider in the following is then the squared sum between $\sigma_{\phi\, orb}$ and the statistical error arising from sinusoidal fitting of the pulse profiles.

The light curves corrected for the orbital motion were then considered in their entire length (~ 1 hr), as no broadening of the pulse profile due to this effect is expected any more. We therefore folded all the available observations around our guess for the spin frequency ν_F (which initially was the M02 estimate). We could detect coherent pulsations until MJD 52377.6, 9 d after the first observation available, when the X-ray flux had become approximately one tenth of the peak flux.

The criterion we considered in order to assess the presence of a periodic signal is simply based on the expected statistic distribution followed by a folded light curve in which no signal is present (see Eq. [2.8]). The hypothesis underlying this criterion is that in the absence of any signal, the statistics S defined by Eq. [2.7], behaves as a chi-squared distribution with $(n-1)$ degrees of freedom, where n is the number of bins used to fold the profile. Such a behaviour is ensured if the number of counts in every bin in which the profile is sampled

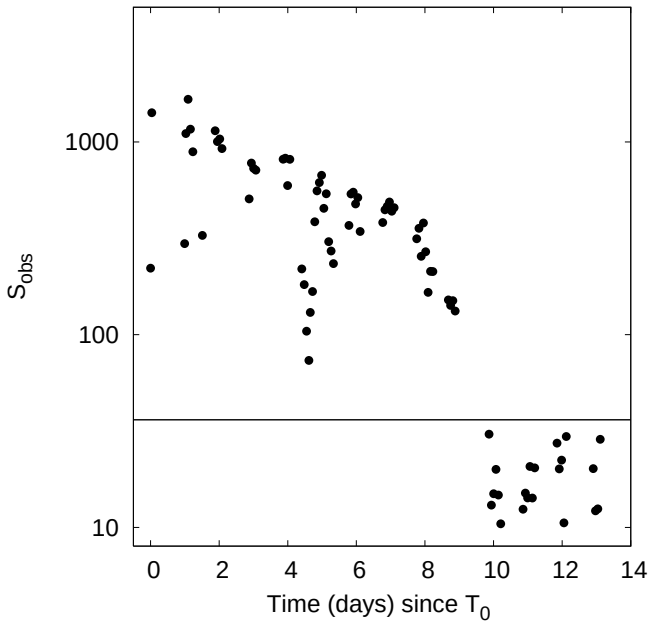

Figure 3.1: Plot of the observed statistics S_{obs} of every considered folded light curve. The horizontal line represents the 99% confidence limit for the detection of pulsations.

is so large that the central limit theorem applies, and a Poisson distribution is indistinguishable from a Gaussian one. In the case of XTE J1751–305 the average count rate is $R \simeq 400$ c/s, so that if we pick $n = 19$ and $\Delta t = 3600$ s, the average number of counts per bin is $RT/n \sim 80000$, thus fully satisfying the above criterion. We note that the same result is obtained if we consider shorter observations, such as the 90 s long we considered above to derive an orbital solution. The chosen level of confidence to firmly state a pulse detection is 99%, so that, according to Eq. [2.8], every folded profile with $S < 36.19$ is withdrawn from the considered sample. In Fig. 3.1 the values of S_{obs} for every folded profile are plotted, together with the threshold just defined. We may therefore conclude that pulsations are detected at a 99% confidence level until the source switches back to its quiescence level, that is, 9 d after the start time of our observations, T_0.

Folded light curves that met the detection criterion were then modelled with a sinusoid with the period fixed to the folding one. We also tried to add an harmonic to the fitting function, but such a component was significantly detected and led to a slightly better quality fit only in a small fraction of the observations ($\leq 10\%$), so that we consider only the phases obtained with a single harmonic sinusoidal function for the purposes of our timing analysis. An example of the pulse profile is shown in Fig. 3.2.

Therefore we modelled phase residuals with a parabolic function

$$\Delta\Phi(t) = 1/\nu_F \times (\delta + \beta t + \gamma t^2), \qquad (3.2)$$

where ν_F is the folding frequency, $\beta = -\Delta\nu_0$ is the correction to ν_F to obtain an estimate of the spin frequency at $t = T_0$, $\gamma = - < \dot{\nu} > /2$ is the term owing to a constant spin frequency derivative and δ is a phase constant (see

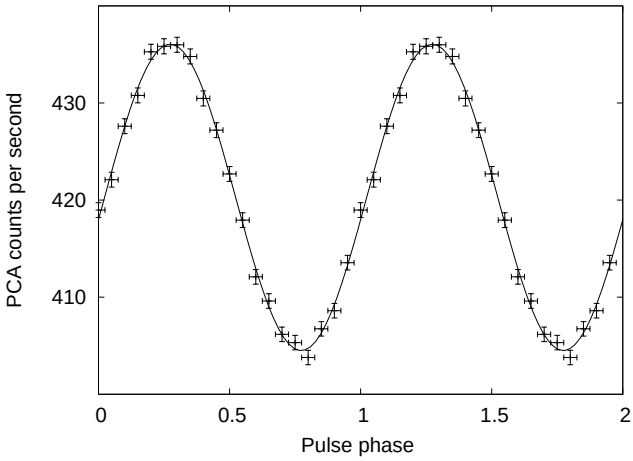

Figure 3.2: Pulse profile produced folding in 20 phase bins around $\nu_0 = 435.31799357$ Hz, all the available observations spanning the time interval from MJD 52370.537 to MJD 52370.776 (OBSID 70131-01-02-00). This time interval does not represents a continuous time series and the effective total integration time is $\simeq$ 14 ks. The solid line is the best fitting sinusoid. The reduced chi squared of this model is $\chi^2_r = 0.78$ and is not significantly improved by adding an harmonic. Two cycles are plotted for clarity.

Sec. 2.2.4). This procedure is repeated several times, correcting each time the frequency over which we fold the light curves, until the linear term of Eq. [3.2] is compatible with being null within the uncertainties. The timing parameters we finally obtain are $\nu_0 = 435.31799357(3)$ Hz and $< \dot{\nu} >= 3.7(8) \times 10^{-13}$ Hz/s, where the numbers in parentheses are the 90% confidence level uncertainties on the last significant figure, as for all the uncertainties quoted in the rest of the chapter.

In Fig. 3.3 we plot the phase residuals $\Delta\Phi(t)$, measured in microseconds, of light curves folded around ν_0, versus the time elapsed since the first observation considered. The plotted error bars refer to the overall 1σ uncertainties on phases, computed by considering both the statistical errors coming from the sinusoidal modelling and the errors induced by the uncertainties on the orbital parameters. The reduced chi squared of the quadratic best fitting model is 81/56, which compared to the one obtained with a linear fit (136/57), gives an F test probability of 8×10^{-8} that the improvement in the variance is purely given by chance.

As it will be shown in Ch. 4 and 5, other sources of this class show the presence of timing noise in the observed phases, probably due to changes in the position of the emitting hot spot on the NS surface, suggesting caution in considering the reliability of the uncertainties on the timing parameters obtained by a simple least square fit to the phase residuals, taken with their uncertainties σ_ϕ. Nevertheless the pulse phase evolution of XTE J1751–305 can be modelled satisfactorily by a general parabolic trend, even if the presence of small timing residuals leads to a reduced χ^2 slightly larger than one. Therefore, in order to get a conservative estimate of the uncertainties affecting the measured spin fre-

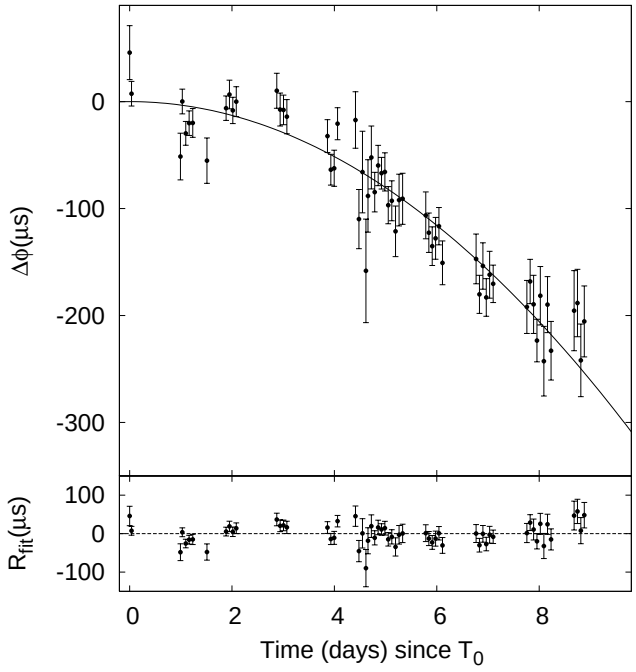

Figure 3.3: Evolution of the pulse phase delays, measured in microseconds, folding every available observation around $\nu_0 = 435.31799357$ Hz. The plotted error bars are the 1σ uncertainties on phases, including both the statistical errors from the pulse profile sinusoidal fitting and the errors induced by the residual uncertainties on orbital parameters. We note that these error bars have not been rescaled by the factor 1.2 that makes $\chi^2_{\rm r} = 1$ (see text for details). The solid line is the best fit constant $\dot{\nu}$ model (upper panel). Residuals with respect to the best-fitting model (lower panel).

quency and its derivative, we amplified all the errors on our phase measurements by a common factor (1.2) until we obtain $\chi^2_r = 1$ from a fit with Eq. [3.2]. We then consider as the most conservative the uncertainties σ_{ν_0} and $\sigma_{\dot{\nu}}$ so obtained. In this way we get to our final estimates of the timing parameters, which are the ones listed in Table 3.2. For sake of clarity we note, however, that the error bars plotted in Fig. 3.3 are not multiplied by any factor and they represent the genuine 1σ uncertainties on the measured phases.

A more physically motivated description of the evolution of phase delays is easily obtained if the dependency of $\dot{\nu}(t)$ on the accretion rate is considered. In Sec. 2.2.4 we derived an expression for the phase residuals produced by a material spin up torque applied at the inner disc radius, R_0. This contribution depends on the initial spin frequency derivative, $\dot{\nu}(T_0) \propto \dot{M}(T_0)\sqrt{R_0(T_0)}$, on the shape of the light curve (Eq. [2.23]), and on the chosen index for the dependency $R_0 \propto \dot{M}^{-\alpha}$. In the case of XTE J1751–305 the light curve has an exponential shape, so that the integral on the r.h.s. of Eq. [2.23] can be performed analytically. We first consider an X-ray light curve whose shape is made by a single exponential decay, that is $F_X(t)/F_X(\bar{T}) = \exp -(t-\bar{T})/\tau_d$. Calling $\tau_\alpha = \tau_d(1-\alpha/2)^{-1}$, and recalling that under the assumption made,

$\dot{\nu}(t) \propto \dot{M}^{1-\alpha/2} \propto F_X^{1-\alpha/2}$, the torque contribution to phase residuals can be written as:

$$\delta\phi_{\dot{\nu}} = -\dot{\nu}(T_0) \int_{T_0}^{t'} \int_{T_0}^{t''} \left[\frac{F_X(t'')}{F_X(T_0)}\right]^{1-\alpha/2} dt'' = \\ = -k\tau_\alpha \dot{\nu}(\bar{T})(t - T_0) - \tau_\alpha^2 \dot{\nu}(\bar{T}) \exp\left[-\frac{(t-\bar{T})}{\tau_\alpha}\right], \quad (3.3)$$

where we ignored constant terms, and introduced an offset between T_0 and $\bar{T}$, $k = \exp -(T_0 - \bar{T})/\tau_\alpha$. Such a term arises as we want to use the GP estimate of flux, $F_X(\bar{T})$, to compare the dynamical estimate of mass accretion rate $\dot{M}_{dyn}(\bar{T})$ needed to explain the observed $\dot{\nu}$, with the photometric estimate derived from the flux, $\dot{M}_{phot}(\bar{T}) = RF_X(\bar{T})4\pi d^2/GM_1$. The spin up model with which we can fit the observed phase delays is then:

$$\Delta\Phi(t) = \frac{1}{\nu_F}\left\{A - [B + k\tau_\alpha C]\,(t - T_0) - C\tau_\alpha^2 \exp\left[-\frac{t-\bar{T}}{\tau_\alpha}\right]\right\}. \quad (3.4)$$

The parameters A, B and C are those determined through a fit, and represent, a phase constant, the correction to the folded spin frequency, $B = \Delta\nu_0 = \nu_F - \nu(T_0)$, and the spin frequency derivative at $t = \bar{T}$, $C = \dot{\nu}(\bar{T}) = (2\pi I)^{-1}[GMR_{in}(\bar{T})]^{1/2}\dot{M}(\bar{T})$, respectively.

We first considered Eq. [3.4] with $\tau_d = 7.2$ d, and fitted the observed phase delays with various values of α, corresponding to different models of disc-magnetosphere interaction. In particular, the case $\alpha = 0$ corresponds to no dependence of R_{in} on the instantaneous accretion rate and in this case we consider $R_{in} = R_C$ where R_C is the corotation radius defined in Eq. [1.19]. On the other hand, $\alpha = 2/7$ is the Alfvenic value obtained both in the approximation of spherical accretion of matter, and according to GL models (Sec. 1.5.1). Unfortunately we succeeded in having no significant improvement in the description of the phase residuals by implementing such torque models, as for example we obtain $\chi^2_r = 79/56$ when $\alpha = 2/7$ is considered.

We also tried other α plausible values, based on a more realistic treatment of the disc structure at the inner rim, which includes different possible regimes, as gas pressure dominated or radiation pressure dominated SS optically thick disc (respectively $\alpha = 0.25$ and 0.15 for models 1G and 1R in Ghosh, 1996 and Psaltis and Chakrabarty, 1999). We did not consider any other model that would lead to significantly higher values of α (e.g. two temperature optically thin gas pressure dominated discs), as the maximum value that this parameter can attain is the one that implies a full excursion of R_{in} during the outburst, from the NS radius to the corotation radius, while the source keeps showing pulsations. Since in the case of XTE J1751–305 a coherent signal can be detected as long as the X-ray flux, which is related to the instantaneous mass accretion rate, has declined to one tenth of its maximum value, the constraint $R_{in}(t_{cut})/R_{in}(T_0) = (F_x(t_{cut})/F_X(T_0))^{-\alpha} < R_C/R_\star$, where $t_{cut} = T_0 + 9$ d is the time at which the pulsations are cut off, leads to $\alpha < 0.4$ for a 1.4 $M_\odot$ NS with a $R_\star = 11.1$ km radius. The available statistics nevertheless revealed itself to be too low to discriminate between these models. This is witnessed by the fact that the goodness of the fit and also the value of the spin frequency derivative remain almost the same when different plausible values of α are chosen. In order to give

a reference value of $\dot{\nu}(\bar{T})$, the spin frequency derivative at $t = \bar{T}$, we consider the Alfvenic/GL case, $\alpha = 2/7$, for which $\dot{\nu}(\bar{T}) = (5.6 \pm 1.0) \times 10^{-13}$ Hz/s. In the same way we operated before, we amplified the actual errors on phases by a common factor until we have $\chi^2_r = 1$ for the best fitting $\alpha = 2/7$ model, thus obtaining the 90% confidence level uncertainty on $\dot{\nu}(\bar{T})$ listed in Table 3.2.

We note that an attempt was also made to model the behaviour of the phase delays in terms of the broken decay effectively observed in the X-ray light curve, rather than considering a single decay taking place throughout the outburst. We thus implemented in Eq. [3.4] the change of the e-folding factor that takes place simultaneously to the break. This attempt anyway led neither to improvements in the quality of the fit nor to variations in the measured parameters for every value of α considered. This is probably due to the shortness of the time interval in which the light curve is described by $\tau_d^{(2)}$ before the pulsations fade away.

We conclude this section by noting that a systematic term due to the uncertainty in the source position has to be considered in order to have a reliable estimate of the uncertainty in the spin frequency as well as in the spin frequency derivative (Sec. 2.2.6). The best position available has a 90% error circle of 0".6 (M02); following the expressions [2.36] and [2.37] we estimate the upper limit on the effects of this uncertainty on the value of ν_0 as $\sigma_{syst\,\nu_0} < 1 \times 10^{-7}$ Hz, while on $\dot{\nu}(\bar{T})$ as $\sigma_{syst\,\dot{\nu}} < 0.3 \times 10^{-13}$ Hz/s. We highlight that the systematic error on $\dot{\nu}$ is one order of magnitude smaller than the spin frequency derivative we measure, and smaller than the error on $< \dot{\nu} >$ quoted above.

3.3 Discussion

In the previous section we described the application of different accretion models, referring to different assumption on the disc-magnetosphere interaction and on the particular structure of the inner region of the accretion disc, to the observed evolution of the pulse phases of XTE J1751–305. Such an interpretation implies the assumption that the curvature observed in the phase delays versus time is indeed a measure of the spin frequency derivative.

The stability of the pulse phase evolution of this source resembles the one shown by IGR J00291+5934 (Burderi et al., 2007, Ch. 5) and XTE J0929–314 (Galloway et al., 2002, Ch. 5) with a smooth variation along the course of the outburst, witnessed by the small post fit residuals obtained even when a simple constant $\dot{\nu}$ model is used. This behaviour is different from the one analysed in an other subset of sources of this class, namely XTE J1814–338 (Papitto et al., 2007, Ch. 4) and XTE J1807–294 (Riggio et al., 2008, Ch. 5), where the phases oscillate around the mean trend clearly anti correlating with rapid ($\sim$ 1 d) X-ray flux variations, and SAX J1808.4–3658 (Burderi et al., 2006, Ch. 5), which shows an even more complex behaviour. A deeper discussion of the puzzling behaviour shown by these sources can be found in Sec. 6. We just note here that XTE J1751–305 joins IGR J00291+5934 and XTE J0929–314 not only in the phase stability, but also as it has almost no harmonic content in the pulse profile, and its light curve is a smooth exponential decay.

These preliminary considerations give us even more confidence in the interpretation of the parabolic trend followed by the phases in terms of a spin frequency evolution, due to the accretion torques acting on the NS when it is efficiently accreting mass. However the attempts made proved unsuccess-

ful in discriminating a constant spin up model from a model in which the spin frequency derivative depends on the instantaneous value of the mass accretion rate, as traced by the observed X-ray flux. In the hypothesis that $\dot{\nu}(t) \propto \dot{M}(t)^{1-\alpha/2} \propto F_X(t)^{1-\alpha/2}$, which we stress is not favoured nor disfavoured by the data, the measurement of the spin frequency derivative of XTE J1751–305 at $t = \bar{T}$, $\dot{\nu}(\bar{T})$, allows a dynamical estimate of the mass accretion rate. This can be further compared with the estimate of the flux observed jointly by *XMM* and *RXTE*, in order to constrain the distance to the source. The evaluation of the torque (Eq. [1.25]) at the time $t = \bar{T}$, together with the estimate of $\dot{\nu}(\bar{T})$ given in the previous section, leads to an expression that relates the mass accretion rate at that time to the lever arm of the spin up torque at the same time, i.e. the inner disc radius:

$$\dot{M}_0 = (30 \pm 6) \times 10^{-10} I_{45} m^{-2/3} \xi^{-1/2} \, M_\odot/yr, \tag{3.5}$$

where I_{45} is the moment of inertia of the compact object in units of 10^{45} g cm^2, m is the mass of the NS in solar units, and $\xi = R_0/R_C$ is a parametrisation of the inner disc radius at $\bar{T}$ in terms of the corotation radius R_C. For XTE J1751–305 we have $R_C = (GM_1/\Omega_S^2)^{1/3} = 26.1 m^{1/3}$ km, where M_1 is the mass and Ω_S is the angular rotational velocity of the neutron star. The use of such a parameter is particularly suited for an accreting pulsar, as it has to be $R_\star/R_C < \xi(t) < 1$ in order for pulsations to be visible at a certain time t (see Sec. 1.5.1). Expressing these boundaries in terms of m and R_6, the radius $R_\star$ of the NS in units of 10^6 cm, one obtains for XTE J1751–305, $0.38 R_6 m^{-1/3} < \xi < 1$, which allows the definition of a range of possible accretion rates at $t = \bar{T}$, by their substitution in Eq. [3.5]:

$$(30 \pm 6) I_{45} m^{-2/3} < \dot{M}_{10}(T_0) < (48 \pm 9) I_{45} R_6^{-1/2} m^{-1/2} \tag{3.6}$$

where $\dot{M}_{10}$ is the mass accretion rate in units of 10^{-10} $M_\odot$/yr.

This estimate of the mass accretion rate can be expressed in terms of X-ray luminosity via the usual relation $L_X = \epsilon G M \dot{M}/R_{NS}$, where $\epsilon \simeq 1$ is the rate of conversion of gravitational energy released in accretion to observable X-ray luminosity. This allows to compare the dynamical estimate of the accretion luminosity we derived from timing analysis with the one obtained by a spectral modelling of the observed X-ray flux, which is obviously dependent on the source distance. Considering the expression given by GP for the bolometric luminosity, $L_X(\bar{T})$, one obtains for the distance d of XTE J1751–305:

$$d = 8.2 \, I_{45}^{1/2} m^{1/6} R_6^{-1/2} \epsilon^{1/2} \xi^{-1/4} kpc \tag{3.7}$$

Considering a moderately stiff EoS for an $m = 1.4$ NS, such as the FPS, one has for a compact object spinning at the rate measured for XTE J1751–305 $I_{45} = 1.24$ and $R_6 = 1.11$ (see e.g. Cook et al., 1994). It is then possible to find a range for the distance d of XTE J1751–305, $9.1 kpc \lesssim d \, \epsilon^{-1/2} \lesssim 11.6 kpc$.

XTE J1751–305 is located only 2° away from the Galactic Centre, so that a distance larger than 8.5 kpc would be highly improbable, if the source shows significant emission at energies of the order of ~ 1 keV (GP estimated $N_H \sim 10^{22}$ cm^{-2}). However, the discrepancy between our lower limit on the distance, 9.1 kpc, and the one implied by this constraint is not large, especially considering the relatively large uncertainties underlying the simple arguments which led to

our distance determination, and the assumptions made on the torque model and on the NS structure. Moreover we recall that, because of the uncertainty in the source position, the estimate of $\dot{\nu}(\bar{T})$ we used to get a dynamical estimate of the mass accretion rate is affected by a systematic error, which can in principle decrease our estimate of the distance below 8.5 kpc. M02 estimated a lower limit on the distance of 7 kpc based on indirect arguments, and our comparison between the observed $\dot{\nu}$ and the measured X-ray flux strongly supports the hypothesis that the source is close to the Galactic Centre.

Nevertheless, we can argue that the limits on the distance we find above may be overestimated due to several reasons, among which, a non isotropic emission from the source or an eclipse of part of the accretion luminosity. In particular, as already noticed by GP, the fact that the pulse shape shown by XTE J1751–305 is almost sinusoidal finds the most probable interpretation in terms of only one spot visible from our line of sight. We can therefore argue that mass is accreting on both the polar caps of the compact object, with a fraction of the emitted accretion luminosity being blocked by an opaque absorber (probably the accretion disc, as the absence of a significant Compton reflection component strongly suggests $i > 60°$, see GP), and re-emitted outside the considered $0.7 - 200$ keV energy band. It could be therefore the case that the value given by GP for the X-ray flux represents an underestimate of the real emission owing to the accretion of matter. This in turn would decrease our distance estimates to values in a better agreement with the constraint of the source not being farther than the Galactic Centre. Defining η as the ratio between the effective accretion luminosity and the one observed, we find lower distance estimates that would place the source not farther than the Galactic Centre for $\eta = 1.2$, and a lower limit of 6.7 kpc corresponding to $\eta = 2$, the maximum value η may reasonably attain.

It has to be highlighted that all these estimates of the source distance are derived by assuming that no negative torque is acting on the NS, due e.g. to threading of the disc by the magnetic field lines in regions where matter in the disc rotates slower than the threading field lines, as it is assumed to explain the rotational behaviour of other source of this class (see e.g. Ch. 4). If this would not have been the case, higher estimates of the mass accretion rate would be obtained, as the observed spin frequency derivative would represent the balance between a negative torque and the positive one due to accretion at R_0. This would straightforwardly lead to higher estimates of the distance.

4

The spin down of XTE J1814–338

Here, a precise timing analysis of the accreting millisecond pulsar XTE J1814–338 during its 2003 outburst, observed by RXTE, is presented. A full orbital solution is given for the first time; Doppler effects induced by the motion of the source in the binary system were corrected, leading to a refined estimate of the orbital period, $P_{orb} = 15388.7229(2)$ s, and of the projected semi major axis, a $\sin i/\mathrm{c} = 0.390633(9)$ light-second. We could then investigate the spin behaviour of the accreting compact object during the outburst. We report here a refined value of the spin frequency [$\nu = 314.35610879(1)$ Hz] and the first estimate of the spin frequency derivative of this source while accreting [$\dot{\nu} = (-6.7 \pm 0.7) \times 10^{14}$ Hz s^{-1}]. This spin-down behaviour arises when both the fundamental frequency and the second harmonic are taken into consideration. We discuss this in the context of the interaction between the disc and the quickly rotating magnetosphere, at accretion rates sufficiently low to allow a threading of the accretion disc in regions where the Keplerian velocity is slower than the magnetosphere velocity. We also present indications of a jitter of the pulse phases around the mean trend, which we argue results from movements of the accreting hotspots in response to variations of the accretion rate. The results of this chapter are included in Papitto et al. (2007).

4.1 Introduction

The X-ray transient XTE J1814–338 was the fifth AMSP discovered in 2003 during scans of the central Galactic plane with RXTE (Markwardt and Swank, 2003, hereafter MS03). This accreting pulsar has a 314 Hz spin frequency and resides in a binary system of orbital period $P_{orb} = 4.275$ hr. Following the same reasoning of Sec. 3.1, and in particular by applying the relation [3.1], it is possible to derive a minimum companion mass of $\simeq 0.15\ M_{\odot}$. This value is the largest among those seven AMSP that show coherent pulsations every time they are observed in outburst.

The 2003 outburst is the only exhibited so far by XTE J1814–338, making its recurrence time $\gtrsim 7$ yr, one of the longest among known AMSP. Considering also that the lone outburst observed is not among the brightest, the deduced long term mass accretion rate is very low, $\sim 5 \times 10^{-12}$ M$_{\odot}$/yr, provided that the system is not considerably farther than considered ($d \simeq 8$ kpc, Strohmayer et al., 2003).

XTE J1814–338 was found in outburst on June 5, 2003 (MJD 52795); the

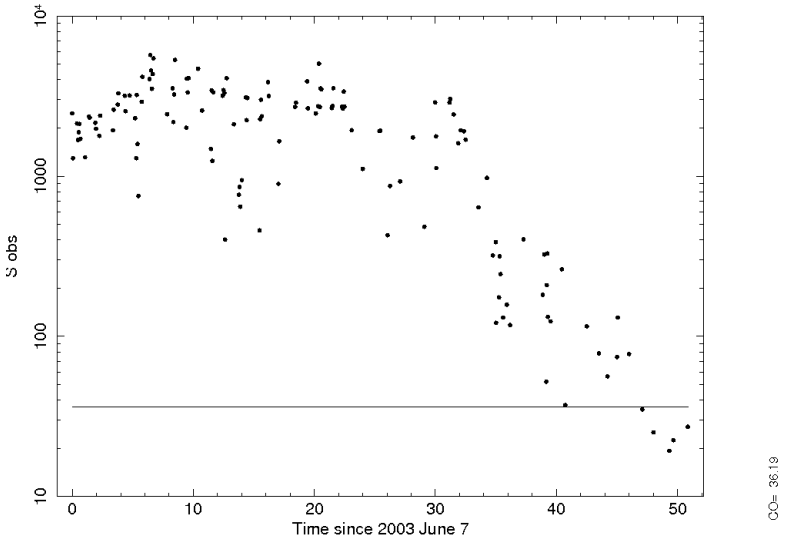

Figure 4.1: Plot of the observed statistics S_{obs} of every considered folded light curve. The horizontal line represents the 99% confidence limit for the detection of pulsations.

outburst lasted for 53 days, and had a peak (2.5–25 keV) flux of 5×10^{10} erg/cm^2/s. After a smooth rise lasting for $\sim$ 5 days, the X-ray flux showed three bumps with variations of $\sim$ 20 per cent on a time-scale of $\sim$ 10 days, until it suffered an abrupt cut off to one fourth of the previous average emission, 33 days from the first detection. Afterwards the source fell below the sensitivity threshold on 2003 July 27 (see upper panel of Fig. 4.6 for the *RXTE/PCA* 2.5–25 keV light curve).

At the moment of undertaking the project of this thesis, only a preliminary timing solution derived from the first five days of observations was available (Markwardt et al., 2003, see left column of Tab.4.4). This was taken as the starting point of our timing approach to obtain a phase connected solution spanning the entire data set available.

4.2 Observations and data analysis

For the timing analysis we consider data from the RXTE Proportional Counter Array, which observed XTE J1814–338 almost on a daily basis until the end of the 60 d long outburst. We use all the energy bandpass (2–60 keV) of Event mode data (64 energy channels and a 125 μs time resolution). The log of observations used is in Tab.4.2.

During the coverage of this outburst performed by *RXTE*, 28 thermonuclear bursts were observed, exhibiting coherent pulsations at the same period and strongly phase locked to the persistent pulsations (Strohmayer et al., 2003). Frequency variability during the course of the burst has been object of deep study, showing no relevant signs of departure from the non burst behaviour, similarly to the few Hz frequency drifts seen in other bursters as SAX J1808.4-3658 (Watts et al., 2005, 2008). As our analysis deals with the timing of coherent

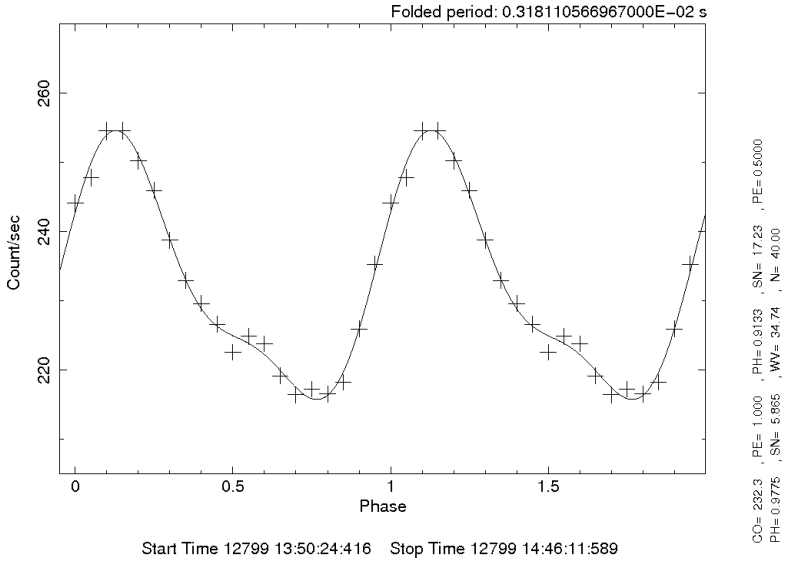

Figure 4.2: Pulse profile produced by folding 3.2 ks of data (OBSID 80418-01-01-02) in 20 phase bins around $\nu_0 = 314.3561088003$ Hz . The solid line is the best fitting model composed by two harmonic components. The reduced chi squared of this model is $\chi^2_r = 0.99$ and is not significantly improved by the addition of a third harmonic. Two cycles are plotted for clarity.

pulsations, we decided to discard an interval of 200 s following the onset of each burst. We have checked anyway that the inclusion of the bursts does not modify significantly the results of the timing.

First of all we corrected the photon arrival times for the motion of the spacecraft with respect to the solar system barycentre, using JPL DE-405 ephemerides along with spacecraft ephemerides. This task was performed with the *faxbary* tool, considering as the best estimate for the source coordinates the optical counterpart position, that has a 90 per cent confidence radius of $0''.2$ (Krauss et al., 2005).

Folding light curves around the frequency 314.3561088003 Hz, we detected coherent oscillations up to MJD 52844, 47 days after the first publicly available observation; the statistics used in the assessment of detections is the one defined in Eq. [2.7], and already used in Ch.3 for the case of XTE J1751–305. The observed values are plotted in Fig. 4.1.

An harmonic fixed at half of the spin period is clearly needed to guarantee a good fit of the pulse profiles, as it can be seen from the folded profile plotted in Fig. 4.2. The ratios between the fractional amplitudes, A, of these two harmonic components and the respective uncertainties σ_A, are instead plotted in Fig. 4.3 in order to show a measure of the significance of each component. We note that while the fundamental frequency component is clearly above the 2σ limit until MJD 52844, the second harmonic fractional amplitude falls below this threshold $\sim$ 35 days after the beginning of the considered observations, limiting the available number of points to perform the timing analysis upon this component.

Table 4.1: Log of the considered PCA observation of XTE J1814–338

OBSID	Obs.Date	Start Time	Exposure (s)
80138-04-03-00	2003-06-07	06:19:39.4	6991
80138-04-04-00	2003-06-07	15:54:06.9	10776
80145-02-01-00	2003-06-07	20:48:07.2	6415
80145-02-01-01	2003-06-07	23:47:34.4	22366
80418-01-01-00	2003-06-08	15:33:07.2	7538
80418-01-01-01	2003-06-09	04:05:51.9	7757
80418-01-01-02	2003-06-09	12:04:07.1	6401
80418-01-01-03	2003-06-10	00:38:02.7	15593
80418-01-01-04	2003-06-10	14:55:07.1	7469
80418-01-01-05	2003-06-11	00:24:07.2	7657
80418-01-01-06	2003-06-11	14:35:31.2	7378
80418-01-01-07	2003-06-12	00:01:33.3	3832
80418-01-01-08	2003-06-12	11:05:39.3	2623
80418-01-01-09	2003-06-12	13:14:39.8	9099
80418-01-02-01	2003-06-13	00:00:06.9	6619
80418-01-02-00	2003-06-13	15:32:06.7	14825
80418-01-02-03	2003-06-13	21:48:35.1	7489
80418-01-02-02	2003-06-15	02:20:32.6	3113
80418-01-02-06	2003-06-15	13:20:17.7	13766
80418-01-02-07	2003-06-16	16:36:07.2	12900
80418-01-02-09	2003-06-17	15:50:44.7	3572
80418-01-02-08	2003-06-17	23:40:47.4	3440
80418-01-02-04	2003-06-18	17:32:07.3	12621
80418-01-02-05	2003-06-19	16:45:04.6	11149
80418-01-03-12	2003-06-20	00:34:48.3	3537
80418-01-03-13	2003-06-20	14:48:12.4	3480
80418-01-03-00	2003-06-20	16:57:06.9	18228
80418-01-03-01	2003-06-21	01:51:56.7	965
80418-01-03-03	2003-06-21	03:26:20.3	978
80418-01-03-04	2003-06-21	05:00:21.3	1157
80418-01-03-05	2003-06-21	06:35:21.1	1275
80418-01-03-02	2003-06-21	14:23:38.4	10239
80418-01-03-06	2003-06-22	17:52:07.4	12108
80418-01-03-07	2003-06-23	10:39:16.4	5306
80418-01-03-08	2003-06-24	07:06:29.1	1620

Table 4.2: Log of the considered PCA observation of XTE J1814–338 (continuation)

OBSID	Obs.Date	Start Time	Exposure (s)
80418-01-03-09	2003-06-24	08:41:29.8	1979
80418-01-03-10	2003-06-25	16:10:44.8	6748
80418-01-03-11	2003-06-26	15:59:59.4	6179
80418-01-04-07	2003-06-27	09:15:42.6	2194
80418-01-04-00	2003-06-27	14:05:58.3	17224
80418-01-04-01	2003-06-28	16:55:14.6	10349
80418-01-04-02	2003-06-29	13:22:27.3	5701
80418-01-04-08	2003-06-29	16:35:25.7	6546
80418-01-04-03	2003-06-30	08:18:36.9	1964
80418-01-04-04	2003-07-01	06:21:00.6	1558
80418-01-04-05	2003-07-02	15:35:15.1	6868
80418-01-04-09	2003-07-03	07:30:23.3	731
80418-01-04-06	2003-07-03	12:34:03.4	1734
80418-01-05-00	2003-07-04	08:29:15.4	2186
80418-01-05-01	2003-07-05	09:51:58.2	3061
80418-01-05-02	2003-07-06	08:38:10.2	697
80418-01-05-03	2003-07-07	05:54:24.8	1629
80418-01-05-04	2003-07-07	07:37:04.2	2810
80418-01-05-05	2003-07-08	10:23:07	6982
80418-01-05-08	2003-07-08	18:35:27.2	1857
80418-01-05-09	2003-07-09	03:41:29.2	1141
80418-01-05-06	2003-07-09	08:31:03.4	3052
80418-01-05-10	2003-07-09	14:51:30.2	2874
80418-01-05-11	2003-07-09	18:19:30.7	1734
80418-01-05-07	2003-07-10	19:36:04.6	1656
80418-01-06-00	2003-07-11	12:42:10.7	2735
80418-01-06-08	2003-07-12	00:03:24.8	1087
80418-01-06-01	2003-07-12	06:12:06.6	2304
80418-01-06-09	2003-07-12	12:41:11	6935
80418-01-06-11	2003-07-13	03:49:18.3	1522
80418-01-06-02	2003-07-13	05:25:53.2	3492
80418-01-06-03	2003-07-14	13:10:21.5	2892
80418-01-06-06	2003-07-16	03:26:57.4	1504
80418-01-06-05	2003-07-16	06:17:10.8	2738
80418-01-06-10	2003-07-16	11:17:11.3	4837

Table 4.3: Log of the considered PCA observation of XTE J1814–338 (continuation)

OBSID	Obs.Date	Start Time	Exposure (s)
80418-01-06-07	2003-07-17	17:04:17.2	2182
80418-01-07-00	2003-07-18	04:27:07.2	1893
80418-01-07-01	2003-07-19	11:54:10.9	1717
80418-01-07-02	2003-07-20	11:50:19.4	741
80418-01-07-03	2003-07-21	05:15:11.2	577
80418-01-07-05	2003-07-22	00:06:07.2	1009
80418-01-07-06	2003-07-22	00:57:03.2	3352
80418-01-07-07	2003-07-22	23:22:11.1	2378
80418-01-07-08	2003-07-24	01:38:58.3	4504
80418-01-07-10	2003-07-24	23:51:53.6	1263
80418-01-08-01	2003-07-25	22:49.53.6	2217
80418-01-08-00	2003-07-26	07:44:11 2	438
80418-01-08-02	2003-07-26	15:27:17.3	3180
80418-01-08-03	2003-07-27	19:57:21.6	2830
80418-01-08-04	2003-07-29	00:08:57.4	2704
80418-01-08-05	2003-07-29	11:39:10.7	2138
80418-01-08-06	2003-07-31	16:59:33.8	887
80418-01-09-00	2003-08-01	22:01:19.8	1460
80418-01-09-02	2003-08-04	11:36:30.8	837

According to the guidelines stated in Sec. 2.2.7, we then divided each observation in 150 s time intervals (in order to avoid a broadening of the folded pulse profiles by the orbital motion) and folded the lightcurves according to our best estimate of the frequency. The phases of the profiles thus obtained were then fitted according to the expression [2.16], without considering the position term R_{ϕ}^{pos} (see below), finally obtaining the orbital solution listed in Table 4.4. The remaining average uncertainty due to the orbital motion is $< \sigma_{\phi\, orb} >= 0.016$ ms in this case, fairly matching the condition $\sigma_{\phi_{orb}} << \delta\phi_{\nu}(t)$, and we can therefore consider it as a "timing noise". The solution we obtain is more precise than the one already present in literature (Markwardt et al., 2003, see Table 4.4) since in our analysis the entire 47 days interval was taken into consideration, and the accuracy in estimating the orbital parameters increases with the length of the time interval spanned by the data.

Having corrected all the arrival times with our best orbital solution, we could then fold each observation around our best estimate of the barycentric spin frequency, sampling every pulse profile in 20 phase bins and finally fitting them with a two harmonics sinusoidal form. The temporal evolution of the phase delays, measured in their natural units (time in units of the folded spin period) of these two components is showed in Fig. 4.4 and Fig. 4.5, exhibiting a clear and coherent spin down trend, superimposed on which a sort of modulation is visible. A fit of the fundamental frequency phase delays evolution with a constant frequency derivative model yields an estimate of $< \dot{\nu}_{fund} >= (-6.7 \pm 0.7) \times 10^{-14}$ Hz/s, whose uncertainty is quoted at the 90 per cent confidence level (see below for details about its derivation). The quality of the fit is greatly affected by the mentioned modulation, whose amplitude can be estimated in

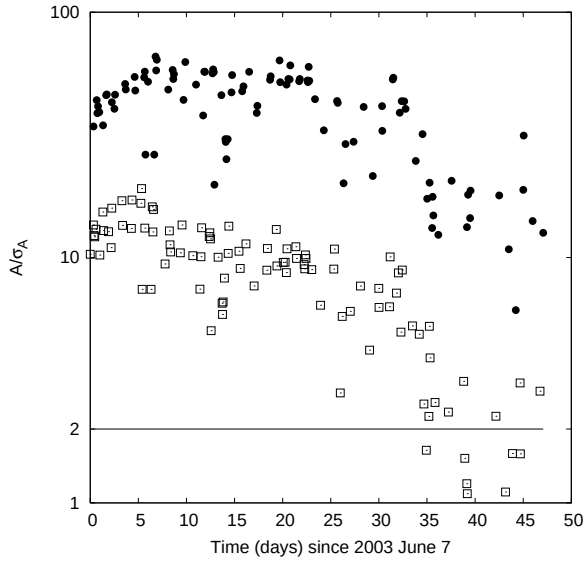

Figure 4.3: Ratios between the fractional amplitudes of the two considered harmonic components (filled circles refer to the fundamental frequency and squares to the second harmonic) and the relative uncertainty σ_A, plotted against the time since the first observation considered. The solid line represents the 2σ confidence level.

Table 4.4: Orbital and spin parameters of XTE J1814–338

	MS03	This work [a]
$a \sin i/c$ (lt-ms)	390.3(3)	390.633(9)
P_{orb} (s)	15388.6(3)	15388.7229(2)
T^* (MJD)		52797.8101689(9)
Eccentricity e		$< 2.4 \times 10^{-5}$ [b]
	First Harmonic	
ν_0 (Hz)	314.35610(2)	314.35610879(1) [c]
$< \dot{\nu} >$ (Hz/s)		$(-6.7 \pm 0.7) \times 10^{-14}$ [d]
	Second Harmonic	
ν_0 (Hz)		314.35610881(1) [c]
$< \dot{\nu} >$ (Hz/s)		$(-8.5 \pm 0.9) \times 10^{-14}$ [d]

[a] Numbers in parentheses are the uncertainties in the last significant figure at the 90 per cent confidence level.

[b] 3σ upper limit

[c] These frequencies refer to the beginning of the observations taken into account, MJD 52797.27387859868. The systematic error driven by position uncertainty is $\sigma_{syst\ \Delta\nu} \leq 3 \times 10^{-8} Hz$ and was not included in the quoted errors.

[d] The systematic error driven by position uncertainty is $\sigma_{syst\ \dot{\nu}} \leq 6 \times 10^{-15} Hz/s$ and was not included in the quoted errors.

$\sim 5 < \sigma >_{fund} \simeq 0.1$ ms, leading to a very poor quality reduced chi squared ($= 1618/97$). A similar fit performed on the second harmonic phases delays, this time on a reduced number of points, as some detections result uncertain 35 days after the first observation considered here, gives slightly better results

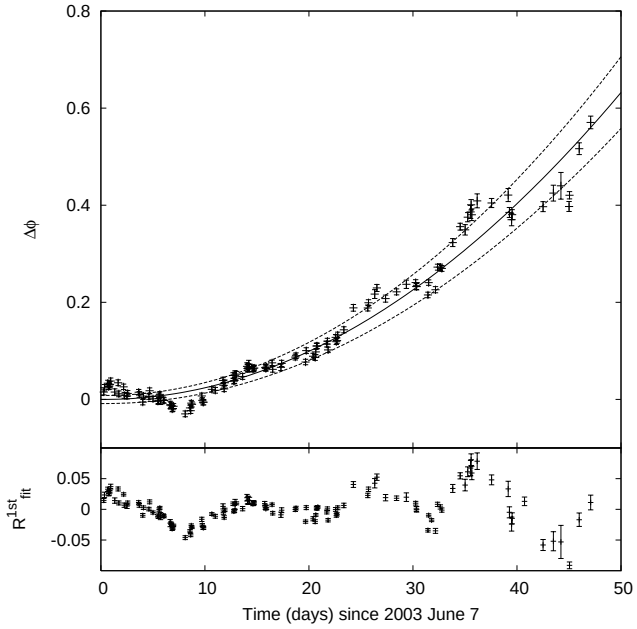

Figure 4.4: Evolution of the pulse phase delays, measured in their natural units, computed upon the fundamental frequency component, folding every available observation around $\nu_0 = 314.35610879$ Hz. The solid line is the best fit constant $\dot{\nu}$ model, while the dashed lines represent the contours of the 90 per cent confidence region (upper panel). Residuals with respect to the best-fitting model (lower panel).

($\chi^2 = 493/88$), as the uncertainties of the measured second harmonic phases are on the average larger than the ones of the fundamental, while the amplitude of the modulation is just slightly smaller. The resulting estimate of the constant frequency derivative in this case is $< \dot{\nu}_{harm} >= (-8.5 \pm 0.9) \times 10^{-14}$ Hz/s. The difference between the obtained values of $\dot{\nu}$ can be attributed to the different baseline on which the two timing analyses were performed, as the second harmonic phases are less sampled in the final part of the outburst. As a matter of fact the restriction to the first 35 days of the outburst (an interval along which the two data sets exactly overlap), yields to values of $\dot{\nu}$ that are comparable ($\dot{\nu}^{0-35}_{fund} = (-8.9 \pm 0.5) \times 10^{-14}$ Hz/s and $\dot{\nu}^{0-35}_{harm} = (-8.6 \pm 0.4) \times 10^{-14}$ Hz/s, respectively).

Beyond affecting the quality parameter of the least-square fit of the phase delays evolution, the presence of a modulation superimposed on a global spin down trend, suggests extreme caution in determining the uncertainties that affect the determination of the neutron star spin parameters, which are, the frequency at the beginning of the observation, and its mean derivative (σ_{ν_0} and $\sigma_{<\dot{\nu}>}$ respectively). Rather than considering the values obtained by a simple least-square fit of the evolution of the phase delays taken with their actual uncertainties ($\sigma_\phi = (\sigma^2_{\phi\ stat} + \sigma^2_{\phi\ orb})^{1/2}$), we amplified all the errors affecting the various points by a common factor (3.5 in the case of the first harmonic) until we obtain $\chi^2_r = 1$ from the fit, and then recomputed σ_{ν_0} and $\sigma_{<\dot{\nu}>}$ accordingly. As the relative weights of the single points remain unchanged applying this

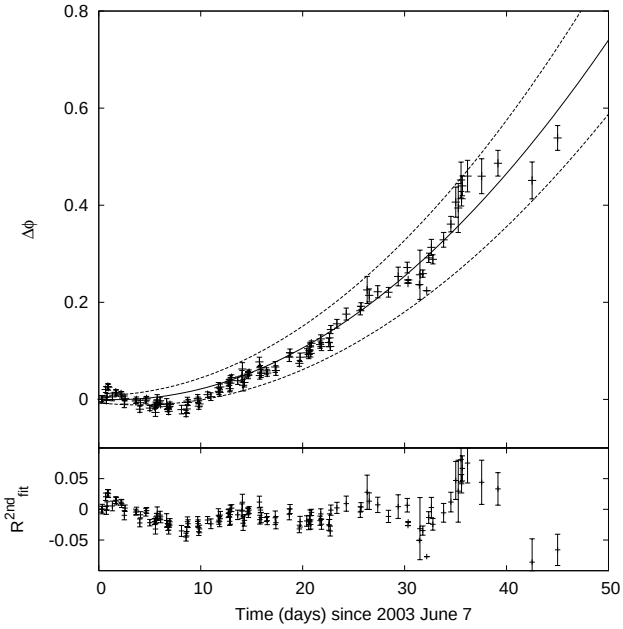

Figure 4.5: Evolution of the pulse phase delays, measured in their natural units, computed upon the second harmonic component, folding every available observation around $\nu_0 = 314.35610879$ Hz. The solid line is the best fit constant $\dot{\nu}$ model, while the dashed lines represent the contours of the 90 per cent confidence region (upper panel). Residuals with respect to the best-fitting model (lower panel).

procedure, the only result is the amplification of the quoted uncertainties on the considered parameters. We believe this is appropriate in response to the presence of residuals that we do not take into account in the rotational model, but that are not normally distributed around the timing solution nor seem to be explainable in terms of a wrong determination of the phases uncertainties (see next section). In this way we obtain values approximately 3 times larger for $\sigma_{<\dot{\nu}>}$, which are the ones we quote throughout this paper. In Fig. 4.4 and Fig. 4.5 the contours of the 90 per cent confidence region are plotted with dashed lines, showing the accuracy with which the global behaviour is reproduced with these assumptions. Furthermore, considering the 90 per cent confidence radius of the position error circle (0".2), the apparent motion of the source affects the determination of $\dot{\nu}$ with a systematic error $\sigma_{syst\,\dot{\nu}} \leq 0.6 \times 10^{-14}$ Hz/s.

4.3 Discussion

The first aspect we have to discuss is the nature of the phase jiggle that affects crucially the quality of the fit performed on the phase delays evolution plots, when either the fundamental frequency or the second harmonic is taken into consideration. This effect appears as a modulation around the mean rotational behaviour, as can be easily seen from the bottom panels of Fig. 4.4 and Fig. 4.5, which reproduce the residuals in their natural units from the best-fitting con-

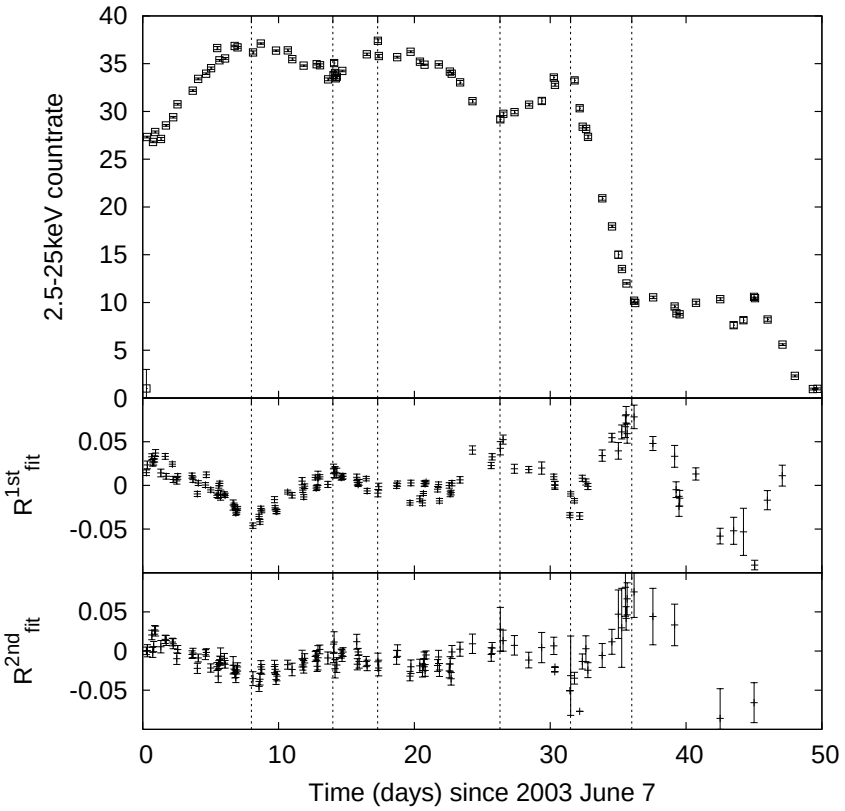

Figure 4.6: (2.5–25keV) light curve of the 2003 outburst of J1814, as taken by the PCA's Unit 2 aboard RXTE, which was the only one to be on during the entire outburst. Each point represents the average count rate in every available observation, which were preliminarily background subtracted according to the faint source model (top panel). In the lower panels we plot the residuals with respect to the best-fitting constant spin down model of phase delays of the fundamental (R^{1st}_{fit}, middle panel) and of the second harmonic (R^{2nd}_{fit}, bottom panel). These plots are the same as lower panels of Fig. 4.4 and Fig. 4.5 respectively, and are plotted here, together with dotted vertical lines, to highlight the correlation between the shape of the light curve and the shape of the residuals of the fundamental and the second harmonic phase delays, respectively.

stant spin down model, R_{fit}, in the respective cases. The time-scale of this modulation is $\sim$ 12 days both for the fundamental and the harmonic, ruling out the possibility that this effect could be yielded by timing errors referred to a wrong position or orbital solution, as these would make the phases oscillate with very different time-scales ($P_\oplus$ and P_{orb}, respectively). Nor this modulation can be explained in terms of accretion torques, as such rapid phase variations on short time-scales would imply spin frequency derivatives of few$\times 10^{-12}$ Hz/s, more than an order of magnitude larger than the one conceivable given the measured mass accretion rate.

A striking anti-correlation can be found indeed with the shape of the X-ray light curve of the observed X-ray flux (see Fig. 4.6). As a matter of fact

when the flux increases, the residuals R_{fit} of both the fundamental and the second harmonic decrease, as the source would be spinning up, and the opposite happens when the flux decreases, as it can be seen by following dashed vertical lines in Fig. 4.6. A linear correlation test performed on the couples of points representing the $2.5 - 25$ keV count rate and R^{1st}_{fit} gives a Pearson coefficient $R = -0.80$, which corresponds for $N = 113$ points to a probability of less than 0.01 per cent for the points to be uncorrelated. We also performed a rank correlation test in order to estimate the probability of a monotonic relationship between the two observables; the Spearman coefficient we obtain is $\rho = -0.78$ with a similarly low probability of the null hypothesis. We have also checked that the maximum of the cross-correlation function between these two time series occurs in correspondence of non shift of the two series.

An attempt was made to model this behaviour as due to alternating spin up/spin down states of the NS, directly related to the varying accretion rate. However, a coherent timing solution could only be found by allowing the NS to undergo a rather crowded and unlikely series of discontinuities in the spin frequency. This is because the instantaneous value of the spin frequency with respect to the folding one, is represented by the slope of the phase time-evolution curve ($\nu(\bar{t}) = d\phi/dt|_{\bar{t}}$), so that a vertex in the $\Delta\phi$ vs t plot implies a change in the spin frequency, taking place on a time shorter than the sampling one (see for example the behaviour of the residuals R^{1st}_{fit} around the day 8 in the middle panel of Fig. 4.6).

An alternative explanation can be proposed in terms of the motion of accretion footprints along the NS surface in response to variations of the accretion rate. This interpretation is the easier and would imply movements of the centre of the accretion spot with an amplitude of $\sim 15°$, around an equilibrium position. A deeper discussion of phase movements in AMSP is deferred to Ch.6, nevertheless we note here that such movements were observed during 3D MHD simulations of disc accretion onto a magnetized NS (Romanova et al., 2004c), and can be interpreted in terms of the different winding of the magnetic field lines that carry accreted mass from the disc to the NS poles.

Besides the appearance of this effect of phase jiggle, the general trend followed by XTE J1814–338 is a coherent spin-down taking place over the whole course of the outburst. We consider the value of the spin frequency derivative computed from the timing on the fundamental frequency, $< \dot{\nu} >= (-6.7 \pm 0.7) \times 10^{-14}$ Hz/s, as the most reliable because it was obtained on the most statistically significant data set.

A spin down of an accreting pulsar is most commonly interpreted in terms of the interaction of the field lines closing beyond the inner disc radius, in regions where the magnetosphere rotate faster than particles in their Keplerian orbit (see Sec.1.5.1). As it was there discussed, this effect is particularly pronounced for fast spinning NS that accrete at low rates. In this case, in fact, the magnetosphere can be free to expand near the corotation radius ($R_d \simeq R_C$) and the disc fraction which is subject to a significant threading raises. Romanova et al. (2002) also showed that even if the mass accretion rate is not able to halt the magnetic field expansion beyond the corotation radius ($R_d \gtrsim R_C$), mass is effectively accreted by the NS thanks to the angular momentum received by the NS, which indeed itself spins down as a result. In Sec.1.5.1 we also recalled an useful formula to account for the torque acting on the NS when the disc terminates at the corotation radius, Eq. [1.27]. We add this term to the usual

material spin up torque, Eq. [1.25], to obtain:

$$2\pi I\dot{\nu} = \dot{M}(GMR_C)^{1/2} - \gamma\frac{\mu^2}{9R_C^3}. \quad (4.1)$$

Following (Rappaport et al., 2004) a term $\gamma \simeq 1$ is introduced to parametrize our uncertainty on the exact mechanism that drives the reconnection of the field lines through the disc.

We therefore use the above expression to evaluate the spin down behaviour of XTE J1814–338. The bolometric flux was estimated by Galloway et al. (2004), who give a peak accretion rate of $6 \times 10^{-10}\ M_\odot/yr$, where the ~ 8 kpc distance estimate is considered (Strohmayer et al., 2003). During the first 35 days of the outburst the flux remained loosely constant, so that at the level of approximation at which Eq. [1.25] was derived, we could consider its average value on this interval ($5.4 \times 10^{-10}\ M_\odot/yr$), and use it together with Eq. [1.27] to estimate the magnetic dipole moment needed to produce such a large spin down. Considering that the corotation radius is $R_C = 36.3$ km for a $1.4M_\odot$ NS in XTE J1814–338, the observed spin down rate leads to a magnetic dipole estimate of:

$$\gamma^{1/2}\mu \simeq 8 \times 10^{26} G\, cm^3. \quad (4.2)$$

This corresponds to a superficial magnetic field of $B_S \simeq 8 \times 10^8 \gamma^{-1/2}\ G$ for a NS of 10 km of radius. This estimate is exactly in the plausible range ($10^8 - 10^9$ G) for the AMSP to be the progenitors of radio millisecond pulsars, but suggests that the distribution of AMSP magnetic fields covers at least this decade of magnetic fields, as other sources were proved to have a field of few$\times 10^8$ G.

5

Rotational properties of AMSP

In this chapter, the rotational behaviour of the other sources considered in our sample is presented. SAX J1808.4–3658, IGR J00291+5934 and XTE J1807–294 joins XTE J1751–305 in showing a clear spin up (see Burderi et al., 2006, 2007; Riggio et al., 2008, respectively). Nevertheless in the last two cases phase shifts similar to those observed in XTE J1814–338 are observed. A detailed discussion of this effect is given in the next chapter. In the case of XTE J0929–314 a spin down is instead measured, indicating a magnetic field of the same order of the one derived in Ch. 4 for the other spinning down source, XTE J1814–338. We therefore attempt to draw some considerations based on the observations performed, bearing in mind that any conclusion cannot have a strict statistical meaning given the low number of outburst displayed by the AMSP, which on the other hand are intrinsically rare objects among LMXB. The measured spin frequency derivatives indicate that AMSP have magnetic fields in the range 10^8–10^9 G, and their spin behaviour nicely correlates with their spin. This is expected according to the theory of equilibrium spin periods, that indeed predicts faster sources to have smaller magnetic fields, and therefore faster spin-ups.

Moreover, being the fastest AMSP known, IGR J00291+5934 is the most promising AMSP to eventually observe the gravitational radiation braking argued by Bildsten (1998) to explain the lack of NS spinning at their break-up frequency.. Unfortunately a mismatch between the dynamical and photometric accretion rate estimates hampers any firm estimate of the mass quadrupole moment implied by this model, which is indeed indicated to be $\lesssim 2 \times 10^{37}$ g cm^2.

5.1 IGR J00291+5934

IGR J00291+5934 was discovered in December 2004 by the ESA Gamma ray observatory *Integral* (Eckert et al., 2004). Subsequent follow-up observations by *RXTE* found coherent pulsations in the X-ray light curve at 598.88 Hz, making this source the fastest accretion powered pulsar discovered so far (Galloway et al., 2005a). After reaching the peak of the 2.5–25 keV light curve on December 4, the source flux decayed linearly on a time-scale of $\simeq 8.5$ d. Subsequently the decay became faster, and the source switched back into quiescence approximately 10 d after the beginning of the outburst, on 2004 December 14. *RXTE* PCA observed the source on a roughly daily basis, and the dataset of publicly

Table 5.1: Orbital and spin parameters of IGR J00291+5934

	G05	F05	This work [a]
$a \sin i/c$ (lt-ms)	64.993(2)	...	...
P_{orb} (s)	8844.092(6)		
T^* (MJD)	53345.1619258(4)		
Eccentricity e	$< 2 \times 10^{-4}$ (3 σ)		
ν_0 (Hz)	598.89213064(1)	598.89213060(1)	598.89213053(2)
$< \dot{\nu} >$ (Hz/s)	$< 0.8 \times 10^{-13}$ (3 σ)	$8.4(6) \times 10^{-13}$	$0.85(0.11) \times 10^{-12}$
$\dot{\nu}$ (Hz/s) ($\alpha = 0$)			$1.17(0.16) \times 10^{-12}$
$\dot{\nu}$ (Hz/s) ($\alpha = 2/7$)			$1.11(0.16) \times 10^{-12}$

[a]Errors in parentheses are given at 1 σ confidence level. The errors quoted for the spin frequency and the spin frequency derivatives do not include systematic errors induced by the source position uncertainty.

available observations covering Dec 7 - Dec 14 was used to derive a timing solution. The light curve shape covering this interval was modelled on the basis of the 3.0–150.0 keV flux measurements described below, obtaining:

$$F_{(3-150)}(t) = F_{3-150}(T_0) \left[1 - \frac{t - T_0}{t_B}\right], \quad (5.1)$$

where T_0 = MJD 53346.18 is the start time of our observations, and $t_B = 8.4 \pm 0.1$ d.

IGR J00291+5934 was observed not only during the outburst in 2004 . Following the discovery of a pulsar in this system, a re-analysis of the ASM light curves revealed that probably the source was active during 1998 November and 2001 September, also. Another episode of activity was detected during 2008 August, this time with a full *RXTE* coverage, but these observations were not yet analysed as they are still under proprietary period, and the outburst was indeed very short ($\simeq$ 3 d, Chakrabarty et al., 2008). Assuming these four outburst, a tentative recurrence time is derived as $\sim$ 2.75 yr, the second shortest among all the AMSP.

We applied to the 2004 data taken by *RXTE* the techniques described in Sec. 2.2.3. For the position of the source we considered that of proposed radio counterpart, which we note is compatible with the proposed optical counterpart (Rupen et al., 2004, and references therein). Using the longer baseline considered, we tried to obtain a more accurate orbital solution than the one given by (Galloway et al., 2005b, G05), which was deducted from a 3 d time interval. No such improvement was achieved, and the solution of G05 is therefore used in our analysis (see Table 5.1), considering the uncertainties on the orbital parameters there stated as a contribution to the overall error on phases, according to Eq. [2.38]. The pulse profile could be modeled with just a sinusoid at the frequency ν_0, and the resulting pulse phases are plotted in Fig. 5.1. IGR J00291+5934 rotational behaviour is very similar to the one showed by XTE J1751–305 (see Ch.3): the pulse profile is described by a single harmonic component, and the pulse phase evolves smoothly indicating a clear spin-up. As it was already noted in the case of XTE J1814–338, these characteristics are not ubiquitous among AMSP, and more examples will be given in the following. The average spin frequency derivative is in extremely good accord with the estimate

given by Falanga et al. (2005) (F05, see Table 5.1). In order to derive a more physically plausible estimate of the spin-up behaviour of IGR J00291+5934, we link the observed $\dot{\nu}$ to the mass effectively accreted by the NS, under the hypothesis that $\dot{M}$ is well tracked by the X-ray flux. We therefore use the relation [2.23], with the light curve shape given in [5.1], obtaining:

$$\delta\phi_{\dot{\nu}} = -\dot{\nu}(T_0)\int_{T_0}^{t'}\int_{T_0}^{t''}\left[\frac{F_X(t'')}{F_X(T_0)}\right]^{1-\alpha/2} dt'' = \simeq -\frac{1}{2}\dot{\nu}(T_0)(t-T_0)^2\left[1-\frac{(2-\alpha)(t-T_0)}{6t_B}\right]. \quad (5.2)$$

Here α is still the index of the relation between the mass accretion rate and the inner disc radius, $R_0 \propto \dot{M}^{-\alpha}$. The term on the right hand side was obtained with a series expansion of the integral, and the term neglected in square brackets is of order of $\xi < \alpha(1-\alpha/2)/24\epsilon^2$, with $\epsilon << 1$. Adding the usual correction term for the spin frequency, $\Delta\nu(t-T_0)$, the above equation is used to fit the phase evolution observed in IGR J00291+5934 (see Fig. 5.1), obtaining the results listed in Table 5.1 for different values of α. Here we recall that $\alpha = 2$ corresponds to the case of a constant $\dot{\nu}$, $\alpha = 0$ to an inner disc radius independent from $\dot{M}$, and $\alpha = 2/7$ to the usual derivation of R_0 from physical assumptions on the exchange of angular momentum between the disc and the magnetosphere (see Sec. 1.5.1 and Eq. [1.22]). A comparison of the χ^2/dof shows that the statistics is not good enough to distinguish between these three possibilities.

Finally, to evaluate the systematic errors on the spin frequency and on its derivative, we adopted the positional uncertainty of $0.06''$ radius reported by Rupen et al. (2004), and using Eq. [2.36] and [2.37] we find $\sigma_{\nu,syst} \sim 2.2\times10^{-8}$ Hz and $\sigma_{\dot{\nu},syst} \sim 4.4\times10^{-15}$ Hz/s, respectively. Note that the systematic error on the spin frequency is comparable with the error derived from the fit of the phase delays and reported in Table 5.1. Moreover, the systematic error on the spin frequency derivative is at least 1 order of magnitude below the error derived from the fit.

Recalling that in Eq. [5.2], $\dot{\nu}(T_0) = (1/2\pi I)\dot{M}(T_0)\sqrt{GMR_0(T_0)}$, we can compute the mass accretion rate through the formula:

$$\dot{M}_{-10} = 5.9\dot{\nu}_{-13}I_{45}m^{-2/3}[R_c/R_0(T_0)]^{1/2}, \quad (5.3)$$

where $\dot{M}_{-10}$ is $\dot{M}(T_0)$ in units of 10^{-10} $M_\odot$/yr, $\dot{\nu}_{-13}$ is $\dot{\nu}(T_0)$ in units of 10^{-13} Hz/s, I_{45} is the moment of inertia of the NS in units of 10^{45} g cm^2, and m is the NS mass in solar units. In the following we adopt the FPS equation of state for the NS matter for $m = 1.4$ and the spin frequency of IGR J00291+5934, which gives $I_{45} = 1.29$ and $R = 1.14\times10^6$ cm (see e.g. Cook et al., 1994). This gives a lower limit in the mass accretion rate of $\dot{M}_{-10} \sim 70 \pm 10$ (case $\alpha = 0$). In the same way we did for XTE J1751–305 (see Sec. 3.3) to compare the experimental estimate of $\dot{M}(T_0)$ with the observed X-ray luminosity, we have to derive the bolometric luminosity $L(t)$ from the observed flux $F_{(3-150)}(t)$. To this end we consider the combined spectra acquired by the PCA (2–60 keV) and by HEXTE ($\sim$ 20–200 keV).

The value of the hydrogen column N_H is poorly constrained in *RXTE* energy band, so we fix $N_H = 2.80\times10^{21}$ cm^{-2}, which is the value obtained by

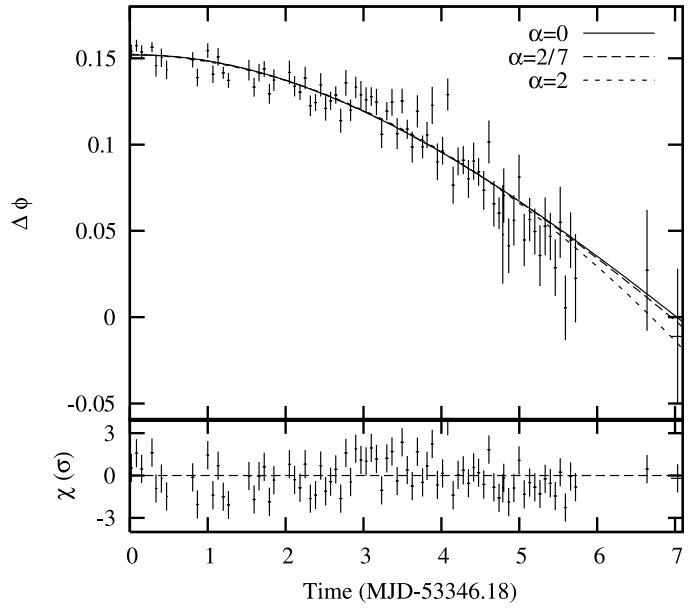

Figure 5.1: Pulse phases computed by folding at the spin period reported in Table 5.1 and plotted vs. time together with the best fit curves (top) and residuals in units of σ with respect to the model with $\alpha = 2/7$ (bottom).

Nowak et al. (2004) analysing Chandra data. The power law is the dominant spectral component as it happens for all the AMSP spectra (see Ch. 7). In particular, we find a quite flat power law index $\alpha = -0.59^{+0.047}_{-0.034}$, and an e-folding energy $E_{fold} \sim 178^{+83}_{-47}$ keV. The ratio of the unabsorbed fluxed in the bands 0.001–1000 keV and 3-150 keV is 1.6, which we assume valid to extrapolate the bolometric flux from our spectral fitting. The luminosity emitted by the power law component is $L_{PL} \simeq F_{PL(0,\infty)} 4\pi d^2 = 0.75^{+0.20}_{-0.15} \times 10^{37}$ d_5^2 erg/s, where d_5 is the distance to the source in units of 5 kpc. A quick comparison with the implied mass accretion rate for a $m = 1.4$ NS following the FPS EoS, $\dot{M}_{-10} = 7.3^{+1.9}_{-1.5}$ d_5^2, reveals that even if we neglected the disc contribution so far, the mass accretion rate implied by the observed power law luminosity is much lower than the one derived from the spin-up, for any reasonable distance to the source. The power law has the most probable origin in the accretion columns above each polar cap, and, as we observe a single-peaked pulse profile, we are probably seeing the emission from just one of those regions. In this case we can therefore take into account the possibility that we are underestimating the total flux in the power law component because one of the two polar caps is never visible. We incorporate this source of uncertainty in a parameter η, which is $\eta = 2$ if we observe exactly half of the emission owing to the hotspots on the NS surface. We thus consider $L_{PL} \simeq \eta F_{PL(0,\infty)} 4\pi d^2 = 0.75^{+0.20}_{-0.15} \times 10^{37} \eta$ d_5^2 erg/s.

The second spectral component is the thermal emission interpreted as emission from a Shakura-Sunyaev accretion disc, which is fitted with the `diskbb` model in the spectral fitting package *XSpec v.11*. We found a temperature of the inner rim of the accretion disc of $T_{in} = 0.68^{+0.20}_{-0.25}$ keV. The disc black body

normalization reflects the flux emitted by the disc at a given inclination angle, but given the poor coverage of *RXTE* at soft X-rays, it is basically unconstrained. We therefore use the inner disc temperature and the virial theorem to infer the bolometric luminosity of the disc as follows. We interpret the inner disc temperature of the accretion disc as derived by the `diskbb` model as the maximum temperature of the disc. Standard disc theories (see e.g. Frank et al., 2002) predict that the temperature of the disc attains a maximum value at a radius of 49/36 R_0. Using this result in Eq. [1.9], we obtain $R_0 = 1.77 m^{1/3} \dot{M}_{-10}^{1/3} T_{keV}^{-4/3}$ km. Combining this with equation [5.3] and adopting $T_{keV} = 0.70$, we solve for the mass accretion rate and the inner disc radius. We therefore find a mass accretion rate $\dot{M}_{-10} = 85 \pm 19$ and an inner disc radius $R_0(T_0) \simeq 1.46^{+0.62}_{-0.49} \times 10^6$ cm, which is exactly within the very narrow range between the NS radius ($\sim 10^6$ cm) and the corotation radius ($\sim 2.4 \times 10^6$ cm for the spin frequency of IGR J00291+5934). The virial theorem allows to calculate the fraction of the total luminosity that is emitted by the disc (see Sec.1.4.2) as $0.5R/R_0(T_0) = 0.39$. Therefore, $L_{BB} = 4.8 \times 10^{36} \eta d_5^2$ erg/s.

The total bolometric luminosity is then $L_0 = 1.23^{+0.45}_{-0.15} \times 10^{37} \eta d_5^2$ erg/s. If we compare this luminosity with the mass accretion rate inferred from the timing analysis, and assuming an efficiency conversion factor of 1, we obtain a distance to the source in the range $(10.5\text{–}15)\eta^{1/2}$ kpc. Note that 10 kpc is close to the edge of our Galaxy in the direction of IGR J00291+5934. If we push the factor η to its maximum value of 2, we obtain a more reasonable range of distances to the source of 7.4–10.7 kpc, consistent with the lower limit of 5 kpc discussed in F05.

5.2 SAX J1808.4–3658

The discovery of 401 Hz coherent pulsations in the X-ray transient SAX J1808.4–3658, during its 1998 April outburst (Wijnands and van der Klis, 1998), established for the first time on an observational basis the link between LMXB and rotation-powered Millisecond Pulsars. This transient was discovered two years earlier by the Wide Field Cameras on-board *BeppoSAX* (in't Zand et al., 2001, and references therein), exhibiting also two thermonuclear X-ray bursts which confirmed the compact object in the system to be a NS. Other outbursts were observed in 2000 February, 2002 October, 2005 June and 2008 September, making SAX J1808.4–3658 the most observationally rich source among the class of AMSP. Its recurrence time can in fact be estimated in $\sim$ 2 yr. Not only for these reasons, SAX J1808.4–3658 can be considered the cornerstone of AMSP. It was in fact the first source where burst oscillations (that are oscillations in the X-ray light curve showed by a larger sample of LMXB during thermonuclear burst events) were reported at the same frequency of coherent oscillations (Chakrabarty et al., 2003), thus allowing a safe interpretation of the frequency derived from the burst oscillations in terms of the NS rotation, and a widening of the sample of LMXB for which the period is known. Moreover it is the first AMSP in which kHz QPOs were observed (Wijnands et al., 2003), thus establishing a fundamental bench mark for all the theories on the origin of aperiodic variability in LMXB (see e.g. Méndez and Belloni, 2007, and references therein). In this section we show how it is also the first source where a complex phase behaviour was observed during its 2002 outburst, thus leading to a still active

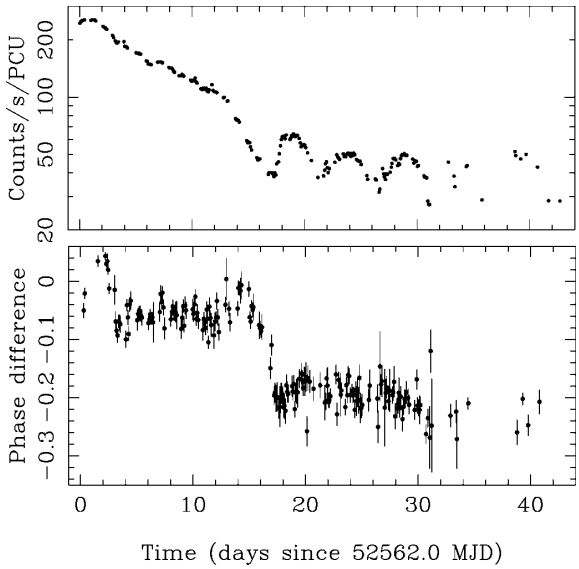

Figure 5.2: Top: PCA count rate of SAX J1808.4–3658 during the 2002 outburst. The start time, T_0, is MJD 52562.0, corresponding to 2002 October 15. Bottom: Phase differences, fundamental minus harmonic, vs. time. The jump of the phase of the fundamental at day 14 is clearly visible in the differences.

debate about the interpretation of the phase evolution in terms of rotational behaviour of the accreting NS. A model particularly well suited to explain this phenomenology is presented in Sec.6.2, while the measure of the inner disc radius from the relativistic broadening of the 6.5 keV iron line, and the orbital evolution we could measure for this source, are discussed in Chapters 7 and 8, respectively.

The complete set of X-ray light curves shown by this transient is given by Hartman et al. (2008, H08) . Apart from the 2000 episode, which was probably caught only in the dimming part because of Solar observational constraints (see e.g. Papitto et al., 2005, and references therein), the light curve shape usually displays an exponential decay with time-scale $\tau \sim 10$ d, a break after $\sim$ two weeks leading to a faster decay, and from then on a flaring tail, with multiple re-brightenings which can proceed for more than two weeks (see the top panel of Fig. 5.2 for the 2002 case). The peak flux is between 4–6$\times 10^{-9}$ erg s^{-1} cm^{-2}, leading to a luminosity of 6–9$\times 10^{36}$ $d_{3.5}^2$ erg/s, where $d_{3.5}$ is the distance in units of 3.5 kpc. We note that an estimate of $d = (3.5 \pm 0.1)$ kpc was obtained by Galloway and Cumming (2006) under the hypothesis that the thermonuclear bursts observed from the source reached the Eddington limit, as they showed the fingerprint of the resultant photospheric radius expansion.

The pulse profile of SAX J1808.4–3658 can be well described by two harmonic components, but disentangled variations of the phases of these two components witness the occurrence of shape changes. The 1998 outburst rotational behaviour is discussed by Papitto (2005, Grad.Thesis). The source then shows an apparent spin up for the first two weeks, and the frequency raises at a rate $< \dot{\nu} >_{98} = (1.1 \pm 0.5) \times 10^{-13}$ Hz/s. Subsequently, a phase shift affects both the

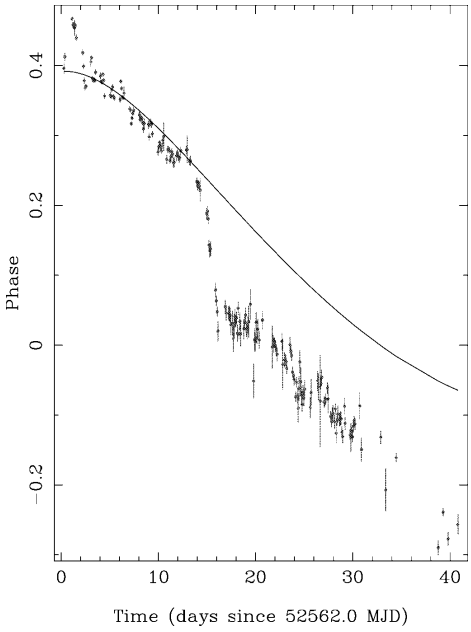

Figure 5.3: Phase vs. time for the first harmonic (fundamental) of the pulse frequency of SAX J1808.4–3658. On top of the data, the best-fit function, Eq. [5.4] to which we added a constant spin-down term, is plotted as a solid line.

first and second harmonic phase evolution (see e.g. Fig. 1 of H08). Here, we present in more detail the behaviour during the 2002 outburst (Burderi et al., 2006). After having corrected for the orbital motion using the most updated orbital solution available when the analysis was performed (Papitto et al., 2005, no significant change is observed if newer ephemerides are used), the phases of the first and second harmonic follow the evolution depicted in Fig. 5.3 and Fig. 5.4, respectively.

The phase delays of the fundamental show a puzzling behaviour, with a clear jump by about 0.2 in phase, occurring 14 days after the beginning of the outburst. In the outburst light curve, interestingly, the 14th day corresponds to a change of the steepness of the exponential flux decay (see Fig. 5.2, top), while before this day the X-ray flux decreases exponentially with a characteristic time of about 10 days. On the other hand, the phase delays of the second harmonic do not show any evidence of such a jump. Note that this is not an effect of the larger error bars of the phases of the harmonic, as it can be seen from Fig. 5.2 (bottom), where we plot the differences between the phase of the fundamental and the phase of the harmonic as a function of time. For a global shift of the pulse profile, like the one exhibited by XTE J1814–338 (see Sec. 4.2), the phases of the fundamental and harmonic should shift by the same amount and the phase differences should therefore remain constant. On the other hand, a phenomenology like the one observed in SAX J1808.4–3658 reflects a shift of the phase of the fundamental with respect to the harmonic caused by a change of the shape of the pulse profile. In the plot of the phase difference (Fig. 5.2, bottom) it is possible to see that the big jump at day 14 is still visible and is much larger

Table 5.2: Timing parameters of 2nd harmonic in SAX J1808.4–3658

Parameter	Value
ν_0 (Hz)	400.97521041(7)
$\dot{\nu}_0$ (Hz/s)	$(4.40 \pm 0.81) \times 10^{-13}$
$\dot{\nu}_{SD}$ (Hz/s)	$(-7.6 \pm 1.5) \times 10^{-14}$

than the associated error bars, meaning that it is present in the fundamental and not in the harmonic. As the evolution deduced from the second harmonic phases is easily interpreted in terms of accretion torques (see below), we argue that at least in this case (but see also the case of XTE J1807–294 treated in the next section) the behaviour of the 2^{nd} harmonic is genuinely simpler than the behaviour of the fundamental.

Accounting for the exponential decay observed in the light curve ($\tau = 9.3$ d), the model we first consider for the phase evolution is, similarly to the XTE J1751–305 case (Eq. [3.4]):

$$\Delta\phi(t) = A - [B + \tau C]\,(t - T_0) - C\tau^2 \exp\left[-\frac{t - T_0}{\tau}\right], \qquad (5.4)$$

where $B = \Delta\nu_0 = \nu_F - \nu(T_0)$ is the correction to the folding frequency, ν_F, and $C = \dot{\nu}(T_0) = (2\pi I)^{-1}[GMR_{in}(T_0)]^{1/2}\dot{M}(T_0)$.

A good description of the second harmonic phases can be found only if we restrict to the first 14 days of data (χ^2/dof=613.1/199).[1] Afterwards, we observe a flattening of the phase delays, to model which we added to the above relation a quadratic term corresponding to a constant spin down. In this way we obtained a significant improvement of the fit (χ^2/dof = 485.0/198; this χ^2 is still large, but now we do not see any systematic trend in the residuals with respect to the best-fit model). Although in this way we have obtained a great improvement of the quality of the fit, the obtained χ^2 is still unacceptable because of localized residuals around day 4 and day 30–31 from the beginning of the outburst. These residuals cannot be taken into account modifying the fitting function, but the uncertainties derived from a fit that is not acceptable in the statistical sense may be underestimated. We therefore increased by a factor 1.5 the errors of all our phase points, to obtain more conservative uncertainties for our best-fit parameters, yielding a $\chi^2 = 215/198$ (that is now very close to 1), and we have recalculated all the uncertainties on our best-fit parameters. The best-fit parameters and the corresponding uncertainties (at 90% c.l.) are shown in Table 5.2; the best-fit function is plotted on top of the data in Fig. 5.4. For a comparison, we have plotted the best-fit function of the second harmonic on top of the fundamental also (Fig. 5.3).

The spin-up is interpreted in terms of the accretion of matter, $\dot{M}(T_0)$, at the corotation radius, $R_0 = R_C = 31 m_{1.4}^{1/3}$ km , where $m_{1.4}$ is the mass of the NS in units of 1.4 $M_\odot$. Recalling the definition of $\dot{\nu}(T_0)$ given above we obtain:

$$\dot{M}(T_0) = 18.3 \times 10^{-10} I_{45} m_{1.4}^{-2/3} M_\odot/yr. \qquad (5.5)$$

[1] Note that fitting these data to simple linear or parabolic functions gives similar (slightly worse) results, corresponding to χ^2/dof = 623.4/200 or χ^2/dof = 622.4/199, respectively.

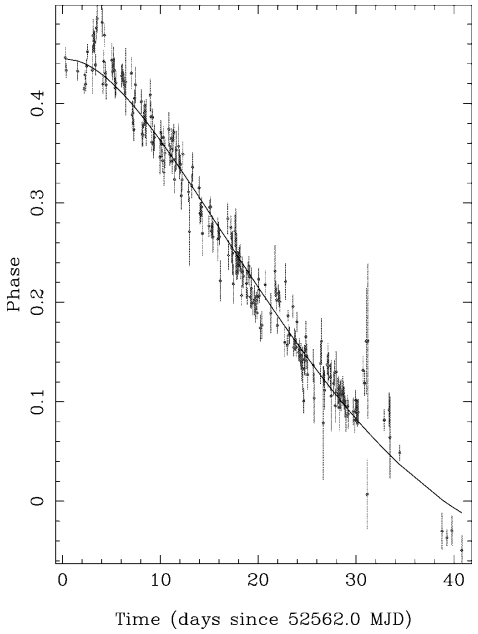

Figure 5.4: Phase vs. time for the second harmonic of the pulse frequency of SAX J1808.4–3658. On top of the data, the best-fit function, Eq. [5.4] to which we added a constant spin-down term, is plotted as a solid line.

As R_C is the maximum inner disc radius to prevent centrifugal inhibition of accretion, this value of $\dot{M}$ can be considered a lower limit under the assumption it is derived from.

The spin-down can instead be understood in terms of the magnetic field threading of the accretion disc. Using the relation [1.27], and inserting the value we obtain for $\dot{\nu}_{SD}$ (see Table 5.2), yields $B \sim (3.5 \pm 0.5) \times 10^8$ G, in perfect agreement with previous constraints (Psaltis and Chakrabarty, 1999; Di Salvo and Burderi, 2003). The spin down term becomes dominant only in the later stages of the outburst, when the mass accretion rate is significantly declined.

For the position of the source, we considered the proposed radio counterpart (Rupen et al., 2002), which has an error circle of $0''.4$ and is compatible with the well studied optical counterpart. The resulting uncertainties on ν_0 and $\dot{\nu}$ are, $\sigma_{\nu,syst} = 8 \times 10^{-8}$ Hz and $\sigma_{\dot{\nu},syst} = 1.8 \times 10^{-14}$ Hz/s, respectively.

In order to compare the derived spin-frequency derivative with the mass accretion rate as inferred from the bolometric X-ray flux of the source, we performed a spectral analysis of the PCA and HEXTE spectra at the beginning of the outburst (i.e., at 2002 October 15 and 16). Keeping the absorption to the source fixed at $N_H = 3.0 \times 10^{21}$ cm^{-2} (the Galactic X-ray absorption in the direction of SAX J1808.4–3658 at a distance of 3.5 kpc; Galloway and Cumming, 2006), a very good fit to the 2.5–200 keV spectrum of SAX J1808.4–3658 is given by a disk black-body plus a cut-off power law, and a Gaussian emission line with centroid fixed at 6.4 keV (the fluorescence K-shell iron line; see also Ch. 7 for the spectrum observed during the 2008 outburst). We extrapolated

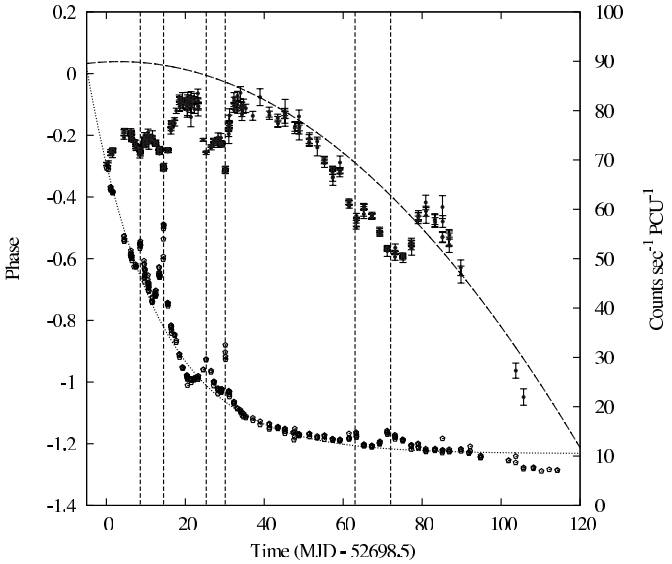

Figure 5.5: Light curve of XTE J1807–294 during the 2003 outburst (pentagons) and phase delays of the first harmonic as a function of time (dots). The dashed vertical lines indicate the times of six clearly visible flares of the X-ray flux, superposed on a global exponential decay. The dotted curve represents the exponential fit of the light curve, obtained after having previously excluded the six flares from the data. The dashed curve represents the parabolic best fit obtained fitting the second-harmonic phase delays and considering the nominal source position. Strong fluctuations of the phase delays are apparent and are strongly anti correlated with the flares present in the X-ray light curve.

the observed X-ray flux in a broadband energy range in order to evaluate the bolometric accretion luminosity, which resulted to be 1×10^{37} erg/s on 2002 October 15, assuming a distance of 3.5 kpc and correcting for the interstellar absorption. The dynamical estimate of the mass accretion rate given in Eq. [5.5], would result in an X-ray luminosity a factor 2 larger than this value. The accord is in general good, given the simplifying assumptions made in the derivation of these values. The discrepancy can be nevertheless understood if we let not all of the mass accreted by SAX J1808.4–3658 to be observed in the X-ray band, because of polar cap screening by the disc, or beaming.

5.3 XTE J1807–294

The 190 Hz X-ray pulsar XTE J1807–294 was discovered by *RXTE* on 2003 February 21 (Markwardt et al., 2003), at the beginning of the only outburst observed so far, which is also the longest for a persistently pulsating AMSP ($\sim$ 120 d). The X-ray light curve has the most common exponential decay shape ($\tau = 17.5(3)$ d), but it also show six evident flares (see pentagons in the lower track of Fig. 5.5). To derive the characteristic time of the decay, we fitted the light curve after the time intervals affected by X-ray flares were removed from the sample. The criterion we choose to flag flare intervals is based on

Table 5.3: Orbital and spin parameters of XTE J1807–294

Parameter	**Value** [a]
$a \sin i/c$ (lt-ms)	4.819(4)
P_{orb} (s)	2404.41665(40)
T^* (MJD)	52720.675603
Eccentricity e	$< 3.6 \times 10^{-4}$
Reference Epoch, T_0 (MJD)	52698.5 [b]
Parabolic fit	
ν_0 (Hz)	190.62350702(4)
$\dot{\nu}$ (Hz/s)	$2.5(7) \times 10^{-14}$
Exponential fit	
ν_0 (Hz)	190.62350694(5)
$\dot{\nu}$ (Hz/s)	$1.25(33) \times 10^{-13}$

[a]Errors on orbital parameters are intended to be at the 1 σ confidence level (c.l.); upper limits are given at 95%c.l. Best-fit spin parameters are derived under both the hypothesis of a constant spin-up and of a flux-dependent spin-up, and the uncertainties include systematics due to the uncertainties in the source position (see text).

[b]This is the epoch to which the reported values of ν and $\dot{\nu}$ are referred.

a flux threshold of 15% with respect to the best-fit exponential model. Such flares deeply contaminate also the pulse phases evolution. As it is clear from Fig. 5.5, where the phases of the fundamental are plotted as dots (upper track), the phase advances up to 0.3 in phase units contemporary to the flares ($\sim 100^\circ$ if translated into NS longitude angle). This anti-correlation has the same sign than the one displayed by XTE J1814–338 (Sec. 4.2).

It has to be noted that these shifts are evaluated from a phase plot, where the profiles were obtained from orbital corrected light curves. It is easy to understand how such drifts make difficult the modelling of the orbital motion, as the times over which the phases vary ($\sim$ days) are now shorter than the torque case ($\sim$ weeks), even if still larger than the orbital period ($\sim$ hours). To this end, Riggio et al. (2007) developed an analysis different from that outlined in Sec. 2.2.5, in the sense that the phase differences induced by the orbital motion between two consecutive discrete times are considered, rather than fitting the phase evolution directly. This applies a low pass band linear filter on the pulse phases plot, selecting only those phase variations due to effects whose time-scale is comparable with the interval between two consecutive times. In this way, any effect on longer time-scales (such as the phase variations simultaneous to the flares, as well as the torque produced long term effects) is dumped, and the orbital solution can be safely recovered. The parameters obtained by this method are listed in Table 5.3.

On the other hand, the phase delays derived from the second harmonic are much more regular (see Fig. 5.6), a behaviour that is similar to that exhibited by SAX J1808.4–3658 (Sec. 5.2). Although a few points (corresponding to the rapid flares in the light curve) appear to be significantly below the general trend, the phase delays of the second harmonic clearly show a parabolic decrease, as is expected in the case of a spinning up of the NS.

Since the phase delays of the second harmonic are much less noisy than the phases derived from the first harmonic, and assuming that the pulse phase de-

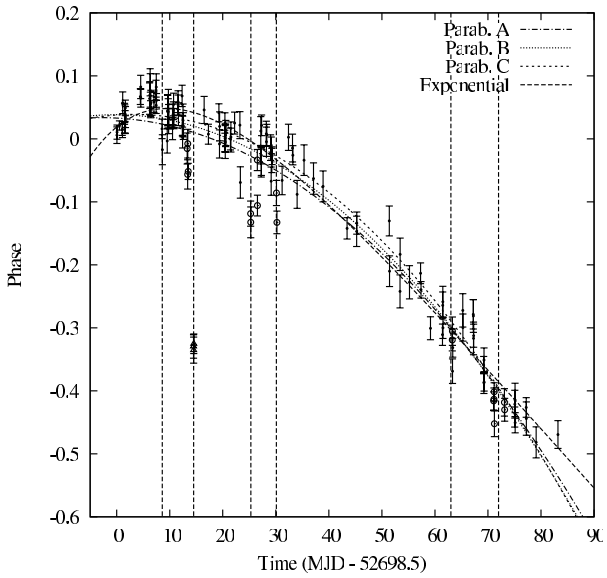

Figure 5.6: XTE J1807–294 second-harmonic pulse phase delays. The four curves represent the parabolic best fit for the nominal source position, respectively, using all the data points (case A), excluding the three points at MJD 52,713.0 (case B, where the points excluded are identified by triangles), and excluding all the data points for which the flux exceeds the best-fit exponential decay by more than 15%(case C, where the points excluded are identified by circles), and the best fit obtained using an exponentially decreasing mass accretion rate (see text). The exponential fit of the light curve was performed on the data subset corresponding to case C.

lays derived from the second harmonic are a good tracer of the spin frequency evolution, we decided to fit the second harmonic in order to find the desired information about the spin frequency behaviour. The results of a phase modelling with a parabola (that is a constant spin-up), and with an exponential decaying function (correspondent to a accretion at the corotation radius with $\dot{\nu} \propto \dot{M}$, see Sec. 2.2.4), are listed in Table 5.3, and plotted in Fig. 5.6. The latter case obviously takes into account the decrease of the X-ray flux through the outburst, an effect which is expected to be particularly prominent in XTE J1807–294 case, which has shown the longest outburst among AMSP. This is confirmed by the statistically significant improvement we obtain with this model ($\Delta\chi^2 = 32$ for a $\chi^2_{red} = 225.21/121$).

Unfortunately, these results are affected by large systematic uncertainties due to the large uncertainty in the source coordinates (about $0''.6$ at 90% confidence level, from a Chandra observation, Markwardt et al., 2003). In the case of XTE J1807–294, because of the low positional precision and the long time span over which the pulsations were visible (up to 106 days from the beginning of the outburst), we obtain from the expressions given in Sec. 2.2.6 the following systematic uncertainties on the spin frequency and the spin frequency derivative, respectively: $\sigma_{\nu,syst} = 4.1 \times 10^8$ Hz and $\sigma_{\dot{\nu},syst} = 0.8 \times 10^{14}$ Hz/s. Since this error is of the same order of magnitude as the best-fit estimate of $\dot{\nu}$, a more careful way than the one depicted in Sec. 2.2.6 is mandatory to draw firm results on the rotational behaviour of XTE J1807–294. The phase delays were

then modelled adding the term owing to the position uncertainty, Eq. [2.33], covering all the possible coordinates within 0.″6 from the source. The statistical uncertainties on the frequency and on its derivative quoted in Table 5.3 are then drawn from the distribution of these values, with respect to the coordinates used in the phase modelling.

From the fit of the phase delays of the second harmonic of XTE J1807–294 with the exponential model discussed above, we find a mass accretion rate of $4(1) \times 10^{10}$ $M_\odot$/ yr at the beginning of the outburst[2]. This mass accretion rate can be then compared with the X-ray flux of the source at the beginning of the outburst, 2×10^{-9} erg cm^{-2} s^{-1} (Falanga et al., 2005), from which we derive an X-ray luminosity of 4.7×10^{36} erg/s and a distance to the source of 4.4(6) kpc. This estimate is barely consistent with the (uncertain) lower limit set by the observed recurrence time and the expected mass accretion rate yielded by the emission of GW (Galloway, 2006).

5.4 XTE J0929–314

XTE J0929–314 is a high-latitude source and was discovered by RXTE in 2002, when it showed an X-ray outburst which started on May 2 and lasted for about 53 days. Galloway et al. (2002) provided an orbital solution for this source, reporting a quite short period of $\sim$ 44 min. With a spin frequency of 185 Hz this is the slowest among the known sample of AMSP. They also performed a timing analysis of the pulse phase delays, showing that the source underwent a steady spin-down while accreting at a rate of $\dot{\nu} = 9.2(4) \times 10^{14}$ Hz/s. We re-analysed the available *RXTE* data using an improved source position on the sky (Giles et al., 2005), and basically confirm the spin-down of the source, although with a revised spin-down rate of $\dot{\nu} = 5.5(4) \times 10^{14}$ Hz/s (Di Salvo et al., 2008b).

The case of XTE J0929–314, despite it seems very simple to understand in terms of magnetic threading, reveals much more puzzling than XTE J1814–338 behaviour (see Ch.4). While the latter exhibited an almost constant X-ray flux, at least for the first month of observation, XTE J0929–314 shows a roughly linear decrease of the X-ray flux during the outburst, similarly to the decay observed in IGR J00291+5934 (Sec. 5.1), with a decay time $t_B \simeq 58.5$ d. This means that, along the outburst, the expected spin-up should decrease, and the global derivative of the spin frequency (that is the sum of the spin-up and spin-down rates) should show an increasing rate of global spin-down along the outburst. However, the pulse phase delays do not show any increasing spin-down, since the best fit suggests a constant (or at most decreasing) value of $\dot{\nu}$. The fact the the decrease of the X-ray flux does not affect the behaviour of the phase delays, could be interpreted if it is argued that the spin-up rate should be always negligible with respect to the observed spin-down, i.e. $\dot{\nu}_{su} << -\dot{\nu}_{sd} \simeq 5.5 \times 10^{14}$ Hz/s. This obviously translates in a requirement on the mass accretion rate that is expected to produce the material torque that adds angular momentum to the NS anyway. If we assume, in agreement with the request above, that the spin-up is at least a factor of 5 lower than the spin-down rate, we find a corresponding mass accretion rate of $\dot{M} < 6 \times 10^{-11}$ $M_\odot$/yr, which would correspond to a quite low bolometric luminosity of $< 6 \times 10^{35}$ erg/s. If we compare this luminosity

[2]For this estimate we adopted $R = R_C = 50.7$ km, $M = 1.4$ $M_\odot$, $R = 10$ km, $I = 10^{45}$ g cm^2

with the observed X-ray luminosity, $L_X \sim 1.0 \times 10^{37} d_5$ erg/s, where d_5 is the distance to the source in units of 5 kpc, we find an upper limit to the source distance of about 1.2 kpc, that is less than the lower limit of 3.6 kpc derived by the expected secular mass accretion rate (driven by gravitational radiation) and a supposed outburst recurrence time > 6.5 yr (Galloway, 2006).

A distance of ~ 1 kpc is unlikely to be correct, although we have to note that XTE J0929–314 is a high latitude source, and therefore the closer is the source, the larger will be the height of the source above the Galactic plane. Otherwise, this large discrepancy could be determined by the used model for the threading (spin-down) torque; in most of the models (see e.g. Eq. [1.27]) this depends only on the magnetic field strength and should therefore remain constant along an X-ray outburst. However, the pulse phase delays seem to suggest that the spin-down in XTE J0929–314 may decrease at the end of the outburst. We then recall that MHD simulations on the interaction between the accretion disc and the magnetosphere of a NS in the spin-down regime (i.e. when the accretion radius is equal or larger than corotation radius) presented by Romanova et al. (2004b, see Sec.1.5.2) show that the spin down torque resulting from this interaction may decrease with decreasing accretion rate, with the material torque owing to the accreted matter relegated to a marginal role in building the overall torque. This behaviour is related to the weaker coupling between the magnetosphere and the disc matter at low accretion rates, which has the effect to weaken the toroidal component of the magnetic field in the magnetosphere, which is the one responsible for the spinning down of the pulsar. We therefore need a correct modelling of the spin-down torque in order to correctly evaluate the upper limit on the mass accretion rate from timing.

If we anyway make the simplifying assumption that the negative torque is constant and described by Eq. [1.27], while we take for the spin up torque the average value implied by the observed outburst fluence[3] for a disc ending at the corotation radius, we obtain $< \nu_{su} > \sim 8 \times 10^{-14}$ d_5^2 Hz/s. The NS magnetic field required to produce an overall spin down at the measured rate would therefore be $\sim 1 \times 10^9$ d_5^2 G at the surface; this estimate has obviously to be considered with caution, as the assumptions used in its derivation, are not supported by data (see above). It should instead be taken as a reference value, indicating how a magnetic field of the order of the one measured in XTE J1814–338 is needed to explain at least grossly the observed spin down behaviour.

5.5 Summary

The results obtained from a timing analysis on the considered AMSP are summarized in Table 5.4, where the sources are sorted on the basis of their rotational frequency. We discuss the issue of the phase variations displayed by three of these sources in the next chapter, while here we consider the observed spin frequency derivative, described in this and in the previous chapters, as a good proxy of the actual behaviour of the NS. In addition, this is done by taking into account the second harmonic behaviour when it gives more reasonable results (that is for SAX J1808.4–3658 and XTE J1807–294). In the rightmost column of Table 5.4 the value of the peak X-ray luminosity reached during outburst is also

[3] $\mathcal{F} = (5.4 \pm 0.3) \times 10^{-3}$ erg cm^{-2} (Galloway, 2006)

Table 5.4: Summary of the observed rotational properties of AMSP.

Source	ν (Hz)	$\dot{\nu}$ (10^{-14}Hz/s)	$\mathbf{L}_X$ (10^{36} erg/s)
IGR J00291+5934	599	117 ± 16	15 η d_5^2
XTE J1751–305	435	56 ± 12	27 $d_{8.5}^2$
SAX J1808.4–3658 (2002)	401	44 ± 8	10 $d_{3.5}^2$
		-7.6 ± 1.5	
XTE J1814–338	314	-6.7 ± 0.7	7 d_8^2
XTE J1807–294	191	12.5 ± 3.3	4.7 $d_{4.4}^2$
XTE J0929–314	185	-5.5 ± 0.4	10 d_5^2

reported, in order to test the expected dependency of the rotational reaction of the NS on the mass that is effectively accreted by the NS. We note however that such estimates are affected by the uncertainties on distance, and the quoted values are therefore to be taken with caution. As a matter of fact, only in the case of SAX J1808.4–3658 the reported distance was derived from the photospheric radius expansion associated with an Eddington limited thermonuclear burst, and is therefore reliable. Among the other considered sources, only XTE J1814–338 also showed such thermonuclear bursts, but no definitive signature of radius expansion was reported. In the other cases the estimates are drawn from the comparison between the observed secular mass accretion rate and the one expected if the orbital evolution is driven by the emission of gravitational waves from the binary (Galloway, 2006). In this way, only lower limits on the distance can be derived indeed, and a great source of uncertainty comes from the assumptions that all the transferred mass is effectively accreted by the NS. This assumption evidently breaks down in the case of SAX J1808.4–3658 (see Ch.8), and could not be tested for the other sources.

The results of our analysis clearly state how the NS reaction to accretion is bimodal; only 4 sources out of 6 gain rotational angular momentum in the accretion process, while for the others the global momentum flow is from the NS to the accretion disc. Assuming that these spin-downs are due to the interaction of the quickly rotating magnetosphere with the accretion disc, this is by itself an indication that larger magnetic must characterise the decelerating sources. As a matter of fact, the total torque acting on the NS is the sum of a positive torque due to the accretion of the (Keplerian) angular momentum at the inner disc radius, R_0 ($\dot{M}\sqrt{GMR_0}$), and a negative torque yielded by the interaction of the field lines which close through the disc beyond the corotation radius ($\sim \mu^2 R_0^{-3}$). If we compare the four slower AMSP in Table 5.4, we clearly note that, despite the mentioned uncertainties on the respective distances, the observed X-ray luminosities are of the same order, while the sign of the spin frequency derivative can be either positive or negative. Given the widely accepted accretion theory stated in Sec. 1.5.1, the only viable option to explain this occurrence implies a stronger magnetic field in the spinning-down sources.

Considering the sample as a whole, there is a tendency to observe spin-ups in faster sources, while the slower ones spin down. This is perfectly in line with the expectations drawn from the spin equilibrium theory (Sec. 1.5.2), and consistent with the distribution of magnetic fields we envisaged above. We have in fact that the magnetic field of the NS dictates to what extent the object can be spun up by an accretion phase. Assuming that the AMSP are in spin equilibrium,

and that their accretion history is similar, we therefore expect the faster sources to have relatively lower magnetic fields. The magnitude of the negative torque would be therefore strongly reduced in these cases, with the consequence that the positive torque would easily take the lead. On the other hand, slower sources are expected to have larger magnetic fields, and consequently decelerate at a given accretion rate. Despite the low number of sources available, this is indeed indicated by our analysis.

If we restrict our discussion to the four spinning up sources, our results indicate faster spin-ups at larger mass accretion rates, as expected. The only source which emits significantly less than what it would be predicted according to the measured spin frequency derivative, is IGR J00291+5934, the fastest AMSP known. Such a discrepancy can be hardly recovered if it is not argued that the observed X-ray flux is less than what is emitted by the source on the entire solid angle, or that the X-ray flux is not a good tracer at all of the mass accretion rate. The latter option is strongly disfavoured, at least in a general sense, by the good match we find in the other considered sources[4]. Similar measurements during the future outbursts this source might display would be of invaluable importance to assess the reason of this mismatch.

IGR J00291+5934 is on the other hand, one of the most promising case to derive important results for what concerns the possible detection of Gravitational Waves effects (see Sec. 1.6). The discrepancy we observe between the dynamical and spectral estimates of the mass accretion rate crosses the efforts to detect a GW driven spin-down under the observed global spin-up, at least to some extent. In principle, a constraint on the mass quadrupole moment of the NS could be derived by arguing that the observed spin-up is the sum of the acceleration imparted to the NS by the accreted matter, and the deceleration produced by the GW emission. If we argue that only half of the flux emitted by the source is observed ($\eta = 2$), and that $d = 7$ kpc is the distance to the source, the expected spin-up due to material torque is $\dot{\nu}_{SU} \lesssim 1.3 \times 10^{-12}$ $\mathrm{m}_{1.4}^{2/3}$ Hz/s. Considering the observed value of $\dot{\nu}$ (Table 5.1), this would translate in an upper limit on the eventual spin-down associated to GW of $\dot{\nu}_{GW} \lesssim 1 \times 10^{-13}$ Hz/s. As the expected slow down rate for GW emission is $2\pi I \dot{\nu}_{GW} = 32GQ^2(2\pi\nu)^5/5c^5$, the mass quadrupole would be limited by $Q \lesssim 2 \times 10^{37}$ g cm^2. However, we remark how this upper limit is crucially dependent on the assumptions on the bolometric correction factor, η, and on the poorly constrained distance, and therefore needs to be confirmed by further estimates.

[4]This is particularly the case for XTE J1807–294, where a model with an $\dot{M}$ dependent spin frequency derivative gives statistically better results than a constant $\dot{\nu}$ model (Sec. 5.3)

6

Phase shifts of AMSP

An unexpected outcome of the research we conducted on the rotational behaviour of AMSP is the discovery of phase shifts in three out of the six sources considered. Here we call shifts those phase movements that cannot be interpreted in terms of the orbital motion of the source, or as due to the accretion torques applied on the NS. Such shifts were observed in XTE J1814–338, SAX J1808.4–3658 and XTE J1807–294, and in all of these cases they appear simultaneously to variations of the emitted X-ray flux. It turns out that the phase behaviour of the second harmonic appears intrinsically more stable than the fundamental. After we have summarized the observations of such shifts, we discuss in this chapter the possible mechanisms which could produce them, focusing an a simple geometrical model accounting for at least part of the phenomenology shown by the AMSP.

6.1 Hot spots motion

The rotational behaviour of AMSP deduced from timing analysis is bimodal not only for what concerns the sign of the spin derivative, but also for the issue of phase stability. While in half of the considered cases the phase evolution can be adequately fit with physically plausible torque models, the same modelling does not give the same good results in the other cases. It is clear from eye inspection of Fig. 4.4, 5.3 and 5.5, that residuals appear from any reasonable modelling of the phase evolution of the sources listed in the following. SAX J1808.4–3658 fundamental phase shows a clear jump of 0.2 (phase units) contemporary to a break in the X-ray light curve, while the second harmonic keeps following a smooth trend. The case of XTE J1807–294 also indicates an enhanced stability for the second harmonic, which was therefore used to model the physical evolution of the source; while the phase computed on the first harmonic deviates by more than 0.3 simultaneously to re-flares in the light curve, the second is in fact more regular. XTE J1814–338 still presents another kind of phenomenology, as both the first and second harmonic phase are modulated around an average spin-down solution. Such variations are nevertheless tightly anti-correlated with changes of the X-ray flux, similarly to what is observed in XTE J1807–294. Two questions appear therefore related to the interpretation of these enigmatic shifts. First, what is the origin of the anti-correlation with the flux, and, second, why the second harmonic phases are intrinsically more stable than the one computed on the first.

That such phase drifts simply reflect accretion torque on the NS can be firmly excluded from simple reasonings. For example the jumps of 0.3 shown by XTE J1807–294 happen on a time-scale of a day. This would imply a spin frequency derivative of $\sim 1 \times 10^{-10}$ Hz/s. According to the accretion theory developed in Sec. 1.5.2, an accretion rate well in excess of the Eddington rate would be implied by such large values. A similar reason excludes the possibility that the phase drifts observed also in the other sources are due to accretion torques. Orbital effects can be also excluded, as these would introduce phase variations on the orbital period time-scale. Free precession of the NS was considered by Chung et al. (2008) to explain the behaviour of XTE J1814–338, but such effect could give an explanation only for unlikely small values of the inclination ($< 0.1°$), and can be therefore reasonably ruled out.

The most appealing interpretation for these phase shifts is in term of the motion of the hotspots on the NS surface, possibly induced by more or less sudden variations of the accretion rate. How it was stated in Sec. 1.5, magnetic field lines truncate the disc at a location R_0, that is where the magnetic stresses removes enough angular momentum from disc matter to end the Keplerian regime. Only those field lines that intercept the disc near the inner rim of the disc have the favourable conditions to drive matter towards the NS surface. Arguing a dipolar magnetic field, simple considerations show that the magnetic colatitude (on the NS surface) of the lines that cross the disc plane at R_0 is $\beta \sim (R_*/R_0)^{1/2}$ (e.g. Frank et al., 2002). This angle can be quite large in an AMSP ($\sim 30°$), as the inner disc radius is of the same order of the NS radius. Defining θ the angle between $\vec{\mu}$ and $\vec{\Omega}$, if $\theta = 0$, the footprints of the accreting lines are two annuli encircling the respective magnetic pole. The angular width of these annuli is a small fraction of β. If instead the magnetosphere is inclined with respect to the disc plane ($\theta > 0°$), only lines near the $\vec{\mu}$–$\vec{\Omega}$ plane are favoured for accretion, and the hotspot is rather bow shaped, letting the typical pulsar lighthouse effect to be observed.

The phases we measure through the timing techniques are thought to reflect the longitude Λ of the hotspot on the NS, $\phi = -\Lambda/2\pi$.[1] Therefore a relation for the dependence $\Lambda(\dot{M})$ would be of fundamental importance to understand the shift–flux (anti-)correlation. An analytical derivation is nevertheless frustrated by the evident complexity of the MHD problem of disc accretion onto a magnetised star. Romanova et al. (2003, 2004d) nevertheless recently reported about the first three-dimensional MHD simulations of the accretion process onto an object with an inclined dipole, and we can try to use their result as a guideline to interpret the phase variations we observed. The theoretical understanding about hotspot formation was indeed confirmed in all its basic ingredients by their results. Two funnel flows appears as soon as the magnetic field is tilted by $\theta \sim$ few degrees from the rotation axis. At least for $\theta \lesssim 45°$, the resulting hot-spots on the surface appear as arcs near the magnetic poles. The value of Λ depends critically on which is the direction of the angular momentum flow between the NS and the accretion disc. Matter at the disc edge rotates faster than the NS for 'slow' rotators, so that the field lines form a trailing spiral which effectively spins up the star. The footprints of the accreting lines are therefore

[1] We refer to longitudes in a system corotating with the NS, with $\Lambda = 0$ along the plane defined by the magnetic dipole, $\vec{\mu}$, and the rotation axis, $\vec{\Omega}$. Longitudes are counted in the same sense of the star's rotation.

shifted downstream up to $\Lambda \sim 30^\circ$ with respect to the $\vec{\mu}$–$\vec{\Omega}$ plane. The opposite happens for spinning down rotators, in which cases the magnetosphere effectively drags in the inner disc matter and the hot-spots are placed upstream of the magnetic dipole ($\Lambda \lesssim 0$). On the other hand, one of the main results of these simulations is that the angular momentum flow is essentially determined and transported by the distortion of magnetic field lines in the azimuthal direction. The pitch of the field lines at the accretion disc, $\gamma_0 = B_\phi/B_p$ (see Sec. 1.5.1), is therefore expected to follow the accretion rate, which is actually the main agent for the spin-up torque determination. According to this picture, we can then imagine how Λ should raise with $\dot{M}$, and the phase ultimately anti-correlate with the flux, that is exactly what we observe in XTE J1807–294 and XTE J1814–338. We note that these two sources show opposite signs of the spin derivative, but the positive spin up torque which depends linearly from $\dot{M}$ is expected to be equally important in both cases.

This qualitative picture relies on the hypothesis that the longitude of the spot reflects the winding of the magnetic field, which is in turn related to the fastness of the rotator with respect to the inner disc edge. We note however that we have ignored so far how Λ should depend on the inner disc radius, which is the other key quantity in the determination of the torque on the NS. In Sec. 1.5.1 we have considered only the dependency of R_0 on the accretion rate. The magnetic pitch nevertheless enters in the relation for R_0 with an opposite dependence, that is $R_0 \propto (\gamma_0 \dot{M}^{-1})^{2/7}$ (see Eq. 1.23). This potentially weakens to what extent R_0 responds to variations of $\dot{M}$, and given also the fact that the torque is less dependent to R_0 than to $\dot{M}$ ($N \propto \dot{M}\sqrt{R_0}$), it leads us to think how Λ should be primarily determined by $\dot{M}$, that is the qualitative indication of the data.

The ideas presented here are to be considered as working hypotheses, given also the fact that they are based on the results of simulations that cover a short time interval and a tiny parameter space. More observations and modelling is therefore needed to truly understand these phase drifts. Despite only qualitative considerations can be drawn, the above discussion shows however how the phase shifts we discovered in AMSP could be in principle an useful probe of the complex environment in the nearby surroundings of a quickly rotating NS.

In the next section we present instead a simple geometrical model developed to explain why the second harmonic phase has generally a smoother behaviour than the one computed on the fundamental frequency.

6.2 A geometrical toy-model

A particular occurrence can be noted on how shifts affect AMSP phases. Despite that a sample of six sources is certainly too poor to draw any, statistically speaking, definitive conclusion, it happens that phase shifts affect sources which have a significant harmonic content. The smoothly evolving pulses are in fact almost nearly sinusoidal. This may indicate that at least part of the shift origin has to be searched in the process which build a pulse profile from the contribution of both antipodal spots. Therefore we first recall how the profile of a pulsar is thought to be formed, and then explore the possibility that phase shifts are simply due to variations of the mass accretion on each polar cap, that is the variations of the strength of the two signals that build the overall pulse profile.

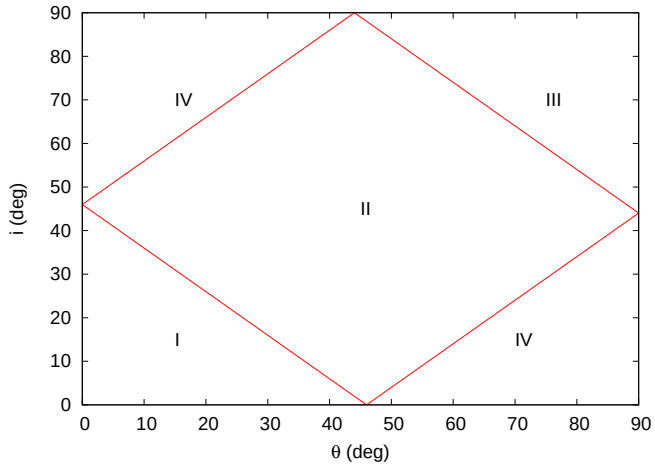

Figure 6.1: Visibility classes for an 1.4 $M_\odot$ pulsar of 10 km of radius. The primary spot is always visible in class I, II and IV, and partially visible in class III. The secondary spot is always visible in class IV, partially visible in class II and III and never observed in class I.

In fact, this simple model naturally yields an enhanced stability in the second harmonic with respect to the first, something we could observe in the cases of SAX J1808.4–3658 and XTE J1807–294 (see Ch. 5).

The theoretical shape of the pulse profile emitted by a fast rotating pulsar was studied analytically by Beloborodov (2002) and Poutanen and Beloborodov (2006), considering small hotspots on the NS surface. The overall signal is made of the contribution of the flux emitted by one or both hotspots, depending on a few visibility conditions (see below). The signal of a single spot is considerably modified by general and special relativity effects with respect to what would be observed from a slowly spinning rotator in a flat space time, where it would be instead a perfect sinusoid, under the assumptions made. The NS compactness significantly curves the space-time at the surface, so that also photons which are not emitted in the direction of the line of sight may become visible. This decreases the pulse amplitude, and modifies the range of angles for which a spot on the NS is visible. Moreover, the spots travel at a speed comparable with that of light in an AMSP ($v/c \simeq 0.1$), so that Doppler boosting and angles aberration skew significantly the profile. The maximum of a pulse is therefore shifted backward, as an observer sees a maximum of the emitted flux when the spot is moving towards him, rather than when it is nearest to the him. These effects introduce therefore an harmonic content in the profile emitted by a single spot, which is no longer a pure sinusoidal function.

Another issue modified by the extreme environment of a fast NS is the visibility of the hot spots for an observer. To understand this, we define as $\hat{n}$ the normal to the spot, and as $\hat{k}$ the unit vector pointing from the spot towards the observer (i.e. along the line of sight). In a flat space-time the condition for a spot to be visible is simply $\cos\psi = \hat{n}\cdot\hat{k} > 0$. Recalling that θ is the tilt between the magnetic and rotation axes, and that i is the inclination of the system[2], we

[2]that is, the angle between the rotation axis and the line of sight

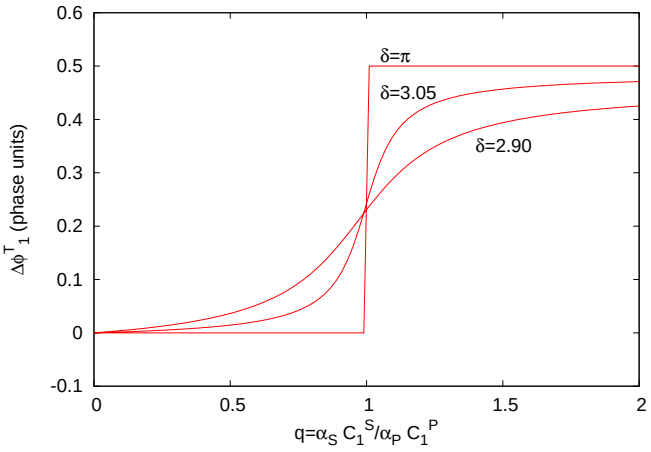

Figure 6.2: Variations of the first harmonic pulse phase (in phase units) vs the relative strength between the two signal, q, the overall profile is composed of. Cases relative to different offsets, $\delta = \Delta\phi_1^P - \Delta\phi_1^S = \pi, 3.05, 2.90$, are shown. The sharp variation of 0.5 in phase units, that is obtained when the two signals are perfectly in anti-phase ($\delta = \pi$), becomes less steep when the anti-phase condition is removed.

have that in a flat environment only one spot is visible for $(\theta + i) < 90°$. In the other cases both spots are visible, but only for a limited range of phases. The star gravity nevertheless creates a curvature that allows an observer to see also otherwise hidden regions. Following Beloborodov (2002) we therefore have four visibility classes (see Fig. 6.1): in class I only one spot is always visible while the other is hidden; in class II, while the primary is still always visible, the secondary also gives a contribution for a certain range of phases; in class III both spots are visible for a limited amount of time, while in class IV both are always visible. The range of values of i and θ covered by these regions is determined by the compactness of the NS, $u = 2GM/Rc^2$.

With these properties in mind, we base our model on the most general assumption that the emission from each polar cap can be described as a periodic signal with period equal to the NS spin period, and with an harmonic content which can in principle be arbitrarily high[3]. In our model the two hot spots do not move at all (as it is nevertheless possible for the reasons envisaged in the previous section). Since the flux from each polar cap is a signal with period equal to the spin period of the NS, it can be described, without any generality loss, via its Fourier series:

$$F^{(k)}(\phi) \propto \alpha^{(k)}\dot{M}\left\{C_0^{(k)} + \sum_{n=1} C_n^{(k)} \cos[n(\phi^{(k)} - \Delta\phi_n^{(k)})]\right\}. \qquad (6.1)$$

Here $k = p, s$ refers to the primary and secondary spot that build the signal, α^k is the fraction of the total accretion rate which is effectively channelled to the k-th spot, n denotes the particular harmonic, ϕ^k is the rotational phase of the k-th spot ($\phi^p = 2\pi\nu t$, $\phi^s = \phi^p + \pi$), and $\Delta\phi_n^{(k)}$ is the proper phase constant of the

[3]We nevertheless know that two harmonics are enough to describe the observed pulse profiles from AMSP, and the discussion is therefore limited to these components.

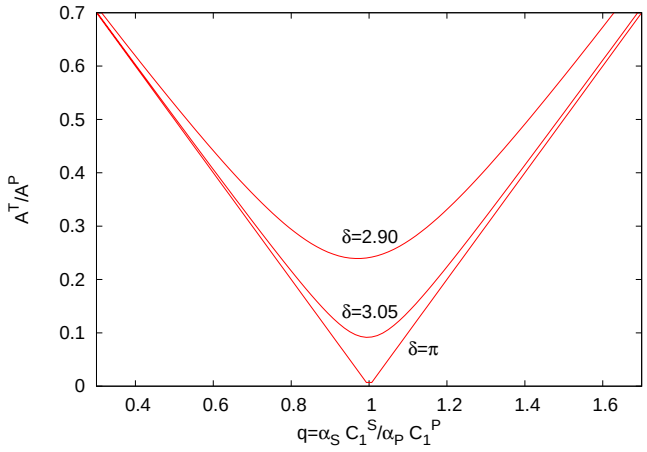

Figure 6.3: Variations of the amplitude of the pulse (in units of the amplitude of the primary signal) vs the relative strength between the two signal, q, the overall profile is composed of. Cases relative to different offsets, $\delta = \Delta\phi_1^P - \Delta\phi_1^S = \pi, 3.05, 2.90$, are shown. When the two signals are perfectly in anti-phase ($\delta = \pi$), the amplitude of the overall profile becomes null if they have the same strength.

n-th harmonic[4]. All the relativity effects described above are taken into account by the coefficients of the Fourier decomposition $(C_n^{(k)}, \Delta\phi_n^{(k)})$, the derivation of which is given by Poutanen and Beloborodov (2006) in terms of the angles i and θ, the compactness parameter M/R, the spin frequency of the NS ν, and a parameter h that allows for the spot emission to be anisotropic. The possibility that a spot is not visible for all the rotational phases is already incorporated in the evaluation of these coefficients.

The total pulse profile is given by the sum, $F^T(\phi) = F^P(\phi) + F^S(\phi)$. It is obviously still a periodic function over the spin period, and thanks to the Fourier theorem it can be expanded in a series expansion similarly to Eq. [6.1]. After simple trigonometric algebra, it can be shown that the amplitudes and the phases of the total pulse profile harmonics can be expressed in terms of those that define the single profiles, as:

$$[C_n^T]^2 = [\alpha^P C_n^P]^2 + [\alpha^S C_n^S]^2 + 2\alpha^P \alpha^S C_n^P C_n^S \cos[\Delta\phi_n^P - \Delta\phi_n^S] \qquad (6.2)$$

$$\tan[n\Delta\phi_n^T] = \frac{C_n^P \sin(n\Delta\phi_n^P) + qC_n^S \sin(n\Delta\phi_n^S)}{C_n^P \cos(n\Delta\phi_n^P) + qC_n^S \cos(n\Delta\phi_n^S)} \qquad (6.3)$$

where in the latter we have defined $q = \alpha_S/\alpha_P$, the ratio between the mass accreted on each spot. It can be easily shown that the derivative of the n-th harmonic total pulse profile phase with respect to q can take fairly large values, depending essentially on the harmonic considered and on the offset $\delta_n = \Delta\phi_n^P - \Delta\phi_n^S$.

This can be understood if it is considered that the each harmonic of the total profile is built by two sinusoidal signal. We first consider the fundamental.

[4]This notation is used here for easier handling with respect to the one defined in Sec 2.2.3). The phase constant defined in (2.13) is equal to $\Delta\phi_n^{(k)} - \pi/2$, thus introducing no loss of generality.

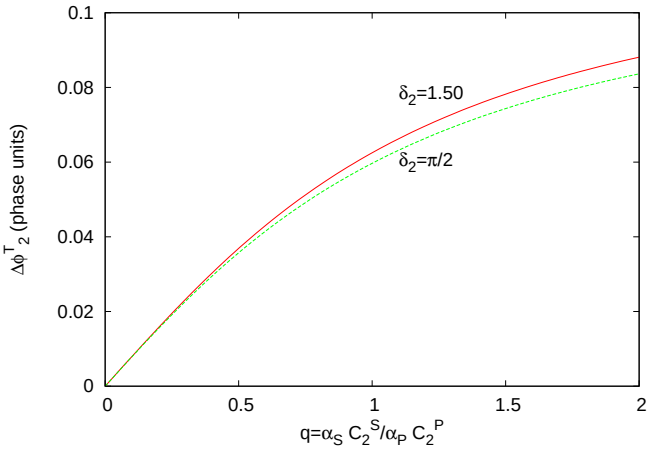

Figure 6.4: Variations of the first harmonic pulse phase (in phase units) vs the relative strength between the two signal, q, the overall profile is composed of. Cases relative to different offsets, $\delta = \Delta\phi_1^P - \Delta\phi_1^S = \pi, 3.05, 2.90$, are shown. The sharp variation of 0.5 in phase units, that is obtained when the two signals are perfectly in anti-phase ($\delta = \pi$), becomes less steep when the anti-phase condition is removed.

In the case of a perfect anti-phase between the two signals ($\delta_1 = \pi$), the total profile depends crucially on the ratio between the amplitudes of the two signals that it is composed of. If these are equal the total profile is washed out (i.e. constant profile), while, as soon as one amplitude exceeds the other, the total profile essentially reflects the dominating profile. In this limiting situation, the phase of the total profile can vary by π responding to slight variations of q from $q < 1$ to $q > 1$, and vice versa. If the two signals are not in perfect anti-phase, the variation of the amplitude and of the phase of the total profile is much smoother; there is no value of the offset δ_1 for which the total profile is washed out, but its phase can still vary significantly with q. To show this properties, we plot in Fig. 6.2 and Fig. 6.3 the phase and the amplitude of the total profile first harmonic as a function of q, respectively[5].

It is thus clear how a change of the relative strength of the two spots can lead to significant variations of the observed phase of the fundamental harmonic. This is particularly true if $q \sim 1$, that is both spots contribute significantly to the total profile. The misalignment angle between the magnetic and rotation axes, θ, is thought to be small in AMSP ($\lesssim 20°$), as the observed profile amplitudes are small ($\lesssim 0.1$, Poutanen and Beloborodov, 2006). By inspection of Fig. 6.1 it is clear that both spots are important in making the total pulse profile only at large inclinations ($i \gtrsim 45°$), while for lower values of i only one spot is visible, and phase shifts can no longer be explained with our model.

Another outcome that naturally turns out from this model is that the second harmonic phase will be intrinsically more stable than those computed on the fundamental. In the case of the second harmonic in fact, the interference between the two polar caps is constructive. As it can be seen in Fig. 6.4, the

[5]Here q is defined $q = \alpha_S C_1^S / \alpha_P C_1^P$ for sake of simplicity, as the plot serves only as a qualitative indication of how the phase of the total profile depends critically on the relative strength of the signals which is made of.

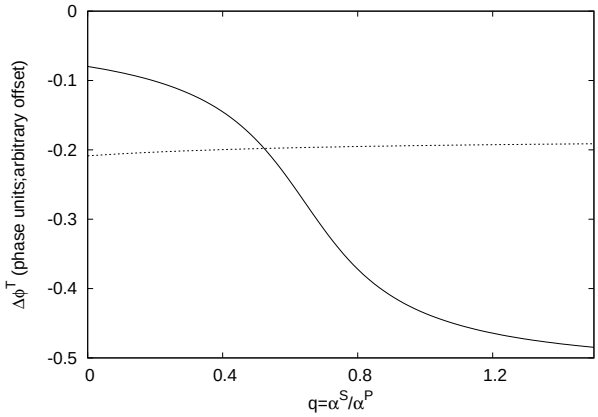

Figure 6.5: Phases (in units of period) of the fundamental frequency (solid line) and the second harmonic (dashed line) as a function of the ratio, q, between the mass accreted by the two spots, in the case $\nu = 314.0$ Hz, $u = 0.3$, $h = 0.6$, $i = 79^\circ$ and $\theta = 12^\circ$ (see text).

second harmonic phase is in fact much less affected by variations of q (note how the y–scale is compressed with respect to Fig. 6.2) . This is essentially because the offset δ_2 in the case of roughly antipodal spots is $\sim \pi/2$ rather than π (as it was the case for the fundamental harmonic). This follows from the fact that the second harmonic has, by definition, a period that is half the one of the NS.

It is thus clear that such a model can explain a phenomenology like the one showed by SAX J1808.4–3658 during its 2002 outburst, that is a sudden change of the fundamental phase which is not present in the second harmonic phases. Only small variations of q are needed to produce this shift, and such small variations are perfectly understandable in the framework of accretion onto a magnetized NS.

We tested our model on the phase evolution showed by XTE J1814–338 also (Papitto et al., 2008). This time we considered the analytical expressions derived by Poutanen and Beloborodov (2006) to give an estimate of the coefficients $(C_n^k, \Delta\phi_n^{(k)})$, which in turn are used to define those of the total profile with the use of relations [6.2] and [6.3]. This is done because the latter can be fixed from what is observed from the source; the peak fractional amplitudes of the observed profile are indeed 0.16 and $\simeq$ 0.5–0.3 for the fundamental and the second harmonic, respectively. A configuration that reproduces the observed amplitudes, and the observed roughly constant phase difference between the fundamental and the second harmonic, $\Delta\phi_1^T - \Delta\phi_2^T$, is found when the parameters $\nu = 314$ Hz, $u = 2GM/(Rc^2) = 0.3$, $h = -0.6$, $i = 79^\circ$ and $\theta = 12^\circ$ are used to calculate the coefficients $(C_n^k, \Delta\phi_n^{(k)})$. Using these parameters we can therefore follow the dependence of the first and second harmonic phases on $q = \alpha_S/\alpha_P$ (see Fig. 6.5), when a physically plausible model for the profile construction is argued. The obtained results show how, despite that this simple model has the promising ability to reproduce the phase and amplitude behaviour of the fundamental only by arguing that the ratio between the mass accreted on each spot varies by a little amount, it fails when the second harmonic behaviour is taken

into consideration. Contrary to what happens in SAX J1808.4–3658, the second harmonic of XTE J1814–338 follows in fact the behaviour of the fundamental, that is the shape of the profile does not vary, but is only drifted cyclically. To successfully apply this model to the case observed in XTE J1814–338 one should hypothesize a different mechanism to produce the second harmonic, leading to different values for the phases than the ones predicted by model of Poutanen and Beloborodov (2006) (according to which, we recall, a second harmonic in the signal of each hotspot is determined by fast rotation and anisotropy of the emitted radiation).

The model considered here, even if still under development, seems therefore able to reproduce the enhanced stability of the second harmonic phases often observed in AMSP (the case of SAX J1808.4–3658 and to some extent that of XTE J1807–294), while fails when both the harmonics show drifting phases. It is nevertheless well possible that also the hotspots motion discussed in Sec. 6.1 has a considerable influence in the determination of the phase behaviour, and this represents indeed the most probable explanation proposed so far (see e.g. Watts et al., 2008, also).

7

The inner disc radius of SAX J1808.4–3658

We report in this chapter on a 63-ks long *XMM-Newton* observation of the AMSP SAX J1808.4–3658 during its latest X-ray outburst which started on September 21st 2008 (Papitto et al., 2009). The mechanisms producing the spectral continuum generally observed from AMSP are first discussed. We then show how we detected a highly significant emission line in the energy band where the iron K-α line is expected, and which we identify as emission from neutral (or mildly ionized) iron. The line profile appears to be quite broad (more than 1 keV FWHM) and asymmetric; the most probable explanation for this profile is Doppler and relativistic broadening from the inner accretion disc. Fitting this profile with a model in which the line is produced by reflection of the hard component in these regions, we measure the size of the inner disc radius as $18.0^{+7.6}_{-5.6}$ km for a 1.4 $M_{\odot}$ neutron star. This is the first time that such a measure can be made for a fast rotating pulsar, and confirms the basic elements of the theory for fast accreting pulsars. The inner disc rim is in fact truncated inside the corotation radius (31 km for SAX J1808.4–3658) in agreement with the fact that the source was still showing pulsations during the XMM-Newton observation.

7.1 The spectra of AMSP

The X-ray spectra exhibited by AMSP during outbursts, and observed mainly by *XMM-Newton* (0.5–11.0 keV) and *RXTE* (2.5–150.0 keV), are reviewed by Poutanen (2006, see also references therein) . The observed continuum spectra are always composed by three components: two soft components with temperatures below one KeV, and a hard power-law like tail extending up to $\sim$ 100 keV. When observations from an instrument sensible to low energies are available (e.g. *XMM-Newton*), the soft components can be generally disentangled. The colder (kT$\sim$ 0.2–0.4 keV) is interpreted as the emission coming from the inner regions of the accretion disc. As it was recalled in Sec. 1.4.2, the spectrum of an optically thick accretion disc is a superimposition of several black body components, each with a temperature value dependent on the radius of the disc where it is emitted from ($T_d(r) \propto r^{-3/4}$). The energy at which the overall spectrum is cut-off reflects the inner regions of the disc, and it happens that for discs extending down to the NS surroundings the cut–off temperature is at

energies detectable by current X-ray telescopes like *XMM-Newton* and *Chandra* (see Gierliński and Poutanen, 2005; Falanga et al., 2005). The other soft component is indeed thought to originate from the NS surface, and probably from only a fraction of it (the hotspots), as its normalization is observed in the range 30–100 km^2, and is modulated at the spin period of the pulsar (while the disc components does not, as it is expected).

However, the overall flux is dominated by an hard power law tail ($\alpha \sim 1.8$–2.1) that cuts off around ~ 100 keV. This component is best fitted by a Comptonization of soft photons into a hot ($kT_e \sim 20$–60 keV) medium with a mild Thomson optical depth ($\tau \sim 0.7$–2.5). As the Comptonized component pulsates itself, the most probable interpretation is that it arises from the accretion column above each hotspot. At luminosities of few per cent of the Eddington rate, the incoming matter is in fact thought to form a shock above the NS surface (Basko and Sunyaev, 1976); gravitational energy is thus dissipated in the shock and electrons are heated by Coulomb collisions. The hard X-ray photons emitted in the shock partially illuminate the NS surface, which therefore heats, and reprocesses this energy as a soft black body component ($\lesssim 1$ keV). The Comptonization of these soft photons is indeed the main cooling mechanism for the accretion column.

A significant reflection component also appears in the spectrum observed from SAX J1808.4–3658 during its 1998 outburst (Gierliński et al., 2002, GDB, see also Heindl and Smith, 1998 and Gilfanov et al., 1998). A reflected spectrum is produced in an X-ray binary when the inclination is favourable to observe those hard photons that are reflected by the inner regions of the disc. This produces a characteristic hump at $\sim 20 - 30$ keV, and an iron emission line at ~ 6.5 keV, often together with an iron absorption edge at energies $\gtrsim 7.1$ keV. An iron line at energies $\simeq 6.5$ keV was indeed observed from SAX J1808.4–3658 at an equivalent width of $\lesssim 100$ eV. The statistics of those *RXTE* observations was nevertheless too low to obtain significant information on the line shape.

Iron lines are commonly observed from LMXB (containing both NS and black hole candidates), as well as from AGNs, and are usually much broadened (FWHM $\gtrsim$ 1 keV). Their energy is within 6.4–6.7 KeV, reflecting the possible ionization states of the K-α emitting iron. To explain their broadening it was proposed that they originate in the inner regions of the accretion disc, where the large velocities of matter in Keplerian orbit, $v \lesssim c/\sqrt{6}$, determine a Doppler broadening of $\Delta E_K/E_K \simeq \sin i/\sqrt{6}$, which can be of few keV for the energy E_K of a K-α iron line. At such large velocities, relativistic beaming plays a role raising the intensity of the 'bluer' end of the line. Moreover, the space-time of the inner regions of an accretion disc is bent by the gravitational influence of the near compact object; the typical double-peaked symmetric profile due to Doppler effect in a disc is thus also affected by Gravitational red-shift that introduces more asymmetry. Such gravitational broadened iron lines were observed in AGNs (e.g. Nandra et al., 1997), LMXB with black hole candidates (e.g. Miller et al., 2004), and more recently also from NS-LMXB (Di Salvo et al., 2005; Bhattacharyya and Strohmayer, 2007; Cackett et al., 2008). It is obvious that in the case of an accretion disc extending down to the NS surface (or to the last stable orbit in the case of a BH), the measure of the relativistic broadening of the iron line places an upper limit on the radius of the compact object, and therefore is an invaluable probe of the regions surrounding these objects.

Another location proposed for the formation of these lines is the Accretion

Disc Corona (ADC, see e.g. Kallman and White, 1989; Brandt and Matt, 1994). These hot coronae probably form for the evaporation of the inner parts of the accretion disc caused by the illumination from the central object (White and Holt, 1982). In this scenario the line is formed by Comptonization in the ADC, and is broadened by the motion of the hot electrons ($\Delta E_K/E_K \simeq (kT_e/m_ec^2)^{1/2}$, where T_e is the temperature of electrons in the ADC). Nevertheless only direct Comptonization can be responsible for the line broadening, as inverse Compton from electrons hotter than the line temperature destroys the line profile. As a matter of fact, it is easy to calculate that in the case of multiple Compton scatterings, the final photon energy is $E = E_0[1+max(\tau,\tau^2)(4kT_e-E_0)/m_ec^2)$ (e.g. Rybicki and Lightman, 1981). In the case of the 1998 outburst of SAX J1808.4–3658, GDB measured a comptonizing medium with a a temperature $\gtrsim$ 35 keV and an optical depth $\tau = 2.7\pm0.4$. The broadening that would be due to inverse Compton of the line photons by this medium is $\Delta E/E \simeq \tau(4kT_e/m_ec^2) \sim 1$, which would ultimately destroy the line profile. We can therefore safely state that the broadening of an iron line in a source with a hard comptonized component like SAX J1808.4–3658 cannot be interpreted in this way.

The observation of a gravitationally broadened iron line in an accreting pulsar would be of obvious fundamental importance, as it would give constraints on the inner disc radius, R_0, which incorporates the bulk of the physics of accretion around a fast rotator (see Sec. 1.5). Motivated by this, and by the previous observations of an iron line in SAX J1808.4–3658, we obtained a 63 ks *XMM-Newton* Target of Opportunity (ToO) observation of this source (performed in the Director Discretionary Time), during the latest outburst in September 2008.

7.2 Observation and data reduction

SAX J1808.4–3658 was found in outburst on 2008 September 21 by *RXTE* , and since then it has been object of an intensive observational campaign. A preliminary analysis of the 2–10 keV *Swift* XRT publicly available light curve shows that the outburst had its maximum around September 24.

XMM-Newton observed SAX J1808.4–3658 as a ToO observation for 63 ks on 2008 October 1 (start time MJD 54739.99517), roughly one week after the assumed outburst peak. The EPIC-pn camera operated in timing mode, to prevent photon pile-up and to allow an analysis of the coherent and aperiodic timing behaviour of the source. The same observing mode was used for EPIC/MOS2 CCDs, while EPIC/MOS1 was operated in small window mode, and the RGS in spectroscopy mode. A bright external flare in the background is present during the first 2 ks of the observation, so that we excluded this time interval from our analysis.

The high source flux saturated the *XMM-Newton* telemetry rate, so that the *XMM-Newton* Science Operations Centre decided to switch off one of the MOS cameras (MOS2) in order to allocate more band to the EPIC–pn instrument, roughly 35 ks after the beginning of the observation. The EPIC–pn spectrum showed no noticeable difference before and after the MOS-2 turning off, and the whole EPIC–pn data set is therefore considered for our analysis. The MOS spectra were severely affected by pile up, and we did not consider them for our analysis.

Data were extracted and reduced using SAS v.8.0.0. We produced a cali-

brated EPIC–pn event list through the *epproc* pipeline, using the most updated calibration tools (*epfast* tool). We extracted the source spectrum selecting a 13 pixel wide stripe around the source position (RAWX=37) equivalent to 53".3 (which should encircle more than 90% of the energy up to 9 keV [1]), and considered only PATTERN≤4 and FLAG=0 events. The background spectrum was extracted in the RAWX=4–15 and RAWY=2–198 CCD region.

The EPIC–pn energy channels were grouped with a compression factor of three so as not to oversample the instrument energy resolution. The count rate observed in the EPIC–pn CCD showed a slight increase during the observation from $\sim$ 700 c/s, at the beginning of the observation, to 780 c/s at the end of the observation.

RGS data were processed using the *rsgproc* pipeline to produce calibrated event lists, first and second order spectra and response matrices. The net count rates observed by the RGS1 and RGS2 in their first order, which are the only considered here, are 17.8 c/s and 20.0 c/s respectively. RGS spectra were binned in order to have at least 25 counts/bin.

To have a benchmark of the pn response, we also analysed, using the standard pipelines, a 1.1 ks Swift XRT observation taken in window timing mode (ObsId 00030034033), which started on MJD 54740.60118, and is therefore simultaneous with the XMM-Newton pointing. The X-ray spectral package we use to model the observed emission is HEASARC *XSPEC* v.12.4.

7.3 Spectral analysis and results

In our spectral analysis, we first considered the combined spectrum of the RGS 1-2 (0.6–2.0 keV) and of the EPIC-pn (2.0–11.0 keV) data. The choice of the lower bound of the RGS is due to the presence of several calibration residuals at $\sim$ 0.5 keV we chose not to model. The model we first focused on is composed of a multi temperature disc emission (`diskbb`) and a power law. We model the effect of the interstellar photoelectric absorption using the `phabs` component. The addition of another (single temperature) soft component is strongly required by the data, as the chi squared improves by $\Delta\chi^2 = 1104$ with the addition of just two parameters for 3156 degrees of freedom (d.o.f.). An edge at 0.871 keV, identified with O VIII absorption, is present in the RGS data at a high significance ($\Delta\chi^2 = 160$ for the addition of 1 parameter). A line at 6.5 keV also clearly emerges in the residuals (see Fig. 7.1), at the energy of Kα fluorescent emission of neutral or mildly ionized iron. We obtain a $\Delta\chi^2 = 399$ for the addition of 3 parameters when we include a Gaussian to fit this component. The line is indeed very broad, as we obtain $\sigma = 1.1 \pm 0.2$ keV. This broadness, together with the apparent asymmetric profile, led us to consider a model in which the iron emission is shifted by relativistic motion near the NS. We therefore found that a `diskline` model (Fabian et al., 1989) fits this feature well, giving an inner disc radius consistent with the range expected from accretion theories onto a pulsar ($6 - 15$ R_g in the case of SAX J1808.4–3658, see discussion). This model, together with residuals, is plotted in Fig. 7.2 and the obtained best fit parameters are listed in the middle column of Table 7.1.

[1] see *XMM-Newton* Users handbook, issue 2.6, available at http://xmm.esac.esa.int/external/xmm_user_support/.

Table 7.1: Fitting parameters of the 0.6-11.0 keV combined RGS + EPIC–pn spectrum (centre) and of the 1.4–11.0 keV EPIC–pn spectrum (right) of SAX J1808.4–3658. The continuum was modelled by a `diskbb` (DBB), a `bbodyrad` (BB) and a power law (PL). Errors on each parameter are quoted at the 90% confidence level, as for the rest of the paper.

Parameter	0.6–11.0 keV	1.4–11.0 keV
nH (10^{22} cm^{-2})[a]	$0.214^{+0.002}_{-0.003}$	$0.214^{+0.002}_{-0.003}$
kT$_{in}$ (keV)	$0.184^{+0.004}_{-0.002}$	0.24 ± 0.01
N$_{DBB}$ ($\times 10^3$)	$36.7^{+8.2}_{-8.0}$	$15.1^{+2.7}_{-2.2}$)
kT$_{BB}$ (keV)	0.36 ± 0.01	0.40 ± 0.02
R$_{BB}$ ($d_{3.5}$ km)	$9.4^{+0.4}_{-0.3}$	$6.8^{+1.0}_{-0.9}$
α	$2.079^{+0.006}_{-0.008}$	$2.078^{+0.007}_{-0.008}$
Edge E (keV)	0.871 (frozen)	
τ O VIII ($\times 10^{-2}$)	$4.6^{+0.5}_{-0.6}$	
LineE (keV)	$6.47^{+0.07}_{-0.08}$	$6.43^{+0.07}_{-0.09}$
Betor	$-2.2^{+0.2}_{-0.3}$	$-2.3^{+0.3}_{-0.2}$
R$_{in}$ (GM/c^2)	$6.0^{+6.0}$	$8.7^{+3.7}_{-2.7}$
R$_{out}$ (GM/c^2)	210^{+150}_{-70}	207^{+111}_{-80}
i (°)	> 58	> 67
N_{K_α} ($\times 10^{-4}$)	7.2 ± 0.9	$7.2^{+0.9}_{-0.7}$
EW (eV)	123^{+29}_{-31}	121^{+20}_{-16}
F$_{2-10}$ (erg/cm^2/s)[b]	$7.58(1) \times 10^{-10}$	$7.57(3) \times 10^{-10}$
F$_{bol}$ (erg/cm^2/s)[c]	4.9×10^{-9}	4.5×10^{-9}
χ^2_{red}	4293.8/3154	809.9/639

[a]The absorption column in the EPIC-pn spectrum was varied in the range indicated by the RGS–EPIC-pn spectrum.
[b]Absorbed flux in the 2.0–10.0 keV band
[c]Unabsorbed flux extrapolated to the 0.05–150 keV band

The final chi squared of the fit in the 0.6–11.0 keV is still quite large and this is due to the presence of several features, especially in the RGS data, which are probably of calibration origin (e.g. at 0.7 and 0.85 keV, see residuals of Fig. 7.2), and which we choose not to fit. Considering that the main goal of the observation was the study of the iron $K\alpha$ line, in order to check the stability of the obtained model, and to prevent spurious effects from a possible wrong cross-calibration between the instruments, we also analysed the EPIC-pn dataset alone, in a bandwidth extending to the lowest energy allowed. We are forced to limit the energy range to the 1.4–11.0 keV band, as below large residuals ($> 6\sigma$) appear with respect to any reasonable continuum model, as we could check with a simultaneous fit with the *Swift* XRT dataset. We fit two evident absorption features at 1.8 and 2.2 keV, which are probably of instrumental origin as they lie near the Si K and Au M edges, which are known to influence the effective area determination if incorrectly calibrated. However, we take advantage of the low energy spectral information given by the RGS data, by taking the absorption column to vary in the range determined by the best fit in the whole RGS/pn energy range. A quick glance at Table 7.1 confirms how the best fit parameters do not change significantly fitting the pn alone. This is especially true for the hard power-law component and the iron emission line parameters, which are

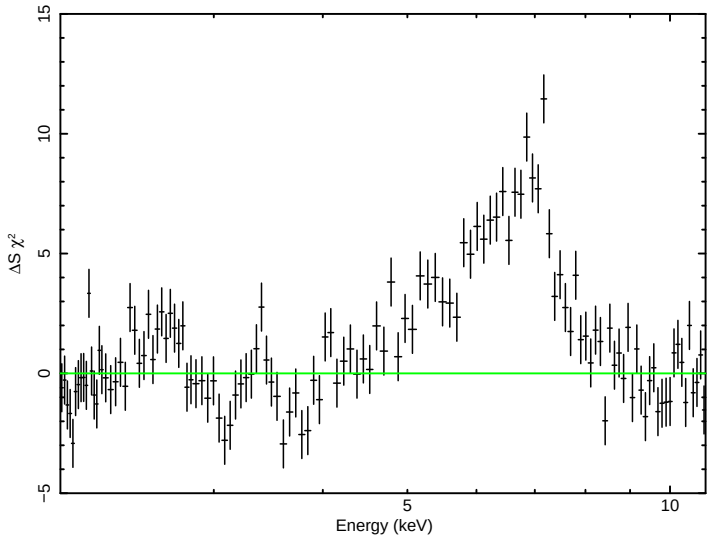

Figure 7.1: Residuals, in units of σ, of the 1.4–11.0 keV EPIC-pn spectrum, with respect to the best fit continuum model (right column of Table 7.1) when the iron line is not included in the fit.

indeed perfectly consistent with those obtained from the fit in the 0.6–11 keV band.

We note that the `diskline` model gives a slightly better fit for the Kα than a symmetric Gaussian profile, with an improvement of $\Delta\chi^2 = 13$ for the addition of three parameters (over 588 d.o.f.) with respect to the Gaussian modelling. Together with the evident difficulties in explaining the observed broadening of this feature with alternative models (see discussion), this definitely leads us to interpret the line profile as being produced in the inner regions of the accretion disc. To be conservative we discuss our results in the light of both the best fits presented in Table 1, which we remark differ significantly only for the soft components, which themselves are less constrained by the EPIC–pn alone.

To obtain an estimate of the unabsorbed bolometric flux we extrapolate the model of Table 7.1 to the 0.05–150 keV band. We are confident about our estimate, as values of $\alpha \simeq 2$ are easily observed in SAX J1808.4–3658 (Gilfanov et al. 1998). We finally remark that the 2–10 keV flux estimate we obtain is in good accord with the one that can be derived by fitting our model to the *Swift* XRT spectrum ($F_{XRT}(2-10) = (7.8 \pm 0.2) \times 10^{-10}$ erg cm^{-2} s^{-1}).

Once the orbital motion is corrected (Patruno et al., 2008), the well known coherent pulsation is easily detected in the pn data at a frequency $\nu = 400.9752102$ Hz, consistent with the 2005 value (H08). The power spectrum at frequencies lower than 300 Hz is presented in Fig. 7.3, and is in line with the typical power spectra observed for this source (see e.g. van Straaten et al., 2003). Three Lorentzians, with central frequencies of 0.92(5) Hz, 1.56(18) Hz, and 34.7(6) Hz, respectively, are used to model the timing features we observe. The first two (labelled A and B in the figure) describe the broad bump already observed below 10 Hz during other outbursts of this source. The third Lorentzian, labelled C, could be tentatively identified with the component observed during

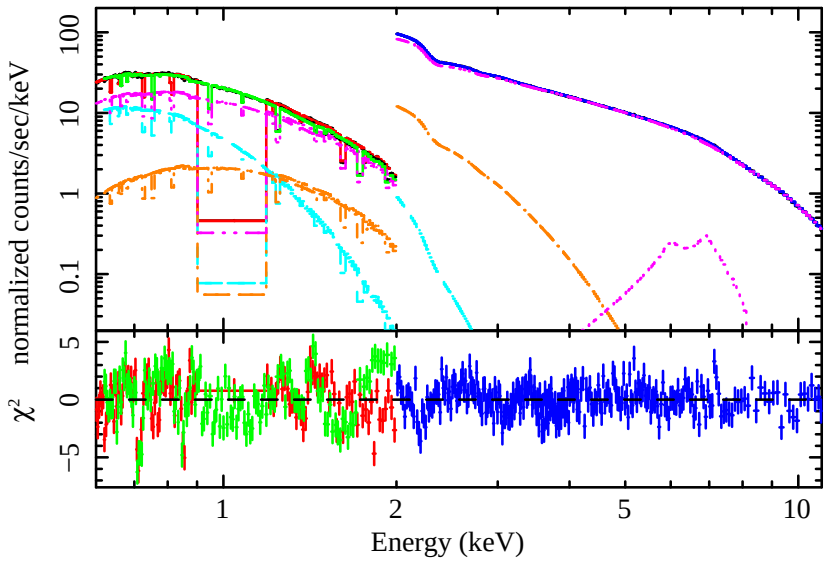

Figure 7.2: 0.6 − 11.0 keV *XMM-Newton* combined RGS+EPIC-pn spectrum of SAX J1808.4–3658 (top) and residuals, in units of σ, with respect to the best fit model given in the central column of Table 7.1. Blue refers to the EPIC-pn, red to RGS1 and green to RGS2 data and residuals. The model components are also plotted: the power law as a magenta solid line, `diskbb` as a light blue dashed line, `bbodyrad` as an orange dash-dotted line and the Kα `diskline` component as a dotted magenta line.

the 2002 outburst by van Straaten et al. (2005), who named it L_h.

7.4 Discussion

The spectrum of the AMSP SAX J1808.4–3658 observed by *XMM-Newton* is of extremely good quality. For the first time this opens the possibility of exploiting its high sensitivity and spectral resolution capabilities to study the innermost regions of the accretion disc around a rapidly rotating pulsar. The estimate of the inner disc radius we obtain from the broadening of the iron Kα fluorescent line is invaluable to test the theories of accretion onto a fast object. This can be used to constrain the truncation disc radius, which is expected to lie within the centrifugal boundary represented by the corotation radius, as indicated by the presence of pulsations at the known 401 Hz frequency in the *XMM-Newton* light curve. Moreover it will be useful for an estimate of the lever arm of the torque exerted on the NS because of accretion, when a timing solution covering the whole outburst will be available.

Despite that the measured asymmetry of the iron line does not exclude a Gaussian profile on a statistical basis, we propose an interpretation of its large broadening in terms of the relativistic motion of the reflecting material in the space-time bent by the gravitational influence of the NS. Disc reflection in fact seems the only viable option to explain the large broadening and the low ionization state measured for the emitting material, in a source whose broadband spectrum is dominated by a hard (high temperature, low optical depth) Comp-

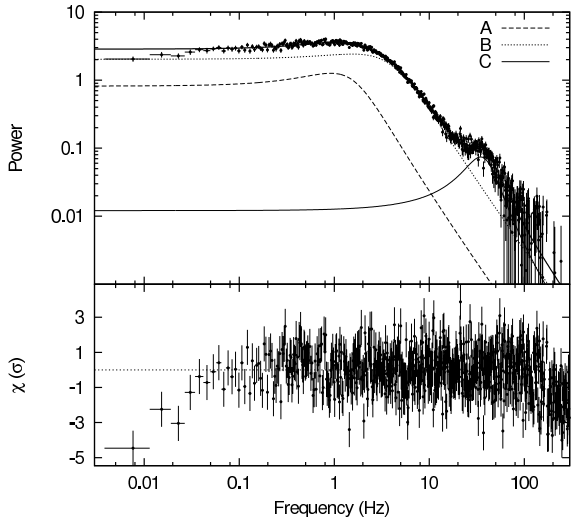

Figure 7.3: (Top panel) White-noise subtracted PSD of the 63 ks *XMM-Newton* observation of SAX J1808.4–3658. The time series was sampled at 125 μs corresponding to a Nyquist frequency of 4000 Hz. The PSD was obtained averaging about 500 power spectra of 2×10^{20} temporal bins ($\simeq$ 133 s) each. The white-noise (1.97423(25)) was estimated by fitting the spectrum between 2 and 3 kHz with a constant. The spectrum was logarithmically re-binned using a factor 1.01. Spurious frequencies related to the 167 Hz instrumental signal (see Juett and Chakrabarty, 2003) were removed from the spectrum. The three components labelled as A, B and C are the Lorentzians used to fit the spectrum. (Bottom panel) Residuals in units of σ.

tonized component (GDB).

For X-ray pulsars, the inner disc radius, R_d, has to meet some observational constraints implied by the presence of pulsations. R_d must be larger than the NS surface, $R_* \simeq 10$ km depending on the equation of state, and not much larger than the corotation radius, defined as the point where the magnetosphere rotation equals that of an assumed Keplerian disc, $R_c = (GMP^2/4\pi^2)^{1/3} = 31 m_{1.4}^{1/3}$ km for SAX J1808.4–3658, where $m_{1.4}$ is the NS mass in units of 1.4 $M_\odot$. If not met, the latter condition implies that the magnetic field is not able to capture matter because it spins more rapidly than the disc, therefore resulting in a centrifugal barrier. Theoretical understanding and 3D MHD simulations (Riggio et al. (2008) and references therein) showed how the corotation condition is not to be taken strictly, as the magnetic field is able to release enough angular momentum to the disc to make it leap over the centrifugal barrier. In any case an inner disc radius well beyond the corotation radius would imply an efficient propeller ejection of matter, which seems not to be the case for SAX J1808.4–3658 (which is observed to show pulsations during this observation, and therefore to accrete matter onto the magnetic poles).

The estimate we made for the inner disc radius from the iron line broadening is $R_{in} = 18.0^{+7.6}_{-5.6}$ $m_{1.4}$ km. While the lower bound essentially overlaps the NS radius, the upper limit we give at a 90% confidence level as $R_{in} < 25.6$ $m_{1.4}$ km is in agreement with the expectation that the inner disc radius is inside the corotation boundary. Also in the case of a more massive 2.0 $M_\odot$ NS, our upper

limit is still of the order of R_c, $R_{in}^{(2.0)}/R_c^{(2.0)} < 1.05$. This measurement thus well fits in the small zone available for a fast rotating NS to efficiently accrete matter.

The line modelling holds if we consider both the broader 0.6–11.0 keV RGS+EPIC–pn spectrum and the restricted 1.4–11 keV bandwidth. The spectral information in the former is nevertheless fundamental to constrain the absorption column to SAX J1808.4–3658. The value we obtain is significantly larger than the average Galactic value (0.13×10^{-22} cm^{-2}). This could in principle indicate the presence of additional neutral in the proximity of the source, possibly revealing mass lost from the system during the Roche Lobe overflow (Di Salvo et al., 2008a). The presence of an evident O VIII edge in the RGS data also indicates the presence of ionized absorbing matter along the line of sight.

The measured continuum is in good agreement with the expectations for these kinds of sources (GDB,(Gierliński and Poutanen, 2005)). We clearly detect two soft components, interpreted as coming from the accretion disc and from the NS surface (or a good fraction of it), as well as a dominant hard component, which is well described by a simple power-law in the XMM-Newton energy band. To derive the bolometric X-ray luminosity, we use our estimate of the 0.05–150.0 keV bolometric flux (see Table 7.1), and obtain $L_X = 6.6 \times 10^{36}$ d$_{3.5}^2$, where d$_{3.5}$ is the distance to the source in units of 3.5 kpc (Galloway and Cumming, 2006). This estimate is in line with the bolometric flux measured for previous outbursts of this source (see e.g. Hartman et al. (2008)). In the hypothesis the X-ray luminosity well tracks the mass accretion rate onto the NS, we obtain a mass accretion rate of $\dot{M} \simeq 5.6 \times 10^{-10}$ d$_{3.5}^2$ R$_6$ m$_{1.4}^{-1}$ M$_\odot$/yr at this stage of the outburst, an estimate however affected by the uncertainties implied by its derivation from a tighter bandwidth spectrum.

The parameters measured for the soft components (see Table 7.1) can be used to obtain further constraints on the geometry of the emitting regions. The normalization of the multi temperature accretion disc black body (`diskbb`), N_{DBB}, can be used to obtain an estimate of the apparent inner radius $r_{in} = 0.35\sqrt{N_{DBB}/\cos i}$ d$_{3.5}$ km, which is indeed of the order of R_{in} (see e.g. Kubota et al. (1998)). In our case we obtain different values from the fit in the two considered spectral bands, $r_{in} \simeq$40–70 $\cos^{-1/2} i$ km, and large uncertainties are still present in the value of the inclination angle i of the system ($i \gtrsim 60°$ as derived from the diskline fit). Despite still being affected by large uncertainties, the range of values we derive for the inner disc radius from the `diskbb` component is still quite reasonable, and in agreement with the measure derived from the line fitting. Note, however, that if we take as a best fit value the one obtained from the `diskbb` component fitted over the whole range, the inner disc radius we derive in this way appears to be larger than the value obtained from the iron line. This would probably indicate that the innermost part of the disc may be embedded in the Comptonizing region, where the hard X-ray spectrum, which is reflected by the disc (producing the observed iron line profile), originates. This would explain both the large equivalent width observed for the iron line and the relatively large inner radius obtained from the soft component, since the innermost part of this component is very efficiently Comptonized and not directly observed.

The single temperature black body component we detect with a high statis-

tical significance in our spectral fits most probably comes from the NS surface (or a good fraction of it) as indicated by the radius of the black body emitting region which is $6 - 10$ km (for a distance to the source of 3.5 kpc, see Table 1), in line with the expectations of a hotspot origin.

Thus, in this chapter we have reported the results obtained from very high quality *XMM-Newton* spectra. Although some systematic features are still present in these spectra (due to the high statistics), the best fit model is stable and the best fit parameters do not dramatically depend on the energy band (or instrument) in which the spectral fit is performed. The most important result we report here concerns the observation of a broad emission line at ~ 6.5 keV. The most probable interpretation of this feature is reflection of the hard Comptonization spectrum in the innermost accretion disc. The inner disc radius derived in this way confirms the expectation that the accretion disc is truncated inside the corotation radius. This is the first time such an estimate can be made for a fast rotating X-ray pulsar, and confirms the basic elements of theories of accretion onto these objects.

8

The orbit of SAX J1808.4–3658

The theory for the orbital evolution of a short period LMXB (see Sec. 1.4.4) has a important test-bed in the transient pulsar SAX J1808.4–3658. This source is particularly suited for such considerations, as it is the only AMSP which showed five outburst in the *RXTE* era, and the presence of pulsations can be used to infer the evolution of the orbital period over a 10 yr time line. A timing analysis on these outbursts reveals how the system is expanding at a rate of $\dot{P}_{orb} = (3.40 \pm 0.18) \times 10^{-12}$. This positive derivative suggests a degenerate or fully convective companion for SAX J1808.4–3658, but is nevertheless too large to be explained by a conservative mass transfer. We therefore propose that a non conservative transfer controls the orbital evolution, with the source that actively loses mass from the inner Lagrangian point during quiescence. This opens the possibility that the evolution of this object is somewhat related to the population of Black Widow pulsars, objects which are observed to efficiently eject the matter transferred by the companion. The issues described in this chapter are included in Di Salvo et al. (2008a) and Burderi et al. (2009).

8.1 The observed evolution

As it is clear from Sec. 2.2.5, the application of timing techniques not only allows to observe the rotational behaviour of a pulsar, but it also yields an orbital solution for the system, in terms of a set of orbital parameters; the semi-major axis of the NS orbit, $a_1 \sin i$, the orbital period, P_{orb}, the epoch of passage of the NS at the ascending node, T^*, and of the eccentricity of the system, e. If the source of interest has recurred more than once since its discovery, a solution can be found for each outburst, thus allowing the study of how the orbital parameters evolve with time. SAX J1808.4–3658 is the only AMSP satisfying this requirement, as it was observed in outburst five times since 1998.

To obtain an orbital solution for each outburst, we considered *RXTE* observations taken during 1998, 2000, 2002 and 2005 outbursts, and a 62 ks long *XMM-Newton* observation taken during the latest episode of activity, which began on 2008 September 24 (see Ch. 7 for further details). We epoch folded the available light curves over 720 s long intervals (1/10 of the orbital period), around the spin frequency $\nu_F = 400.975210308$ Hz. The choice of the time interval length is such to meet the constraint defined in (2.28), as a longer interval would introduce a broadening in the obtained pulse profiles due to the Doppler effect induced by the orbital motion. The folding frequency was kept constant

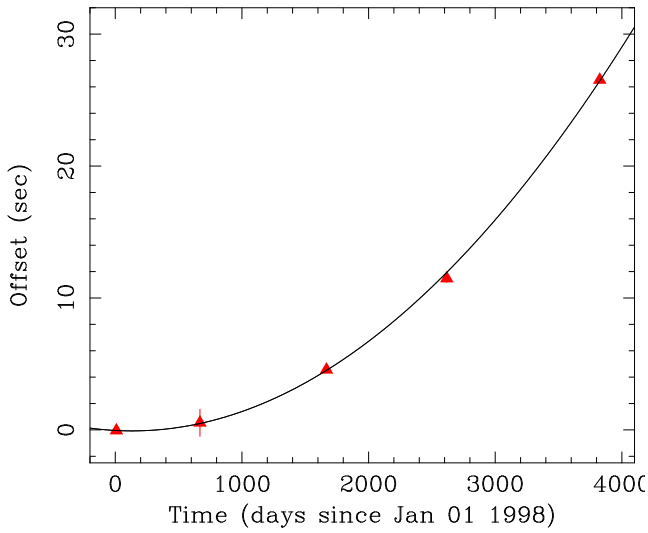

Figure 8.1: Triangles are the offsets, $\Delta T = T_N - T_0$, measured for the five outbursts exhibited by SAX J1808.4–3658. The solid line is the best fit evolution tracks according to Eq. [8.1]. All the times are computed with respect to the beginning of the 1998 outburst, $T_0 = MJD50914.8099$

for all the outbursts. In fact, the determination of the pulse phases is insensitive to the exact value of the period chosen to fold the light curves providing that this value is not very far from the true spin period of the pulsar. Note that Hartman et al. (2008) have measured a secular derivative of the spin frequency in SAX J1808.4–3658, that is $\dot{\nu} = (-5.6 \pm 2.0) \times 10^{-16}$ Hz/s. This is a quite small value, and they do not find evidence of variations of the spin frequency during a single outburst. In order to choose a value of the spin frequency as close as possible to the true one, we used the value above, that is in between the best-fitting spin frequency reported by Chakrabarty and Morgan (1998) for the 1998 outburst and the best-fitting spin frequency reported by Burderi et al. (2006) for the 2002 outburst (see Sec. 5.2). The profiles were modelled with two sinusoids, and the phases computed on the fundamental were considered, as they have the best statistics.

We then looked for differential corrections to the adopted orbital parameters, which can be done by fitting the pulse phases as a function of time for each outburst (see Eq.[2.31]). In general, any residual orbital modulation is superimposed to a long-term variation of the phases, for example, caused by a variation of the spin. However, as it is noted in Sec. 5.2 for the 2002 outburst, SAX J1808.4–3658 shows a very complex behaviour of the pulse phase evolution with time. Phase shifts probably caused by variations of the pulse shape are indeed present, and their modelization is rather tricky (see Ch. 6 for a discussion of this effect). To avoid any fitting of this complex long-term variation of the phases, we preferred to restrict the fit of the differential corrections to the orbital parameters to intervals in which the long-term variation and/or shifts of phases are negligible. We therefore considered consecutive intervals with a duration of at least four orbital periods (depending on the statistics), and fit-

Table 8.1: Best fitting orbital parameters for SAX J1808.4–3658

Parameter	Value[a]
T_0^* (d)	50914.79452952(85)
P_{orb} (s)	7249.156444(23)
$\dot{P_{orb}}$ (s s^{-1})	$3.89(15) \times 10^{-12}$
$a_1 \sin i$ (lt-ms)	62.8106(20)[b]
e	$< 1.2 \times 10^{-4}$
χ^2 / d.o.f.	3.1/2

[a]The reference time at which the orbital period, P_{orb} and its derivative, $\dot{P_{orb}}$, are referred to is the beginning of the 1998 outburst, that is $T_0 = 50914.8099 MJD$. Numbers in parentheses are the uncertainties in the last significant digits at 90 per cent c.l. Upper limits are at 95 per cent c.l. Uncertainties are calculated conservatively increasing the errors on the fitted points in order to reach a χ^2/d.o.f. $\simeq 1$, as described in the text.

[b]The value of $a_1 \sin i$ and its 1σ error are from Chakrabarty and Morgan (1998)

ted the phases of each of these intervals with the formula for the differential corrections to the orbital parameters [2.31]. The selection of the intervals is somewhat arbitrary; we have verified, however, that the results do not change using a different choice. No significant corrections were found on the adopted values of the orbital period, P_{orb}, the projected semi major axis of the NS orbit, $a_1 \sin i/c$, and the eccentricity of the orbit.

On the other hand, we found that the times of passage of the NS at the ascending node at the beginning of each outburst, T_N, were significantly different from their predicted values, $T_0 + NP_{orb}$, where T_0 is the adopted time of ascending node passage at the beginning of the 1998 outburst, and the integer N is the exact number of orbital cycles elapsed between two different ascending node passages, that is N is the integer part of $(T_N - T_0)/P_{orb}$ under the assumption that $|T_N(T_0 + NP_{orb})| < P_{orb}$ that we have also verified a posteriori. We therefore fixed the values of P_{orb}, $a_1 \sin i/c$ and the eccentricity, and derived the differential corrections, ΔT, to the time of passage at the ascending node, obtaining a cluster of points for each outburst. We then checked that every point in a cluster (that is relative to a single outburst) is consistent with the global solution. We could therefore safely state that any systematic uncertainty on the arrival times of the pulses (such as phase shifts or other kind of noise), not already included in our estimated uncertainties for the pulse phases, did not significantly affect the determination of the orbital parameters. We, hence, combined all the measurements corresponding to each outburst computing the error-weighted mean of the corresponding points, obtaining the five points shown in Fig. 8.1.

The 'observed minus calculated' residuals in the epochs of ascending node passage, $\Delta T = T_N - T_0$, are perfectly analogous to the phase residuals defined in Eq. [2.15] for the purposes of timing analysis of the coherent pulsation (see e.g. Bozzo et al., 2007, where this technique was used to infer the presence of a third body orbiting that LMXB). To study their evolution we can therefore use a relation similar to Eq.[2.18], where the spin frequency is replaced by $2\pi/P_{orb}$, and the (supposed constant) spin frequency derivative, $\dot{\nu}$, is replaced

by $\dot{P}_{orb}/P_{orb}^2$. We have therefore:

$$\Delta T = \delta T_0^* + \delta P_{orb} \times N + (1/2)\dot{P}_{orb} P_{orb} \times N^2. \quad (8.1)$$

Here the time since the first outburst is expressed as $t - T_0^* = NP_{orb}$ (see above). Fitting the observed residuals with this relation, we can find the best fitting values $T_0^* + \delta T_0^*$, $P_{orb} + \delta P_{orb}$ and $\dot{P_{orb}}$ at $t = T_0$ (that is the beginning of the 1998 outburst), listed in Table 8.1, with a $\chi^2 = 1.55$ for 2 degrees of freedom. This corresponds to a probability of 21 per cent of obtaining a χ^2 larger than the one we found. Our result is therefore acceptable (or, better, not rejectable), since the probability we obtained is above the conventionally accepted significance level of 5 per cent (in this case, in fact, the discrepancy between the expected and observed values of χ^2 is not significant since the two values are within less than 2σ from each other, see e.g. Bevington and Robinson, 2003).

The derivative we found for the orbital period is highly significant, as it is evident from the curvature of the best fitting function shown in Fig. 8.1. We note that similar values were obtained by Di Salvo et al. (2008a), $\dot{P_{orb}} = (3.40 \pm 0.18) \times 10^{-12}$ s s^{-1}, and by Hartman et al. (2008), $\dot{P_{orb}} = (3.5 \pm 0.2) \times 10^{-12}$ s s^{-1}, considering only the first four outburst displayed by the source. The fact that the same orbital evolution keeps on being observed as the outburst number grows, gives a very strong indication about its concreteness.

8.2 The proposed scenario

To understand the implications of our measurement, we have to compare it with the expectations of the standard evolution theory for close LMXB. In Sec. 1.4.4 we have seen how the mass transfer tends to widen the orbit of a LMXB. In the first evolutionary stages of a LMXB the companion ($\sim$ M$_\odot$) responses to mass loss contracting (that is $R \propto M^n$, with $n \geq 0$), so that angular momentum losses are needed for the binary to keep the mass transfer going. The main mechanisms which assure the binary to shrink are magnetic braking at larger periods, and emission of gravitational waves when the system has a shorter orbital period. Given its orbital period ($\simeq$ 2 hr), SAX J1808.4–3658 evolution is certainly affected by the latter mechanism. Note that, as it becomes clear in the following, the orbit of SAX J1808.4–3658 indeed widens, but as we observe mass transfer, this is an indication that the the companion has already became totally degenerate or completely convective ($n < 0$)[1]. The angular momentum lost because of GW emission can be evaluated from Eq.[1.14] in terms of the inclination, using the measured value of $a_1 \sin i/c$ (see Table 8.1).

Another possible sink of angular momentum is the ejection of a fraction β of the mass transferred by the companion (i.e. $\dot{M}_1 = -\beta \dot{M}_2$). The amount of the angular momentum which can be removed from the binary in this way depends on the specific angular momentum carried away by the mass ejected by the system (αj_2, where j_2 is the specific angular momentum of the secondary), that is, essentially, where the mass is ejected from. A binary like SAX J1808.4–3658

[1] According to the measured mass function, $f(M_1, M_2, i) = 3.8 \times 10^{-5}$ M$_\odot$ (see Eq.[3.1]), the companion mass of SAX J1808.4–3658 is at a 95 % confidence level within 0.04 M$_\odot$ and 0.18 M$_\odot$, where the NS mass is varied in the 1.4–2.0 M$_\odot$ range

is therefore expected to loose angular momentum at a rate (see Eq.[1.12]):

$$\frac{\dot{J}_b}{J_b} = \frac{\alpha(1-\beta)}{1+q}\frac{\dot{M}_2}{M_2} + \frac{\dot{J}_{GW}}{J_{GW}}, \tag{8.2}$$

where we recall that $q = M_2/M_1$.

The fact that, despite being a transient, SAX J1808.4–3658 keeps transferring mass, translates in a condition which relates the mass transfer rate in a binary to the rate at which loses angular momentum, and to the index n of the mass radius relation (see Eq.[1.17]). Using $n = -1/3$ for the companion star (see below), and assuming the mass transfer to be conservative ($\beta = 0$, $\dot{J}_b = \dot{J}_{GW}$), the predicted mass transfer rate is $\dot{M}_{GR} \simeq 5 \times 10^{-11}\ m_{2\,0.1}^2\ m_1^{2/3}\ P_{2h}^{-8/3}\ M_\odot/yr$ (Verbunt, 1993), where m_1 is the mass of the NS in solar masses, $m_{2\,0.1}$ is the companion mass in units of 0.1 $M_\odot$, and P_{2h} is the orbital period in units of 2 hr. This mass transfer rate can be expressed in terms of the expected orbital period derivative. To this end we use Eq.[8.2] in [1.11], which express the rate of change of the orbital separation, together with the 3^{rd} Kepler law. We therefore obtain in terms of $\dot{P}_{orb}$:

$$\frac{\dot{P}_{orb}}{P_{orb}} = 3\frac{\dot{J}_{GW}}{J_b} - 3\left[1 - \beta q - \frac{(\alpha + q/3)(1-\beta)}{1+q}\right]\frac{\dot{M}_2}{M_2}, \tag{8.3}$$

which is of general validity, as we did not assume conservative transfer in its derivation. In we instead assume it, it is possible to obtain:

$$\dot{P}_{orb} = -1.4 \times 10^{-13} m_1 m_{2\,0.1} m^{-1/3} P_{2h}^{-5/3} \times \left[\frac{n - 1/3}{n + 5/3 - 2q}\right]\ ss^{-1}, \tag{8.4}$$

(Verbunt, 1993), where we used m to express the total mass of the system in solar units. From this expression it is clear that a system can widen and keep the companion in contact with its Roche Lobe, only of $n < 1/3$, suggesting a degenerate or fully convective companion, which is indeed indicated by our analysis (see below). However, the $\dot{P}_{orb}$ we measure is more than an order of magnitude larger than the one predicted by conservative GR driven evolution.

How large this discrepancy is can be further seen if we take the limiting case in which the binary does not gain orbital angular momentum, a fairly conservative assumption as the source belong to the Galactic field and is very hardly subject to tidal interactions with other gthereforealactic objects. If we then consider mass loss as the only possible sink of angular momentum, and that the sign of the left hand side is positive, Eq.[8.3] translates in an upper limit on the orbital period derivative, given the details of the mass transfer:

$$\frac{\dot{P}_{orb}}{P_{orb}} \leq 3\left[-\frac{\dot{M}_2}{M_2} g(\beta, q, \alpha)\right], \tag{8.5}$$

where $g(\beta, q, \alpha) = 1 - \beta q - [(1-\beta)(\alpha + q/3)/(1+q)]$, and the parameter α appears as we are also considering the orbital evolution driven by eventual mass loss (see Eq.[1.12]). Assuming a conservative mass transfer, $\beta = 1$, we have $g(\beta, q, \alpha) = 1 - q \simeq 1$, where we used the fact that q is known to be very small from the mass function measured for SAX J1808.4–3658. Hence for conservative mass transfer, $\dot{P}_{orb}/P_{orb} \leq 3(-\dot{M}_2/M_2)$. Since SAX J1808.4–3658 accretes for

about 30 d every 2 yr, an order of magnitude estimate for the average luminosity emitted by SAX J1808.4–3658 is $L_X \sim 4 \times 10^{34}$ erg/s, which corresponds to $3(-\dot{M}_2/M_2) = 6.6 \times 10^{-18}$ s^{-1}. It is easy to see that the measured $\dot{P}_{orb}/Porb$, 5.2×10^{-16} $s\ s^{-1}$, is roughly 80 times larger than the value predicted in the conservative mass transfer case, hence excluding this scenario.

Assuming a totally non-conservative mass transfer, $\beta = 0$, we find that $g(0, q, \alpha) = (1 - \alpha + 2q/3)/(1 + q) \simeq 1 - \alpha$, implying that $\dot{P}_{orb}/P_{orb} \leq 3(1 - \alpha)(-\dot{M}_2/M_2)$. Since the first term is positive we find that $\alpha < 1$ and the specific angular momentum with which matter is expelled from the system must be less than the specific angular momentum of the secondary. For matter leaving the system with the specific angular momentum of the primary, we have $\alpha = q^2 \sim 0$. In this case, therefore, we find the same result of the conservative case where no angular momentum losses from the system occur. This is due to the fact that the specific angular momentum of the primary is so small that there is no difference with respect to the conservative case. Since the specific angular momentum of the mass lost must be in between the specific angular momentum of the primary and that of the secondary, a reasonable hypothesis is that matter leaves the system with the specific angular momentum of the inner Lagrangian point. In this case, $\alpha = [1-0.462(1+q)^{2/3}q^{1/3}]^2 \simeq 0.7$, where we have used for the Roche-lobe radius the approximation given by Paczyński (1971). We therefore find $\dot{P}_{orb}/P_{orb} \leq (\dot{M}_2/M_2)$. Using the measured value of the quantity $\dot{P}_{orb}/P_{orb} = 5.2 \times 10^{-16}$ s^{-1}, we find that to explain this result in a totally non-conservative scenario the mass-transfer rate must be: $-\dot{M}_2 = \dot{M}_{ej} \geq 9 \times 10^{-10}$ M$_\odot$/yr (evaluated for a 1.4 M$_\odot$ MS). We can therefore explain the measured derivative of the orbital period of the system assuming that the system is expelling matter at a quite large rate, that may be as high as 10^9 M$_\odot$/yr, and this is found just assuming the conservation of the angular momentum of the system, and independently of the secular evolution adopted.

8.2.1 Possible secular evolution for the system

In order to verify the feasibility of an explanation of the orbital evolution of SAX J1808.4–3658 in terms of mass (and angular momentum) lost by the system, we explicitly express the GR term in Eq.[8.3], and evaluate it for the two extreme cases of conservative ($\beta = 1$) and totally non conservative ($\beta = 0$) mass transfer, obtaining:

$$\dot{P}_{orb} = -1.38 \times 10^{-12} \left[\frac{n - 1/3}{n - 1/3 + 2g}\right] m_1^{5/3} q (1+q)^{-1/3} P_{2h}^{-5/3}\ ss^{-1}. \quad (8.6)$$

The mass transfer rate is instead obtained from Eq.[1.17]:

$$\dot{M} = -\dot{M}_2 = 4.03 \times 10^{-9} \left[\frac{1}{n - 1/3 + 2g}\right] m_1^{8/3} q^2 (1+q)^{-1/3} P_{2h}^{-8/3} M_\odot/yr. \quad (8.7)$$

In the case of conservative mass transfer, $g = 1 - q$ (it is easy to see how the result of Eq.[8.4] is recovered), while $g = 1 - (\alpha + q/3)/(1 + q)$ for totally non conservative mass transfer.

These relations confirms the previous findings: (a) the companion has to have an index of the mass-radius relation $n < 1/3$, and (b) a conservative mass transfer cannot account for the observed orbital period derivative (GR predicts

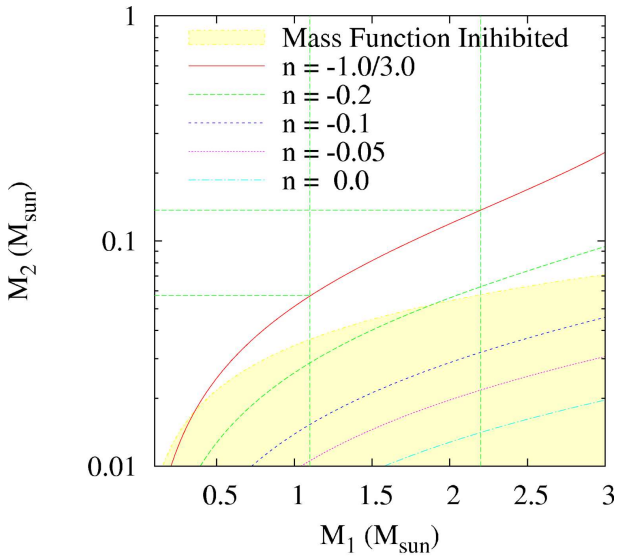

Figure 8.2: Companion star mass versus NS mass in the hypothesis of totally non-conservative mass transfer (with matter leaving the system with the specific angular momentum at the inner Lagrangian point) and assuming the $\dot{P}_{orb}$ measured for SAX J1808.43658. Different curves correspond to different values of the mass-radius index n of the secondary. Horizontal lines indicate the limits for the secondary star mass corresponding to reasonable limits for the NS mass and to $n = -1/3$.

in fact $\dot{P}_{orb} \sim 10^{-13}$ s s^{-1}). We are therefore left with the possibility of a non conservative evolution of the system. If we assume that during X-ray quiescence the companion star is still overflowing its Roche lobe but the transferred mass is not accreted on to the NS and is instead ejected from the system, we find a good agreement between the measured and expected orbital period derivative assuming that the matter leaves the system with the specific angular momentum at the inner Lagrangian point, $\alpha = [1(2/3^{4/3})q^{1/3}(1+q)^{2/3}]^2$. Adopting the measured value for $\dot{P}_{orb}$, and the other parameters measured for SAX J1808.4–3658, Eq.[8.6] translates in a relation between the masses of the two stars of the binary system, m_1 and m_2, and the mass-radius index n. This is plotted in Fig. 8.2.1 for different values of n, ranging from 0 to -1/3. The constraint on m_1 and m_2 imposed by the mass function is also plotted, thus excluding all the masses in the shadowed region. This plot clearly indicates how the most probable value for n is $-1/3$, which in turn indicates a degenerate, or most probably, a fully convective companion star. In fact, in a system with orbital period less than 3 h, where the mass of the Roche-lobe filling companion is below 0.2–0.3 $M_\odot$, the companion star becomes fully convective with a mass-radius hydrostatic equilibrium equation $R \propto M^{1/3}$ (e.g. King, 1988; Verbunt, 1993).

Assuming therefore $n = -1/3$ we have plotted in Fig. 8.2.1 the corresponding non-conservative mass-transfer rate as a function of m_1 (Eq.[8.7]). We find that for $m_1 = 1.5$, the mass-transfer rate must be of the order of 10^9 $M_\odot$/yr, much larger than what is expected in a conservative GR driven mass transfer case. Note that this high $\dot{M}$ might explain the spin period evolution reported by

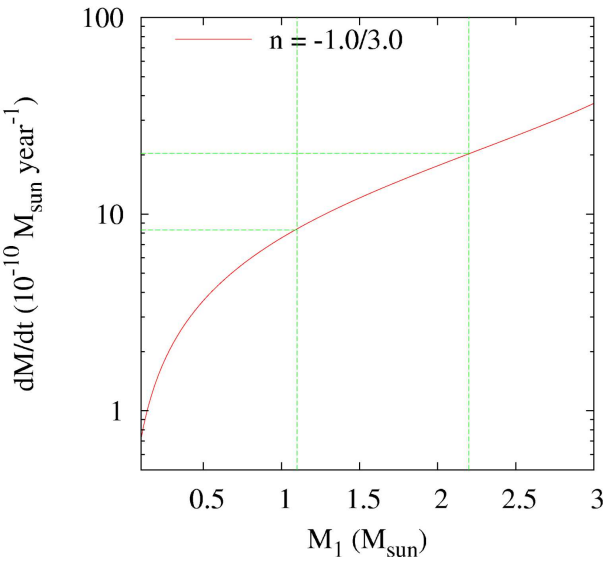

Figure 8.3: Mass rate outflowing the secondary Roche lobe in the hypothesis of totally non-conservative mass transfer (see caption of Fig. 8.2.1) and assuming $n = -1/3$.

Burderi et al. (2006, see Sec. 5.2, but also Hartman et al. (2008), who could not detect a spin period derivative during the outbursts). Actually, during the X-ray outbursts the mass transfer is conservative since the transferred matter is accreted on to the NS. However, the accretion phase duty cycle, about 40 d/2 yr = 5 per cent, is so small that the totally non-conservative scenario proposed above is a good approximation.

8.2.2 Is SAX J1808.4–3658 a hidden black widow pulsar?

If the hypothesis of a highly non-conservative mass transfer in SAX J1808.43658 is correct, the question to answer is why is accretion inhibited during X-ray quiescence while the companion star is transferring mass at a high rate? We propose that the answer has to be found in the radiation pressure of the magneto dipole rotator emission, with a mechanism that is similar to what is proposed to explain the behaviour of the so-called black widow pulsars (see e.g. Tavani, 1991a; King et al., 2003, 2005; Burderi et al., 2001). Indeed, the possibility that the magneto-dipole emission is active in SAX J1808.4–3658 during X-ray quiescence has been invoked by Burderi et al. (2003) to explain the optical counterpart of the source, which is observed to be over-luminous during quiescence. In this scenario, the optical luminosity in quiescence is explained by the spin-down luminosity of the magneto-dipole rotator [with a magnetic field of (1–5) $\times$ 10^8 G] which is reprocessed by the companion star and/or a remnant accretion disc. Interestingly, similar evidence of a strongly irradiated companion star during quiescence has been found also for IGR J00291+5934, the fastest among the known AMSPs (D'Avanzo et al., 2007), which moreover shares with SAX J1808.4–3658 similar orbital properties (see Table 1.1).

In other words, a temporary reduction of the mass-accretion rate on to the NS (note that the so-called disc Instability Model, DIM – see e.g. Lasota, 2001, and Sec. 1.4.3 – usually invoked to explain the transient behaviour of these sources, may play a role in triggering or quenching the X-ray outbursts in SAX J1808.4–3658) may cause the switch on of the emission of the magneto-dipole rotator, and, in some cases, even if the mass-transfer rate has not changed, the accretion of matter on to the NS can be inhibited because the radiation pressure from the radio pulsar may be capable of ejecting out of the system most of the matter overflowing from the companion (see e.g. Burderi et al., 2001, and references therein). This phase has been termed radio ejection. One of the strongest predictions of this model is the presence, during the radio-ejection phase, of a strong wind of matter emanating from the system: the mass overflowing from the companion is swept away by the radiation pressure of the pulsar. Indeed, the existence of hidden millisecond pulsars, whose radio emission is completely blocked by material engulfing the system that is continuously replenished by the mass outflow driven by companion irradiation, has already been predicted by Tavani (1991a).

A beautiful confirmation of this model was provided by the discovery of PSR J1740–5340, an eclipsing millisecond radio pulsar, with a spin period of 3.65 ms, located in the globular cluster NGC 6397 (D'Amico et al., 2001). It has the longest orbital period ($P_{orb} \simeq 32.5$ h) among the 10 eclipsing pulsars detected up to now. The peculiarity of this source is that the companion is a slightly evolved turn-off star still overflowing its Roche lobe. This is demonstrated by the presence of matter around the system that causes long lasting and sometimes irregular radio eclipses, and by the shape of the optical light curve, which is well modelled assuming a Roche-lobe deformation of the mass-losing component (Ferraro et al., 2001). An evolutionary scenario for this system has been proposed by Burderi et al. (2002), who provided convincing evidence that PSR J1740–5340 is an example of a system in the radio-ejection phase, by modelling the evolution of the possible binary system progenitor. In other words, PSR J17405340 can be considered a star-vaporizing pulsar of type II in the terminology used by Tavani (1991a). In this case the mass transferred by the companion is ejected by the pulsar radiation, but the $\dot{M}$ is enough large that overflowing mass is blocked closer to the NS by the pulsar radiation, leading, together with the effects of Coriolis forces, to an asymmetric curtain around the system. The observed eclipses are therefore irregular.

We believe that the behaviour of SAX J1808.4–3658 is very similar to the one of PSR J1740–5340, the main differences being the orbital period, which is 32 h in the case of PSR J1740– 5340 and 2 h in the case of SAX J1808.4–3658, and the mass transfer rate from the companion, which has been estimated to be $\sim 10^{10}$ $M_\odot$/yr for PSR J1740–5340 and one order of magnitude higher for SAX J1808.4–3658. Both these factors will increase the local Dispersion Measure (DM) to the source in the case of SAX J1808.4–3658, and hence will predict a much higher free–free absorption in the case of SAX J1808.4–3658. This is in agreement with the fact that, although widely searched, no radio pulsations have been detected from SAX J1808.4–3658 up to date (Burgay et al., 2003). In other words, SAX J1808.4–3658 can be considered a hidden millisecond pulsar or a star-vaporizing pulsar of type III in the terminology used by Tavani (1991a). In type III star-vaporizing pulsar, the larger mass transfer rate completely enshroud the NS, the radiation of which is nevertheless able to stop the accretion.

A similar highly non-conservative mass transfer, triggered by irradiation of the secondary and/or of an accretion disc by the primary (according to the model of Tavani, 1991b), has been proposed to explain the large orbital-period derivative observed in the ultra-compact Low Mass X-ray Binary X 1916–053, composed of a NS and a semi-degenerated white dwarf, exhibiting periodic X-ray dips. In this case, $\dot{P}_{orb}/P_{orb} \simeq 5.1 \times 10^{15}$ s^{-1}, which implies a mass-transfer rate of $\sim 10^8$ M$_\odot$/yr, with 60–90 per cent of the companion mass loss outflowing from the system (Hu et al., 2008).

As predicted by several authors (e.g. Chakrabarty and Morgan, 1998; King et al., 2005), and in agreement with our interpretation of the orbital-period derivative in SAX J1808.4–3658 as due to a highly non-conservative mass transfer, we propose therefore that SAX J1808.4–3658, and other similar systems, belong to the population of the so-called black widow pulsars (or are evolving towards black widow pulsars); these are millisecond radio pulsars thought to ablate the companion and likely able to produce large mass outflows. When (or if) the pressure of the outflowing matter becomes sufficiently high to temporarily overcome the radiation pressure of the magneto-dipole rotator, the source experiences a transient mass accretion episode, resulting in an X-ray outburst. Indeed, SAX J1808.4–3658 and the other known AMSPs are all transient systems (accreting just for a very short fraction of the time), with small values of the mass function (implying small minimum mass for the secondary) and short orbital periods (less than a few hours).

8.3 The P_{orb}–M_2 plane

That such a link between AMSP and black widow pulsars may exist is also indicated by the distribution of orbital periods and companion masses of rotation powered millisecond pulsar in binary systems (bMsP), accreting millisecond pulsar (AMSP), and low mass X-ray binary which do not show persistent pulsations (simply named here as LMXB). Following Deloye (2008) we plot in the P_{orb}–M_2 plane the known MsP (blue asterisks), AMSP (red filled squares) and LMXB (red hollow circles) belonging to Galactic field (see Fig. 8.3). We exclude those belonging to Globular Cluster as their evolution might be significantly altered with respect to the standard picture by tidal interactions with the other objects populating the cluster. It is easy to note by eye inspection that, strikingly, AMSP and MsP populate different regions of this plot. While the former have short periods ($\lesssim$ few hours) and very light companions ($M_2 \lesssim 0.2$ M$_\odot$), the bulk of Galactic bMsP have generally larger orbital periods and companion masses. This poses an important question on what is actually the progeny left by the known AMSP.

In Sec. 1.4.5 we focused on the evolutionary histories followed by LMXB which underwent stable mass transfer only. The evolution of systems with low mass donors ($\lesssim 1$ M$_\odot$) depends critically on the evolutionary state of the companion when the mass transfer begins:

- **(a) CV-like Stable transfer** If the companion is not significantly evolved (i.e. on their main sequence, or short after the turn off), the evolution is controlled by angular momentum losses (magnetic braking and GW emission) so that the system shrinks as the mass is transferred. When the

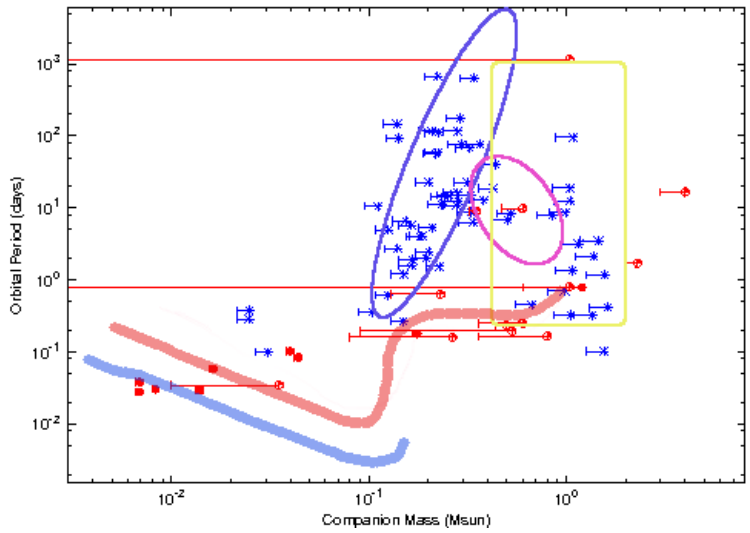

Figure 8.4: Distribution of binary MsP (blue asterisks), AMSP (red filled squares) and non pulsating LMXB (red empty circles) belonging to the Galactic field. The points were derived from the ATNF Pulsar Catalogue, available at http://www.atnf.csiro.au/research/pulsar/psrcat/, and from the LMXB catalogues compiled by Liu et al. (2007b) and Ritter and Kolb (2008). The median values derived from the mass function ($i = 60°$), and the error lines extend to the minimum mass allowed ($i = 90°$) are plotted. The assumed NS mass is 1.35 $M_\odot$. The blue ellipsis encircles possible evolutionary endpoints following RGB/AGB stable transfer channel, the magenta ellipsis those coming from Thermal Time-scale mass transfer, and yellow rectangle systems which underwent a common envelope phase and then widened. The blue track represents a possible evolution for a CV-like system, while the red one characterise a close system after common envelope (see text for details). The possible endpoints for the binary evolution, as well as the approximate evolutionary tracks, are taken from Deloye (2008), and are plotted here only for representative purposes.

companion becomes fully convective, and nuclear burning has completely shut off, the companion reacts adiabatically to mass loss. As the mass–radius index is now reversed, the P_{orb} evolution changes sign and the binary widens.

- **(b) RGB/AGN Stable transfer** If mass transfer begins when the companion is already evolved, the evolution is controlled by the nuclear evolution of the companion. Despite mass transfer tends to widen the orbit, the companion may expand faster, thus keeping contact with its Roche Lobe. The system therefore evolves towards large orbital periods.

Three other evolutionary channels can nevertheless describe the evolution of a LMXB, and concern a mass transfer which is not stable, at least initially (see e.g. Deloye, 2008, and references therein):

- **(c) Thermal Time-scale (TT) mass transfer** This mode of mass transfer occurs for intermediate mass donors ($2M_\odot \lesssim M_2^{(i)} \lesssim 4M_\odot$) which make contact with their Roche Lobe before they evolve off the main se-

quence. As $q > 1$, the companion Roche Lobe shrinks when mass is transferred, and the companion keeps the transfer going on the time-scale over which it tries to restore its thermal equilibrium. The lifetimes of these systems ($\lesssim 10^8$ yr) is shorter than those of stably transferring systems ($\lesssim 10^{10}$ yr). The initial evolution towards short periods reverses when q is significantly reduced.

- **(d) Common envelope - Ultra Compact LMXB** Once a massive donor reach the RGB it has developed a deep convective envelope (CE). Mass transfer in this case is dynamically unstable, so that the envelope of the companion fully enshrouds the binary system. The orbital energy is used to expel the donor's envelope, and the binary greatly shrinks down to orbital periods of few $\times 10$ min. The system is now so close that GW emission can bring the donor's remnant in contact again, so that the system shines again as an ultra-compact LMXB (UC-LMXB). The following evolution is towards larger periods as the companion is now semi (or fully) degenerate.

- **(e) Common envelope - Wide systems** The evolution of these systems is similar to the previous case, but the orbital separation when the CE phase ends is too large for GW emission to bring the donor back into contact with its Roche Lobe. No LMXB phase therefore ensues.

We therefore plot in Fig. 8.3, the approximate endpoints of the binary evolution channels described so far. The blue region corresponds to RGB/AGN Stable transfer (b), magenta to TT mass transfer (c), yellow to CE Wide (e). The blue stripe is a possible evolutionary track for a $\sim$ M$_\odot$ star which commences mass transfer approximately in the Hertzsprung gap [larger minimum orbital periods, ~ 80 min, are obtained for MS stars, Podsiadlowski et al., 2002 and follows case (a)]. The red stripe is instead the approximate evolution of a system which has undergone CE and started mass transfer at orbital periods of $\sim$ few minutes as an UC-LMXB. We note that tracks and regions there plotted are approximate reproductions of those appearing in Deloye (2008), and are considered here only for descriptive purposes.

According to the distribution of Fig. 8.3, bMsP seem to descend from channels (b), (c) and (e). On the other hand AMSP evolution can be grossly explained according to the scenarios (a) and (d). Systems with $P_{orb} \gtrsim 1$ hr (XTE J1814–338, SAX J1808.4–3658, IGR J00291+5934 and HETE J1900.1–2455) are thought to descend from a CV-like evolution, while ultra-compact systems ($P_{orb} \lesssim 1$ hr, XTE J1751–305, XTE J0929–314, SWIFT J1756.9–2508, XTE J1807–294) have the typical short periods of binaries which experienced a common envelope phase. Despite that SAX J1808.4–3658 and IGR J00291+5934 lie in the vicinity of CV-like evolutionary tracks, Deloye (2008) noted how they have larger donor masses for their P_{orb}. This is in principle an indication that irradiation could have an important role in determining these system's evolution. As a matter of fact an irradiated donor is bloated and thus is expected to transfer mass on shorter time-scales than what it could predicted from the actual value of their mass (see e.g. Podsiadlowski, 1991, but also Hameury et al., 1993, and Ritter, 2008). We recall that indications of the role played by irradiation of the companion in SAX J1808.4–3658 and IGR J00291+5934 arise from the observed optical photometry in quiescence (Homer et al., 2001; D'Avanzo

et al., 2007). The amount of the reprocessed energy is indeed too large to be accounted for by the X-ray flux in quiescence, and that a magneto-dipole rotator switches on has to be argued (Burderi et al., 2003).

An indication supporting the scenario we propose to explain the observed orbital evolution of SAX J1808.4–3658 comes from the lack of bMsP in the region of the P_{orb}–M_2 plane occupied by AMSP. We have in fact that only three bMsP are near the actual location of SAX J1808.4–3658 and IGR J00291+5934. It is striking to note that 2 out of these 3 are indeed black widow pulsars, the only two discovered in the field so far, PSR B1957+20 (Backer et al., 1982), and PSR J2051-0827 (Stappers et al., 1996). The other system in that region, PSR J0610-2100 (Burgay et al., 2006), despite being not much studied, has nevertheless the promising property of being only visible at large radio frequencies (1400 MHz, Lorimer et al., 2007), an indication of a large amount of absorbing material along the line of sight. We can therefore suggest also on an evolutionary basis that the lack of a bMsP progeny from AMSP may be simply due to the fact that these systems (or at least those with a CV like evolution) evolve like black widow pulsars, and may or may not leave a remnant after the accretion phase ends. It has also to be noted in fact that the function in square brackets on the left hand side of Eq.[8.7], $f = [1/(n - 1/3 + 2g)]$, has an unstable behaviour for low values of q. If we take $n = 1/3$, and argue that mass is lost by the system from the inner Lagrangian point, the function f explodes for q approaching 0.03 from larger values. This would lead to a rapid increase of the mass transfer rate, in a limit cycle which ultimately drives to the complete evaporation of the donor. Despite this does not result from an auto-consistent evolutionary scenario, it nevertheless indicates how a mass losing system (like SAX J1808.4–3658 has to be if the orbital evolution we observe has to find an interpretation), may experience a runaway evolution, with the mass of the companion more and more efficiently ablated, until the donor detaches from its Roche Lobe or it is completely evaporated.

It is important to note that the above discussion concerns only the progeny of the *observed* AMSP, and not the recycling scenario as a whole. NS in LMXB are in fact generally thought to spin already at millisecond period (as it is also observed from burst oscillations), and it could well be that the progenitors of bMsP in the upper right region of Fig. 8.3, are simply not observed as AMSP, possibly because they accrete at a larger rate than AMSP. Further observations of the orbital evolution followed by the other AMSP (and in particular by IGR J00291+5934) are nevertheless needed to establish the link between AMSP and black widow pulsars, which is however strongly indicated both on an observational and evolutionary basis.

9

Conclusions and future prospects

I presented in this thesis the results of a comprehensive analysis of the rotational behaviour and of the orbital evolution of AMSP. Such analysis was performed mainly by the means of timing analysis on the two fundamental periodicities shown by these systems, the spin frequency of the NS and the orbital period of the binary system. Nevertheless it also relies on the high resolution spectral information we could acquire in the case of one of these sources.

The main issue discussed here is the reaction of the NS to the torques exerted on it during disc accretion of mass. The accretion torques can be roughly split in two terms, a positive material torque due to the release to the NS of the specific angular momentum owned by the accreted mass, and a negative magnetic torque arising from the interaction of the magnetic field lines threading the accretion disc beyond the corotation radius. In this region, in fact, field lines travel faster than disc particles. While the first term is always present in the case of disc accretion, the second becomes important only for fast rotators like AMSP.

The first important result we got is indeed the measurement of the tiny effects produced by these torques on the NS spin. As a matter of fact timing analysis on AMSP is hampered by two reasons; the accretion radius has to be very close to the NS for a fast rotator to accrete, thus diminishing the lever arm of the material torque, and, most importantly, AMSP are all transients and accrete for at most a couple of months yielding a limited available integration time for the timing analyses with respect to what concerns, e.g., rotation-powered pulsars. These issues forced us to develop an alternative formalism to treat the various effects that determine the phase evolution of the pulse profile of a pulsar. As a matter of fact, together with a possible *real* spin frequency derivative, the probe we use to deduce the NS rotational state (i.e. the phase of the pulse profile) depends also on the orbital motion of the NS in the binary system it belongs to, and on the uncertainty on the source position. While for the latter effect it was only possible to derive upper limits on its effect on the parameters we want to measure, we disentangled the orbital motion effects on phases from those owing to the spin evolution of the NS. This was possible as it was realized that the time-scales over which these two effects work are very different in the case of AMSP. The developed formalism allowed us to finally measure the phase evolution of AMSP, a goal which is worth to recall was not fulfilled yet at the time of starting this research project in 2005.

In this work I discuss in great details the timing analysis performed on the two sources I focused on the most, XTE J1751–305 and XTE J1814–338. These two sources show quite nicely how the rotational behaviour of AMSP

can be diverse. In the first case a spin-up was observed at a rate consistent with what is predicted by the simple relation that links the spin-up rate to the mass accretion rate of particles in a Keplerian accretion disc. While it was not possible to constrain the location of the inner disc radius due to the low statistics, we checked how our measure is consistent with the theory from a comparison between the mass accretion rate needed to explain the observed spin-up rate and the mass accretion rate indicated by the observed X-ray flux. Equating a dynamical and a photometric estimate of a quantity we naturally get to an estimate of the distance to the system. The one we get to in this case is perfectly consistent with previous and independent constraints, confirming the indication that the source has to be close to the Galactic Centre.

XTE J1814–338 reveals instead a more puzzling behaviour. Its average spin trend is that of a spin-down, reflecting how the magnetic field is important in the determination of the rotational state of a fast pulsar. Using simple models we could give a value for the magnetic field of the NS in XTE J1814–338 that is roughly one order of magnitude larger ($\simeq 10^9$ G) than what is generally found for spinning up AMSP. The importance of the magnetic field in the determination of the spin properties of an AMSP is confirmed when the measured behaviour of all the six (out of ten) AMSP considered in this work is accounted for. Despite the large uncertainties on distances, AMSP show X-ray luminosities which are at most different by a factor 5. If these sources had the same magnetic fields we would expect the very same reaction to the accretion of mass, but this is definitely not observed. Two sources spin-down while the others four spin-up, and this can only be interpreted in terms of the former having larger field strengths than the latter. This indication is further confirmed by the correlation observed between the spin frequency and the spin states of the AMSP considered. Despite there is not enough statistics to establish this as a reliable conclusion, a clear indication that faster sources tend to spin-up more easily than slower sources appears. This can be easily understood if we argue that AMSP are spinning at their spin equilibrium, which is defined as the period the pulsar is expected to attain after it had accreted for enough time that the positive material torques are exactly cancelled on the average by the negative magnetic torques. The value of the spin equilibrium period mainly depends on the magnetic field strength, and larger rotation rates are expected for smaller fields. If AMSP spin at their equilibrium value (or in the vicinity of) it is therefore straightforward to understand why positive torques tend to overcome the magnetic negative torques in the faster sources, given a roughly constant mass accretion rate.

Furthermore, the analysis presented here for XTE J1814–338 represents the first case in which phase variability was observed in connection with variations of the X-ray flux. It was observed indeed that the phases computed on both the fundamental and the second harmonic are modulated around the average spin-down solution. This modulation is clearly anti-correlated with the changes in the mass accretion rate reflected by the X-ray light curve. As this behaviour cannot be interpreted in terms of accretion torques, the most appealing interpretation is in terms of movements of the hot spot longitude on the NS surface, reflecting a change in the geometry of the accretion columns that lead mass from the disc to the accretor. This interpretation is qualitatively indicated by the results of 3D MHD simulations of accretion onto a magnetized rotator, which show indeed how the magnetic pitch of the field lines (that is, how large they are

distorted in the azimuthal direction by the differential rotation with respect to disc matter) is influenced by the accretion rate. Despite a quantitative relation to effectively test this hypothesis is still missing, the observed phenomenon opens the possibility to observe on a timing basis the relation between the geometry of the accretion column and the accretion rate. Such phase movements were observed also in two other sources. While in the case of XTE J1807–294 we observed the same qualitative behaviour of XTE J1814–338 (despite the source is spinning up), the 2002 outburst of SAX J1808.4–3658 is even more puzzling, with a large shift of the phase computed on the fundamental frequency which is not accompanied by a similar shift in the second harmonic phases. I then also present a simple geometrical toy model to give a possible explanation of this peculiar phenomenology in terms of variations of the relative intensity strength of the two emitting polar caps.

The results of the temporal analysis presented here confirm the basic results of the accretion theories on fast rotators, despite the uncertainty coming from the appearance of these shifts still has to be better addressed, as it will when more observations will be available. We could confirm how (i) the spin frequency derivative depends on the mass accretion rate, (ii) the inner disc radius, the lever arm of the accretion torque, is located between the NS radius and the corotation radius, (iii) the compact object may spin-down even while accreting if it has a larger than usual magnetic field. The second statement is further confirmed by the high resolution spectrum I could acquire from SAX J1808.4–3658. It was in fact observed a broadened iron line, whose only possible formation region is the inner accretion disc. From this observation I could derive an independent estimate of the size of the inner rim of disc, which happens to be located exactly in the small region allowed for accretion to occur unimpeded. This is the first time such a measure is given, and it will surely be an invaluable benchmark for every detailed theory concerning the accretion onto a fast NS, the resulting torques acting on it, and possibly the formation mechanism of QPOs. It moreover opens the possibility to study similar lines in other AMSP, and to evaluate how its shape and energy varies with the accretion rate.

Finally I show in this work how temporal analysis was used also to establish the orbital evolution followed by the only source which recurred more than once, SAX J1808.4–3658. This evolution is much faster than what is expected according to any reasonable scenario of conservative mass transfer. The only viable option to understand it is to argue that a great majority of the mass transferred by the companion star is lost, together with its specific angular momentum. The most probable location of the mass ejection is the inner Lagrangian point, and this supports the hypothesis formulated on other grounds that a rotation powered pulsar switches on in this system during its quiescent phases. Despite much work is still needed to firmly establish the viability of this ejection mechanism, SAX J1808.4–3658 could provide a beautiful example of an accretion powered NS which is evolving into a rotation powered millisecond pulsar. Despite this evolutionary link is predicted by the recycling scenario, an unexpected consequence could come out of it. Mass ejection indicates in fact that SAX J1808.4–3658 is behaving much similarly to a Black Widow Pulsar (BWP), a rotation powered pulsar which ablate the companion that is trying to transfer mass to it. This similarity could have an evolutionary consequence in the sense that AMSP may not leave an *usual* binary millisecond pulsar as a descendant when accretion ends, while it might rather produce a BWP or

an isolated rotation powered millisecond pulsar, if the companion is completely used up in the mass transfer phase.

The results presented here cover much of the advancements performed about these object recently, and I also tried to account for those achieved by the rest of the community working on AMSP. These sources were discovered not long ago, so that much still has to be understood yet. I nevertheless showed how different observational techniques, in particular temporal and spectral, can provide a wealth of important information to better address the physics of these key systems. It is easy to understand how important these systems are for the astrophysics of X-ray binaries, as they possess an invaluable additional probe with respect to other systems, the X-ray pulsations. Among the others just mentioned, an evident reason supporting the importance of these studies and their continuation is given by the fact that these are among the most important candidates for the detection of gravitational waves (GW). Further studies on the the fastest AMSP known, IGR J00291+5934, may in fact lead to the measure of the mass quadrupole moment of an accreting NS (for which only an upper limit is given here), and therefore to an estimate of the GW flux expected to be emitted. We tried to exploit the peculiarity represented by X-ray pulsations its best, but still much await to be done especially when more statistics (i.e. more outbursts from the known sources and more newly discovered sources) will be available.

A list of the articles the group I belong to produced while carrying on this scientific project, and this thesis is naturally based on, is given in the following:

- Papitto, A., M. T. Menna, L. Burderi, T. Di Salvo, F. DAntona, and N. R. Robba. "Revised Orbital Parameters of the Accreting Millisecond Pulsar SAX J1808.4-3658.", 2005, ApJ, 621, L113L116.

- Papitto, A., L. Burderi, T. di Salvo, M. T. Menna, and L. Stella. "Temporal Analysis of the Millisecond X-ray Pulsar SAX J1808.4-3658 During the 2000 Outburst.", 2005, in L. Burderi, L. A. Antonelli, F. DAntona, T. di Salvo, G. L. Israel, L. Piersanti, A. Tornamb'e, and O. Straniero (Eds.), Interacting Binaries: Accretion, Evolution, and Outcomes, Volume 797 of American Institute of Physics Conference Series, pp. 110115.

- Burderi, L., T. Di Salvo, G. Lavagetto, M. T. Menna, A. Papitto, A. Riggio, R. Iaria, F. DAntona, N. R. Robba, and L. Stella. "Timing an Accreting Millisecond Pulsar: Measuring the Accretion Torque in IGR J00291+5934", 2007, ApJ, 657, 961966.

- Burderi, L., T. Di Salvo, M. T. Menna, A. Riggio, and A. Papitto. "Order in the Chaos: Spin-up and Spin-down during the 2002 Outburst of SAX J1808.4-3658.", 2006, ApJ, 653, L133L136.

- Papitto, A., T. di Salvo, L. Burderi, M. T. Menna, G. Lavagetto, and A. Riggio. "Timing of the accreting millisecond pulsar XTE J1814-338.", 2007, MNRAS, 375, 971976.

- Riggio, A., T. di Salvo, L. Burderi, R. Iaria, A. Papitto, M. T. Menna, and G. Lavagetto. "Precise determination of orbital parameters in system with slowly drifting phases: application to the case of XTE J1807- 294.", 2007, MNRAS, 382, 17511758.

- Papitto, A., M. T. Menna, L. Burderi, T. di Salvo, and A. Riggio. "Measuring the spin up of the accreting millisecond pulsar XTEJ1751- 305.", 2008, MNRAS, 383, 411416.

- Riggio, A., T. Di Salvo, L. Burderi, M. T. Menna, A. Papitto, R. Iaria, and G. Lavagetto. "Spin-up and Phase Fluctuations in the Timing of the Accreting Millisecond Pulsar XTE J1807-294.", 2008, ApJ, 678, 12731278.

- Di Salvo, T., L. Burderi, A. Riggio, A. Papitto, and M. T. Menna. "Order in the chaos? The strange case of accreting millisecond pulsars.", 2008, in American Institute of Physics Conference Series, Volume 1054, pp. 173182.

- Di Salvo, T., L. Burderi, A. Riggio, A. Papitto, and M. T. Menna. "Orbital evolution of an accreting millisecond pulsar: witnessing the banquet of a hidden black widow?", 2008, MNRAS, 389, 18511857.

- Papitto, A., A. Riggio, T. Di Salvo, L. Burderi, and M. T. Menna. " Enlightening differences in AMSPs behavior: XTE J1751–305 vs. XTE J1814–338", 2008, in American Institute of Physics Conference Series, Volume 1068, pp. 51-54.

- Papitto, A., T. Di Salvo, A.D'Aì, R.Iaria, L.Burderi, A.Riggio, M.T. Menna and N.R. Robba. "*XMM-Newton* detects a relativistically broadened iron line in the spectrum of the ms X-ray pulsar SAX J1808.4–3658", 2009, A&A, 493, L39

- Burderi, L., A. Riggio, T. Di Salvo, A. Papitto, M. T. Menna, A.D'Aì, R. Iaria and N.R. Robba. "Timing of the 2008 outburst of SAX J1808.4–3658 with *XMM-Newton*: a stable orbital period derivative over the last ten years.", 2009, A&A, accepted (arXiv: 0902.2128)

Bibliography

Alpar, M. A., A. F. Cheng, M. A. Ruderman, and J. Shaham (1982, December). A new class of radio pulsars. Nature 300, 728–730.

Alpar, M. A. and J. Shaham (1985, July). Is GX5 - 1 a millisecond pulsar? Nature 316, 239–241.

Altamirano, D., P. Casella, A. Patruno, R. Wijnands, and M. van der Klis (2008, February). Intermittent Millisecond X-Ray Pulsations from the Neutron Star X-Ray Transient SAX J1748.9-2021 in the Globular Cluster NGC 6440. ApJ 674, L45–L48.

Arons, J. (2007, August). Pulsars: Progress, Problems and Prospects. ArXiv e-prints, 0708.1050 708.

Atkinson, R. d. and F. G. Houtermans (1929). Quantenmechanik der alpha-Strahlung. Zeits. f. Physik 54, 656.

Baade, W. and F. Zwicky (1934). Cosmic Rays from Super-novae. Proceedings of the National Academy of Science 20, 259–263.

Backer, D. C., S. R. Kulkarni, C. Heiles, M. M. Davis, and W. M. Goss (1982). A millisecond pulsar. Nature 300, 615–618.

Balbus, S. A. and J. F. Hawley (1991). A powerful local shear instability in weakly magnetized disks. I - Linear analysis. II - Nonlinear evolution. ApJ 376, 214–233.

Basko, M. M. and R. A. Sunyaev (1976, May). The limiting luminosity of accreting neutron stars with magnetic fields. MNRAS 175, 395–417.

Bell Burnell, S. J. (1977). Petit Four. In M. D. Papagiannis (Ed.), Eighth Texas Symposium on Relativistic Astrophysics, Volume 302 of New York Academy Sciences Annals, pp. 685–+.

Beloborodov, A. M. (2002, February). Gravitational Bending of Light Near Compact Objects. ApJ 566, L85–L88.

Bethe, H. (1939). Energy Productions in Stars. Phys.Rev. 55, 434.

Bethe, H. and C. Critchfield (1938). On the Formation of Deuterons by Proton Combination. Phys.Rev. 54, 862.

Bevington, P. R. and D. K. Robinson (2003). Data reduction and error analysis for the physical sciences. Data reduction and error analysis for the physical sciences, 3rd ed., by Philip R. Bevington, and Keith D. Robinson. Boston, MA: McGraw-Hill.

Bhattacharya, D., R. A. M. J. Wijers, J. W. Hartman, and F. Verbunt (1992). On the decay of the magnetic fields of single radio pulsars. A&A 254, 198–212.

Bhattacharyya, S. and T. E. Strohmayer (2007, August). Evidence of a Broad Relativistic Iron Line from the Neutron Star Low-Mass X-Ray Binary Serpens X-1. ApJ 664, L103–L106.

Bildsten, L. (1998, July). Gravitational Radiation and Rotation of Accreting Neutron Stars. ApJ 501, L89+.

Bisnovatyi-Kogan, G. S. and B. V. Komberg (1974). Pulsars and close binary systems. Soviet Astronomy 18, 217–+.

Blandford, R. and S. A. Teukolsky (1976, April). Arrival-time analysis for a pulsar in a binary system. ApJ 205, 580–591.

Boersma, J. (1961). Mathematical theory of the two-body problem with one of the masses decreasing with time. Bull. Astron. Inst. Netherlands 15, 291–301.

Bozzo, E., M. Falanga, A. Papitto, L. Stella, R. Perna, D. Lazzati, G. Israel, S. Campana, V. Mangano, T. Di Salvo, and L. Burderi (2007, December). X-ray eclipse time delays in 4U 2129+47. A&A 476, 301–306.

Bradt, H. V. D. and J. E. McClintock (1983). The optical counterparts of compact galactic X-ray sources. ARA&A 21, 13–66.

Brandt, W. M. and G. Matt (1994, June). Iron K-Alpha Lines from Ionized Discs in Z-Type X-Ray. MNRAS 268, 1051–+.

Burderi, L., F. D'Antona, and M. Burgay (2002, July). PSR J1740-5340: Accretion Inhibited by Radio Ejection in a Binary Millisecond Pulsar in the Globular Cluster NGC 6397. ApJ 574, 325–331.

Burderi, L., T. Di Salvo, F. D'Antona, N. R. Robba, and V. Testa (2003, June). The optical counterpart to SAX J1808.4-3658 in quiescence: Evidence of an active radio pulsar? A&A 404, L43–L46.

Burderi, L., T. Di Salvo, G. Lavagetto, M. T. Menna, A. Papitto, A. Riggio, R. Iaria, F. D'Antona, N. R. Robba, and L. Stella (2007, March). Timing an Accreting Millisecond Pulsar: Measuring the Accretion Torque in IGR J00291+5934. ApJ 657, 961–966.

Burderi, L., T. Di Salvo, M. T. Menna, A. Riggio, and A. Papitto (2006, December). Order in the Chaos: Spin-up and Spin-down during the 2002 Outburst of SAX J1808.4-3658. ApJ 653, L133–L136.

Burderi, L., A. Possenti, M. Colpi, T. Di Salvo, and N. D'Amico (1999, July). Neutron Stars with Submillisecond Periods: A Population of High-Mass Objects? ApJ 519, 285–290.

Burderi, L., A. Possenti, F. D'Antona, T. Di Salvo, M. Burgay, L. Stella, M. T. Menna, R. Iaria, S. Campana, and N. d'Amico (2001, October). Where May Ultrafast Rotating Neutron Stars Be Hidden? ApJ 560, L71–L74.

Burderi, L., A. Riggio, T. Di Salvo, A. Papitto, M. T. Menna, A. D'Ai', and R. Iaria (2009, February). Timing of the 2008 Outburst of SAX J1808.4-3658 with XMM-Newton: A Stable Orbital Period Derivative over Ten Years. ArXiv e-prints.

Burgay, M., L. Burderi, A. Possenti, N. D'Amico, R. N. Manchester, A. G. Lyne, F. Camilo, and S. Campana (2003, June). A Search for Pulsars in Quiescent Soft X-Ray Transients. I. ApJ 589, 902–910.

Burgay, M., B. C. Joshi, N. D'Amico, A. Possenti, A. G. Lyne, R. N. Manchester, M. A. McLaughlin, M. Kramer, F. Camilo, and P. C. C. Freire (2006, May). The Parkes High-Latitude pulsar survey. MNRAS 368, 283–292.

Cackett, E. M., J. M. Miller, S. Bhattacharyya, J. E. Grindlay, J. Homan, M. van der Klis, M. C. Miller, T. E. Strohmayer, and R. Wijnands (2008, February). Relativistic Iron Emission Lines in Neutron Star Low-Mass X-Ray Binaries as Probes of Neutron Star Radii. ApJ 674, 415–420.

Casella, P., D. Altamirano, A. Patruno, R. Wijnands, and M. van der Klis (2008, February). Discovery of Coherent Millisecond X-Ray Pulsations in Aquila X-1. ApJ 674, L41–L44.

Chadwick, J. (1932). Possible existence of a neutron. Nature 129, 312.

Chakrabarty, D. (2008, September). The Spin Distribution of Millisecond X-ray Pulsars. ArXiv e-prints, 0809.4031.

Chakrabarty, D. and E. H. Morgan (1998, July). The two-hour orbit of a binary millisecond X-ray pulsar. Nature 394, 346–348.

Chakrabarty, D., E. H. Morgan, M. P. Muno, D. K. Galloway, R. Wijnands, M. van der Klis, and C. B. Markwardt (2003, July). Nuclear-powered millisecond pulsars and the maximum spin frequency of neutron stars. Nature 424, 42–44.

Chakrabarty, D., J. H. Swank, C. B. Markwardt, and E. Smith (2008, August). Accreting Millisecond Pulsar IGR J00291-5934 in Outburst Again. The Astronomer's Telegram 1660, 1–+.

Chandrasekhar, S. (1931, July). The Maximum Mass of Ideal White Dwarfs. ApJ 74, 81–+.

Chung, C. T. Y., D. K. Galloway, and A. Melatos (2008, November). Does the accreting millisecond pulsar XTE J1814-338 precess? MNRAS 391, 254–267.

Cook, G. B., S. L. Shapiro, and S. A. Teukolsky (1994, April). Rapidly rotating neutron stars in general relativity: Realistic equations of state. ApJ 424, 823–845.

D'Amico, N., A. Possenti, R. N. Manchester, J. Sarkissian, A. G. Lyne, and F. Camilo (2001, November). An Eclipsing Millisecond Pulsar with a Possible Main-Sequence Companion in NGC 6397. ApJ 561, L89–L92.

Damour, T. and J. H. Taylor (1991, September). Strong-field tests of relativistic gravity and binary pulsars. NASA STI/Recon Technical Report N 92, 19818–+.

D'Avanzo, P., S. Campana, S. Covino, G. L. Israel, L. Stella, and G. Andreuzzi (2007, September). The optical counterpart of IGR J00291+5934 in quiescence. A&A 472, 881–885.

Deloye, C. J. (2008, February). The Connection Between Low-Mass X-ray Binaries and (Millisecond) Pulsars: A Binary Evolution Perspective. In C. Bassa, Z. Wang, A. Cumming, and V. M. Kaspi (Eds.), 40 Years of Pulsars: Millisecond Pulsars, Magnetars and More, Volume 983 of American Institute of Physics Conference Series, pp. 501–509.

Di Salvo, T. and L. Burderi (2003, January). Constraints on the neutron star magnetic field of the two X-ray transients SAX J1808.4-3658 and Aql X-1. A&A 397, 723–727.

Di Salvo, T., L. Burderi, F. D'Antona, and N. Robba (2005, October). Accretion and Magneto-Dipole Emission in Fast-Rotating Neutron Stars: New Spin-Equilibrium Lines. In L. Burderi, L. A. Antonelli, F. D'Antona, T. Di Salvo, G. L. Israel, L. Piersanti, A. Tornambè, and O. Straniero (Eds.), Interacting Binaries: Accretion, Evolution, and Outcomes, Volume 797 of American Institute of Physics Conference Series, pp. 95–102.

Di Salvo, T., L. Burderi, A. Riggio, A. Papitto, and M. T. Menna (2008a, October). Orbital evolution of an accreting millisecond pulsar: witnessing the banquet of a hidden black widow? MNRAS 389, 1851–1857.

Di Salvo, T., L. Burderi, A. Riggio, A. Papitto, and M. T. Menna (2008b, September). Order in the chaos? The strange case of accreting millisecond pulsars. In American Institute of Physics Conference Series, Volume 1054 of American Institute of Physics Conference Series, pp. 173–182.

Di Salvo, T., R. Iaria, M. Méndez, L. Burderi, G. Lavagetto, N. R. Robba, L. Stella, and M. van der Klis (2005, April). A Broad Iron Line in the Chandra High Energy Transmission Grating Spectrum of 4U 1705-44. ApJ 623, L121–L124.

Eckert, D., R. Walter, P. Kretschmar, M. Mas-Hesse, G. G. C. Palumbo, J.-P. Roques, P. Ubertini, and C. Winkler (2004, December). IGR J00291+5934, a new X-ray transient discovered with INTEGRAL. The Astronomer's Telegram 352, 1–+.

Ehle, M., M. G. Breitfellner, L. Tomas, M. Santos Lleo, E. Verdugo, P. G. Jonker, G. Nelemans, P. Groot, M. van der Klis, J. Hjorth, A. Delsanti, B. Stappers, and M. Calkins (2002, April). XTE J1751-305. IAU Circ. 7872, 1–+.

Fabian, A. C., M. J. Rees, L. Stella, and N. E. White (1989, May). X-ray fluorescence from the inner disc in Cygnus X-1. MNRAS 238, 729–736.

Falanga, M., J. M. Bonnet-Bidaud, J. Poutanen, R. Farinelli, A. Martocchia, P. Goldoni, J. L. Qu, L. Kuiper, and A. Goldwurm (2005, June). INTEGRAL spectroscopy of the accreting millisecond pulsar XTE J1807-294 in outburst. A&A 436, 647–652.

Falanga, M., L. Kuiper, J. Poutanen, E. W. Bonning, W. Hermsen, T. Di Salvo, P. Goldoni, A. Goldwurm, S. E. Shaw, and L. Stella (2005, December). INTEGRAL and RXTE observations of accreting millisecond pulsar IGR J00291+5934 in outburst. A&A 444, 15–24.

Ferraro, F. R., A. Possenti, N. D'Amico, and E. Sabbi (2001, November). The Bright Optical Companion to the Eclipsing Millisecond Pulsar in NGC 6397. ApJ 561, L93–L96.

Finzi, A. and R. A. Wolf (1969, February). Possible Conversion of Rotational Energy of the Neutron Star in the Crab Nebula Into Energy of Relativistic Electrons. ApJ 155, L107+.

Fowler, R. H. (1926). On dense matter. MNRAS 87, 114–122.

Frank, J., A. King, and D. J. Raine (2002). Accretion Power in Astrophysics: Third Edition. Accretion Power in Astrophysics, by Juhan Frank and Andrew King and Derek Raine, pp. 398. ISBN 0521620538. Cambridge, UK: Cambridge University Press, February 2002.

Fruchter, A. S., D. R. Stinebring, and J. H. Taylor (1988). A millisecond pulsar in an eclipsing binary. Nature 333, 237–239.

Galloway, D. K. (2006, June). Accretion-powered Millisecond Pulsar Outbursts. In F. D'Amico, J. Braga, and R. E. Rothschild (Eds.), The Transient Milky Way: A Perspective for MIRAX, Volume 840 of American Institute of Physics Conference Series, pp. 50–54.

Galloway, D. K., D. Chakrabarty, E. H. Morgan, and R. A. Remillard (2002, September). Discovery of a High-Latitude Accreting Millisecond Pulsar in an Ultracompact Binary. ApJ 576, L137–L140.

Galloway, D. K. and A. Cumming (2006, November). Helium-rich Thermonuclear Bursts and the Distance to the Accretion-powered Millisecond Pulsar SAX J1808.4-3658. ApJ 652, 559–568.

Galloway, D. K., A. Cumming, and D. Chakrabarty (2004, August). The fuel composition in thermonuclear bursts from millisecond X-ray pulsars. In Bulletin of the American Astronomical Society, Volume 36 of Bulletin of the American Astronomical Society, pp. 954–+.

Galloway, D. K., C. B. Markwardt, E. H. Morgan, D. Chakrabarty, and T. E. Strohmayer (2005a, March). Discovery of the Accretion-powered Millisecond X-Ray Pulsar IGR J00291+5934. ApJ 622, L45–L48.

Galloway, D. K., C. B. Markwardt, E. H. Morgan, D. Chakrabarty, and T. E. Strohmayer (2005b, March). Discovery of the Accretion-powered Millisecond X-Ray Pulsar IGR J00291+5934. ApJ 622, L45–L48.

Gamow, G. (1938). Nuclear Energy Sources and Stellar Evolution. Phys.Rev. 53, 595.

Ghosh, P. (1996, March). Disk Diagnostics and Torque Mapping of X-Ray Pulsars: BATSE Observations of A0535+262. ApJ 459, 244–+.

Ghosh, P. (2007). Rotation and Accretion Powered Pulsars. Rotation and Accretion Powered Pulsars: World Scientific Series in Astronomy and Astrophysics – Vol. 10. Edited by Pranab Ghosh. ISBN-10 981-02-4744-3; ISBN-13 978-981-02-4744-7. Published by World Scientific Publishing Co., Pte. Ltd., Singapore, 2007.

Ghosh, P. and F. K. Lamb (1979a). Accretion by rotating magnetic neutron stars. II - Radial and vertical structure of the transition zone in disk accretion. ApJ 232, 259–276.

Ghosh, P. and F. K. Lamb (1979b). Accretion by rotating magnetic neutron stars. III - Accretion torques and period changes in pulsating X-ray sources. ApJ 234, 296–316.

Giacconi, R., H. Gursky, and P. F.R. (1962). Evidence for X-rays from Sources outside the Solar System. Phys.Rev. 9, 439.

Giacconi, R., H. Gursky, E. Kellogg, E. Schreier, and H. Tananbaum (1971). Discovery of Periodic X-Ray Pulsations in Centaurus X-3 from UHURU. ApJ 167, L67+.

Gierliński, M., C. Done, and D. Barret (2002, March). Phase-resolved X-ray spectroscopy of the millisecond pulsar SAX J1808.4-3658. MNRAS 331, 141–153.

Gierliński, M. and J. Poutanen (2005, June). Physics of accretion in the millisecond pulsar XTE J1751-305. MNRAS 359, 1261–1276.

Giles, A. B., J. G. Greenhill, K. M. Hill, and E. Sanders (2005, August). The optical counterpart of XTE J0929-314: the third transient millisecond X-ray pulsar. MNRAS 361, 1180–1186.

Gilfanov, M., M. Revnivtsev, R. Sunyaev, and E. Churazov (1998, October). The millisecond X-ray pulsar/burster SAX J1808.4-3658: the outburst light curve and the power law spectrum. A&A 338, L83–L86.

Gold, T. (1968). Rotating Neutron Stars as the Origin of the Pulsating Radio Sources. Nature 218, 731–+.

Goldreich, P. and W. H. Julian (1969, August). Pulsar Electrodynamics. ApJ 157, 869–+.

Grindlay, J. E. (1984). Globular Cluster Origin of X-Ray Bursters. In S. E. Woosley (Ed.), American Institute of Physics Conference Series, Volume 115 of American Institute of Physics Conference Series, pp. 306–+.

Hameury, J. M., A. R. King, J. P. Lasota, and F. Raison (1993, September). Structure and Evolution of X-Ray Heated Compact Binaries. A&A 277, 81–+.

Harding, A. K., A. G. Muslimov, and B. Zhang (2002, September). Regimes of Pulsar Pair Formation and Particle Energetics. ApJ 576, 366–375.

Hartman, J. M., A. Patruno, D. Chakrabarty, D. L. Kaplan, C. B. Markwardt, E. H. Morgan, P. S. Ray, M. van der Klis, and R. Wijnands (2008, March). The Long-Term Evolution of the Spin, Pulse Shape, and Orbit of the Accretion-powered Millisecond Pulsar SAX J1808.4-3658. ApJ 675, 1468–1486.

Heindl, W. A. and D. M. Smith (1998, October). The X-Ray Spectrum of SAX J1808.4-3658. ApJ 506, L35–L38.

Hessels, J. W. T., S. M. Ransom, I. H. Stairs, P. C. C. Freire, V. M. Kaspi, and F. Camilo (2006, March). A Radio Pulsar Spinning at 716 Hz. Science 311, 1901–1904.

Hewish, A., S. J. Bell, J. D. Pilkington, P. F. Scott, and R. A. Collins (1968). Observation of a Rapidly Pulsating Radio Source. Nature 217, 709–+.

Homer, L., P. A. Charles, D. Chakrabarty, and L. van Zyl (2001, August). The optical counterpart to SAX J1808.4-3658: observations in quiescence. MNRAS 325, 1471–1476.

Hu, C.-P., Y. Chou, and Y.-Y. Chung (2008, June). A Parameterization Study of the Properties of the X-Ray Dips in the Low-Mass X-Ray Binary X1916-053. ApJ 680, 1405–1411.

Illarionov, A. F. and R. A. Sunyaev (1975). Why the Number of Galactic X-ray Stars Is so Small? A&A 39, 185–+.

in 't Zand, J. J. M., P. Lowes, J. Heise, A. Bazzano, and P. Ubertini (2002, April). XTE J1751-305. IAU Circ. 7867, 2–+.

in't Zand, J. J. M., R. Cornelisse, E. Kuulkers, J. Heise, L. Kuiper, A. Bazzano, M. Cocchi, J. M. Muller, L. Natalucci, M. J. S. Smith, and P. Ubertini (2001, June). The first outburst of SAX J1808.4-3658 revisited. A&A 372, 916–921.

Juett, A. M. and D. Chakrabarty (2003, December). X-Ray Spectroscopy of the Low-Mass X-Ray Binaries 2S 0918-549 and 4U 1543-624: Evidence for Neon-rich Degenerate Donors. ApJ 599, 498–508.

Kaaret, P., E. H. Morgan, R. Vanderspek, and J. A. Tomsick (2006, February). Discovery of the Millisecond X-Ray Pulsar HETE J1900.1-2455. ApJ 638, 963–967.

Kaaret, P., Z. Prieskorn, J. J. M. in 't Zand, S. Brandt, N. Lund, S. Mereghetti, D. Götz, E. Kuulkers, and J. A. Tomsick (2007, March). Evidence of 1122 Hz X-Ray Burst Oscillations from the Neutron Star X-Ray Transient XTE J1739-285. ApJ 657, L97–L100.

Kallman, T. and N. E. White (1989, June). Iron K lines from low-mass X-ray binaries. ApJ 341, 955–960.

Kaspi, V. M., M. S. E. Roberts, and A. K. Harding (2004, February). Isolated Neutron Stars. ArXiv Astrophysics e-prints, 0402136.

King, A. R. (1988, March). The evolution of compact binaries. QJRAS 29, 1–25.

King, A. R. (2006). Accretion in compact binaries, pp. 507–546. Compact stellar X-ray sources.

King, A. R., M. E. Beer, D. J. Rolfe, K. Schenker, and J. M. Skipp (2005, April). The population of black widow pulsars. MNRAS 358, 1501–1504.

King, A. R., M. B. Davies, and M. E. Beer (2003, October). Black widow pulsars: the price of promiscuity. MNRAS 345, 678–682.

King, A. R., U. Kolb, and L. Burderi (1996). Black Hole Binaries and X-Ray Transients. ApJ 464, L127+.

King, A. R., J. E. Pringle, and M. Livio (2007). Accretion disc viscosity: how big is alpha? MNRAS 376, 1740–1746.

King, A. R. and H. Ritter (1998). The light curves of soft X-ray transients. MNRAS 293, L42–L48.

Krauss, M. I., Z. Wang, A. Dullighan, A. M. Juett, D. L. Kaplan, D. Chakrabarty, M. H. van Kerkwijk, D. Steeghs, P. G. Jonker, and C. B. Markwardt (2005, July). The X-Ray Position and Optical Counterpart of the Accretion-powered Millisecond Pulsar XTE J1814-338. ApJ 627, 910–914.

Krimm, H. A., C. B. Markwardt, C. J. Deloye, P. Romano, D. Chakrabarty, S. Campana, J. R. Cummings, D. K. Galloway, N. Gehrels, J. M. Hartman, P. Kaaret, E. H. Morgan, and J. Tueller (2007, October). Discovery of the Accretion-powered Millisecond Pulsar SWIFT J1756.9-2508 with a Low-Mass Companion. ApJ 668, L147–L150.

Kubota, A., Y. Tanaka, K. Makishima, Y. Ueda, T. Dotani, H. Inoue, and K. Yamaoka (1998, December). Evidence for a Black Hole in the X-Ray Transient GRS 1009-45. PASJ 50, 667–673.

Lamb, F. K. and S. Boutloukos (2007, May). Accreting Neutron Stars in Low-Mass X-Ray Binary Systems. ArXiv e-prints, 0705.0155.

Lamb, F. K., C. J. Pethick, and D. Pines (1973, August). A Model for Compact X-Ray Sources: Accretion by Rotating Magnetic Stars. ApJ 184, 271–290.

Landau, L. D. and E. M. Lifshitz (1962). The Classical Theory of Fields. Oxford, Pergamon.

Landau, L. D. and E. M. Lifsits (1976). Meccanica Quantistica. Teoria non relativistica. Roma, Italia: Editori Riuniti.

Lasota, J.-P. (2001). The disc instability model of dwarf novae and low-mass X-ray binary transients. New Astronomy Review 45, 449–508.

Lattimer, J. M. and M. Prakash (2001, March). Neutron Star Structure and the Equation of State. ApJ 550, 426–442.

Lattimer, J. M. and M. Prakash (2007, April). Neutron star observations: Prognosis for equation of state constraints. Phys. Rep. 442, 109–165.

Leahy, D. A. (1987, June). Searches for pulsed emission - Improved determination of period and amplitude from epoch folding for sinusoidal signals. A&A 180, 275–277.

Leahy, D. A., W. Darbro, R. F. Elsner, M. C. Weisskopf, S. Kahn, P. G. Sutherland, and J. E. Grindlay (1983, March). On searches for pulsed emission with application to four globular cluster X-ray sources - NGC 1851, 6441, 6624, and 6712. ApJ 266, 160–170.

Linares, M., R. Wijnands, and M. van der Klis (2007, April). XTE J1751-305 going back to its quiescent state. The Astronomer's Telegram 1055, 1–+.

Lindblom, L. (1984, March). Limits on the gravitational redshift form neutron stars. ApJ 278, 364–368.

Liu, Q. Z., J. van Paradijs, and E. P. J. van den Heuvel (2007a). A catalogue of low-mass X-ray binaries in the Galaxy, LMC, and SMC (Fourth edition). A&A 469, 807–810.

Liu, Q. Z., J. van Paradijs, and E. P. J. van den Heuvel (2007b, July). A catalogue of low-mass X-ray binaries in the Galaxy, LMC, and SMC (Fourth edition). A&A 469, 807–810.

Lorimer, D. R., M. A. McLaughlin, D. J. Champion, and I. H. Stairs (2007, July). PSR J1453+1902 and the radio luminosities of solitary versus binary millisecond pulsars. MNRAS 379, 282–288.

Lyne, A. G. and F. Graham-Smith (1990). Pulsar astronomy. Cambridge, England and New York, Cambridge University Press (Cambridge Astrophysics Series, No. 16), 1990, 285 p.

Manchester, R. N., G. B. Hobbs, A. Teoh, and M. Hobbs (2005, April). The Australia Telescope National Facility Pulsar Catalogue. AJ 129, 1993–2006.

Manchester, R. N. and W. L. Peters (1972, April). Pulsar Parameters from Timing Observations. ApJ 173, 221–+.

Markwardt, C. B., M. Juda, and J. H. Swank (2003, March). XTE J1807-294. IAU Circ. 8095, 2–+.

Markwardt, C. B., T. E. Strohmayer, and J. H. Swank (2003, June). Revised Orbit and Burst Oscillations from the Millisecond Pulsar XTE J1814-338. The Astronomer's Telegram 164, 1–+.

Markwardt, C. B. and J. H. Swank (2003, June). XTE J1814-338. IAU Circ. 8144, 1–+.

Markwardt, C. B., J. H. Swank, T. E. Strohmayer, J. J. M. in 't Zand, and F. E. Marshall (2002, August). Discovery of a Second Millisecond Accreting Pulsar: XTE J1751-305. ApJ 575, L21–L24.

Méndez, M. and T. Belloni (2007, October). Is there a link between the neutron-star spin and the frequency of the kilohertz quasi-periodic oscillations? MNRAS 381, 790–796.

Miller, J. M., A. C. Fabian, C. S. Reynolds, M. A. Nowak, J. Homan, M. J. Freyberg, M. Ehle, T. Belloni, R. Wijnands, M. van der Klis, P. A. Charles, and W. H. G. Lewin (2004, May). Evidence of Black Hole Spin in GX 339-4: XMM-Newton/EPIC-pn and RXTE Spectroscopy of the Very High State. ApJ 606, L131–L134.

Nandra, K., I. M. George, R. F. Mushotzky, T. J. Turner, and T. Yaqoob (1997, March). ASCA Observations of Seyfert 1 Galaxies. II. Relativistic Iron K alpha Emission. ApJ 477, 602–+.

Nowak, M. A., A. Paizis, J. Wilms, K. Ebisawa, T. J.-L. Courvoisier, J. Rodriguez, R. Walter, M. del Santo, and P. Ubertini (2004, December). IGR J00291+5934: an observation with Chandra. The Astronomer's Telegram 369, 1–+.

Oppenheimer, J. R. and R. Serber (1938). On the Stability of Stellar Neutron Cores. Phys.Rev. 54, 540.

Oppenheimer, J. R. and G. M. Volkoff (1939). On Massive Neutron Cores. Phys.Rev. 55, 374.

Ostriker, J. P. and J. E. Gunn (1969, September). On the Nature of Pulsars. I. Theory. ApJ 157, 1395–+.

Paczyński, B. (1971). Evolutionary Processes in Close Binary Systems. ARA&A 9, 183–+.

Papitto, A., L. Burderi, T. Di Salvo, M. T. Menna, and L. Stella (2005, October). Temporal Analysis of the Millisecond X-ray Pulsar SAX J1808.4-3658 During the 2000 Outburst. In L. Burderi, L. A. Antonelli, F. D'Antona, T. Di Salvo, G. L. Israel, L. Piersanti, A. Tornambè, and O. Straniero (Eds.), Interacting Binaries: Accretion, Evolution, and Outcomes, Volume 797 of American Institute of Physics Conference Series, pp. 110–115.

Papitto, A., T. Di Salvo, L. Burderi, M. T. Menna, G. Lavagetto, and A. Riggio (2007, March). Timing of the accreting millisecond pulsar XTE J1814-338. MNRAS 375, 971–976.

Papitto, A., T. Di Salvo, A. D'Aı, R. Iaria, L. Burderi, A. Riggio, M. T. Menna, and N. R. Robba (2009, January). XMM-Newton detects a relativistically broadened iron line in the spectrum of the ms X-ray pulsar SAX J1808.4-3658. A&A 493, L39–L43.

Papitto, A., M. T. Menna, L. Burderi, T. Di Salvo, F. D'Antona, and N. R. Robba (2005, March). Revised Orbital Parameters of the Accreting Millisecond Pulsar SAX J1808.4-3658. ApJ 621, L113–L116.

Papitto, A., M. T. Menna, L. Burderi, T. Di Salvo, and A. Riggio (2008, January). Measuring the spin up of the accreting millisecond pulsar XTEJ1751-305. MNRAS 383, 411–416.

Papitto, A., A. Riggio, T. Di Salvo, L. Burderi, and M. Menna (2008, October). Enlightening differences in AMSPs behavior: XTE J1751–305 vs. XTE J1814–338. In American Institute of Physics Conference Series, Volume 1068 of American Institute of Physics Conference Series, pp. 51–54.

Patruno, A., J. M. Hartman, R. Wijnands, M. van der Klis, D. Chakrabarty, E. H. Morgan, and C. Markwardt (2008, October). Pulse timing of the ongoing outburst of SAX J1808.4-3658 with RXTE. The Astronomer's Telegram 1760, 1–+.

Podsiadlowski, P. (1991, March). Irradiation-driven mass transfer low-mass X-ray binaries. Nature 350, 136–138.

Podsiadlowski, P., S. Rappaport, and E. D. Pfahl (2002). Evolutionary Sequences for Low- and Intermediate-Mass X-Ray Binaries. ApJ 565, 1107–1133.

Poutanen, J. (2006). Accretion-powered millisecond pulsars. Advances in Space Research 38, 2697–2703.

Poutanen, J. and A. M. Beloborodov (2006, December). Pulse profiles of millisecond pulsars and their Fourier amplitudes. MNRAS 373, 836–844.

Psaltis, D. and D. Chakrabarty (1999, August). The Disk-Magnetosphere Interaction in the Accretion-powered Millisecond Pulsar SAX J1808.4-3658. ApJ 521, 332–340.

Radhakrishnan, V. and G. Srinivasan (1982). On the origin of the recently discovered ultra-rapid pulsar. Current Science 51, 1096–1099.

Rappaport, S. A., J. M. Fregeau, and H. Spruit (2004, May). Accretion onto Fast X-Ray Pulsars. ApJ 606, 436–443.

Rhoades, C. E. and R. Ruffini (1974). Maximum mass of a neutron star. Physical Review Letters 32, 324–327.

Riggio, A., T. Di Salvo, L. Burderi, R. Iaria, A. Papitto, M. T. Menna, and G. Lavagetto (2007, December). Precise determination of orbital parameters in system with slowly drifting phases: application to the case of XTE J1807-294. MNRAS 382, 1751–1758.

Riggio, A., T. Di Salvo, L. Burderi, M. T. Menna, A. Papitto, R. Iaria, and G. Lavagetto (2008, May). Spin-up and Phase Fluctuations in the Timing of the Accreting Millisecond Pulsar XTE J1807-294. ApJ 678, 1273–1278.

Ritter, H. (2008, May). Is irradiation important for the secular evolution of low-mass X-ray binaries? New Astronomy Review 51, 869–877.

Ritter, H. and U. Kolb (2008, July). Cataclysmic Binaries, LMXBs, and related objects (Ritter+, 2008). VizieR Online Data Catalog 1, 2018–+.

Romanova, M. M., G. V. Ustyugova, A. V. Koldoba, and R. V. E. Lovelace (2002). Magnetohydrodynamic Simulations of Disk-Magnetized Star Interactions in the Quiescent Regime: Funnel Flows and Angular Momentum Transport. ApJ 578, 420–438.

Romanova, M. M., G. V. Ustyugova, A. V. Koldoba, and R. V. E. Lovelace (2004a, December). The Propeller Regime of Disk Accretion to a Rapidly Rotating Magnetized Star. ApJ 616, L151–L154.

Romanova, M. M., G. V. Ustyugova, A. V. Koldoba, and R. V. E. Lovelace (2004b, December). The Propeller Regime of Disk Accretion to a Rapidly Rotating Magnetized Star. ApJ 616, L151–L154.

Romanova, M. M., G. V. Ustyugova, A. V. Koldoba, and R. V. E. Lovelace (2004c, August). Three-dimensional Simulations of Disk Accretion to an Inclined Dipole. II. Hot Spots and Variability. ApJ 610, 920–932.

Romanova, M. M., G. V. Ustyugova, A. V. Koldoba, and R. V. E. Lovelace (2004d, August). Three-dimensional Simulations of Disk Accretion to an Inclined Dipole. II. Hot Spots and Variability. ApJ 610, 920–932.

Romanova, M. M., G. V. Ustyugova, A. V. Koldoba, J. V. Wick, and R. V. E. Lovelace (2003, October). Three-dimensional Simulations of Disk Accretion to an Inclined Dipole. I. Magnetospheric Flows at Different Θ. ApJ 595, 1009–1031.

Ruderman, M., J. Shaham, and M. Tavani (1989). Accretion turnoff and rapid evaporation of very light secondaries in low-mass X-ray binaries. ApJ 336, 507–518.

Ruderman, M. A. and P. G. Sutherland (1975). Theory of pulsars - Polar caps, sparks, and coherent microwave radiation. ApJ 196, 51–72.

Rupen, M. P., V. Dhawan, and A. J. Mioduszewski (2004, December). Further radio observations of IGR J00291+5934. The Astronomer's Telegram 364, 1–+.

Rupen, M. P., V. Dhawan, A. J. Mioduszewski, B. W. Stappers, and B. M. Gaensler (2002, October). Sax J1808.4-3658. IAU Circ. 7997, 2–+.

Rybicki, G. B. and A. P. Lightman (1981). Radiative Processes in Astrophysics. pp. 382. ISBN 0-47-104815-1. Wiley, New York, NY, 1981.

Schreier, E., R. Levinson, H. Gursky, E. Kellogg, H. Tananbaum, and R. Giacconi (1972). Evidence for the Binary Nature of Centaurus X-3 from UHURU X-Ray Observations. ApJ 172, L79+.

Shakura, N. I. and R. A. Syunyaev (1973). Black holes in binary systems. Observational appearance. A&A 24, 337–355.

Shklovskii, I. S. (1967). The Nature of the X-Ray Source Sco X-1. AZh 44, 930–+.

Smarr, L. L. and R. Blandford (1976). The binary pulsar - Physical processes, possible companions, and evolutionary histories. ApJ 207, 574–588.

Staelin, D. H. and E. C. Reifenstein (1968, December). Pulsating radio sources near the Crab Nebula. Science 162, 1481–1483.

Stappers, B. W., M. Bailes, A. G. Lyne, R. N. Manchester, N. D'Amico, T. M. Tauris, D. R. Lorimer, S. Johnston, and J. S. Sandhu (1996, July). Probing the Eclipse Region of a Binary Millisecond Pulsar. ApJ 465, L119+.

Strohmayer, T. E., C. B. Markwardt, J. H. Swank, and J. in't Zand (2003, October). X-Ray Bursts from the Accreting Millisecond Pulsar XTE J1814-338. ApJ 596, L67–L70.

Swank, J. and C. Markwardt (2001). Populations of Transient Galactic Bulge X-ray Sources. In H. Inoue and H. Kunieda (Eds.), New Century of X-ray Astronomy, Volume 251 of Astronomical Society of the Pacific Conference Series, pp. 94–+.

Swank, J. H., C. B. Markwardt, and E. A. Smith (2005, March). RXTE PCA Observations of XTE J1751-305. The Astronomer's Telegram 449, 1–+.

Tauris, T. M. and E. P. J. van den Heuvel (2006). Formation and evolution of compact stellar X-ray sources, pp. 623–665. Compact stellar X-ray sources.

Tavani, M. (1991a, October). 'Hidden' millisecond pulsars. ApJ 379, L69–L73.

Tavani, M. (1991b, May). Orbital evolution of low-mass X-ray binaries due to radiation driven mass transfer. Nature 351, 39–41.

Usov, V. V. (2002). Two-stream Instability in Pulsar Magnetospheres. In W. Becker, H. Lesch, and J. Trümper (Eds.), Neutron Stars, Pulsars, and Supernova Remnants, pp. 240–+.

Ustyugova, G. V., A. V. Koldoba, M. M. Romanova, and R. V. E. Lovelace (2006, July). "Propeller" Regime of Disk Accretion to Rapidly Rotating Stars. ApJ 646, 304–318.

van der Klis, M. (1988). Fourier Techniques in X-ray Timing. In Timing Neutron Stars, eds. H. Ogelman and E.P.J. van den Heuvel. NATO ASI Series C, Vol. 262, p. 27-70. Dordrecht: Kluwer, 1988., pp. 27–70.

van der Klis, M., F. Jansen, J. van Paradijs, W. H. G. Lewin, E. P. J. van den Heuvel, J. E. Trumper, and M. Szatjno (1985, July). Intensity-dependent quasi-periodic oscillations in the X-ray flux of GX5 - 1. Nature 316, 225–230.

van Paradijs, J. (1996). On the Accretion Instability in Soft X-Ray Transients. ApJ 464, L139+.

van Straaten, S., M. van der Klis, and M. Méndez (2003, October). The Atoll Source States of 4U 1608-52. ApJ 596, 1155–1176.

van Straaten, S., M. van der Klis, and R. Wijnands (2005, January). Relations Between Timing Features and Colors in Accreting Millisecond Pulsars. ApJ 619, 455–482.

Vaughan, B. A., M. van der Klis, K. S. Wood, J. P. Norris, P. Hertz, P. F. Michelson, J. van Paradijs, W. H. G. Lewin, K. Mitsuda, and W. Penninx (1994, November). Searches for millisecond pulsations in low-mass X-ray binaries, 2. ApJ 435, 362–371.

Verbunt, F. (1993). Origin and evolution of X-ray binaries and binary radio pulsars. ARA&A 31, 93–127.

Verbunt, F. and E. P. J. van den Heuvel (1995). Formation and Evolution of Neutron Stars and Black Holes in Binaries, pp. 457. Cambridge University Press.

Verbunt, F. and C. Zwaan (1981, July). Magnetic braking in low-mass X-ray binaries. A&A 100, L7–L9.

Vietri, M. (2006). Astrofisica delle Alte Energie. Torino, Italia: Bollati Boringhieri.

Wang, Y.-M. (1987, September). Disc accretion by magnetized neutron stars - A reassessment of the torque. A&A 183, 257–264.

Wang, Y.-M. (1995, August). On the Torque Exerted by a Magnetically Threaded Accretion Disk. ApJ 449, L153+.

Wang, Y.-M. (1996). Location of the Inner Radius of a Magnetically Threaded Accretion Disk. ApJ 465, L111+.

Watts, A. L., A. Patruno, and M. van der Klis (2008, November). Coherence of Burst Oscillations and Accretion-Powered Pulsations in the Accreting Millisecond Pulsar XTE J1814-338. ApJ 688, L37–L40.

Watts, A. L., T. E. Strohmayer, and C. B. Markwardt (2005, November). Analysis of Variability in the Burst Oscillations of the Accreting Millisecond Pulsar XTE J1814-338. ApJ 634, 547–564.

White, N. E. and S. S. Holt (1982, June). Accretion disk coronae. ApJ 257, 318–337.

Wijnands, R. and M. van der Klis (1998, July). A millisecond pulsar in an X-ray binary system. Nature 394, 344–346.

Wijnands, R., M. van der Klis, J. Homan, D. Chakrabarty, C. B. Markwardt, and E. H. Morgan (2003, July). Quasi-periodic X-ray brightness fluctuations in an accreting millisecond pulsar. Nature 424, 44–47.

Zel'Dovich, Y. B. and N. I. Shakura (1969, October). X-Ray Emission Accompanying the Accretion of Gas by a Neutron Star. Soviet Astronomy 13, 175–+.